Development of Highly Efficient Thermally Activated Delayed Fluorescence Materials and Their Application in Organic Light-Emitting Diodes

李, 世淵

https://doi.org/10.15017/1500675

出版情報：九州大学, 2014, 博士（工学）, 課程博士
バージョン：
権利関係：全文ファイル公表済

2015

Doctoral thesis

Development of Highly Efficient Thermally Activated Delayed Fluorescence Materials and Their Application in Organic Light-Emitting Diodes

Sae Youn Lee

Department of Chemistry and Biochemistry

Graduate School of Engineering

Kyushu University

Table of contents

Table of contents

Chapter 3. Luminous Butterflies: Efficient Exciton Harvesting by Benzophenone Derivatives for Full-Color Delayed Fluorescence OLEDs

Chapter 4. X-Shaped Benzoylbenzophenone Derivatives with Crossed Donors and Acceptors for Highly Efficient Thermally Activated Delayed Fluorescence

Chapter 5. Thermally Activated Delayed Fluorescence Polymers for Efficient Solution-Processed Organic Light-Emitting Diodes

Chapter 1
General Introduction

Chapter 1
General Introduction

1.1 Organic Light-Emitting Diodes (OLEDs)

Recently, organic light-emitting diodes (OLEDs) have been the subject of intense development for application in next-generation displays and lighting due to their advantages of wide viewing angles, light weight, improved brightness, and the possibility for flexible panels.

In OLEDs, excitons are forming recombination of holes and electrons. The excitons loss their energy through the radiative decay process in an emitting layer (EML). In an electroluminescence (EL) process, recombined holes and electrons generate excitons with four different spin combination of one singlet (antiparallel spins) and three triplets (parallel spins). Therefore, statistically, 25% of singlet excitons 75% of triplets excitons are formed, resulting in different radiative decay processes (see more detail in section 1-2). The fundamental structure of OLEDs with carrier flow are shown in Fig. 1-1. Hole are injected into the hole conduction level (E_v) and electrons are injected into the electron conduction level (E_e) from anode and cathode layers. We call this phenomenon the carrier injection. Successively, these carriers are transported in hole-transporting layer (HTL) and electron-transporting layer (ETL) and injected into the interfaces between the organic layers should be reduced. Here, in the anode side, a hole-injection layer (HIL) having small energy gap to the work function of an anode layer and a HTL which transports holes to an EML are introduced for effective hole injection and transport to an EML. In the case of cathode side, an electron-injection layer (EIL) having rather deep E_e and an ETL with high electron mobility are introduced for effective electron injection and transport. This multilayer structure of OLEDs can improve carrier injection and transport efficiencies, resulted in recombination of holes and electrons in an EML. Furthermore, electron- and hole-blocking layers (EBL and HBL) with low E_e and E_v are widely introduced for the charge balance of holes and electrons, preventing carrier leakage from an EML to adjacent layers.

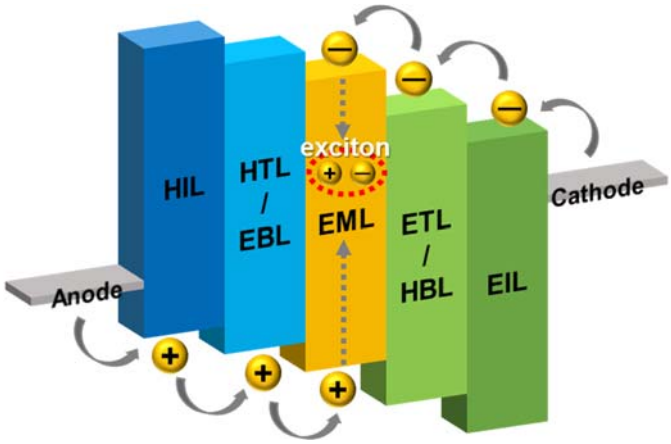

Figure 1-1. Operating process in OLEDs (HIL: hole-injection layer, HTL: hole-transport layer, EBL: electron-blocking layer, EML: emitting layer, ETL: electron-transport layer, HBL: hole-blocking layer, EIL: electron-injection layer).

The first study on OLEDs was reported in 1950 with Bernanaonose's observation of luminescence from organic dye-containing polymer thin films when applying a high alternating current (AC) voltage. Successively in 1965, emission of blue light was observed from an anthracene single crystal by applying a high voltage.[1)] During the study of these devices, the recombination of holes and electrons was found to result in the generation of both singlet and triplet excitons.[2)] However, single-crystal OLEDs were unsuitable for display applications because very high driving voltages are necessary for light emission. In 1982, OLEDs based on a thin film of anthracene fabricated by vacuum deposition were shown to emit light at a low voltage of 12 V.[3)]

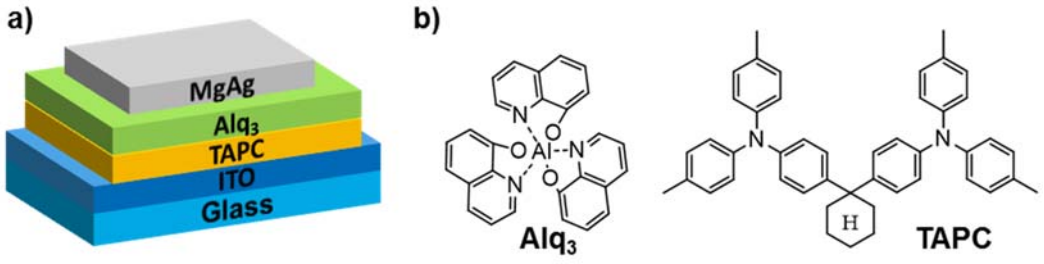

Figure 1-2. a) Structure of double layer OLED reported by C. W. Tang et al. b) Molecular structures of tris(8-quinolinolato)aluminum(III) (Alq_3) as emitter and 4,4'-cyclohexylidenebis[*N*,*N*-bis(4-methylphenyl)benzenamine] (TAPC) as hole-transport

Further advanced studies on multi-layer OLEDs were reported by C. W. Tang et al in 1987.[4] The OLED, using tris(8-quinolinolato)aluminium(III) (Alq_3) and aromatic amines as an ETL (EML) and a HTL, respectively, and Mg:Ag as a cathode, exhibited luminance of 1000 cd A^{-1} at 10 V and an external quantum efficiency (η_{ext}) of nearly 1% (Fig. 1-2). In later work, doping of dicyanomethylene (DCM) and coumarin in an EML, the emission color was well controlled with more than two times increase of η_{ext}.[5]

In addition, not only small-molecular materials but also polymer materials are being applied to thin-film OLEDs. In the early study using poly(vinylcarbazole) (PVK) as a host material, basic operation of EL had been confirmed.[6] In 1990s, polymer OLEDs based on poly(*p*-phenylenevinylene) (PPV) as an EML was reported by J. H. Brruoughes.[7] After that, various studies on luminescent polymer materials including polyphenylenes and polythiophenes were actively developed. In 1997, the first commercial application of OLEDs for a car radio system was realized. Nowadays, OLEDs have been widely used in mobile phones, tablet computers, lighting, and television. Since the first reports of OLEDs, various kinds of organic light-emitting materials have been designed and synthesized.

1.2 Luminescence Mechanism of Organic Materials

1.2.1 Fluorescence and Phosphorescence

The luminescence phenomena in organic materials can be explained by the following photophysical interpretation when the materials are excited by a light source. The absorption of a photon in an organic material causes an electron to be excited from its S_0 to an S_1. After photo-excitation, the excited electron losses its energy through photoluminescence (PL), intermolecular energy transfer, intramolecular energy transfer, isomerization, or dissociation (Fig. 1-3).[8] The PL efficiency of organic materials are estimated by PL quantum efficiency (Φ_{PL}) which is defined as photons emitted per photons absorbed by molecules. The luminescence can be more specifically described as fluorescence or phosphorescence. These two emission processes can be distinguished by the lifetime of their luminescence (τ). While τ for fluorescence ranges from 10^{-9} to 10^{-5} s, τ for phosphorescence is much longer and range from 10^{-6} to 10^{2} s (Table 1-1).

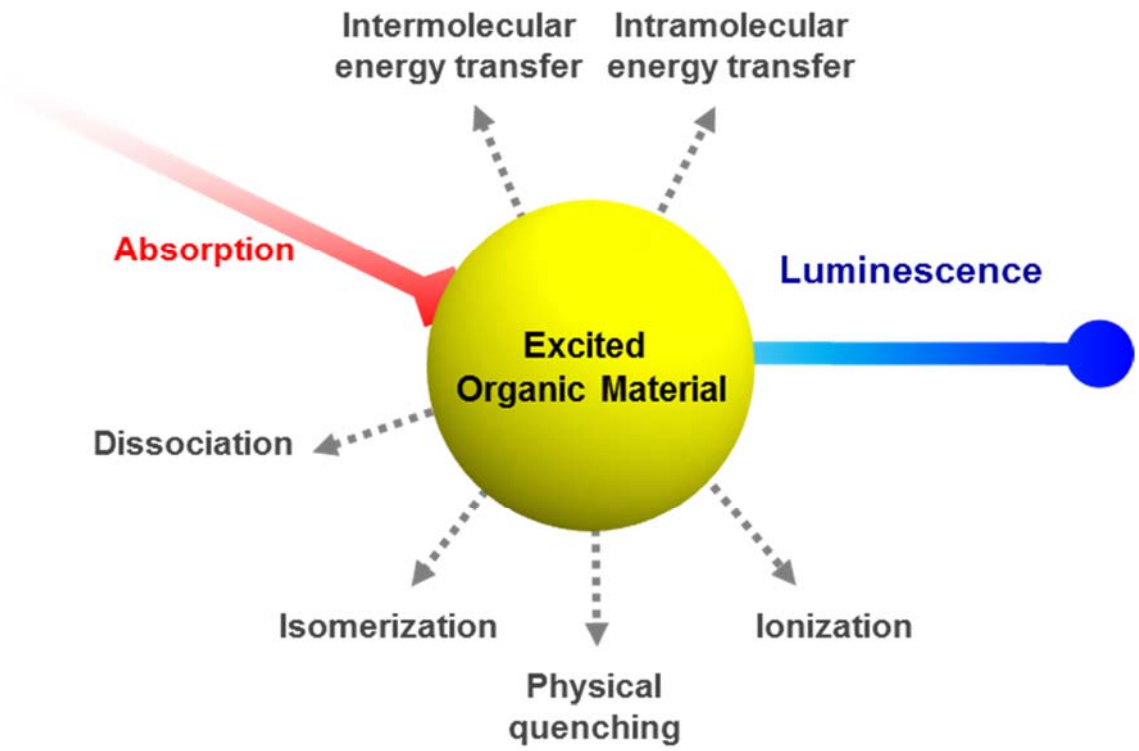

Figure 1-3. Relaxation routes of optically excited organic molecules.

Table 1-1. Transition time of absorption, internal conversion, intersystem crossing, fluorescence, phosphorescence and thermally activated delayed fluorescence (TADF).

	Transition time (s)
Absorption	10^{-15}
Internal conversion	$10^{-15} - 10^{-10}$
Fluorescence	$10^{-9} - 10^{-5}$
Intersystem crossing	$10^{-8} - 10^{-5}$
Phosphorescence	$10^{-6} - 10^{2}$
TADF	$10^{-6} - 10^{-2}$

In the case of fluorescence, excited electrons relax directly from a singlet excited state (S_1) to S_0 to produce light emission (Equ. 1-1). On the other hand, phosphorescence occurs from a triplet excited state (T_1), which is created by intersystem crossing (ISC) from S_1 (Equ. 1-2). Since phosphorescence is a spin forbidden process, the lifetime is usually longer than that of fluorescence.

$$\text{(Fluorescence)} \qquad S_0 + h\nu_{ex} \rightarrow S_1 \rightarrow S_0 + h\nu_{em} \qquad (1\text{-}1)$$

$$\text{(Phosphorescence)} \qquad S_0 + h\nu_{ex} \rightarrow S_1 \xrightarrow[\text{system crossing}]{\text{Inter}} T_1 \rightarrow S_0 + h\nu_{em} \qquad (1\text{-}2)$$

When luminescence is produced by electrical excitation, *i.e.*, EL, the emission can again result from both fluorescence and phosphorescence (Fig. 1-4). Fluorescent OLEDs utilize singlet excitons for luminescence, while phosphorescent OLEDs utilize triplet excitons for luminescence. Due to the branching ratio of singlet and triplet excitons, the production efficiency of singlet excitons is limited to 25%. In contrast, phosphorescent OLEDs can utilize

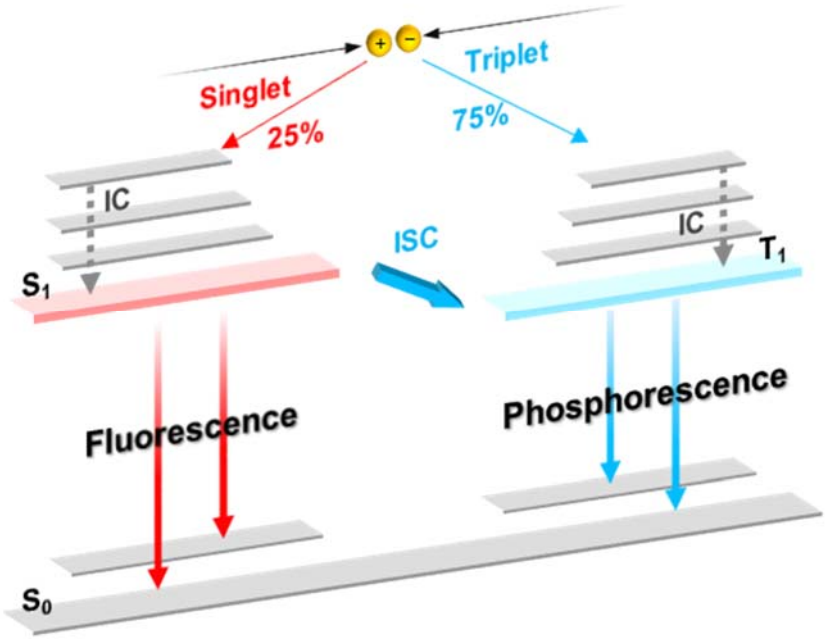

Figure 1-4. Jablonski diagram of electronic transitions after recombination of hole and electron for fluorescence (S_1−S_0), and phosphorescence (T_1−S_0).

both singlet and triplet excitons to for luminescence. Therefore, nearly 100% of electro-generated excitons can be harvested for luminescence.

Here, the η_{ext} of OLEDs is given by the following equation:

$$\eta_{ext} = \eta_{int} \times \eta_{out} = \gamma \times \eta_{ST} \times \Phi_{PL} \times \eta_{out} \qquad (1\text{-}3)$$

where γ is charge-balance factor, η_{ST} is exciton production efficiency, η_{int} is internal quantum efficiency, and η_{out} is light out-coupling efficiency (Fig. 1-5). To maximize η_{ext}, all of these factors should be nearly 100%. A high γ can be attained by the construction of appropriate multilayer structures.[9,10] High Φ_{PL} can be achieved by using emissive materials that have been developed by suppressing non-radiative recombination, and these materials are often doped into a wide energy gap host layer to minimize the quenching of excitons that usually occurs at high concentrations.

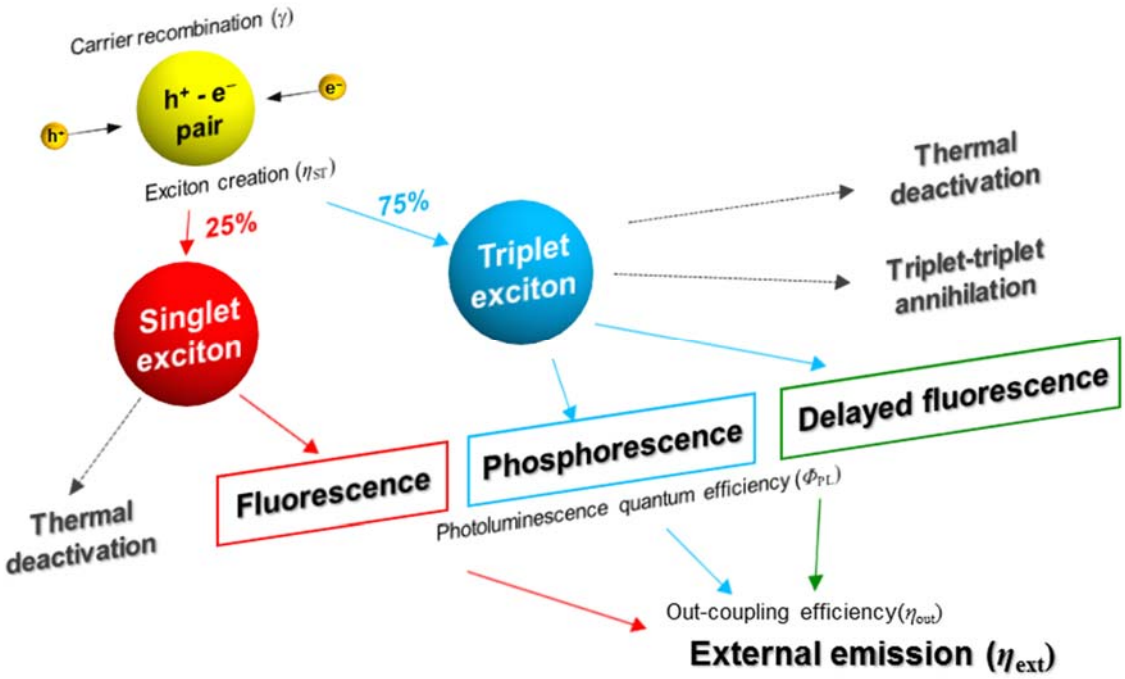

Figure 1-5. Schematic representation of OLEDs process: charge carrier recombination, production of molecular excitons, internal emissions of fluorescence, phosphorescence, and delayed fluorescence, and external emission.

Since singlet and triplet excitons are formed in the ratio of 1:3, η_{ST} for fluorescent materials is only 25%. Thus, the maximum η_{ext} of fluorescent OLEDs is limited to 5% assuming an η_{out} of about 20%, which results from optical reflections and losses in organic layers.[11] Meanwhile, phosphorescent OLEDs can utilize both singlet and triplet excitons for luminescence, allowing η_{ST} to reach nearly 100% and η_{ext} to reach 20%.[12] However, rather long τ of the phosphorescence process leads to strong non-radiative annihilations (See more detail in section 1.4).[13]

1.2.2 Thermally Activated Delayed Fluorescence (TADF)

To overcome the aforementioned disadvantages of fluorescent and phosphorescent OLEDs and further enhance η_{ext}, a new mechanism for achieving a high production efficiency of excitons at the S_1 in OLEDs has been proposed in our group: thermally activated delayed fluorescence (TADF, Fig. 1-6).[14]

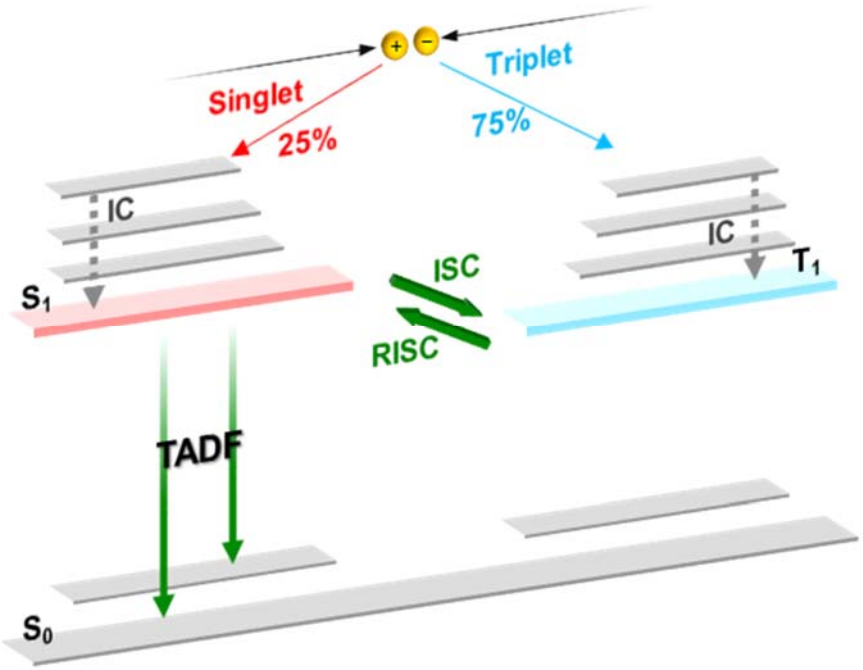

Figure 1-6. Jablonski diagram of electronic transitions after recombination of holes and electrons for TADF.

$$\text{(TADF)} \qquad S_0 + h\nu_{ex} \rightarrow S_1 \rightarrow T_1 \rightarrow S_1 \rightarrow S_0 + h\nu_{em} \qquad (1\text{-}4)$$

The emission pathway of TADF upon photoexcitation is expressed by Equ. 1-4. In optical exciation, excited electrons relax to T_1 from S_1 through ISC. Next, the excited electrons are up-converted to S_1 by absorbing thermal energy through the process of reverse intersystem crossing (RISC). Finally, the singlets undergo the same radiative relaxation route, that producing fluorescence (S_1 to S_0). Therefore, the PL spectrum of TADF should be almost the same as that of fluorescence. Although the phenomenon of TADF has been known for many years, it had been observed in only a few materials, such as xanthene dyes,[15,16] aromatic ketones[17,18] and thiones,[19,20] metal poryphyrins[21], and aromatic hydrocarbons, and was through to be almost useless for application to OLEDs.[22,23]

Another pathway for up-conversion from T_1 to S_1 is triplet−triplet annihilation (TTA). The collision of two triplet excitons produces an S_1 and S_0. A relatively high up-conversion efficiency as large as 28% was achieved using palladium tetrakis-quinoxalino-porphyrin as a sensitizer and rubrene as an emitter.[24] However, this value still limits the maximum η_{int} to well below 100%. On the other hand, TADF has the potential to significantly improve η_{ext} because the up-conversion efficiency from T_1 to S_1 can theoretically reach almost 100%.

To obtain TADF with a high conversion efficiency, a small energy gap (ΔE_{ST}) between S_1 and T_1 levels is necessary for the luminescent materials, which can be realized by having a small orbital overlap between the highest occupied molecular orbital (HOMO) and the lowest unoccupied molecular orbital (LUMO) of emitter molecules.[25] The ΔE_{ST} of luminescent molecules can be described by the following equations:

$$E_S = (E_U - E_L) + K_{LU} \qquad (1\text{-}5)$$

$$E_T = (E_U - E_L) - K_{LU} \qquad (1\text{-}6)$$

$$\Delta E_{ST} = E_S - E_T = 2K_{LU} \qquad (1\text{-}7)$$

where E_U is a ground level (the highest occupied molecular level, U-level), E_L is an excited level (the lowest unoccupied molecular level, L-level), and K_{LU} is an exchange energy. Furthermore, K_{LU} is given by the following equation:[26]

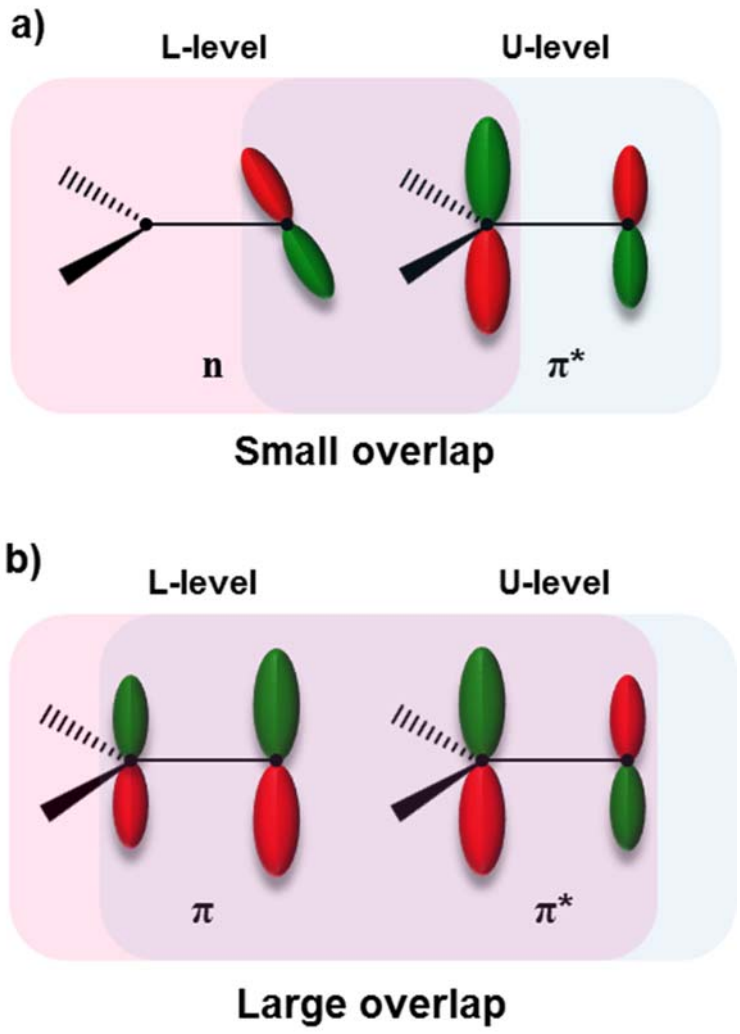

Figure 1-7. n-π* orbital overlap a) and π-π* orbital overlap b) in benzophenone.

$$K_{\mathrm{LU}} = \iint \varphi_{\mathrm{U}}(1)\varphi_{\mathrm{L}}(2)\frac{1}{r_{12}}\varphi_{\mathrm{U}}(2)\varphi_{\mathrm{L}}(1)d\tau_1\tau_2 \qquad (1\text{-}8)$$

where φ_{L} and φ_{U} are the wave functions of the U- and L-level orbitals, respectively, and r_{12} is distance between electron (1) and (2). As shown in Eq. 1-8, K_{LU} is determined by φ_{L} and φ_{U} and should generally decrease as their overlap decreases.

Evidence of this relationship can be found in several known materials. For example, in the case of benzophenone, the electronic transition from a non-bonding n orbital to a π* orbital (i.e., n-π* transition) is well-known to possess a small ΔE_{ST} as a consequence of the orthogonal

overlap between n and π* orbitals (Fig. 1-7a). In contrast, π-π* transitions normally possess large ΔE_{ST} because of the parallel overlap between π and π* orbitals (Fig.1-7b). Thus, small orbital overlapping between the HOMO and the LUMO should be necessary for small ΔE_{ST}. However, a high luminescence efficiency could not be attained in conventional materials with small ΔE_{ST} because n-π* characteristics usually cause a small radiative decay rate (k_r). Therefore, the development of new luminescent materials having both small ΔE_{ST} and large k_r is required for realizing highly efficient TADF.

Although TADF has been observed in several materials since the first discovery of TADF in xanthene dyes, TADF had not been applied to OLEDs until recently. In 2009, a new class of OLEDs featuring TADF from a poryphyrin derivatives was developed; however, the quantum yield of TADF was still very low (TADF quantum efficiency (Φ_{TADF}) = 0.55% at 300 K and Φ_{TADF} = 2.43% at 400 K).[25] More recently, a bipolar triazine derivative, 2-biphenyl-4,6-bis(1,2-phenylindolo[2,3-*a*]carbazol-11-yl)-1,3,5-triazine (**PIC-TRZ**), was synthesized and used as an emitting material in OLEDs.[27] The reported η_{ext} of 5.3% for the OLED was the first demonstration of the potential of TADF for realizing high performance OLEDs.

However, the efficiency of TADF OLEDs was still lower than that of phosphorescence OLEDs and move efficient exciton harvesting with high Φ_{PL} has been anticipated. To achieve this issue, design of novel TADF molecules based on the direct connection of donor and acceptor units with inducing strong steric hindrance for less overlapping between HOMO and LUMO provided a guide line. Suitable combination of donor and acceptor units for effective CT emission and preventing exciton quenching from CT states to localized excited state (LE) to increase Φ_{PL} should be also considered.[28,29] Our design strategy for effective TADF molecules will be discussed on chapter 2 through 6.

1.3 Photophysical Properties of Emissive Organic Molecules

1.3.1 Solvatochromic Shifts

The energy of emitting states can be changed by polarization effects caused by interaction with the surrounding medium, which is called solvent relaxation.[30,31] Most polar aromatic molecules based on CT emissive states including TADF molecules have longer dipole moments

in the excited state than in the ground state. Therefore, after excitation of a molecule in a solution, the dipoles of the solvent interact with dipole moment of the excited molecule, and the dipoles reorganize to minimize the free energy, resulting in a relaxed excited state. As the solvent polarity is increased, the solvent relaxation affect is increased, and emission shifts to lower energies and, therefore, longer wavelength (Fig1-8).

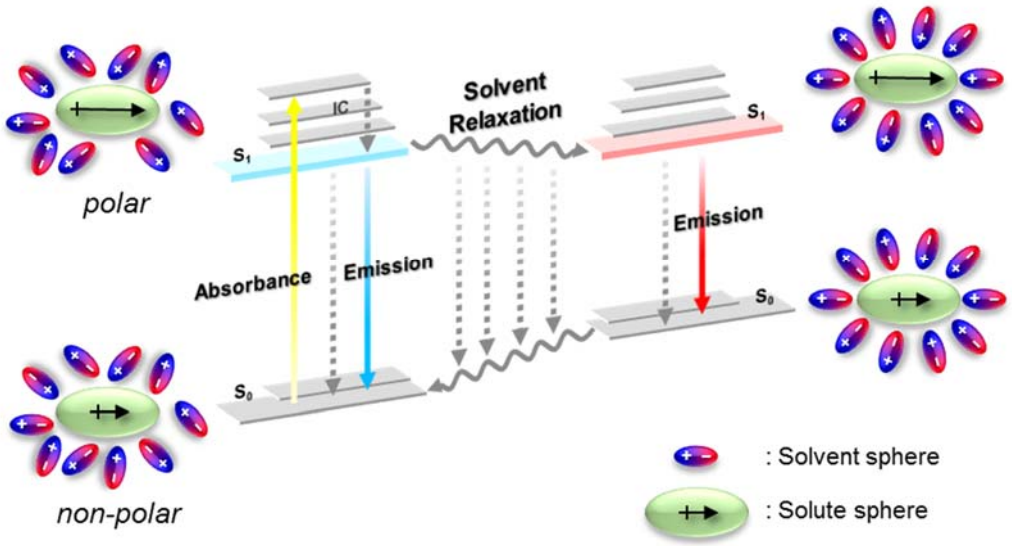

Figure 1-8. Jablonski diagram for effect of solvent relaxation, resulting in solvatochromic shifts in solute-solvent system.

The solvatochromic shifts in the wavenumbers of absorption and emission for such a mechanism are given by the following equations, respectively:

$$\overline{\nu}_a = -\frac{2}{hc}\mu_g(\mu_e - \mu_g)a^{-3}\Delta f + const. \quad (1\text{-}9)$$

$$\overline{\nu}_f = -\frac{2}{hc}\mu_e(\mu_g - \mu_e)a^{-3}\Delta f + const. \quad (1\text{-}10)$$

where h is Plank's constants, c is the velocity of light, a is the radius of the cavity in which the solute resides, μ_g and μ_e are the transition dipole moments in ground states and excited states, and Δf is the orientation polarizability defined as

$$\Delta f = f(\varepsilon) - f(n^2) = \frac{\varepsilon-1}{2\varepsilon+1} - \frac{n^2-1}{2n^2+1} \qquad (1\text{-}11)$$

The Δf of each solvent is calculated using its dielectric constant (ε) which varies for each solvent. (Table 1-2).

Subtraction of Equ. 1-9 and 1-10 leads to the Lippert-Mataga equation:[32)]

$$\overline{\nu}_a - \overline{\nu}_f = \frac{2}{hc}\left(\mu_e - \mu_g\right)^2 a^{-3}\Delta f + const. \qquad (1\text{-}12)$$

As shown in Equ. 1-12, the Stoke's shift depends only on the absolute magnitude of the charge transfer dipole moment ($\mu_e - \mu_g$) and it can be approximated using this equation. General emissive molecules exhibit a linear relationship when Stoke's shift is plotted against Δf, which is called a Lippert's plot.

In the case of intermolecular charge transfer (ICT) emissive states for molecules having donor-acceptor (D-A) combined molecular frameworks, $\overline{\nu}_f$ is very sensitive to changes in Δf compared to non-CT state emissive molecules, so the Lippert's plots for these materials exhibit steep slope. Therefore, we can predict the origination of emission process using solvatochromic properties. For instance, strong CT emission based TADF molecules is expected to exhibit very sensitive with solvent polarity and steep slope of Lippert's plots.

Solvatochromic shift phenomenon of TADF molecules is specifically discussed in chapter 5.

Table 1-2. Dielectric constant (ε, at 20 ºC) and orientation polarizability of solvents.

solvent	ε	Δf
Cyclohexane	2.023	0.001
Toluene	2.397	0.013
Chloroform	4.806	0.149
Dichloromethane	9.08	0.219
Dimethylsulfoxide	48.9	0.265
N,*N*-Dimethylformamide	37.6	0.275
Acetonitrile	25.07	0.306
Methanol	33.62	0.309

1.3.2 Aggregation Induced Emission (AIE)

Most aromatic compounds exhibit concentration quenching at high concentrations because of the formation of sandwich-shaped excimers and exciplexes by the collision between aromatic molecules.[33,34] For example, disk type molecules often have strong π-π stacking, which promotes aggregation of molecules and leads to more efficient non-radiative decay. This mechanism is called aggregation-caused quenching (ACQ, Fig. 1-9a).[35]

On the other hand, for aggregation-induced emission (AIE), the aggregation of molecules promotes emission while no emission is observed in the dissolved solvent state (Fig. 1-9b).[36] Free rotations around single bonds in molecules causes the non-radiative decay in solvent. However, restriction of the intramolecular rotation (RIR) in the aggregate state such as in nanoparticle suspensions in polar solvents or in solid-state films, leads to strong emission. Silole,[37] polyphenylene,[38] and pyran[39] derivatives are the representative of AIE molecules. Moreover, crystals of organic molecules can emit phosphorescence at room-temperature based on crystallization-induced emission because the restricted molecular motion in the crystal state suppresses the non-radiative decay of T_1.[40]

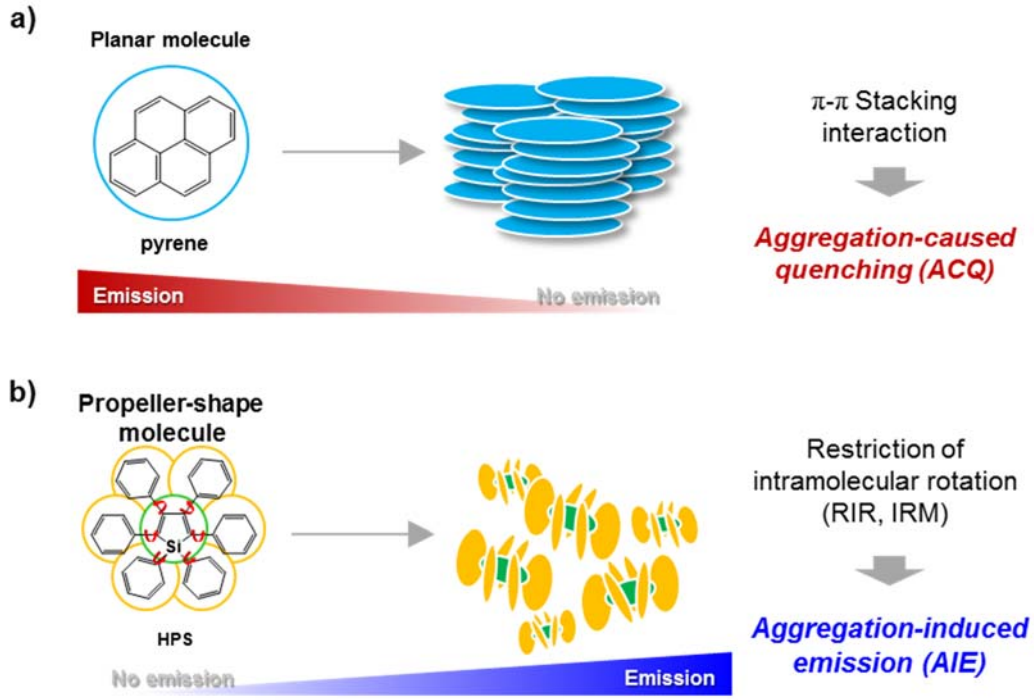

Figure 1-9. Schematic illustration of a) aggregation-caused quenching (ACQ) and b) aggregation-induced emission (AIE).

The phenomenon of AIE can find uses in chemical sensors, biological probes,[41] and host-free OLEDs.[42] Some of TADF molecules discussed in this thesis exhibit AIE, producing Φ_{PL} that is more than two or three times higher in solid thin films than in solvents, and are discussed in more detail in later chapters.

1.3.3 Energy Transfer in Host−Guest System

To prevent efficiency decrease in OLEDs by concentration quenching of excitons in EMLs, most emissive materials are doped in a host matrix at very low concentrations. In a host−guest system, there are two kinds of energy transfer mechanisms from the host (exciton donor) to the guest (exciton acceptor): Förster and Dexter energy transfer (Fig. 1-10).[43,44]

Förster energy transfer is a long-range (up to ~10 nm) dipole-dipole coupling interaction between host and guest molecules (Fig. 1-10a).[45] Förster energy transfer is only allowed between host singlet to guest singlet state because the transitions between terms of the same multiplicity are spin-allowed, while transitions between terms of different multiplicity are spin-forbidden (Wingner rule). The rate constant of Förster energy transfer for a host−guest system is given by the following equation:

$$k_{FET} = k_H \left(\frac{R_0}{R_{HG}}\right)^6 \qquad (1\text{-}13)$$

where k_H is the radiative decay rate of the host, R_{HG} is the separation between the host and guest molecules, and R_0 is the Förster transfer radius. R_0 can be calculated from the following equation:

$$R_0^6 = \frac{9000\kappa^2 \ln 10 \varphi_H}{128\pi^5 n^4 N_A} \int_0^\infty F_H(\lambda)\varepsilon_G(\lambda)d\lambda \qquad (1\text{-}14)$$

where κ^2 is an orientation factor, φ_H is Φ_{PL} of the host, n is refractive intensity of the medium, N_A is Avogadro constant, $F_H(\lambda)$ is normalized host PL intensity. $\varepsilon_G(\lambda)$ is molar absorption coefficient of the guest, and λ is wavelength. From these equations, the rate constant of Förster energy transfer can be determined by the fluorescence spectrum of the host and the absorption spectrum of the guest. To increase the Förster rate constant, a large overlap

of host emission and guest absorption spectra, a large $\varepsilon_G(\lambda)$, and a small distance between host and guest molecules are needed.

Dexter energy transfer is a short-range (up to ~1 nm) intramolecular electron exchange process from host to guest (Fig. 1-10b). The Dexter energy transfer is allowed between host singlet and guest singlet, and host triplet and guest triplet. The rate constant of Dexter energy transfer is given by following equation:

$$k_{DEX} = \left(\frac{2\pi}{h}\right)\kappa^2 \exp\left(\frac{-2R_{HG}}{L}\right)\int_0^\infty F_H(\lambda)\varepsilon_G(\lambda)d\lambda \quad (1\text{-}15)$$

where R_{HG} is the distance between host and guest molecules and L is the sum of Van der Waals radius for the two molecules. The rate constant of Dexter energy transfer strongly depends on the distance between the host and guest molecules and is also affected by the overlap between $F_H(\lambda)$ and $\varepsilon_G(\lambda)$.

In the case of phosphorescence and TADF emission, both Förster and Dexter processes contribute to energy transfer between the host and guest molecules because both singlet and triplet excitons are used for emission. Therefore, selection of the proper host is very important for effective energy transfer to achieve high efficiency. In chapter 2 of this thesis, various the dependence of TADF properties on host are discussed using a variety of host materials.

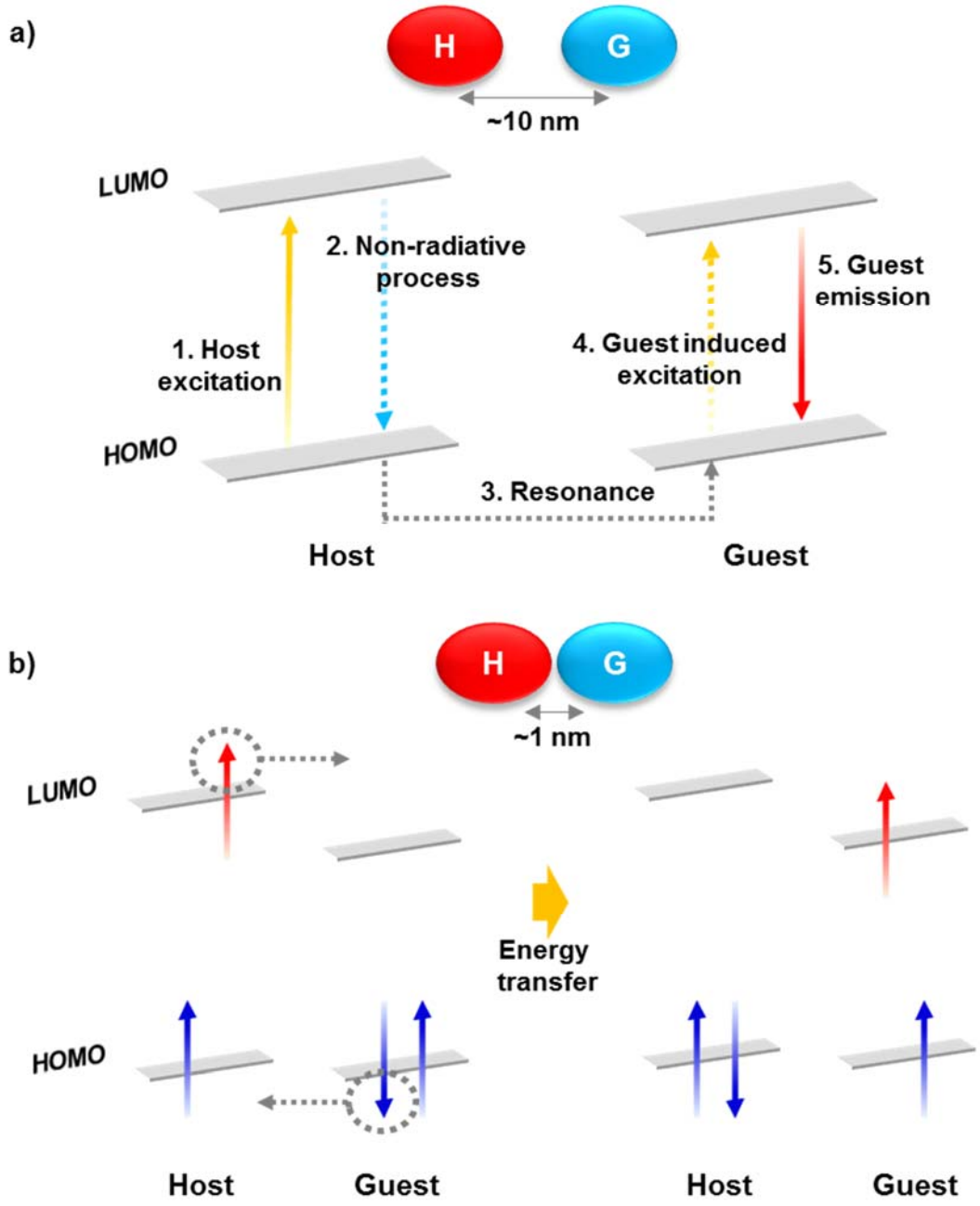

Figure 1-10. Schematic diagram for a) Förster and b) Dexter energy transfer.

1.4 Electroluminescence Properties of OLEDs

1.4.1 Roll-Off in OLEDs

Roll-off is the decrease of efficiency with increasing brightness or current density in OLEDs. This phenomenon is present in all OLEDs, and the causes are very complicated. To realize wide-application of OLEDs in displays, lasers, and lighting sources, high brightness and stability must be achieved, meaning that roll-off should be minimized. Roll-off characteristics can be compared by using the critical current density ($J_{50\%}$) at which the η_{ext} is dropped to 50% of its maximum value.[13)]

Figure 1-11 shows exciton annihilation processes leading to roll-off. For instance, polaron/exciton and exciton/excitons annihilation, field-induced quenching, charge carrier imbalance, Joule heating, and degradation can effect efficiency.[46)]

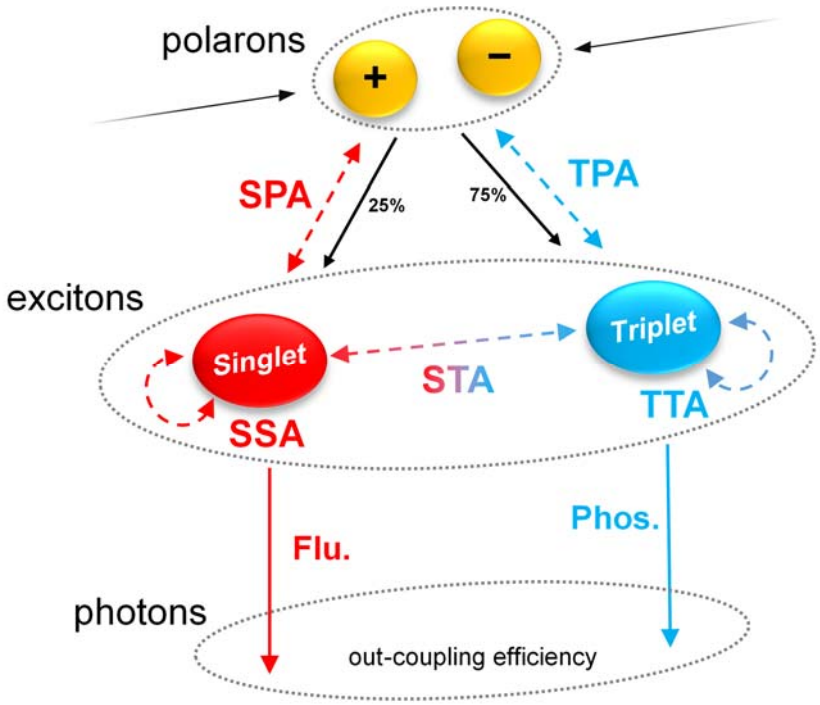

Figure 1-11. Schematic illustration of roll-off process in OLEDs (SPA: Singlet−Polaron Annihilation, TPA: Triplet−Polaron Annihilation, SSA: Singlet−Singlet Annihilation, TTA: Triplet−Triplet Annihilation, and STA: Singlet−Triplet Annihilation).

The most relevant roll-off process in phosphorescent OLEDs is TTA because of the long τ of phosphorescence emission and the high density of triplet excitons.[47] Reducing the molecular distance between dopant molecules in a host-guest system can further increase TTA.[48] Devices based on TADF are also strongly effected by TTA because of the long-lived nature of the excitons.

The process of TTA can be characterized by the following equations:

$$4\left({}^3M^* + {}^3M^*\right) \rightarrow {}^1M^* + {}^3M^* + 4M \quad (1\text{-}16)$$

$$\frac{d[{}^3M^*]}{dt} = -\frac{[{}^3M^*]}{\tau} - \frac{k_q}{2}\left[{}^3M^*\right]^2 + \frac{J}{qd} \quad (1\text{-}17)$$

$$\frac{\eta_{50\%}}{\eta_0} = \frac{J_{50\%}}{4J}\left[\sqrt{1 + 8\frac{J}{J_{50\%}}} - 1\right] \quad (1\text{-}18)$$

where ${}^3M^*$ and M refer to molecules in triplet excited and ground states, respectively, $[{}^3M^*]$ is triplet exciton density, d is width of the recombination zone, k_q is TTA rate constant, q is fundamental electric charge, J is current density, and η_0 is maximum η_{ext}. Relationships between TTA and the efficiency of TADF-OLEDs will be discussed in more detail in chapter 6.

Among these processes, singlet−singlet annihilation (SSA) has been observed in anthracene crystal and affects the singlet excitons density and lifetime.[49] Singlet−triplet annihilation (STA) usually occurs at high concentrations of guest doping and high current densities over 100 mA cm^{-2}.[50] Polarons can also interact with both singlet and triplet excitons, leading to exciton−polaron annihilation. Triplet−polaron annihilation (TPA) occurs in both fluorescent and phosphorescent OLEDs because of the long excited state lifetime of triplets. Holes generally lead to stronger TPA than electrons. Singlet−polaron annihilation (SPA) is of great concern in organic lasers, since very high current densities are applied.[51] Further, filed-induced quenching, charge carrier imbalance, Joule heating, and degradation can effect OLED efficiency.[46]

To suppress the roll-off and achieve high-brightness in OLEDs, decreasing the local exciton density is crucial. Decreasing the luminescence exciton lifetime,[51] reducing molecular aggregation,[52] and broadening the recombination zone[53] are all routes for reducing the exciton

density. Moreover, reducing the spectral overlap between emission and polaron absorption can decrease polaron annihilation.[51)]

1.4.2 White Emissive OLEDs

White OLEDs (WOLEDs) are receiving great attention and being developed as the next generation of solid-state light sources. However, their low brightness, device stability, and expensive manufacturing cost currently limit their application. To overcome these disadvantages, many of researchers have been studying the development of effective emitter molecules and optimized device structures.

In the case of white emission, the emission spectrum covers large visible regions from 400 to 800 nm. Typically, emissive molecules show narrow emission with a width of 50−100 nm that can be recognized as colors such as red, green or blue. To realize white emission, different colors of emission should be mixed to cover a broad emission spectrum, for example, by combining red, green and blue or blue and orange emissions. The combination of each emission can be controlled by various device structures for high efficiency in pure white emission (Fig. 1-13).[54,55)]

The simplest method to obtain white emission is by blending different color luminophores in a single layer (Fig. 1-13a). The first single-layer WOLEDs were fabricated by blending of PVK with orange, green, and blue laser dyes using solution-processing.[56)] After that, other researchers reported fabricating WOLEDs by vacuum depositing a blend of three kinds of phosphorescent luminophores.[57)] In spite of this advantage of simple device fabrication, single-layer devices exhibited phase-separation in an EML, which causes color shifts and an increase of current density.

Another method for fabricating WOLEDs is using a multi-layer device structure (Fig. 1-13b).[58,59)] This multi-layer device emits from multiple EMLs and a combination of the colors generates the white emission. In this device structure, excitons can be created in an EML by direct recombination of holes and electrons or by energy transfer from a neighboring EML. This method exhibits the best efficiency, spectral coverage, and device lifetime compared to other WOLED architectures. However, the emission spectrum often changes depending on the applied driving voltage in the multi-layer devices, but this can be solved by controlling the

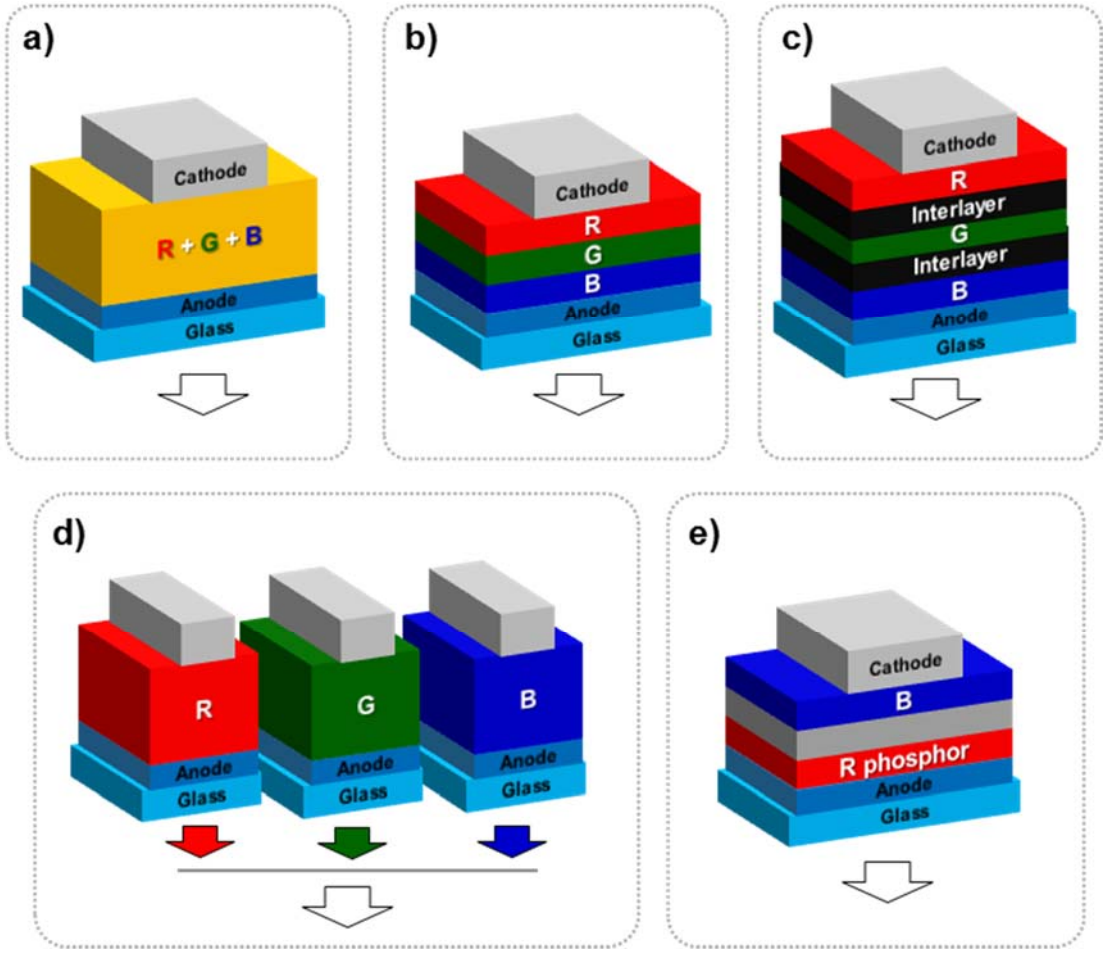

Figure 1-13. Schematic illustration of OLEDs (WOLEDs) structure for white emission.

recombination zone and width of the EMLs.[60)]

The EMLs can be further isolated for to reduce their interaction and suppress brightness-dependent color shifts even at very high operating voltages (Fig. 1-13c).[61)] In the extreme case of isolating the EMLs, white emission can be generated from monochrome pixels consisting of OLEDs (or striped WOLEDs, Fig. 1-13d). Striped WOLEDs generate white emission using independent red, green, and blue emitting devices. However, the manufacturing process of these types of devices is very complicated, resulted in high cost. In this thesis, highly efficient and pure WOLEDs based on TADF emitters are demonstrated using a simple multilayer device structure, as discussed in chapter 3.

1.4.3 Solution-Processed OLEDs

The main methods for fabricating multilayer OLEDs are thermal evaporation under high vacuum[4] and solution processing using solvents.[7] Thermal evaporation is the most widely used method for the fabrication of efficient and stable OLEDs, while it has disadvantages of complexity and high production costs.[62] Solution-processing methods such as spin-coating,[63] ink-jet printing,[64] and spray process[65] have garnered great attention for the fabrication of flexible and large-area OLEDs because of the simplicity and low cost of the processes.

Mainly phosphorescent polymers and small molecules have been studied as emitters for highly efficient solution-processed OLEDs. After the first reports of solution-processed OLEDs using the polymer PPV,[7] phosphorescent conjugated polymers having high solubility and good morphology were developed, amied for highly efficient polymer-based OLEDs.[66–68] However, the long conjugation length of the polymers leads to a low T_1 energy level and decreased device efficiency.[69,70] To solve these problems, phosphorescent emitters have been dispersed into non-conjugated polymers, resulting in improved efficiency.[71,72]

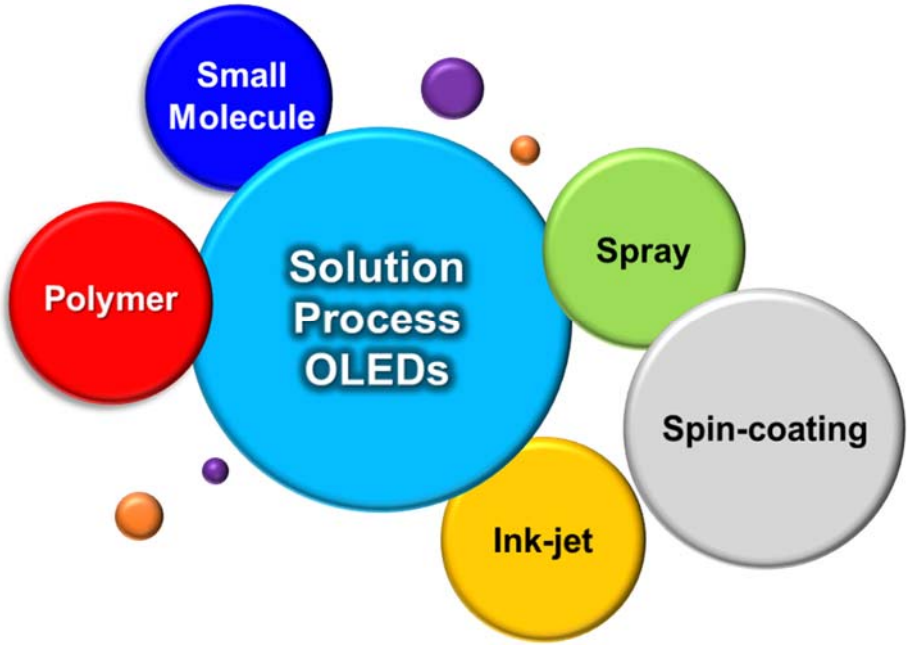

Figure 1-14. Schematic illustration of solution process OLEDs.

Small molecules are mainly used in vacuum thermal evaporation and have advantages of having high Φ_{PL} and being easily purified. For application of small molecules in solution-processed OLEDs, the problems of low solubility, poor morphology, and strong crystallization should be solved. Newly designed small molecules incorporating alkyl or alkoxy and flexible groups have been reported for use with solution processes.[73,74] Rigid molecules such as spirofluorene have been introduced in core unit to increase the glass transition temperature (T_g), which suppresses crystallization.[75] Using small-molecules, highly efficient solution-processed OLEDs based on Ir(III) and Pt(II) complexes have been reported.[76,77]

In this thesis, the first TADF polymer emitters are designed, synthesized, and applied to highly efficient solution-processed OLEDs (Chapter 5).

1.5 Objective of this Thesis

The objective of this thesis is to develop highly efficient novel TADF materials and to apply these materials in OLEDs. Until now, fluorescent and phosphorescent molecules are the most widely used and studied emitters for display and lighting sources. However, research on TADF molecules is in the inchoate stage compared to the studies of other emissive organic materials.

In this thesis, molecular designs with combinations of newly explored electron donating and accepting units for realizing small ΔE_{ST} and efficient TADF emission are proposed, and the various photo- and electro-physical characteristics of the new TADF molecules and OLEDs are analyzed. To demonstrate efficient TADF emission over the whole visible region from blue to red, various donor and acceptor units are introduced to control the energy gap (E_g) between HOMO and LUMO. In addition, a very simple method to fabricate pure WOLEDs is proposed based on the blends of TADF emitters.

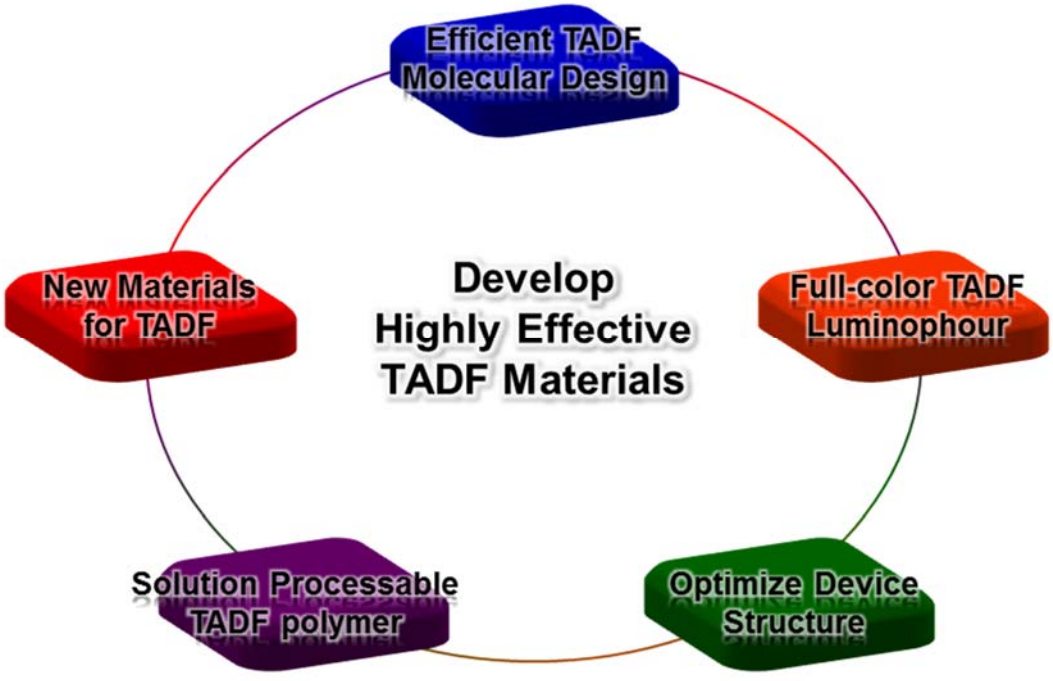

Figure 1-15. Objectives of this thesis.

Furthermore, highly efficient solution-processed OLEDs using TADF polymers as emitters are reported. Carefully optimized device structures, layer thicknesses, and hole- and electron-transporting materials are reported to achieve efficient and balanced hole and electron injection and carrier recombination in TADF-OLEDs.

Finally, a strategy for designing TADF molecules with η_{int} of nearly 100% are discussed, and routes to achieving OLEDs reaching the maximum theoretical limitation of η_{ext} are suggested.

1.6 Outline of this Thesis

In this thesis, advanced molecular designs and new materials are explored for efficient TADF emission. Newly designed molecules are synthesized, and their luminescent properties under photo- and electro-excitation are evaluated. Chapters 2 through 6 consist of studies on TADF emitters for OLEDs.

Chapter 2 reports highly efficient TADF emitters based on a triazine derivative having bicarbazole substituents, and optimized device structure for effective exciton harvesting in OLEDs are presented. Moreover, host dependence of the PL properties are investigated to understand the criteria for the selection of host materials for effective energy transfer in host-guest systems with a TADF guest. The calculation of theoretical maximum η_{ext} is revisited and modified for TADF emitters to evaluate the optimization of the fabricated OLEDs.

Chapter 3 introduces a simple molecular design for realizing full-color TADF OLEDs, in addition to a pure white emissive OLEDs, using butterfly-shaped luminescence benzophenone derivatives. Correlation between ΔE_{ST} and the electronic transitions of benzophenone derivatives are investigated.

Chapter 4 suggests a new molecular design strategy to suppress non-radiative decay processes and realize efficient TADF emission using strongly twisted X-shaped luminophores based on not only the electron donating unit but also bulky benzoylbenzophenone electron-accepting units.

Chapter 5 discusses the molecular design and synthesis of the first TADF polymers and their application in highly efficient solution-processed OLEDs. The solvatochromic properties are tested in various kinds of solvent and determined emission process in TADF polymers.

Chapter 6 presents molecules with η_{int} of nearly nearly 100% based on a heteroatom bridged molecular structure. Different kinds of heteroatom elements are introduced to control emission color and realize deep-blue TADF emission with high η_{ext}.

Finally, chapter 7 summarizes the conclusions that can be drawn from this work and proposes future studies for organic light-emitting molecules.

1.7 References

[1] W. Helfrich and W. G. Schneider, *Phys. Rev. Lett*., **1965**, 14, 229.

[2] W. Helfrich and W. G. Schneider, *J. Chem. Phys*., **1966**, 44, 2902.

[3] P. S. Vincentt, W. A. Barlow, R. A. Hann, and G. G. Roberts, *Thin Solid Films*, **1982**, 94, 171.

[4] C. W. Tang and S. A. Vanslyke, *Appl. Phys. Lett*., **1987**, 51, 913.

[5] C. W. Tang, S. A. Vanslyke, and C. H. Chen, *J. Appl. Phys*., **1989**, 65, 3610.

[6] R. H. Partridge, *Polymer*, **1983**, 24, 748.

[7] J. H. Burroughes, D. D. Bradley, A. R. Brown, R. N. Marks, K. Mackay, R. H. Friend, P. L. Burns, and A. B. Holmes, *Nature*, **1990**, 347, 539.

[8] C. E. Wayne and R. P. Wayne, *Photochemistry*, **1995**, Oxford Chemistry Primers.

[9] E. Aminaka, T. Tsutsui, and S. Saito, *J. Appl. Phys*., **1996**, 79, 8808.

[10] C. W Tang, S. A Vanslyke, and C. H. Chen, *J. Appl. Phys*., **1989**, 65, 3610.

[11] J. S. Kim, P. K. H. Ho, N. C, Greenham, and R. H. Friend, *J. Appl. Phys*., **2000**, 88, 1073.

[12] C. Adachi, M. A. Baldo, M. E. Thompson, and S. R. Forrest, *J. Appl. Phys.*, **2001**, 90, 5048.

[13] C. Adachi, M. A. Baldo, and S. R. Forrest, *Phys. Rev. B*, **2000**, 62, 10967.

[14] C. Baleizão and M. N. Berberan-Santos, *J. Chem. Phys*., **2007**, 126, 204510.

[15] S. K. Lam and D. Lo, *Chem. Phys. Lett*., **1997**, 281, 35.

[16] R. Duchowicz, M. L. Ferrer, and A. U. Acuña, *Photochem. Photobiol*., **1998**, 68, 494.

[17] M. W. Wolf, K. D. Legg, R. E. Brown, L. A. Singer, and J. H. Parks, *J. Am. Chem. Soc*., **1995**, 97, 4490.

[18] A. M. Turek, G. Krishnammorthy, K. Phipps, and J. Saltiel, *J. Phys. Chem. A*, **2002**, 106, 6044.

[19] A. Maciejewski, M. Szymanski, and R. P. Steer, *J. Phys. Chem*., **1986**, 90, 6314.

[20] H. Eisenberger and B. Nickel, *J. Chem. Soc., Faraday Trans*., **1996**, 92, 733.

[21] S. Yusa, M. Kamachi, and Y. Morishima, *Photochem. Photobiol*., **1998**, 67, 519.

[22] J. L. Kropp and W. R. Dawson, *J. Phys. Chem*., **1967**, 71, 4499.

[23] B. Nickel and D. Klemp, *Chem. Phys*., **1993**, 174, 297.

[24] Y. Y. Cheng, T. Khoury, R. G. C. R. Clady, M. J. Y. Tayebjee, N. J. Ekins-Daukes, M. J. Crossley, and T. W. Schmidt, *Phys. Chem. Chem. Phys*., **2010**, 12, 66.

[25] A. Endo, M. Ogasawara, A. Takahashi, D. Yokoyama, Y. Kato, and C. Adachi, *Adv. Mater*., **2009**, 21, 4802.

[26] N. J. Turro, *Modern molecular photochemistry*, **1991**, University science book.

[27] A. Endo, K. Sato, K. Yoshimura, T. Kai, A. Kawasa, H. Miyazaki, and C. Adachi, *Appl. Phys. Lett*., **2011**, 98, 083302.

[28] Q. Zhang, J. Li, L. Shizu, S. Huang, S. Hirata, H. Miyazaki, and C. Adachi, *J. Am. Chem. Soc*., **2012**,134, 14706.

[29] Q. Zhang, B. Li, S. Huang, H. Nomura, H. Tanaka, and C. Adachi, *Nat. Photon*., **2014**, 8, 326.

[30] B. Valeur, *Molecular Fluorescence : Principle and Applications*, **2001**, Wiley-VHC Weinheim.

[31] J. R. Lakowicz, *Principles of Fluorescence Spectroscopy*, **2006**, Springer.

[32] N. Mataga, Y. Kaifu, and M. Koizumi, *Bull. Chem. Soc. Jpn*., **1956**, 29, 465.

[33] J. B. Birks, *Photophysics of Aromatic Molecules*, **1970**, Wiley-Interscience.

[34] J. Malkin, *Photopysical and Photochemical Properties of Aromatic Compounds*, **1992**, CRC.

[35] S. W. Thomas III, G. D. Joly, and T. M. Swager, *Chem. Rev*., **2007**, 107, 1339.

[36] Y. Hong, J. W. Y. Lam, and B. Z. Tang, *Chem. Commun*., **2009**, 4332.

[37] B. Z. Tang, X. Zhan, G. Yu, P. P. S. Lee, Y. Liu, and D. Zhu, *J. Mater. Chem*., **2001**, 11, 2974.

[38] Q. Zheng, Z. Li, Y. Dong, C. Di, A. Qin, Y. Hong, L. Ji, Z. Zhu, C. K. W. Jim, G. Yu, Q. Li, Z. Li, Y. Liu, J. Qin, and B. Z. Tang, *Chem. Commun*., **2007**, 70.

[39] H. Tong, Y. Hong, Y. Dong, Y. Ren, M. Haeussler, J. W. Y. Lam, K. S. Wong, and B. Z. Tang, *J. Phys. Chem. B*, **2007**, 111, 2000.

[40] Y. Dong, J. W. Y. Lam, A. Qin, Z. Li, J. Sun, H. H. Y. Sung, I. D. Williams, and B. Z. Tang, *Chem. Commun*., **2007**, 40.

[41] M. Nakamura, T. Sanji, and M. Tanaka, *Chem. Eur. J*., **2011**, 17, 5344.

[42] J. Huang, X. Yang, J. Wang, C. Zhong, L. Wang, J. Qin, and Z. Li, *J. Mater. Chem*., **2012**, 22, 2478.

[43] T. Förster, *Discuss Faraday Soc*., **1959**, 27, 7.

[44] D. L. Dexter, *J. Chem. Phys*., **1953**, 21, 836.

[45] B. P. Lyons and A. P. Monkman, *Phys. Rev. B*, **2005**, 71, 235201.

[46] C. Murawski, K. Leo, and M. C. Gather, *Adv. Mater*., **2013**, 25, 6801.

[47] M. A. Baldo, D. F. O'Brien, Y. You, A. Shoustikov, S. Sibley, M. E. Thompson, and S. R. Forrest, *Nature*, **1998**, 395, 151.

[48] J. Kalinowski, J. Mezyk, F. Meinardi, R. Tubino, M. Cocchi, and D. Virgili, *J. Appl. Phys*., **2005**, 98, 063532.

[49] S. D. Babenko, V. A. Benderskii, V. I. Gol'Danskii, A. G. Lavrushko, and V. P. Tychinskii, *Chem. Phys. Lett*., **1971**, 8, 598.

[50] D. Kasemann, R. Brückner, H. Fröb, and K. Leo, *Phys. Rev. B*, **2011**, 84, 115208.

[51] M. A. Baldo, R. J. Holmes, and S. R. Forrest, *Phys. Rev. B*, **2002**, 66, 035321.

[52] S. Reineke, K. Walzer, and K. Leo, *Phys. Rev. B*, **2007**, 75, 125328.

[53] D. Song, S. Zhao, and H. Aziz, *Adv. Funct. Mat*., **2011**, 21, 2311.

[54] M. C. Gather, A. Kohnen, and K. Meerholz, *Adv. Mater*., **2011**, 23, 233.

[55] S. Reineke, M. Thomschke, B. Lussem, and K. Leo, *Rev. Mod. Phys*., **2013**, 85, 1245.

[56] J. Kido, K. Hongawa, K. Okuyama, and K. Nagai, *Appl. Phsy. Lett*., **1994**, 64, 815.

[57] H. A. Al Attar, A. P. Monkman, M. Tavasli, S. Bettington, and M. R. Bryce, *Appl. Phys. Lett*., **2005**, 86, 121101.

[58] G. Schwartz, K. Fehse, M. Pfeiffer, K. Walzer, and K. Leo, *Appl. Phys. Lett*., **2006**, 89, 083509.

[59] Y. Tomita, C. May, M. Toerker, J. Amelung, M. Eritt, F. Loeffler, C. Luber, K. Leo, K. Walzer, K. Fehse, and Q. Huang, *Appl. Phys. Lett*., **2007**, 91, 253501.

[60] Y. R. Sun, N. C. Giebink, H. Kanno, B. W. Ma, M. E. Thompson, and S. R. Forrest, *Nature*, **2006**, 440, 908.

[61] T. W. Lee, T. Noh, B. K. Choi, M. S. Kim, D. W. Shin, and J. Kido, *Appl. Phys. Lett*.,

2008, 92, 043301.

[62] H. Kim, Y. Byun, R. R. Das, B. K. Choi, and P. S. Ahn, *Appl. Phys. Lett*., **2007**, 91, 093512.

[63] J. P. J. Markham, S.-C. Lo, S. W. Magennis, P. L. Burn, and I. D. W. Samuel, *Appl. Phys. Lett*., **2002**, 80, 2645.

[64] F. Villani, P. Vacca, G. Nenna, O. Valentino, G. Burrasca, T. Fasolino, C. Minarini, and D. D. Sala, *J. Phys. Chem, C*, **2009**, 113, 13398.

[65] J. Ju, Y. Yamagata, and T. Higuchi, *Adv. Mater*., **2009**, 21, 4343.

[66] H. Yersin, *Highly Efficient OLEDs with phosphorescent Materials*. **2008**, Willey-VCH.

[67] W. Zhu, W. Mo, M. Yaun, W. Yang, and Y. Cao, *Appl. Phys. Lett*., **2002**, 80, 2045.

[68] C. Jiang, W. Yang, J. Pengm S. Xiao, and Y. Cao, *Adv. Mater.*, **2004**, 16, 537.

[69] M. Sudhakar, P. I. Djurovich, T. E. Hogen-Esch, and M. E. Thompson, *J. Am. Chem. Soc*., **2003**, 125, 7769.

[70] A. van Dijken, J. J. A. M. Bastiaansen, N. M. M. Kiggen, B. M. W. Langeveld, C. Rothe, A. Monkman, I. Bach, P. Stossel, and K. Brunner, *J. Am. Chem. Soc*., **2004**, 126, 7718.

[71] S. A. Choulis, V. E. Choong, A. Patwardhan, M. K. Mathai, and F. So, *Adv. Funct. Mater*., **2006**, 16, 1075.

[72] B. C. Krummacher, M. K. Mathai, V. E. Choong, S. A. Choulis, and F. So, and A. Winnacker, *Org. Electron*., **2006**, 7, 313.

[73] J. A. Cheng, C. H. Chen, and C. H. Liao, *Chem. Mater*., **2004**, 16, 2862.

[74] J. Qiao, L. D. Wang, J. F. Xie, G.T. Lei, G. S. Wu, and Y. Qui, *Chem. Commun*., **2005**, 4560.

[75] Y. Shirota, *J. Mater. Chem*., **2005**, 15, 75.

[76] N. Rehmann, D. Hertel, K. Meerholz, H. Beckers, and S. Heun, *Appl. Phys. Lett*., **2007**, 91, 103507.

[77] G. J. Zhou, W. Y Wong, B. Yao, Z. Xie, and L. Wang, *J. Mater. Chem*., **2008**, 18, 1799.

Chapter 2

High-Efficiency Organic Light-Emitting Diodes utilizing Thermally Activated Delayed Fluorescence from Triazine-Based Donor-Acceptor Hybrid Molecules

Chapter 2

High-Efficiency Organic Light-Emitting Diodes utilizing Thermally Activated Delayed Fluorescence from Triazine-Based Donor-Acceptor Hybrid Molecules

Abstract

We have designed and synthesized a high-efficiency purely organic luminescent material, 2,4-bis{3-(9*H*-carbazol-9-yl)-9*H*-carbazol-9-yl}-6-phenyl-1,3,5-triazine (**CC2TA**) comprising bicarbazole donor and phenyltriazine acceptor units, which is capable of emitting TADF. The molecular design of **CC2TA** allows spatial separation of HOMO and LUMO on the donor and acceptor fragments, respectively, leading to an exceptionally small ΔE_{ST} (0.06 eV) together with a high triplet energy. Furthermore, a high η_{ext} as high as 11% ± 1% has been achieved in sky-blue OLEDs employing **CC2TA** as an emitter.

2.1 Introduction

As mentioned in chapter 1, nearly 100% η_{int} has been achieved in the past decade by employing transition metal-centered phosphorescent emitters such as iridium(III) and platinum(II) organometallic complexes using fast ISC for phosphorescence emission.[1−3] However, the efficiency and stability of blue phosphorescent OLEDs are much lower than those reported for their green and red counterparts. Moreover, a severe efficiency roll-off at high current densities due to TTA or TPA is a significant issue for phosphorescent OLEDs.[4]

In contrast, OLEDs incorporating fluorescent emitters provide remarkably high reliability and stability, but their η_{int} should be theoretically limited to ~25% under electrical excitation.

Hence, it still remains a challenge to develop new luminescent materials rendering high singlet exciton generation efficiency in fluorescent OLEDs. To maximize the actual efficiency in fluorescent OLEDs, we have recently demonstrated a brand new viable mechanism for EL, that is, TADF.[5,6] We previously revealed that a triazine derivative having a rather small ΔE_{ST} (0.11 eV), **PIC-TRZ**, exhibited efficient TADF and a high η_{ext} of 5.3% as an emitter in OLEDs, which is the first report that demonstrates the possibility of high performance OLEDs utilizing the TADF mechanism.[6]

In this study, we focus on advanced molecular design of triazine-based TADF luminophors having small ΔE_{ST} between the singlet and triplet energy levels for realizing highly-efficient OLEDs and design 2,4-bis{3-(9*H*-carbazol-9-yl)-9*H*-carbazol-9-yl}-6-phenyl-1,3,5-triazine (**CC2TA**) (Fig. 2-1). This design concept is expected to lead to molecules with large distortion between the donor and acceptor constituents. A triazine core has been commonly used to construct bipolar host materials[7] because of its strong electron-withdrawing ability. Bicarbazole substituents function as donor and make a proper donor-acceptor balance, giving a clear spatial separation of the HOMO and LUMO distribution. By introducing such π-extended donor substituents, a large k_r and a high luminescence efficiency based on π-π* transition is achieved in these D-A hybridized molecules.

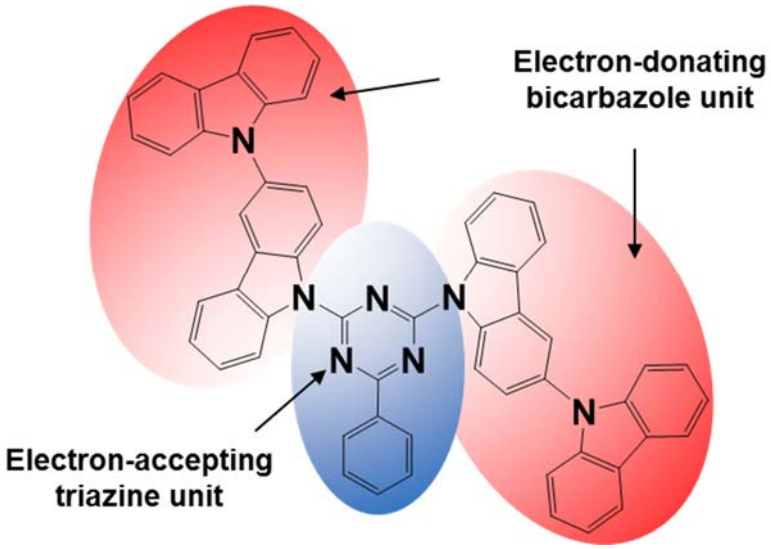

Figure 2-1. Molecular structure of **CC2TA**.

2.2 Results and Discussion

2.2.1 Characterization of Geometric and Electronic Structure of CC2TA

To understand the electronic and geometrical structure of **CC2TA**, quantum chemical calculations were performed using the TD-DFT/B3LYP/6-31G(d,p) method.[8] As can be seen in Fig. 2-2b, the HOMO of **CC2TA** is mainly distributed over the outermost carbazolyl units whereas the LUMO is localized on the central electron-accepting triazine and its phenyl substituent. Accordingly, **CC2TA** provides evident spatial separation of the HOMO and LUMO distributions, resulting in a notably small calculated ΔE_{ST} of 0.06 eV (S_1 = 2.91 eV and T_1 = 2.85 eV), which is favorable for a reverse ISC process from T_1 to S_1 states. On the other hand, 2,4-bis(9*H*-carbazol-9-yl)-6-phenyl-1,3,5-triazine (**Cz2TA**), having a mono-carbazole electron-donating substituent, exhibited a large ΔE_{ST} of 0.35 eV because of a large overlap between HOMO and LUMO (Fig. 2-2a).

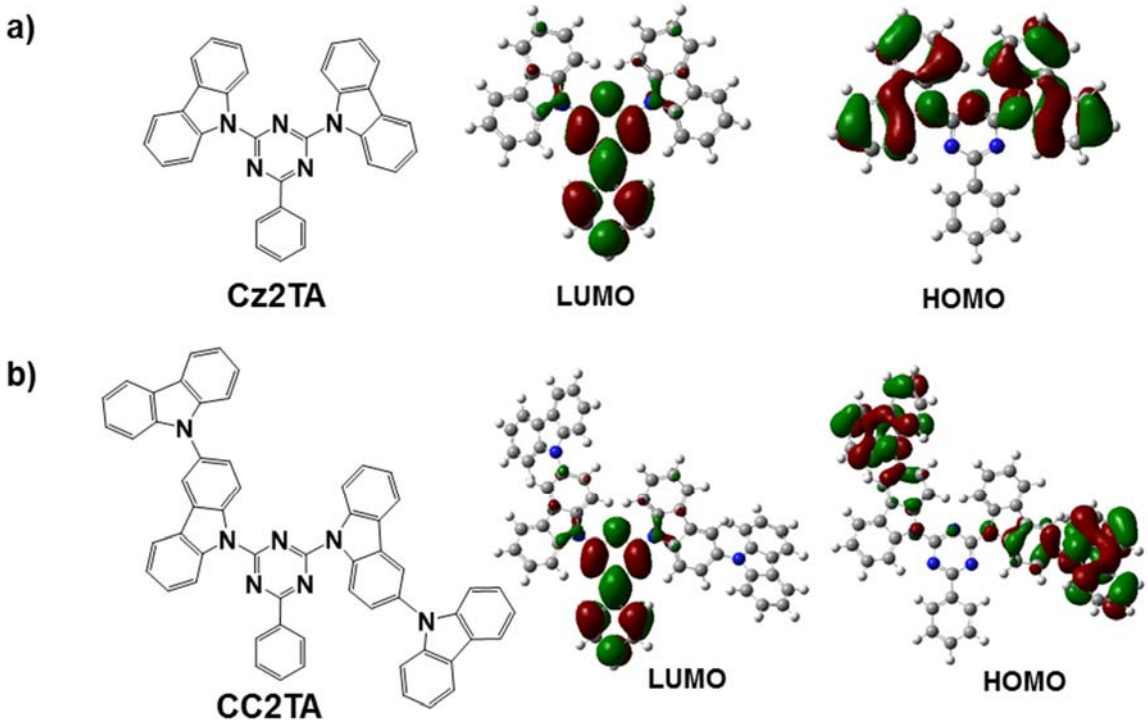

Figure 2-2. HOMO and LUMO distributions of a) mono-carbazole substituted analog **Cz2TA** and b) bi-carbazole substituted analog **CC2TA**.

2.2.2 PL Properties of CC2TA

Figure 2-3 depicts the absorption and PL spectra of **CC2TA** measured in different solvents. The lowest-energy absorption peak appears at about 340 nm, which is almost independent of solvent polarity. In sharp contrast, the PL peak of **CC2TA** displays an obvious red-shift from 435 nm in non-polar cyclohexane to 513 nm in highly polar THF with a gradual decrease of emission intensity. This solvatochromic behavior in PL is attributable to the intramolecular photoinduced charge transfer from the peripheral bicarbazole donor to the central triazine acceptor in **CC2TA**, leading to a large change in dipole moment in the excited state. As presented in Fig. 2-4, a 6 wt%-**CC2TA**: bis[2-(diphenylphosphino)phenyl]ether oxide (DPEPO)[9] film unambiguously indicates both prompt and delayed fluorescence components, and the PL decay can be fitted by a biexponential model. Because the emission spectra for prompt (τ = 27 ns) and delayed (τ = 22 μs) components coincide with one another, the long tail emissions should be considered to originate from TADF (Fig. 2-4a). The transient PL properties of the **CC2TA**: DPEPO film were further studied over a wide range of temperature (Fig. 2-4b). Whilst the delayed component is almost negligible below 150 K, Φ_{TADF} evidently increases with increasing temperature form 150 to 325 K. Thus, the overall Φ_{PL} reaches to 62%, including 46% from Φ_{TADF}, at room-temperature (300 K).

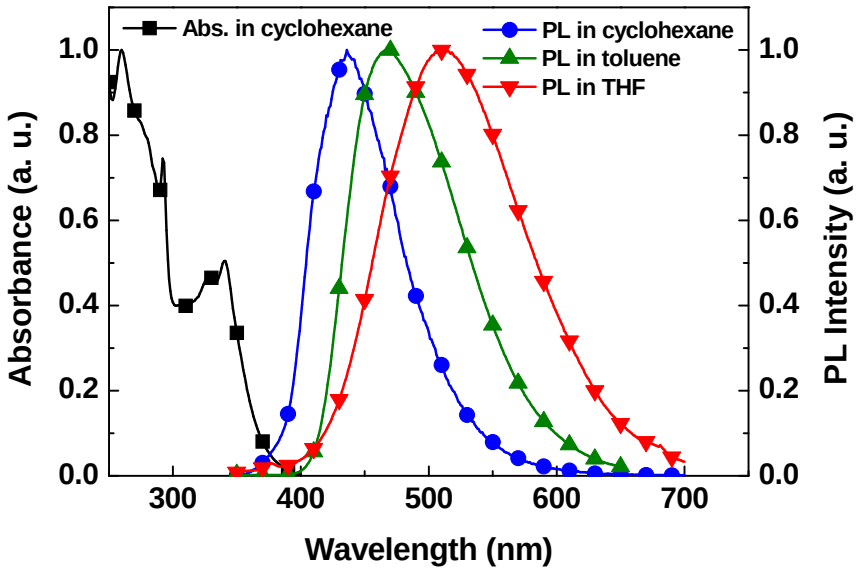

Figure 2-3. Room-temperature absorption and PL spectra of **CC2TA** in different solvents.

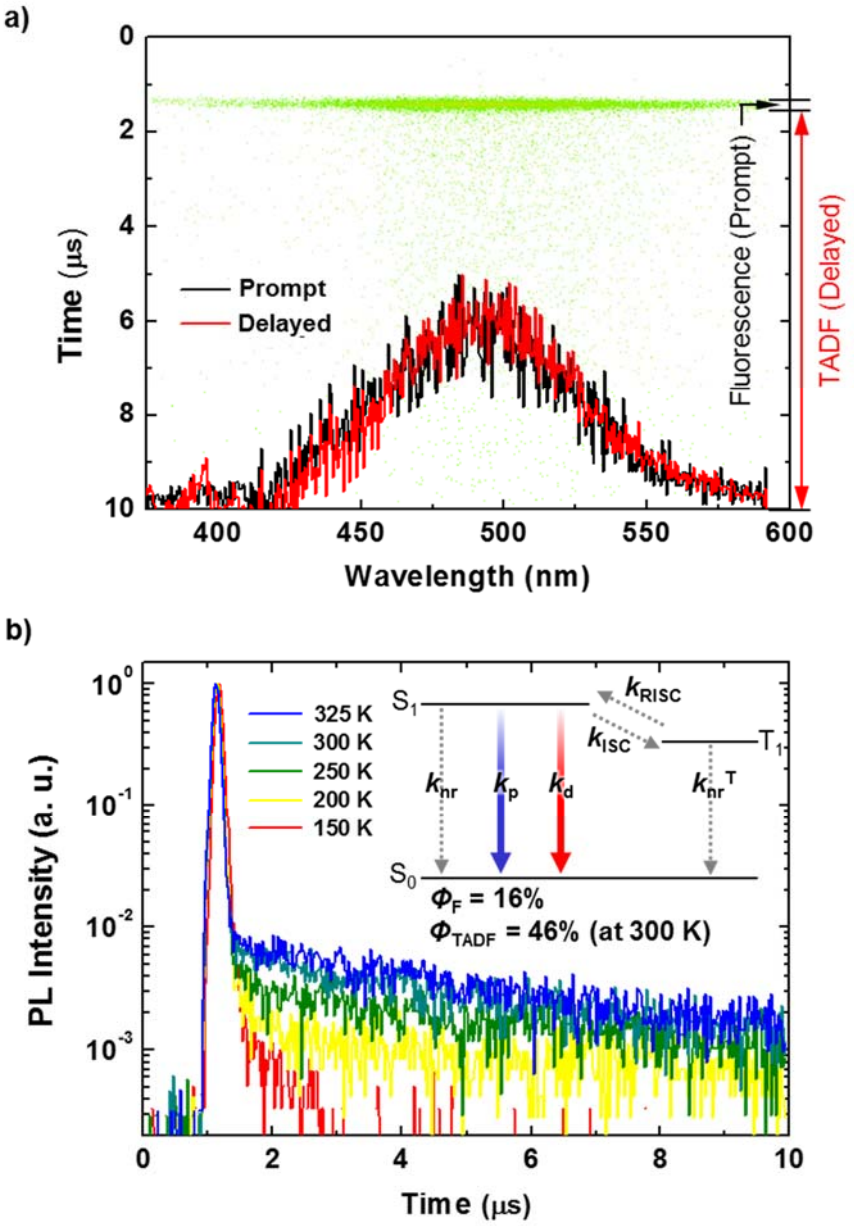

Figure 2-4. a) Streak image and PL spectra of a 6 wt%-**CC2TA**: DPEPO film showing the prompt (fluorescence, black) and delayed (TADF, red) components. b) PL decay profiles for a 6 wt%-**CC2TA**: DPEPO film measured at 150–325 K. The inset shows an energy diagram for **CC2TA** (k_p: fluorescence decay rate; k_d: TADF decay rate; k_{nr}: non-radiative decay rate from S_1 to S_0; k_{ISC}: intersystem crossing rate; k_{RISC}: reverse intersystem crossing rate; k_{nr}^T: non-radiative decay rate from T_1 to S_0; Φ_F: fluorescence efficiency; Φ_{TADF}: TADF efficiency).

2.2.3 Φ_{PL} Dependence on Host Materials

Host materials for **CC2TA** (TADF emitter) with triplet energy levels higher than that of **CC2TA** are desirable to prevent reverse energy transfer and to confine triplet excitons on **CC2TA** molecules (Fig. 2-5). To verify the dependence of TADF efficiencies on the T_1 energy levels of hosts, thin films of **CC2TA** in several representative host materials were fabricated for transient PL measurements. Here, 1,3-bis(carbazol-9-yl)benzene (mCP, T_1 = 2.90 eV),[10] 3,5-bis(carbazol-9-yl)pyridine (PYD2, T_1 = 2.93 eV),[11] 1,4-bis(triphenylsilyl)benzene (UGH-2, T_1 = 3.5 eV),[12] and DPEPO (T_1 = 3.1 eV) were utilized as host materials for **CC2TA** (Fig. 2-6). It is noteworthy that, by using DPEPO and UGH-2 hosts that possess T_1 levels higher than 3.1 eV, enhanced Φ_{TADF} exceeding 45% could be obtained. In contrast, mCP and PYD2, having T_1 similar to **CC2TA**, yield lower Φ_{TADF}, which can be attributed to triplet exciton quenching by possible reverse triplet energy transfer from **CC2TA** to the host molecules.

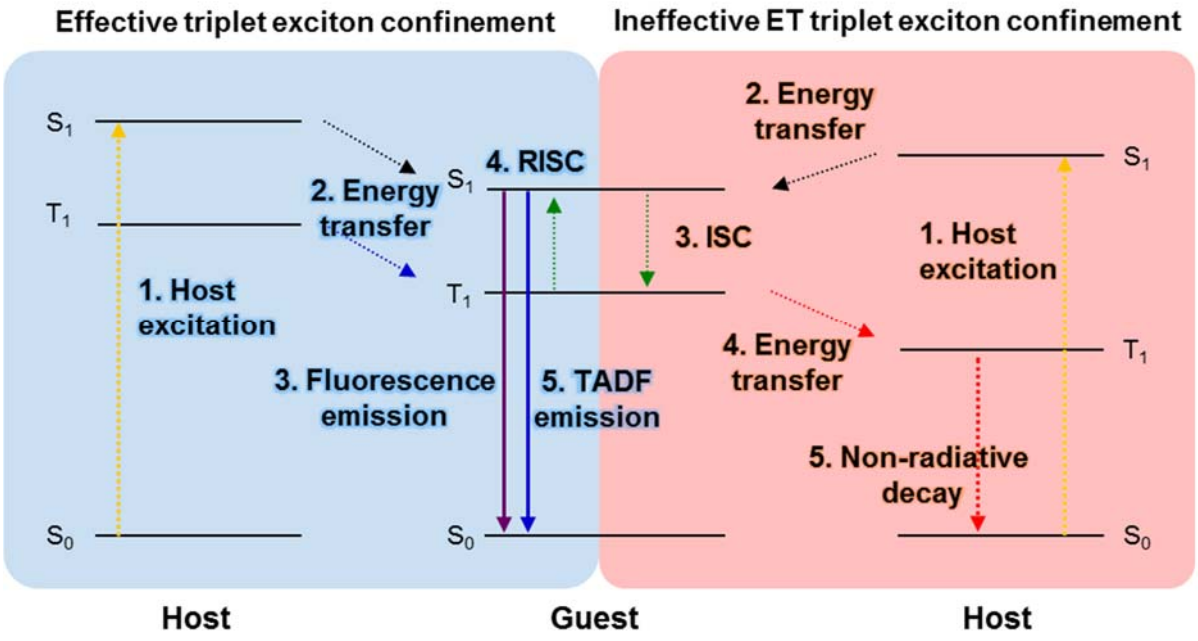

Figure 2-5. Effective and ineffective triplet excitons confinement after photo excitation between host and guest molecules.

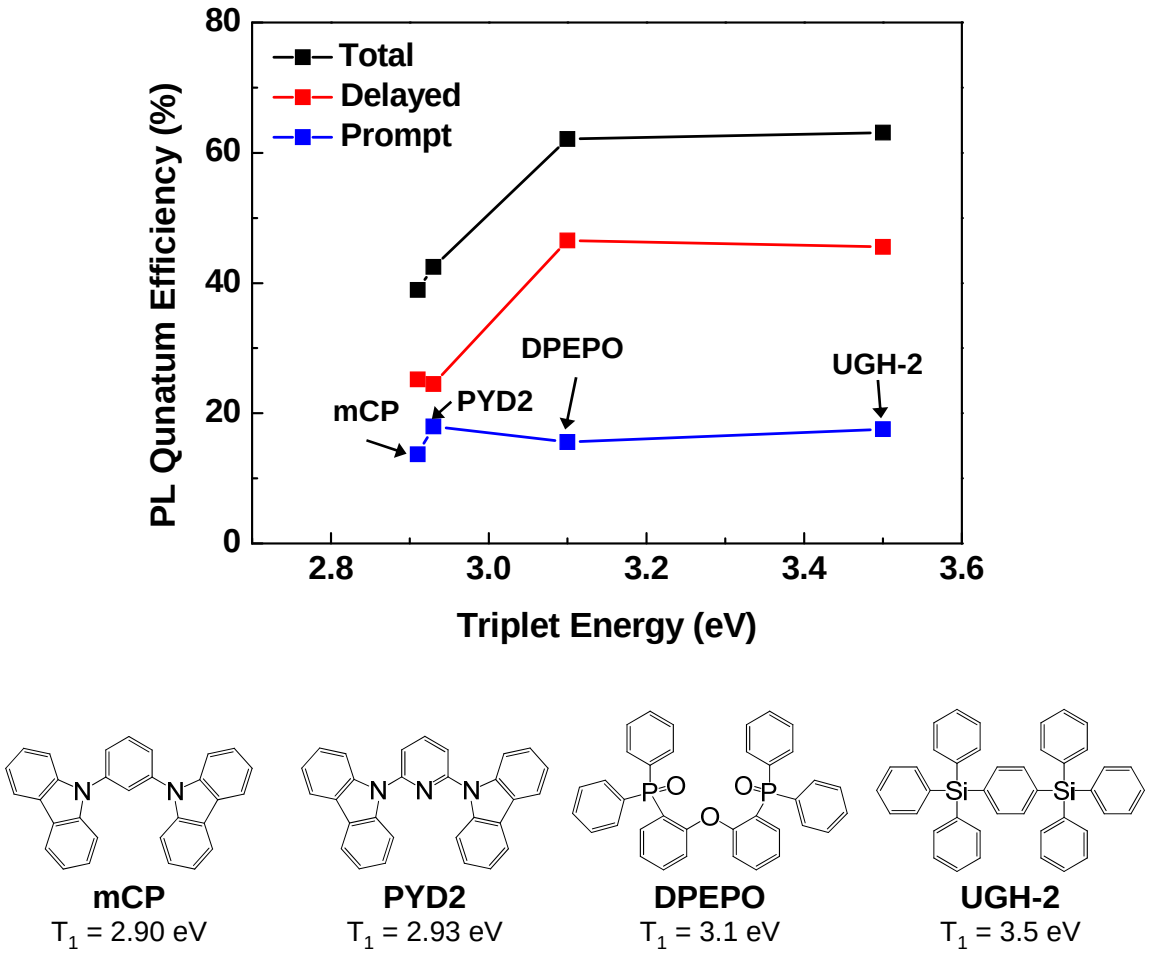

Figure 2-6. Molecular structures and relationship between T_1 of host materials and PL quantum efficiencies of 6 wt%-**CC2TA**: host films.

2.2.4 Determination of Theoretical Maximum η_{ext}

Co-deposited films of **CC2TA**: DPEPO were employed as an EML in TADF OLEDs. Firstly, the theoretical maximum η_{ext} of the TADF-based OLEDs was calculated using the prompt and delayed Φ_{PL}. Under electrical excitation in OLEDs exhibiting TADF, the triplet excitons are directly generated by carrier recombination and are then converted into the S_1 state through reverse ISC. On this basis, the theoretical maximum of η_{int} can be given by the following equation:

$$\eta_{int} = \eta_r^S \times \Phi_F + \eta_r^S \times \Phi_{TADF} + \eta_r^T \times \Phi_{TADF} / \Phi_{ISC} \qquad (2\text{-}1)$$

where η_r^S is the singlet-exciton production efficiency (25%), η_r^T is the triplet-exciton production efficiency (75%), Φ_F is the fluorescence quantum efficiency (16%, see Fig. 2-7), Φ_{TADF} is 47%, and Φ_{ISC} is the ISC efficiency (~ 84%). Therefore, η_{int} is estimated to be 56%.

Finally, the theoretical maximum of η_{ext} can be estimated using Equ. 2-2 and assuming a light η_{out} of ca. 20%. (Fig. 2-7b):

$$\eta_{ext} = \gamma \times \eta_{int} \times \eta_{out} = 1 \times 0.56 \times 0.2 \times 100 = 11.3\%. \qquad (2\text{-}2)$$

In conventional fluorescent OLEDs, the maximum η_{ext} is limited to only 3.1% when Φ_{PL} is 62.1% because fluorescence utilizes only singlet excitons for luminescence. In the case of TADF-based OLEDs featuring **CC2TA** as the emitter, a high η_{ext} (11.3%) that is almost four times higher than that of conventional fluorescent OLEDs is expected from the foregoing theoretical assumptions. To realize the high theoretical η_{ext} and low driving voltages, the optimization of the device structure is of great importance.

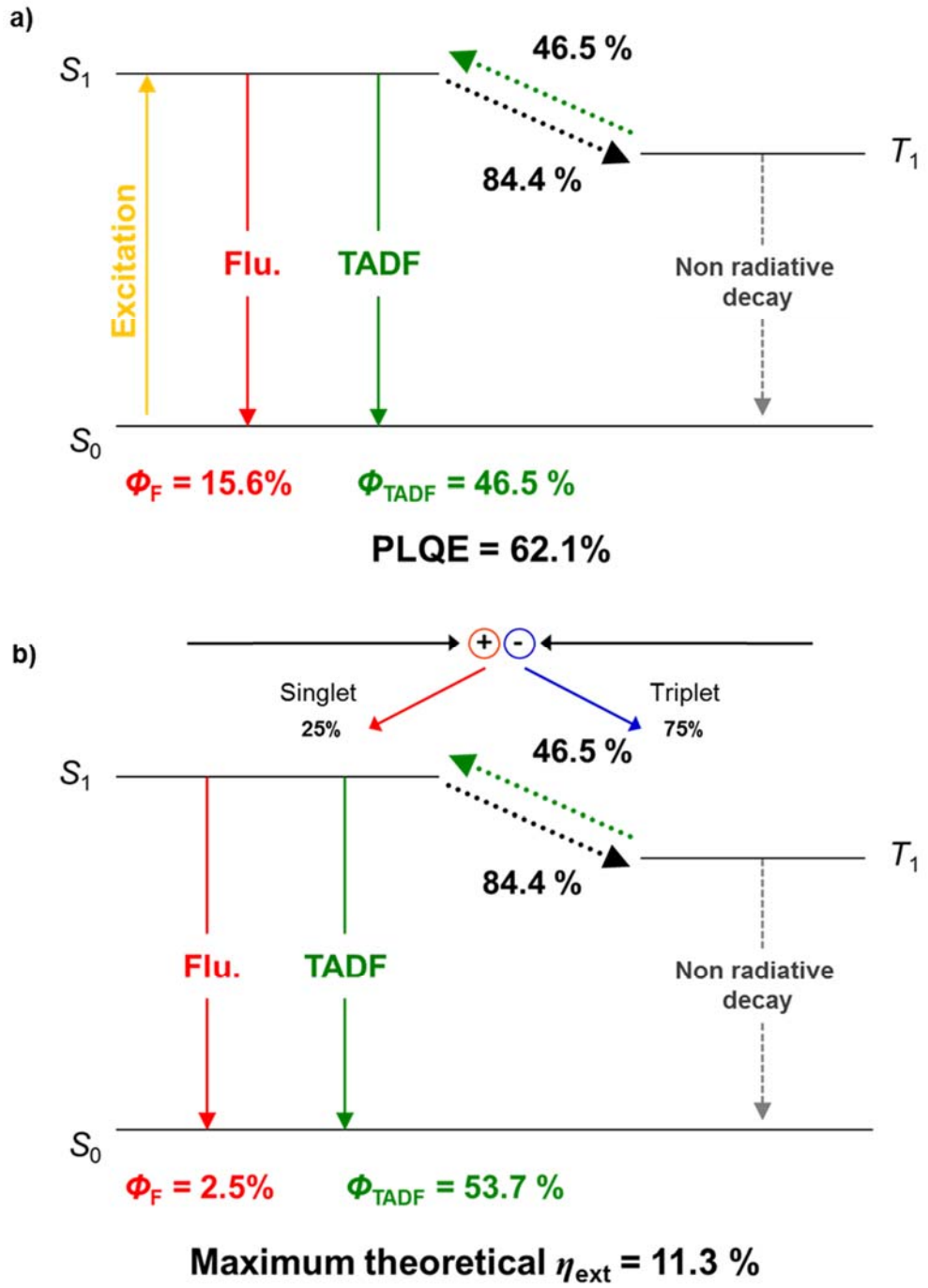

Figure 2-7. a) PL process of 6 wt%-**CC2TA**: DPEPO co-deposited film and Φ_{PL} of fluorescence and TADF. b) Electroluminescence process and maximum theoretical η_{ext} of a 6 wt%-**CC2TA**: DPEPO co-deposited film as an EML.

2.2.5 Device Optimization and EL Properties

To demonstrate the practical utility of **CC2TA** as a TADF emitter, suitable carrier transport and host materials were explored for the fabrication of multilayer OLEDs. The compounds 4,4'-bis[*N*-(1-naphthyl)-*N*-phenyl]biphenyl diamine (α-NPD), 1,3,5-tris(1-pheny-1*H*-benzo[*d*]imidazole-2-yl)benzene (TPBi), mCP, and DPEPO were used for the fabrication of three types of OLED devices.

As shown in Fig. 2-8, device **A** was fabricated with the following configuration: indium-tin-oxide (ITO)/ α-NPD (40 nm)/ mCP (10 nm)/ 6 wt%-**CC2TA**: DPEPO (20 nm)/ DPEPO (40 nm)/ LiF (0.8 nm)/ Al (80 nm). In this device, α-NPD and DPEPO serve as a HTL and an ETL, respectively, and LiF is used as an electron-injecting material. Sky-blue light-emission with a peak λ_{EL} at 490 nm and a maximum η_{ext} of 10 ± 1% at 0.01 mA cm^{-2} was observed in device **A** (Fig. 2-9b). However, device **A** showed a relatively high driving voltage of 16.8 V at 10 mA cm^{-2} presumably because of the low electron mobility of DPEPO (Fig. 2-9a) and a high electron-injection barrier between the cathode and the ETL.

To reduce the driving voltage of device **A**, a 30 nm-thick TPBi layer was introduced as an ETL instead of DPEPO in device **B** (Fig. 2-8). Using TPBi in device **B**, the driving voltage decreased considerably from 16.8 V (in device **A**) to 11.9 V at 10 mA cm^{-2} (Fig. 2-9b). The lower LUMO level of TPBi than that of DPEPO should provide a smaller electron injection

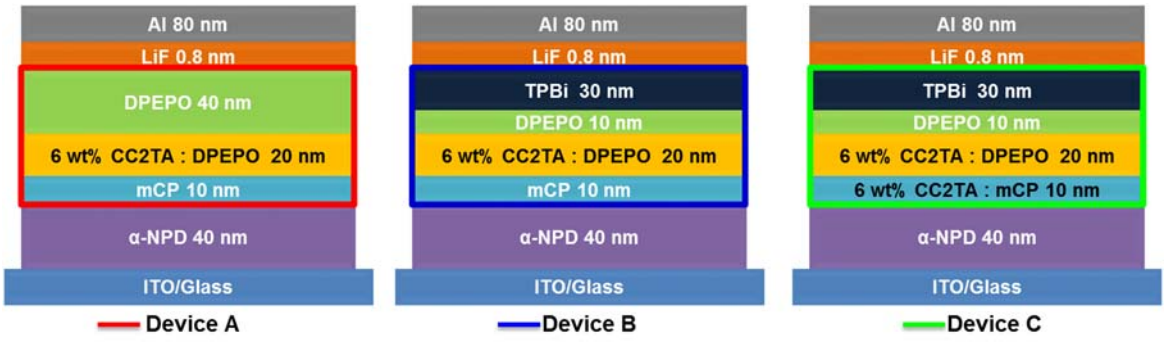

Figure 2-8. Configuration of devices **A**, **B**, and **C** using **CC2TA** as emitter.

barrier from the cathode to the ETL. However, the high electron mobility of TPBi most likely disrupted the balance of holes and electrons and caused a shift of the recombination position toward the mCP layer, which acts as an EBL, leading to an increase in emission intensity in the range of 410−450 nm.

To obtain high η_{ext} in TADF-based OLEDs, all excitons should be confined and used for light-emission in the EML. In the case of device **B**, the EL spectra included mCP emission in the range of 410−450 nm, which confirms that not all excitons contributed to light emission from **CC2TA** (Fig. 2-10). To use all of the excitons for light-emission from **CC2TA**, **CC2TA** was doped into both the mCP and DPEPO layers in device **C**.[13] The λ_{EL} was observed at 493 nm (Fig. 2-9b) and the emission from mCP in the range of 410−450 nm was suppressed.

In addition, a much lower driving voltage of 9.2 V at 10 mA cm^{-2} was achieved, attributable to a lower hole-injection barrier between HTL and EBL in device **C** (Fig. 2-9a), which originates from the high HOMO level of **CC2TA** doped in mCP. As a result, device **C** achieved the highest η_{ext} of 11 ± 1% among the three devices, which is nearly the same as the theoretical η_{ext}. Therefore, almost 100% of excitons could be used effectively for light-emission from **CC2TA** in device **C** utilizing double-doped emitting and EML (Fig. 2-8).

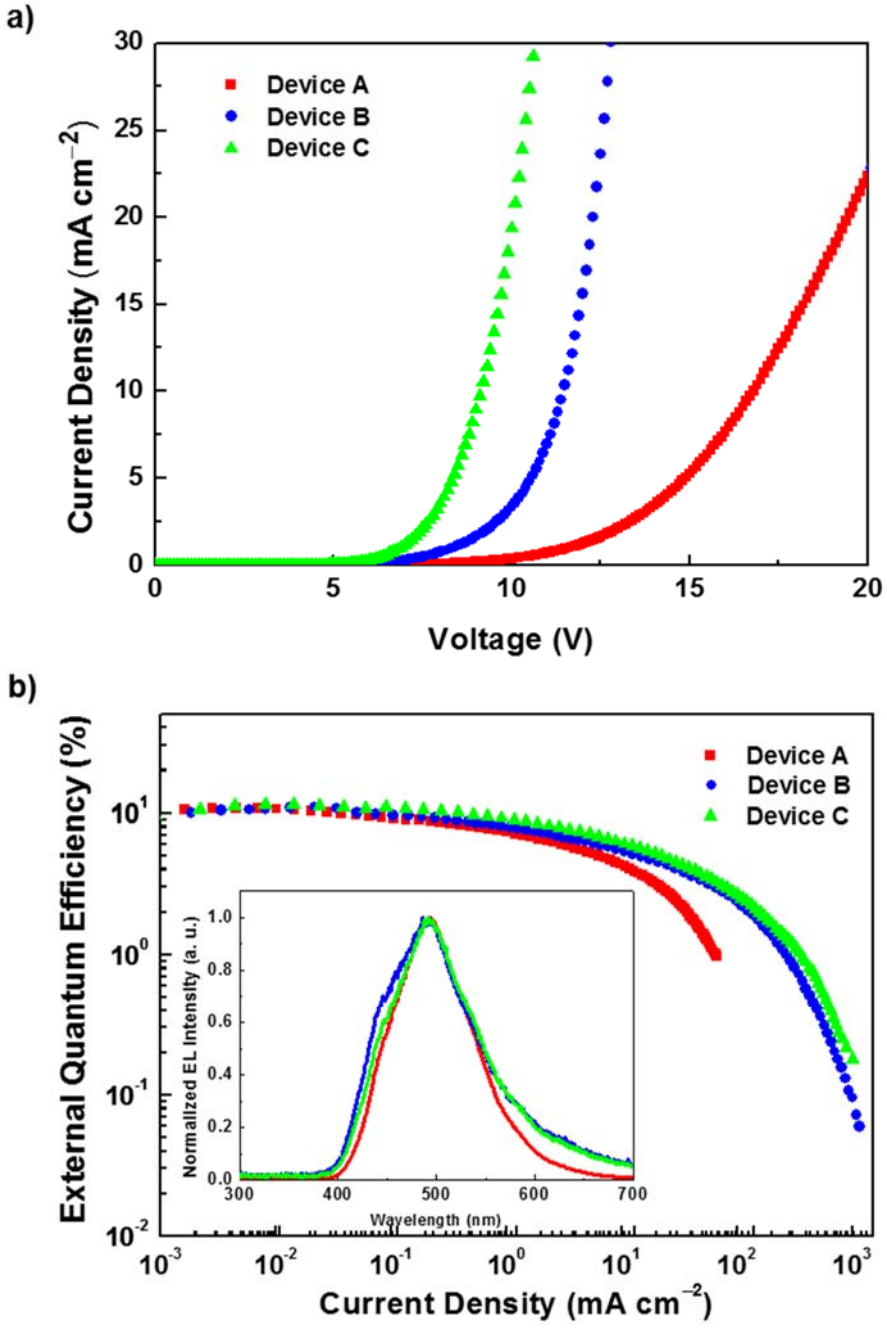

Figure 2-9. a) Current density–voltage (*J*–*V*) characteristics and b) η_{ext}–*J* plots of the OLEDs **A**, **B**, and **C** containing the TADF emitter **CC2TA** (inset: normalized EL spectra measured at 10 mA cm^{-2}).

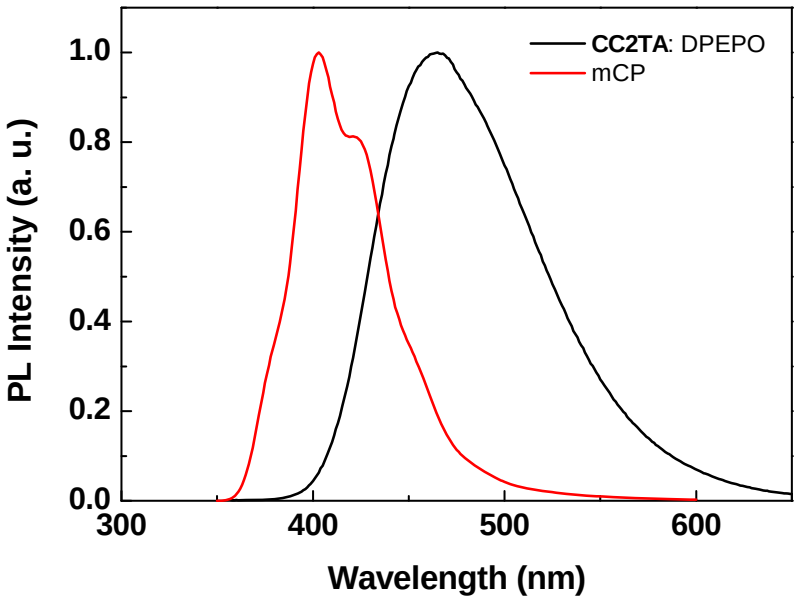

Figure 2-10. PL spectra of 6 wt%-**CC2TA**: DPEPO co-deposited (black line) and mCP neat (red line) films.

2.3 Conclusion

In summary, we developed a novel efficient TADF material **CC2TA** incorporating bicarbazole donor and phenyltriazine acceptor fragments. By employing **CC2TA** as an emitter, we have successfully achieved high-performance TADF-based OLEDs exhibiting η_{ext} as high as 11 ± 1%, which is one of the highest efficiencies in fluorescence-based OLEDs ever reported. Using the electron-accepting triazine building block tethered by appropriate electron-donating segments is a versatile and promising strategy to construct high-performance TADF materials and OLEDs.

2.4 Experimental Section

2.4.1 General Methods

NMR spectra were recorded on an Avance III 500 spectrometer (Bruker). Chemical shifts of ^{1}H NMR signals were quoted to tetramethylsilane (δ = 0.00) as an internal standard. Matrix-assisted laser desorption ionization time-of-flight (MALDI-TOF) mass spectra were collected on a Autoflex III spectrometer (Bruker Daltonics) using dithranol as the matrix. Elemental analyses were carried out with a Yanaco MT-5 CHN corder. The UV/vis absorption and PL spectra of organic films were measured with a UV-2550 (Shimadzu) and a FluoroMax-4 spectrofluorometer (Horiba Scientific), respectively. The Φ_{PL} was measured using an absolute PL quantum yield measurement system (Hamamatsu Photonics C9920-02, PMA-11). Luminescence intensity and lifetime of solutions and organic films were measured with a Quantaurus-Tau (Hamamatsu Photonics). The solution samples were excited by LED lamp (λ = 340 nm, frequency 50 Hz). The density-functional theory (DFT) computations were performed on the Gaussian 03 program package,[8] using the B3LYP functional with the 6-31G(d,p) basis set.

2.4.2 Temperature-Dependent Luminescence Lifetime and Intensity Measurements

Luminescence intensity and lifetime of organic films were measured with a Streak camera (Hamamatsu Photonics C4334). The organic films were excited by a N_2 gas laser (λ = 337 nm, pulse width = 500 ps, repetition rate 20 Hz) under a vacuum of $< 4 \times 10^{-1}$ Pa. Samples were cooled down to 28 K with a cryostat (Iwatani Industrial Gases).

2.4.3 OLED Fabrication and Measurement

To measure EL of the **CC2TA** devices, clean glass substrates precoated with a 110-nm-thick ITO layer with a sheet resistance of $< 20\ \Omega\ \square^{-1}$ were used. The substrates were degreased with distilled water, a neutral detergent, acetone, and isopropyl alcohol and cleaned in a UV-ozone

chamber (Nippon Laser and Electrics lab. NLUV253) before being loaded into an evaporation system. The organic layers were thermally evaporated on the substrates under a vacuum of < 3 × 10^{-4} Pa with an evaporation rate of < 0.3 nm s^{-1}. In all devices, a cathode aluminum (Al) layer was deposited through a 1 mm-diameter opening in a shadow mask. The current density and voltage (*J*−*V*) characteristics of OLEDs were measured using a semiconductor parameter analyzer (Agilent E5273A). The EL spectra were recorded by multichannel analyzer (Ocean Optics SD2000) at current densities of 1, 10, and 100 mA cm^{-2}. The brightness of the OLEDs was measured using an optical powermeter (Newport 1930C).

2.4.4 Materials and Synthesis of CC2TA

All reagent and solvent were purchased from, Sigma-Aldrich, Tokyo Chemical Industry (TCI), or Wako Pure Chemical Industries, and used as received unless otherwise noted. The synthetic route to obtain **CC2TA** is outlined in Scheme 2-1. All reactions were performed under an N_2 atmosphere in dry solvents.

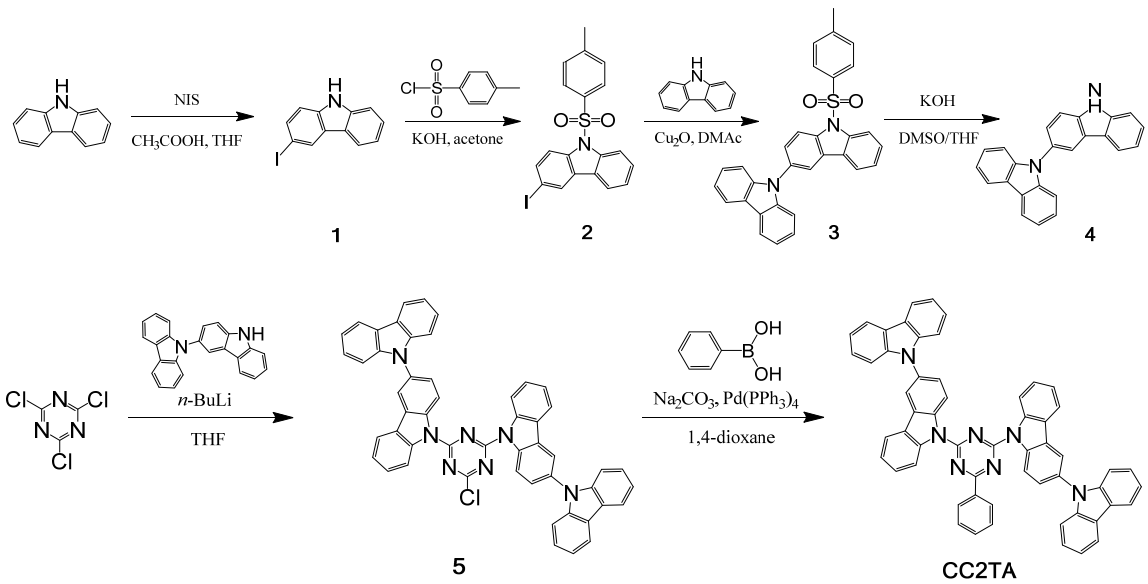

Scheme 2-1. Synthetic route for **CC2TA**.

3-Iodo-9H-carbazole **(1).** To a stirred solution of 9*H*-carbazole (10.0 g, 59.8 mmol) in THF (200 mL) was added *N*-iodosuccinimide (13.5g, 59.8 mmol) slowly at 0 °C. The mixture was stirred for 20 h at room-temperature. The reaction mixture was poured into water and then extracted with ethyl acetate. The combined organic layers were washed with water and dried over anhydrous $MgSO_4$. After the filtration and evaporation, the crude product was recrystallized from methanol. The product was dried under vacuum to afford compound **1** as a white solid (yield = 12.7 g, 72%). ^{1}H NMR (500 MHz, $CDCl_3$): δ 8.39 (d, J = 1.5 Hz, 1H), 8.07 (br, 1H), 8.01 (dd, J = 8.0, 1.5 Hz, 1H), 7.66 (dd, J = 8.5, 2.0 Hz, 1H), 7.46-7.41 (m, 2H), 7.27-7.21 (m, 2H).

3-Iodo-9-(tosylsulfonyl)-9H-carbazole **(2).** To a mixture of compound **1** (12.5 g, 42.7 mmol) and tosyl chloride (9.67 g, 51.2 mmol) in dry acetone (200 mL) was added KOH (3.45 g, 61.4 mmol) under N_2 atmosphere. The mixture was stirred for 5 h at 80 °C. After cooling to room-temperature, the reaction mixture was poured into cool water (700 mL) and stirred for 1 h. The formed precipitate was collected by filtration. The product was recrystallized from methanol, and dried under vacuum to afford compound **2** as a white solid (yield = 14.7 g, 77%). ^{1}H NMR (500 MHz, $CDCl_3$): δ 8.31 (d, J = 8.5 Hz, 1H), 8.21 (d, J = 9.0 Hz, 1H), 8.02 (d, J = 2.0 Hz, 1H), 7.85 (d, J = 7.5 Hz, 1H), 7.67 (d, J = 8.5 Hz, 2H), 7.58 (dd, J = 9.0, 2.0 Hz, 1H), 7.52 (td, J = 7.5, 1.0 Hz, 1H), 7.37 (td, J = 7.5, 1.0Hz, 1H), 7.11 (d, J = 8.0 Hz, 2H), 2.28 (s, 3H)

9-(9-Tosyl-9H-carbazol-3-yl)-9H-carbazole **(3).** To a mixture of compound **2** (14.4 g, 32.1 mmol) and 9*H*-carbazole (6.46 g, 38.6 mmol) in dry DMAc (30 mL) was added copper(I) oxide (11.1 g, 77.2 mmol) under N_2 atmosphere. The mixture was stirred for 20 h at 170 °C. After cooling to room-temperature, the reaction mixture was poured into water and extracted with toluene. The combined organic layers were washed with water, and dried over anhydrous $MgSO_4$. The resulting solution was filtered through a Celite pad and followed by an aluminium oxide pad to remove insoluble materials. The filtrate was concentrated by evaporation. The product was dried under vacuum to afford compound **3** as an orange oil (yield = 14.7 g, 94%). ^{1}H NMR (500 MHz, $CDCl_3$): δ 8.54 (d, J = 8.8 Hz, 1H), 8.39 (d, J = 8.5 Hz, 1H), 8.16 (d, J = 7.8 Hz, 2H), 8.07 (d, J = 2.2 Hz, 1H), 7.87 (d, J = 7.5 Hz, 1H), 7.81 (d, J = 7.5 Hz, 2H), 7.66 (dd, J = 8.8, 2.2 Hz, 1H), 7.55 (t, J = 8.0 Hz, 1H), 7.42-7.35 (m, 5H), 7.29 (t, J = 8.5 Hz, 2H), 7.20 (d, J = 8.8 Hz, 2H), 2.34 (s, 3H). MS (MALDI): *m/z* 486.17 $[M]^{+\cdot}$; calcd 486.14.

9-(9H-Carbazol-3-yl)-9H-carbazole (4).[2] A mixture of compound **3** (14.7 g, 30.2 mmol) and KOH (19.3 g, 0.343 mmol) in THF (40 mL), DMSO (20 mL), and water (6 mL) was stirred for 5 h at 70 °C. After cooling to room-temperature, the reaction mixture was poured into water. The solution was neutralized with an aqueous H_2SO_4 and extracted with chloroform. The combined organic layers were washed with water and dried over anhydrous $MgSO_4$. After the filtration and evaporation, the crude product was recrystallized from methanol and isopropyl alcohol. The product was dried under vacuum to afford compound **4** as a white solid (yield = 5.84 g, 58%). ^{1}H NMR (500 MHz, $CDCl_3$): δ 8.24 (br, 1H), 8.22 (d, J = 2.0 Hz, 1H), 8.19 (d, J = 7.8 Hz, 2H), 8.05 (d, J = 7.8 Hz, 1H), 7.62 (d, J = 8.4 Hz, 1H), 7.55 (dd, J = 8.4, 2.0 Hz, 1H), 7.53-7.46 (m, 2H), 7.43-7.36 (m, 4H), 7.31-7.25 (m, 3H). MS (MALDI): *m/z* 332.05 $[M]^{+\cdot}$; calcd 332.13.

2-Chloro-4,6-bis{3-(9H-carbazol-9-yl)-9H-carbazol-9-yl}-1,3,5-triazine **(5).** To a stirred solution of compound **4** (2.71 g, 8.5 mmol) in dry THF (50 mL) was added dropwise *n*-butyllithium (5.0 mL, 8.0 mmol) at 0 °C. To this solution was added, dropwise, a solution of cyanuric chloride (0.74 g, 4.0 mmol) in dry THF (20 mL). The resulting orange solution was stirred overnight at 70 °C. The crude product was precipitated by the addition of hexane (100 mL) and washed with plenty of water. The yellow solid was filtered off and dried under vacuum to give compound **5** as a pale yellow powder (yield = 2.67 g, 85%). ^{1}H NMR (500 MHz, $CDCl_3$): δ 9.24 (dd, J = 9.4, 2.5 Hz, 2H), 8.79 (d, J = 7.2 Hz, 4H), 8.35-8.32 (m, 2H), 7.89 (dd, J = 9.0, 2.0 Hz, 2H), 7.79 (d, J = 8.0 Hz, 4H), 7.69-7.40 (m, 16H). MS (MALDI): *m/z* 775.4 $[M]^+$; calcd 775.23.

2,4-bis{3-(9H-carbazol-9-yl)-9H-carbazol-9-yl}-6-phenyl-1,3,5-triazine **(CC2TA).** Compound **5** (1.50 g, 1.9 mmol) and phenylboronic acid (0.39 g, 1.9 mmol) were dissolved in dry 1,4-dioxane (40 mL). To the solution were added an aqueous sodium carbonate (2 M, 7 mL) and tertrakis(triphenylphosphine)palladium(0) (0.11 g, 0.09 mmol). After the complete addition, the mixture was stirred for 48 h at 90 °C. After cooling to room-temperature, the reaction mixture was poured into water. The product was extracted with chloroform. The combined organic layers were washed with water and dried over anhydrous $MgSO_4$. After the filtration and evaporation, crude product was purified by column chromatography on silica gel (eluent: chloroform) and dried under vacuum to give a yellow powder (yield = 1.38 g, 87%). This compound was further purified by temperature-gradient sublimation under vacuum. ^{1}H

NMR (500 MHz, $CDCl_3$): δ 9.32 (d, J = 8.5 Hz, 2H), 9.15 (d, J = 8.5 Hz, 2H), 8.81 (d, J = 8.0 Hz, 2H), 8.29 (d, J = 2.0 Hz, 2H), 8.20 (d, J = 7.5 Hz, 4H), 8.10 (d, J = 8.0 Hz, 2H), 7.76-7.72 (m, 5H), 7.62 (t, J = 7.8 Hz, 2H), 7.51-7.42 (m, 10H), 7.32 (t, J = 7.5 Hz, 4H). $^{13}C\{^1H\}$ NMR (125 MHz, $CDCl_3$): δ 173.50, 164.82, 141.43, 139.52, 137.83, 135.97, 133.30, 129.30, 129.18, 128.05, 127.79, 126.11, 126.06, 126.02, 123.85, 123.38, 120.39, 120.14, 119.94, 118.73, 118.56, 117.76, 109.77. MS (MALDI): m/z 818.26 $[M+H]^+$; calcd 818.30. Anal. calcd (%) for $C_{57}H_{35}N_7$: C, 83.70; H, 4.31; N, 11.99; found: C, 83.90; H, 4.20; N, 12.04.

2.5 References

[1] M. A. Baldo, D. F. O'Brien, Y. You, A. A. Shoustikov, S. Sibley, M. E. Thompson, and S. R. Forrest, *Nature*, **1998**, 395, 151.

[2] C. Adachi, M. A. Baldo, M. E. Thompson, and S. R. Forrest, *J. Appl. Phys*., **2001**, 90, 5048.

[3] L. Xiao, S.-J. Su, Y. Agata, H. Lan, and J. Kido, *Adv. Mater*., **2009**, 21, 1271.

[4] S. Reineke, K. Walzer, and K. Leo, *Phys. Rev. B*, **2007**, 75, 125328.

[5] J. B. Birks, *Photophysics of Organic Molecules*, **1970**, Wiley.

[6] A. Endo, K. Sato, K. Yoshimura, T. Kai, A. Kawada, H. Miyazaki, and C. Adachi, *Appl. Phys. Lett*., **2011**, 98, 083302.

[7] H. Inomata, K. Goushi, T. Masuko, T. Konno, T. Imai, H. Sasabe, J. J. Brown, and C. Adachi, *Chem. Mater*., **2004**, 16, 1285.

[8] M. J. Frisch, G. W. Trucks, H. B. Schlegel, G. E. Scuseria, M. A. Robb, J. R. Cheeseman, J. A. Montgomery, Jr., T. Vreven, K. N. Kudin, J. C. Burant, J. M. Millam, S. S. Iyengar, J. Tomasi, V. Barone, B. Mennucci, M. Cossi, G. Scalmani, N. Rega, G. A. Petersson, H. Nakatsuji, M. Hada, M. Ehara, K. Toyota, R. Fukuda, J. Hasegawa, M. Ishida, T. Nakajima, Y. Honda, O. Kitao, H. Nakai, M. Klene, X. Li, J. E. Knox, H. P. Hratchian, J. B. Cross, C. Adamo, J. Jaramillo, R. Gomperts, R. E. Stratmann, O. Yazyev, A. J. Austin, R. Cammi, C. Pomelli, J. W. Ochterski, P. Y. Ayala, K. Morokuma, G. A. Voth, P. Salvador, J. J. Dannenberg, V. G. Zakrzewski, S. Dapprich, A. D. Daniels, M. C. Strain, O. Farkas, D. K. Malick, A. D. Rabuck, K. Raghavachari, J. B. Foresman, J. V. Ortiz, Q. Cui, A. G. Baboul, S. Clifford, J.

Cioslowski, B. B. Stefanov, G. Liu, A. Liashenko, P. Piskorz, I. Komaromi, R. L. Martin, D. J. Fox, T. Keith, M. A. Al-Laham, C. Y. Peng, A. Nanayakkara, M. Challacombe, P. M. W. Gill, B. Johnson, W. Chen, M. W. Wong, C. Gonzalez, and J. A. Pople, Gaussian 03, Gaussian, Inc., Pittsburgh PA, **2003**.

[9] C. Han, Y. Zhao, H. Xu, J. Chen, Z. Deng, D. Ma, Q. Li, and P. Yan, *Chem. Eur. J.*, **2011**, 17, 5800.

[10] R. J. Holmes, S. R. Forrest, Y.-J. Tung, R. C. Kwong, J. J. Brown, S. Garon, and M. E. Thompson, *Appl. Phys. Lett.*, **2003**, 82, 2422.

[11] K. S. Son, M. Yahiro, T. Imai, H. Yoshizaki, and C. Adachi, *J. Photopolym. Sci. Technol.*, **2007**, 20, 47.

[12] X. Ren, J. Li, R. J. Holmes, P. I. Djurovich, S. R. Forrest, and M. E. Thompson, *Chem. Mater.*, **2004**, 16, 4743.

[13] X. Zhou, D. S. Qin, M. Pfeiffer, J. Blochwitz-Nimoth, A. Werner, J. Drechsel, B. Maennig, K. Leo, M. Bold, P. Erk, and H. Hartmann, *Appl. Phys. Lett.*, **2002**, 81, 4070.

Chapter 3

Luminous Butterflies: Efficient Exciton Harvesting by Benzophenone Derivatives for Full-Color Delayed Fluorescence OLEDs

Chapter 3
Luminous Butterflies: Efficient Exciton Harvesting by Benzophenone Derivatives for Full-Color Delayed Fluorescence OLEDs

Abstract

Butterfly-shaped luminescent benzophenone derivatives possessing small ΔE_{ST} are used to achieve efficient delayed fluorescence covering the full color spectrum. OLEDs with emissive layers doped with these benzophenone derivatives generate EL ranging from blue to orange-red and white, with maximum η_{ext} of up to 14.3%. Triplet excitons are efficiently harvested through delayed fluorescence processes.

3.1 Introduction

In the previous chapter, OLEDs emitting sky-blue emission with an η_{ext} of 11% were achieved by developing the emitter, **CC2TA**, which harvests electrically-generated triplet excitons through TADF to produce fluorescence. However, the application of OLEDs to full-color flat-panel displays and solid-state lighting requires the development of red, green, and blue (RGB) emitting materials that can cover the full color spectrum. While RGB emission from phosphorescent materials with high luminescence quantum efficiencies has been achieved,[1−4] the organic emitting materials generally suffer from instability in practical applications, especially for blue and white emission. Realizing high-efficiency RGB EL through a simple organic materials system to reduce the production cost and simplify the manufacturing processes is pivotal for next-generation OLED technology.

Herein, a series of butterfly-shaped TADF-emitting benzophenones featuring donor-acceptor-

donor (D-A-D) electronic configurations is developed. Benzophenone is well known as a non-metallic phosphorescence molecule and its photophysical processes have been widely investigated. Small overlap between the HOMO and LUMO of benzophenone results in a small ΔE_{ST} of 0.2 eV and a fast ISC rate constant of 10^{11} s^{-1} from the S_1 (n-π*) to T_1 (n-π*) state, which accelerates RISC from T_1 (n-π*) to S_1 (n-π*) and enables the emission of delayed fluorescence at room-temperature (Fig. 3-1).[5–7] Thus, molecules designed based on benzophenone framework are expected to be able to achieve small ΔE_{ST}, high up-conversion efficiency, and strong delayed fluorescence emission. Furthermore, the simple molecular structure of benzophenone should allow easy modification and synthesis of newly designed molecules, and the large E_g of benzophenone makes is suitable for blue emission.

Benzophenone itself was previously explored as a blue phosphorescence emitter in OLEDs using benzophenone dispersed in Poly(methyl methacrylate) (PMMA) films as an EML, but the devices exhibited relatively low efficiency at room-temperature.[8,9] However, practical EL from benzophenone derivatives at ambient temperature has yet to be demonstrated. A remarkable feature of the system developed here (Fig. 3-2) is that OLEDs employing such D-A-D-structured benzophenones as light-emitting centers can generate highly efficient blue to orange-red TADF via up-conversion and realize η_{ext} far exceeding the theoretical limit for conventional fluorescence OLEDs. Moreover, highly efficient TADF benzophenones based WOLEDs are reported.

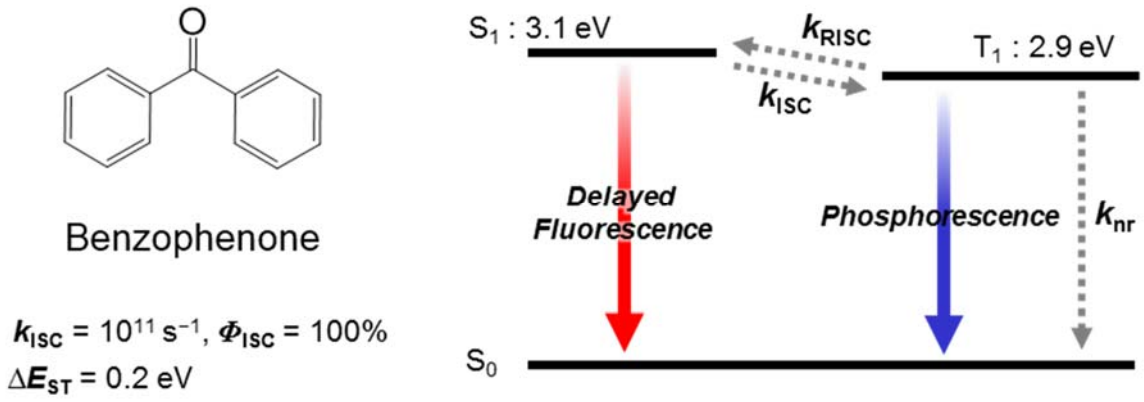

Figure 3-1. Molecular structure and schematic representation of PL decay of benzophenone.

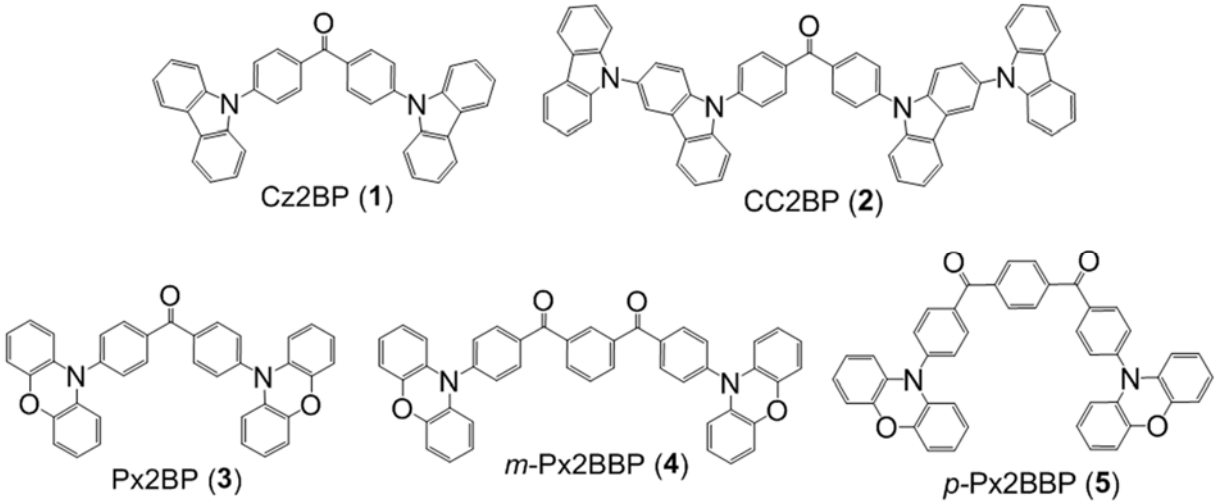

Figure 3-2. Molecular structures of butterfly-shaped benzophenone derivatives **1**−**5**.

3.2 Results and Discussion

3.2.1 Characterization of the Geometric and Electronic Structures of Benzophenone Derivatives Using TD-DFT Calculations

In principle, ΔE_{ST} should decrease upon decreasing the exchange interaction integral of the HOMO and LUMO wavefunctions of a molecule.[10] Consequently, careful selection of appropriate donor units is crucial for designing full-color TADF molecules, which should have their HOMO and LUMO localized on different constituents. To gain insight into the geometric and electronic structures of **1**−**5**, TD-DFT calculations were performed at the B3LYP/6-31G (d,p) level. All of the molecules were found to exhibit clear separation of their HOMO and LUMO distributions.

As exemplified in Fig. 3-3 for **1**−**3**, the LUMO is predominantly located on the central electron-accepting benzophenone core whereas the HOMO is mainly localized on the electron-donating peripheral carbazole or phenoxazine substituents because of the highly twisted geometry between the donor and acceptor constituents. In their optimized ground-state structures, the dihedral angles between the phenyl rings of the benzophenone unit and adjacent

carbazoles are calculated to be 51° for **1** and 61° for **2** and that with phenoxazines to be 85° for **3**. This evident special separation of the frontier orbitals leads to small ΔE_{ST} of 0.01−0.32 eV (Table 3-1), suggesting the possibility of exciton harvesting by $T_1 \rightarrow S_1$ up-conversion. Furthermore, all of the investigated lowest-excited states corresponded to ICT with a small exchange energy, which are mainly described by the HOMO→LUMO transition.

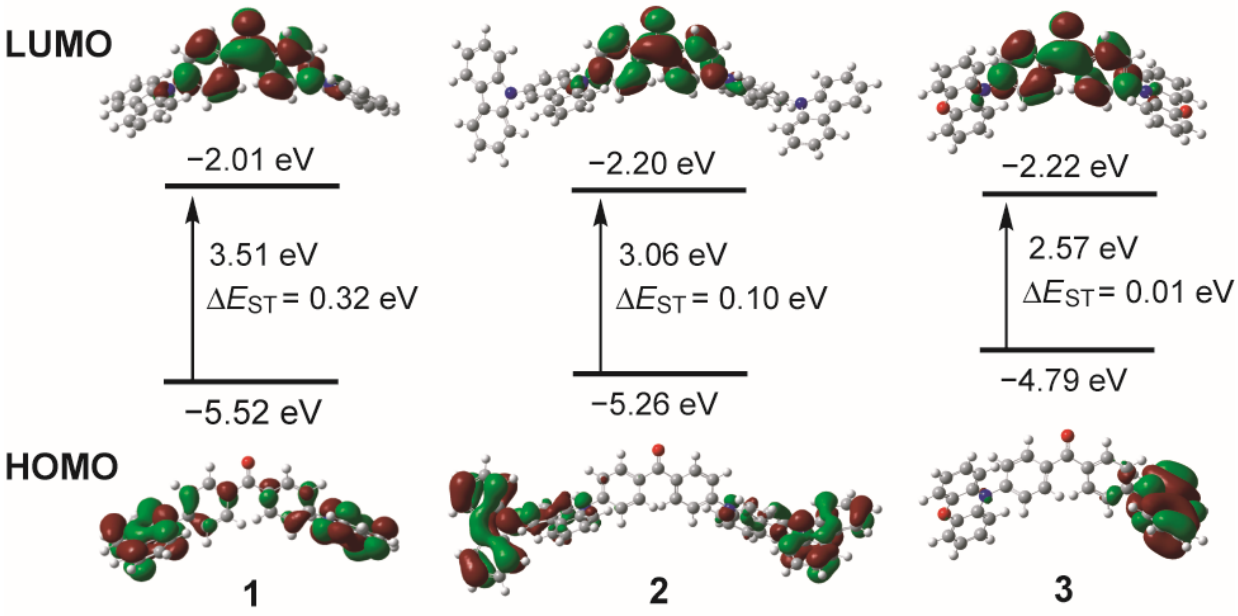

Figure 3-3. Frontier molecular orbital distributions, energy levels, and energy gaps (ΔE_{ST}) between S_1 and T_1 characterized by TD-DFT calculations for **1**−**3**.

Table 3-1. Triplet and singlet excitation energies (vertical transition), oscillator strength (*f*), and transition configurations of the benzophenone derivatives **1**−**5** calculated by TD-DFT at the B3LYP/6-31G (d,p) level

Compound	State	*E* (eV)	*f*	Main Configuration [a)]		ΔE_{ST} (eV)
Cz2BP (**1**)	S_1	3.035	0.3619	H → L	0.702	0.32
	S_2	3.158	0.0357	H−1 → L	0.703	
	T_1	2.716	0	H−1 → L	0.564	
	T_2	2.795	0	H → L	0.651	
CC2BP (**2**)	S_1	2.735	0.1529	H → L	0.692	0.10
	S_2	2.767	0.0092	H−1 → L	0.699	
	T_1	2.634	0	H−1 → L	0.566	
	T_2	2.660	0	H → L	0.631	
Px2BP (**3**)	S_1	2.070	0.0063	H → L	0.699	0.01
	S_2	2.102	0.0182	H−1 → L	0.699	
	T_1	2.059	0	H → L	0.619	
	T_2	2.063	0	H−1 → L	0.617	
m-Px2BBP (**4**)	S_1	2.120	0.0200	H−1 → L	0.484	0.02
				H−1 → L+1	−0.407	
	S_2	2.125	0.0074	H → L	0.478	
	T_1	2.095	0	H−1 → L	0.529	
				H−1 → L+1	−0.444	
	T_2	2.096	0	H → L	0.519	
				H → L+1	0.456	
p-Px2BBP (**5**)	S_1	1.898	0.0235	H → L	0.693	0.02
	S_2	1.905	0.0090	H−1 → L	0.693	
	T_1	1.877	0	H−1 → L	0.687	
	T_2	1.878	0	H → L	0.688	

a) H → L represents the HOMO to LUMO transition. Excitation configurations with the highest contributions are presented, together with the corresponding transition symmetry and nature of the involved orbitals.

3.2.2 Photophysical Properties of Benzophenone Derivatives

Consistent with the calculations, emission color tuning can be confirmed by observations with the naked eye: **1**−**5** exhibit bright PL in solution with emission varying from blue to green to orange-red (Fig. 3-4a). This indicates that changing the degree of ICT indeed effectively modulates the emission wavelength of the molecules. The steady-state UV/vis absorption and PL spectra of **1**−**5** in toluene are depicted in Fig. 3-4b, and the photophysical properties are summarized in Table 3-2.

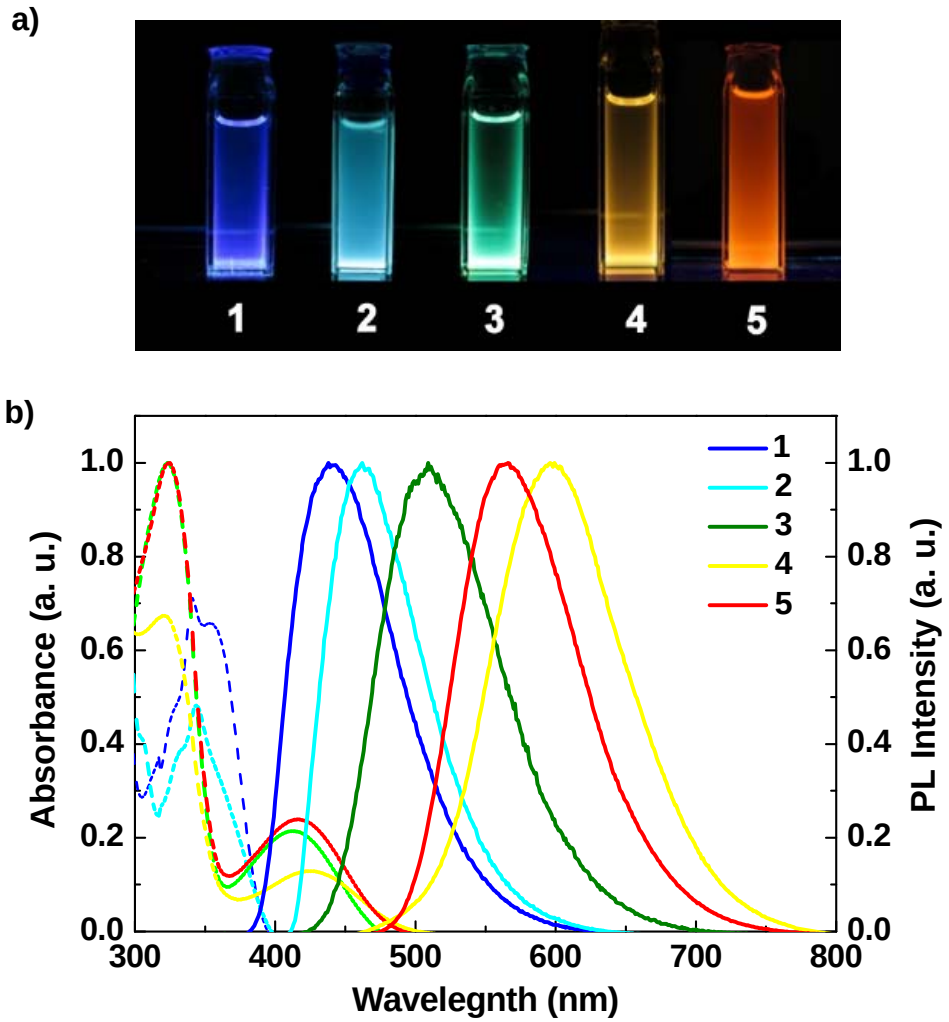

Figure 3-4. a) Images of **1**−**5** in toluene under UV irradiation (365 nm). b) Absorption (left) and PL (right) spectra of **1**−**5** in toluene at room-temperature.

In oxygen-free toluene solution, **1**−**5** exhibited broad structureless emission with Φ_{PL} of 10−44%, but the PL intensity drastically decreased in the presence of triplet oxygen ($^3O_2$) in aerated solutions. Adopting phenoxazine instead of carbazoles as the donor units resulted in a red shift of the PL emission peak (λ_{PL}), as can be seen for **3** (λ_{PL} = 509 nm). Depending on the substitution mode of an additional benzoyl group on the innermost benzene ring, considerable red shifts of λ_{PL} compared with **3** were observed in bis(benzoyl)benzenes **4** (λ_{PL} = 566 nm) and **5** (λ_{PL} = 600 nm) in solution. Therefore, the additional electron-withdrawing benzoyl unit with the *para*-linkage is thought to stabilize the LUMO and decrease the bandgap energy more than that with the *meta*-linkage. Thus, fine tuning of the luminescence properties was achieved by simple chemical modification of benzophenone.

Table 3-2. Photophysical properties of the benzophenone-based TADF luminophores **1**−**5**

Compound	λ_{PL} (nm) sol[a] / film[b]	Φ_{PL} (%)[c] sol[a] / film[b]	τ_p (Φ_F) (ns (%))[d]	τ_d (Φ_{TADF}) (μs (%))[d]	HOMO (eV)[e]	LUMO (eV)[f]	ΔE_{ST} (eV)	Calc. ΔE_{ST} (eV)[g]
1	438 / 444	21 / 55	59 (5)	710 (50)	−5.74	−2.64	0.21	0.32
2	462 / 475	38 / 73	62 (11)	460 (62)	−5.65	−2.63	0.14	0.10
3	509 / 538	44 / 70	23 (41)	12 (29)	−5.44	−2.92	0.03	0.01
4	566 / 541 (575)	36 / 71 (29)	24 (44)	13 (27)	−5.64	−3.03	0.10	0.02
5	600 / 555	10 / 36	26 (26)	2.9 (10)	−5.62	−3.13	0.06	0.02

a) Measured in oxygen-free toluene solution at room-temperature. b) 6 wt%-doped film in a host matrix (host = DPEPO for **1** and **2**; mCP for **3**; mCBP for **4** and **5**). The data for a neat film are given in parentheses. c) Absolute Φ_{PL} evaluated using an integrating sphere. d) τ_p and τ_d decay components for the 6 wt%-doped film measured at 300 K under vacuum. The fractional contributions of Φ_F and Φ_{TADF} to the total Φ_{PL} (%) are given in parentheses. e) Determined by photoelectron yield spectroscopy in thin films. f) Deduced from the HOMO and optical E_g. g) Calculated by TD-DFT at the B3LYP/6-31G (d,p) level.

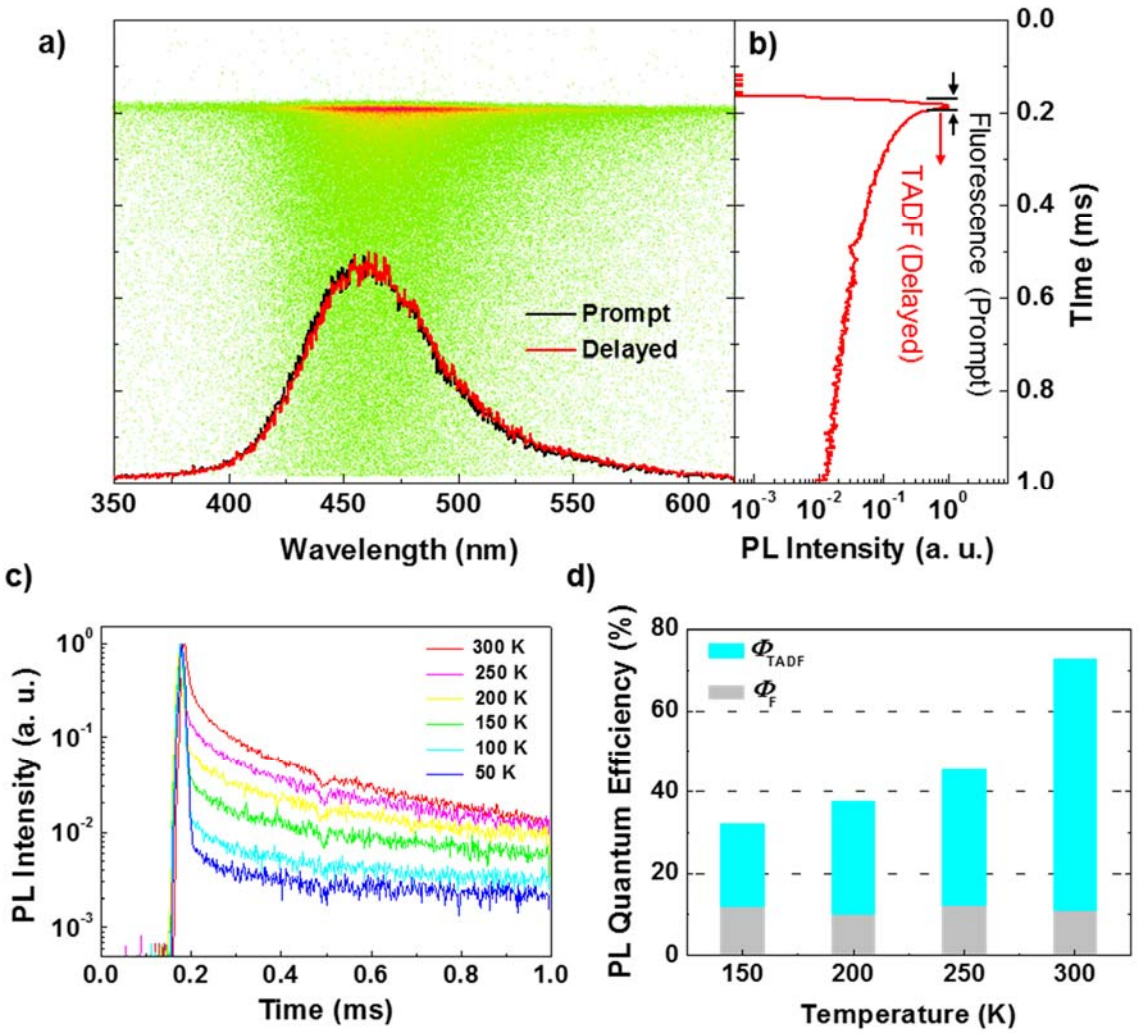

Figure 3-5. a) Streak image and corresponding time-dependent emission spectra, and b) transient PL decay profile of a 6 wt%-**2**: DPEPO co-deposited film recorded at 300 K. Prompt fluorescence (black) and TADF (red) components are shown. Each dot in the streak image represents a PL photon count. c) Temperature dependence of transient PL decay. d) The fractional contribution of fluorescence and TADF to the total Φ_{PL}.

To better understand the nature of the emitting states, the transient PL characteristics and their temperature dependence were analyzed using a streak camera (Fig. 3-5). Co-deposited guest:host thin solid films containing low concentrations of the guest emitters **1**−**5** were used to avoid emitter concentration quenching and complications by solvent phase changes. For the blue emitters, **1** and **2**, DPEPO[11] with higher S_1 and T_1 energies (E_S/E_T = 3.5/3.1 eV) was selected as a host to prevent backward excited energy transfer from the guest to host. The Φ_{PL} for **1**−**5** in suitable amorphous host matrices are approximately two to three times larger than those measured in dilute solutions (Table 3-2). This is likely because of reduced non-radiative relaxation through suppression of intramolecular torsional/vibrational motions in the solid thin films.[12]

As displayed in Fig. 3-5b, a 6 wt%-**2**: DPEPO codeposited film exhibits a two-component decay consisting of a nano-second-scale prompt component (τ_p = 62 ns) and a micro-second-scale delayed component (τ_d = 460 μs) at 300 K. Because the delayed emission has the same spectral distribution as the prompt fluorescence stemming from the S_1 state but with a longer decay time, the long-lived emission can be assigned to TADF. Furthermore, the TADF emission intensity is found to increase with increasing temperature from 50 to 300 K (Fig. 3-5c). At ambient temperature (300 K), the upper-lying S_1 state is significantly populated via thermally-activated up-conversion from the T_1 state, and in turn emits efficient TADF. Hence, the overall Φ_{PL} of the **2**: DPEPO doped film reaches 73 ± 2% at room-temperature, including quantum efficiencies of 11 ± 2% for Φ_F and 62 ± 2% for Φ_{TADF}, as listed in Table 3-2.

3.2.3 Correlation between Rate Constant and ΔE_{ST}

Using the PL efficiency and lifetime data measured at 300 K, the k_r^S, k_{ISC}, and k_{RISC} of benzophenone-based TADF luminophores **1**−**5** were calculated in Table 3-3.[13] The correlations between experimental ΔE_{ST}, dihedral angle between the of donor and acceptor, and k_{RISC} of the benzophenone-based TADF luminophores **1**−**3** were investigated (Table 3-4). The experimental ΔE_{ST} were determined from the energy difference between the high-energy onset positions of the fluorescence (300 K) and phosphorescence (5 K) spectra. As shown in Fig. 3-6a, compound **1**, which has a small dihedral angle of 51°, exhibited a large ΔE_{ST} of 0.21 while a small ΔE_{ST} of 0.03 eV was observed in compound **3**, which has a large dihedral angle of 85°.

Table 3-3. Rate constants and quantum efficiencies for decay processes in **1**−**5**[a)]

Compound	k_r^S (s^{-1})	k_{ISC} (s^{-1})	k_{RISC} (s^{-1})	Φ_{ISC} (%)	Φ_{RISC} (%)
1	8.5×10^5	1.6×10^7	1.5×10^3	95	53
2	1.8×10^6	1.4×10^7	1.4×10^4	89	69
3	1.8×10^7	2.5×10^7	1.0×10^5	59	50
4	1.8×10^7	2.4×10^7	8.3×10^4	56	48
5	9.9×10^6	2.8×10^7	1.8×10^5	74	14

a) Measured with 6 wt%-doped films in a host matrix (host = DPEPO for **1** and **2**; mCP for **3**; mCBP for **5**). Data for **4** were obtained from a neat film.

The ΔE_{ST} of molecules is related to the orbital overlap between HOMO and LUMO (see chapter 1.3). Thus, a large dihedral angle between donor and acceptor of the benzophenone-based TADF luminophores helps to reduce the overlap of HOMO and LUMO and achieve a small ΔE_{ST}.

Figure 3-6b depicts the correlation between ΔE_{ST} and k_{RISC} of the benzophenone-based TADF luminophores **1**−**3**. The k_{RISC} is given by the following equations (more details can be found in section 3.4.3):

$$k_{RISC} = \frac{k_p k_d}{k_{ISC}} \frac{\Phi_{TADF}}{\Phi_F} \qquad (3\text{-}1)$$

From this equation, k_{RISC} can be seen to be strongly effected by Φ_{TADF}, which is in turn related to ΔE_{ST}. As such, compound **3** has a small ΔE_{ST} of 0.03 eV and a very fast k_{RISC} of 1.0×10^5 s^{-1} as compared to compound **1** with a k_{RISC} of 1.5×10^3 s^{-1} and a large ΔE_{ST} of 0.21 (Fig. 3-6b). These results for benzophenone-based TADF luminophores **1**−**3** are in good agreement with the idea that a small ΔE_{ST} is necessary for high up-conversion efficiency in TADF emitters.

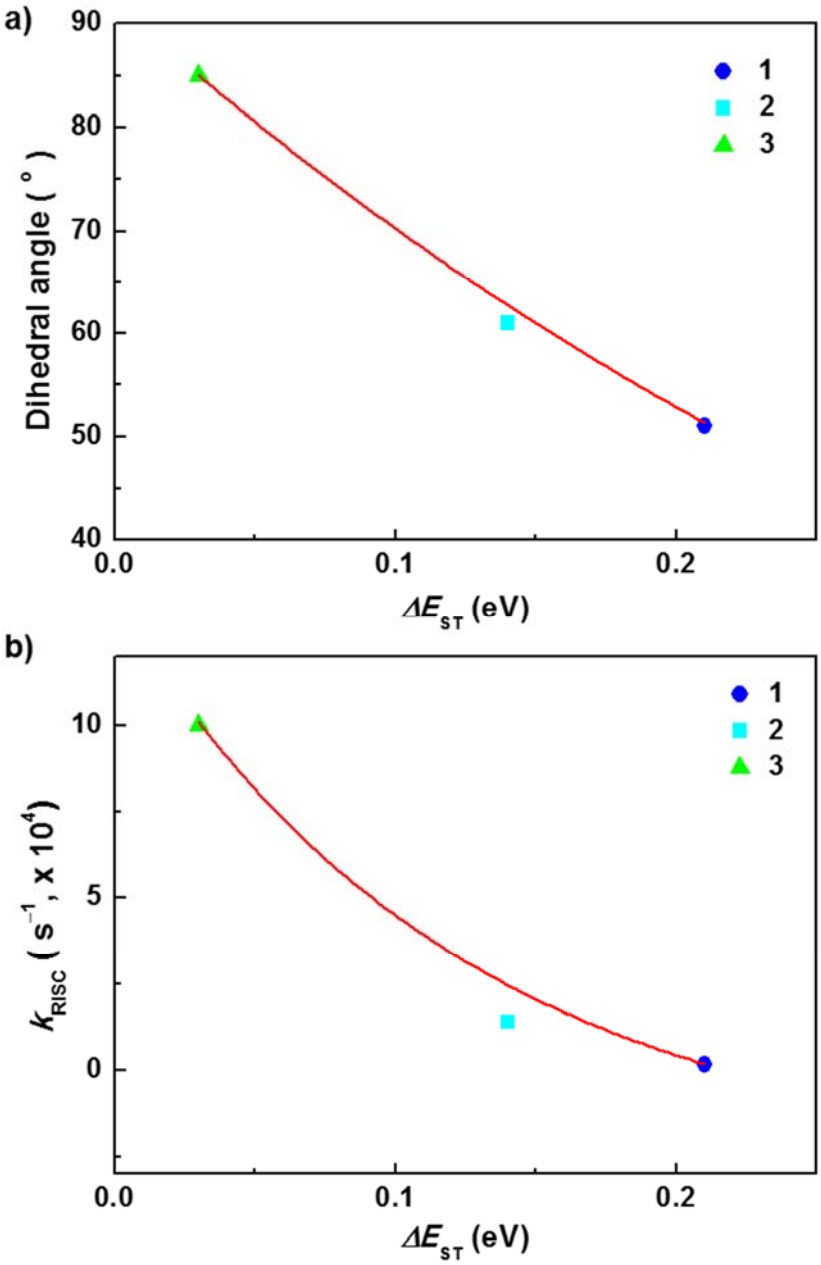

Figure 3-6. Correlation between ΔE_{ST} and a) dihedral angle between donor and acceptor and b) k_{RISC} of the benzophenone-based TADF luminophores **1**−**3**.

Table 3-4. Dihedral angles between donor and acceptor, experimental ΔE_{ST}, and k_{RISC} of the benzophenone-based TADF luminophores **1**−**5**

Compound	dihedral angle between donor and acceptor (°)[a)]	ΔE_{ST} (eV)[b)]	k_{RISC} (s^{-1}, × 10^4)
1	51	0.21	0.15
2	61	0.14	1.4
3	85	0.03	10
4	82	0.10	8.3
5	79	0.06	18

a) Optimized molecular structures calculated by Gaussian 03 at the B3LYP/6-31G (d, p) level.
b) Estimated from PL spectra of 6 wt% emitter: host co-deposited films at 300 and 5K.

3.2.4 Fabrication and EL Properties of Full-Color Delayed Fluorescence OLEDs

As expected, the photophysical properties of the D-A-D-structured benzophenones, with high Φ_{TADF} values of ca. 36−73% in their doped films, are favorable for developing highly efficient OLEDs. To evaluate the performance of **1**−**5** as emitters, multilayer OLED devices **A**−**E** were fabricated with structures of ITO/ α-NPD (35 nm)/ mCP (5 nm)/ emitter:host (20 nm)/ DPEPO (10 nm)/ TPBi (30 nm)/ LiF (0.8 nm)/ Al (80 nm) for **1** and **2** (i.e., devices **A** and **B**) and ITO/ α-NPD (40 nm)/ emitter:host (20 nm)/ TPBi (40 nm)/ LiF (0.8 nm)/ Al (80 nm) for **3**−**5** (*i.e.*, devices **C**−**E**). In these devices, α-NPD was used as an HTL and TPBi as an ETL. For devices **A** and **B**, thin layers of mCP and DPEPO, which have sufficiently high E_T, were inserted at the EML/HTL and ETL interfaces, respectively, to confine T_1 excitons in the EML and suppress T_1 exciton quenching in the devices with blue emitters. For the orange-red emitting device **E**, compound **4** was used as a non-doped EML. An energy level diagram of the devices and the chemical structures of the used materials are provided in Fig. 3-7.

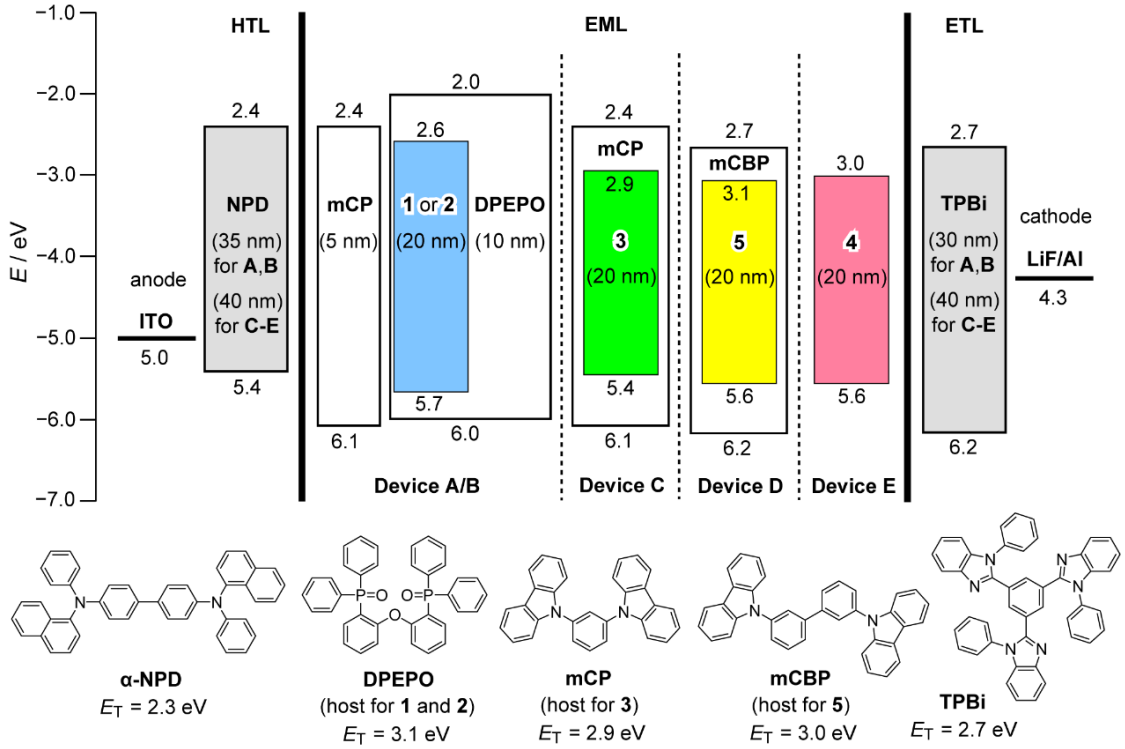

Figure 3-7. Energy level diagram showing the HOMO/LUMO levels of the materials used in devices **A**–**E** and the chemical structures of the materials.

Table 3-5. TADF-OLED performance of devices **A**–**F**[a)]

Device	**A**	**B**	**C**	**D**	**E**	**F**
Emitter	**1**	**2**	**3**	**5**	**4**	**2/5**
Host	DPEPO	DPEPO	mCP	mCBP	none	PPF/mCBP
λ_{EL} (nm)	446	484	539	548	586	489/548
V_{on} (V)	4.3	4.4	3.2	3.6	2.8	5.0
L_{max} (cd m^{-2})	510	3900	86100	57120	50820	9800
η_c (cd A^{-1})	9.3	25.5	35.9	20.1	11.1	16.4
η_{ext} (%)	8.1	14.3	10.7	6.9	4.2	6.7
CIE (x, y)	0.16, 0.14	0.17, 0.27	0.37, 0.58	0.49, 0.51	0.58, 0.36	0.32, 0.39

a) Abbreviations: λ_{EL} = EL emission maximum; V_{on} = turn-on voltage at 1 cd m^{-2}; L_{max} = maximum luminance; η_c = maximum current efficiency; η_{ext} = maximum external EL quantum efficiency (at L > 1 cd m^{-2}); CIE = Commission Internationale de l'Éclairage color coordinates measured at 10 mA cm^{-2}.

Figure 3-8 presents *J*−*V* characteristics, η_{ext}−*J* plots, and EL spectra of the fabricated devices. The key characteristics are summarized in Table 3-5. All devices based on **1–5** exhibited EL spectra similar to the corresponding PL spectra of their doped (or neat) films (Fig. 3-8b), confirming that EL emission was generated solely from the emitters themselves through the same radiative decay process. As illustrated in the Commission Internationale de l'Éclairage (CIE) chromaticity diagram in Fig. 3-12, the EL emission color can be tuned from blue (0.16, 0.14; device **A**) to orange-red (0.58, 0.36; device **E**) using the TADF benzophenones **1**−**5**.

The current efficiency (η_c) and power efficiency (η_p) versus *J* plots for devices **A**−**E** are shown in Fig. 3-9. The sky-blue emitting device **B** incorporating **2** achieved a high maximum η_{ext} of 14.3% and η_c of 25.5 cd A^{-1} at low *J*. With increasing *J*, η_{ext} of device **B** and blue emitting device **A** decrease more rapidly than those of other devices. This efficiency roll-off at high *J* is mainly attributed to excess T_1 excitons in the EML, which cause exciton quenching via TTA and/or STA.[14,15)]

The green emitting device **C** incorporating **3** also displayed notable EL efficiencies: maximum η_{ext} = 10.7% and η_c = 35.9 cd A^{-1} with a high maximum luminance (L_{max}) of 86100 cd m^{-2}. At a high current density of 100 mA cm^{-2}, the η_{ext} of device **C** was still as high as 5%, indicating a reduced efficiency roll-off, presumably because of the relatively short TADF lifetime (12 μs) for the doped film of **3**. Although the performance of blue-emitting device **A** and yellow-emitting device **D** was lower than that of device **C**, maximum η_{ext} values of 8.1% and 6.9% were obtained for devices **A** and **D**, respectively, which are much higher than the 5% theoretical limit for the η_{ext} of OLEDs based on conventional fluorescence. The orange-red-emitting device **E** exhibited a very low turn-on voltage of 2.8 V and better efficiency roll-off characteristics at high current densities.

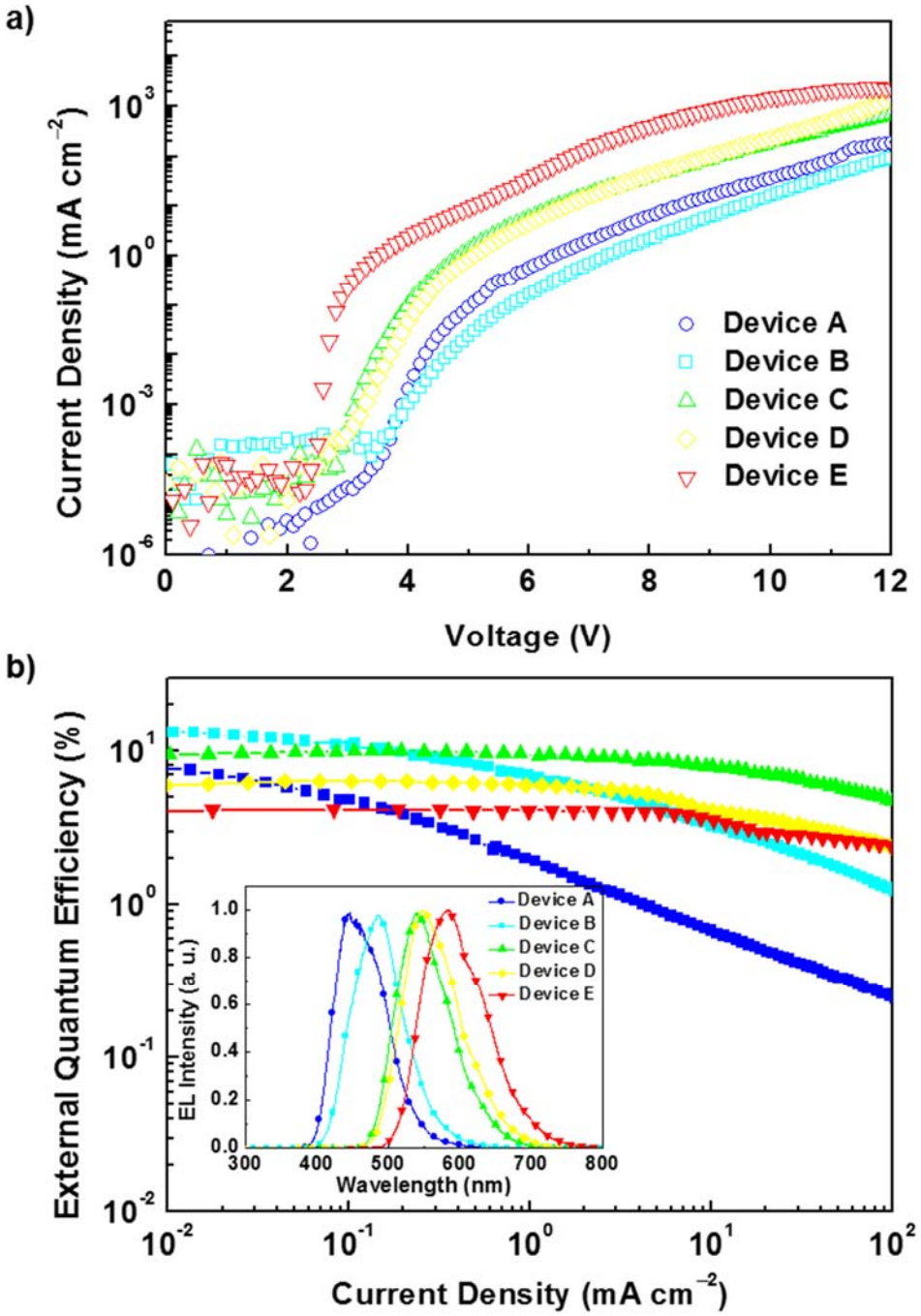

Figure 3-8. a) Current density−voltage (*J*−*V*) curves and b) η_{ext}–*J* plots (inset: normalized EL spectra measured at 10 mA cm^{-2}) of the OLEDs **A**−**E** containing the TADF emitters **1**−**5**.

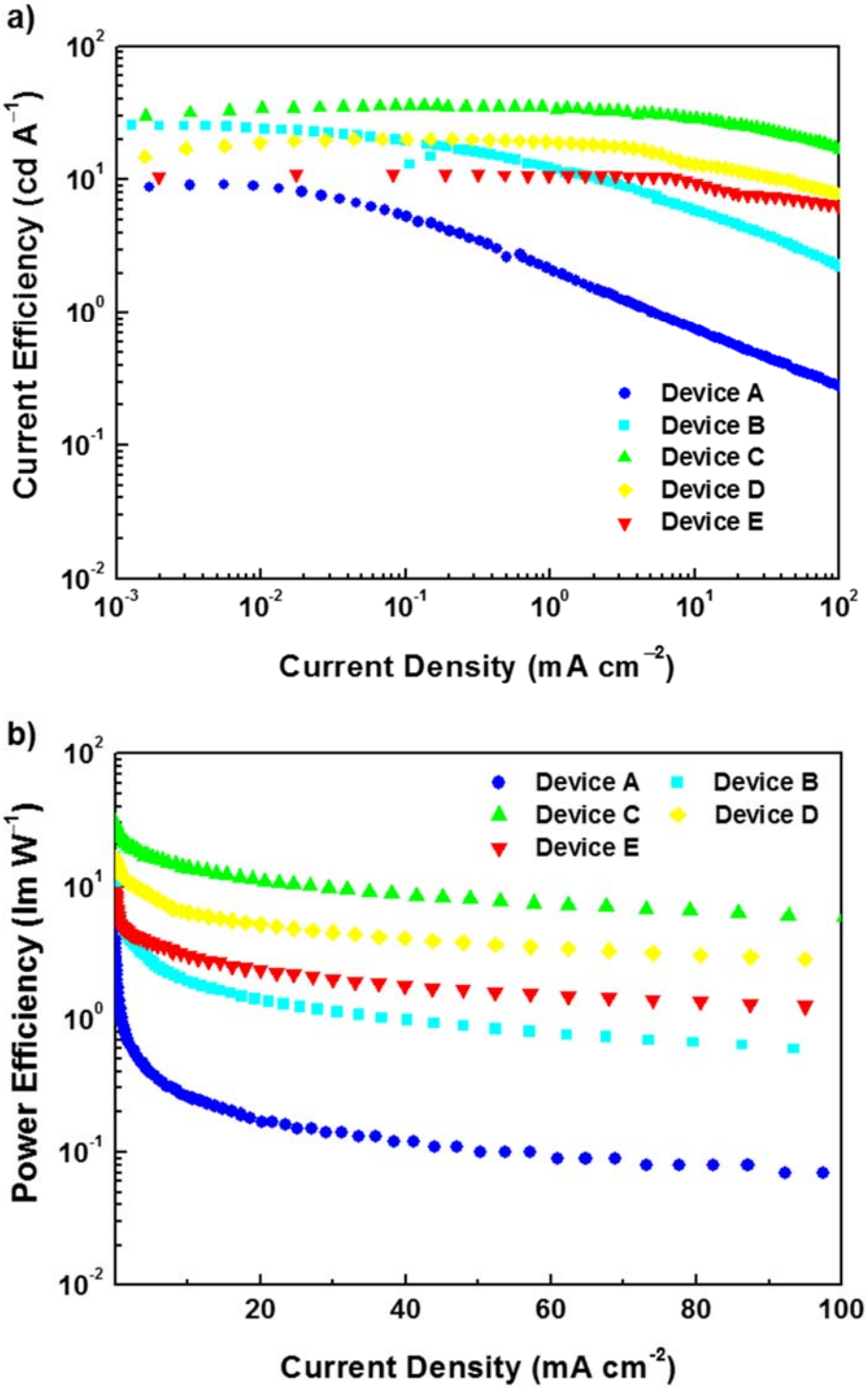

Figure 3-9. a) Current efficiency and b) power efficiency versus *J* plots for devices **A**–**E**.

3.2.5 TADF-Based White OLEDs using Benzophenone Derivatives

Using a combination of these TADF benzophenones with emission wavelengths spanning the whole visible region, the fabrication of TADF-based WOLEDs should be possible. There are two approaches for generating white light from OLEDs: three-primary-color (RGB) and two-color (blue/yellow) emitting systems.[16,17] Because of the simpler device fabrication process, we adopted a two-color-based device configuration (device **F**) with a structure of ITO/ α-NPD (35 nm)/ 18 wt%-**5**: mCBP (4 nm)/ 6 wt%-**2**: 2,8-bis(diphenylphosphoryl)dibenzo[*b*,*d*]furan[18] (PPF, 14 nm)/ PPF (40 nm)/ LiF (0.8 nm)/ Al (80 nm). In the case of blue and yellow EML combined multilayer WOLEDs, charge balance is very important because position of hole and electron recombination zone determined color purity of white emission. The yellow emissive molecules of **5** has lower S_1 and T_1 state than blue emissive molecules of **2**. And to prevent energy down conversion from blue to yellow EML and decrease blue emission intensity, recombination zone should be located on blue EML or interface of blue and yellow EML. As shown in Fig. 3-10, very deep homo energy of PPF molecules was introduced as host of blue EML and HBL for exction generation at interface of blue and yellow EML. And to reduce self-absorption of blue emission from yellow EML, very thin layer (4 nm) was fabricated. As expected, device **F** emitted white EL with CIE coordinates of (0.32, 0.39) at 10 mA cm^{-2}, which are close to those of pure white light CIE (0.33, 0.33), and achieved an η_{ext} of as high as 6.7% (Table 3-5). The resulting EL spectrum exhibited component peaks at 489 and 548 nm, corresponding to emission from **2** and **5**, respectively (Fig. 3-11). As shown in the inset of Fig. 3-11b, EL spectra of device **F** was slightly changed by current density. The emission intensity of blue emission (λ_{EL} = 498 nm) decreased with increase of current density. It should be the broadening of hole and electron recombination zone at higher current density lead to increase direct exciton generation on yellow EML and yellow emission intensity is relatively increased compare to blue emission. However, actual CIE coordinates of EL spectra of each current density are slight changed (0.31, 0.38 at 1 mA cm^{-2}, 0.32, 0.39 at 10 mA cm^{-2}, and 0.33, 0.40 at 100 mA cm^{-2}). From these result, we can confirmed the well optimized device structure of **2** and **5** based WOLEDs.

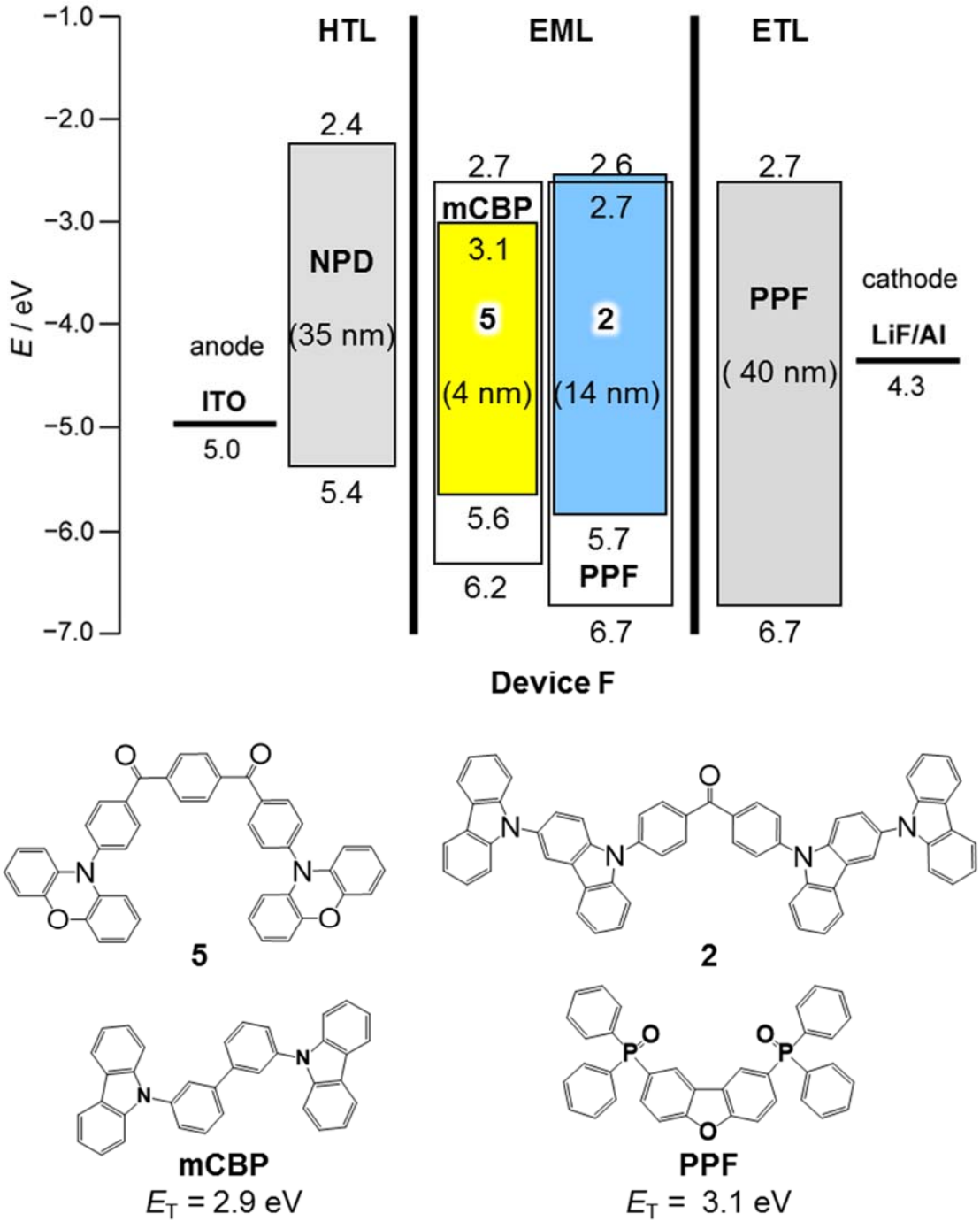

Figure 3-10. Energy level diagram showing the HOMO/LUMO levels of the materials used in devices **F** and the molecular structures of the materials.

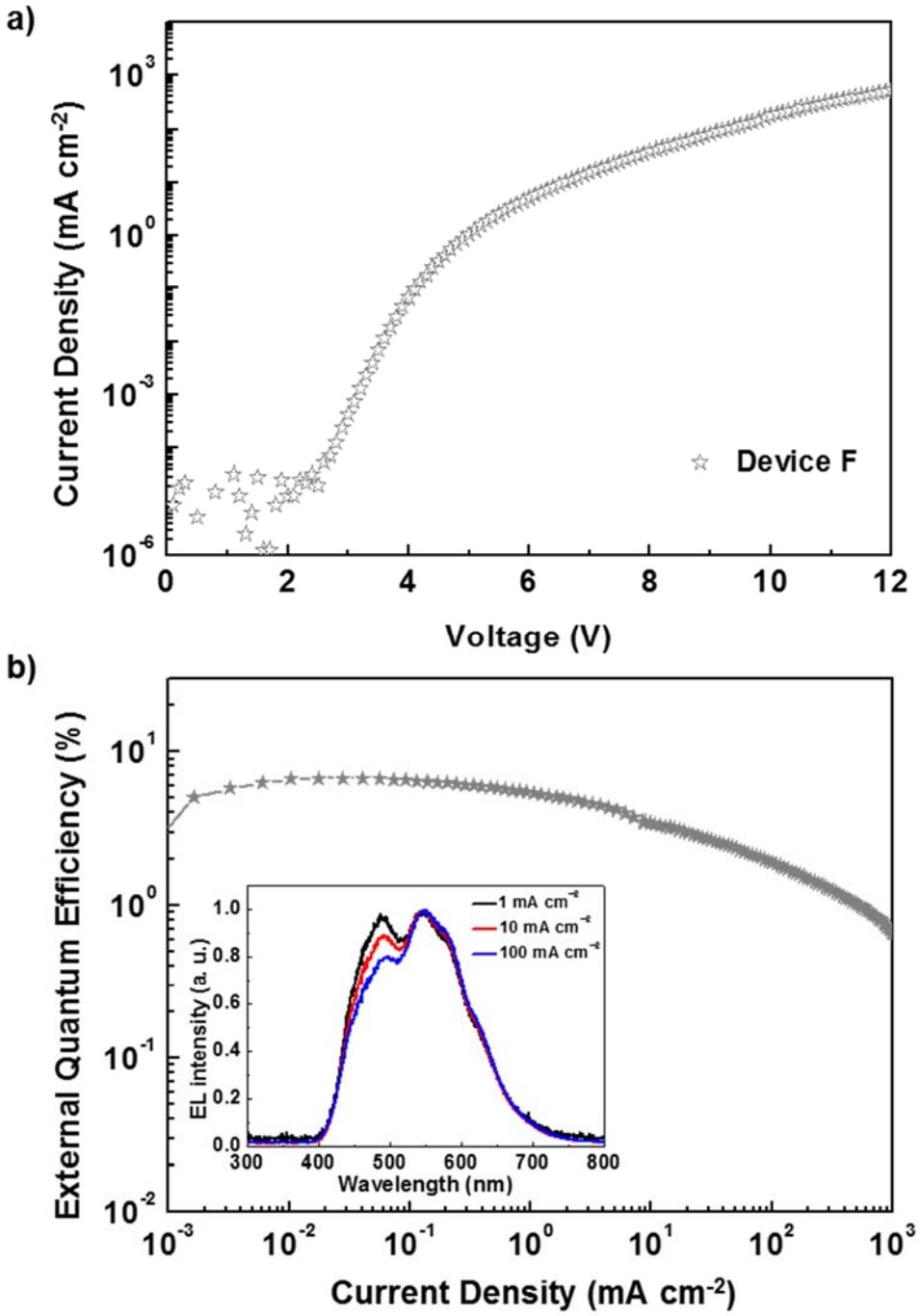

Figure 3-11. a) *J*–*V* curves and b) η_{ext}–*J* plots (inset: normalized EL spectra measured at 1, 10, and 100 mA cm^{-2}) for OLED **F** containing the TADF emitters **2** and **5**.

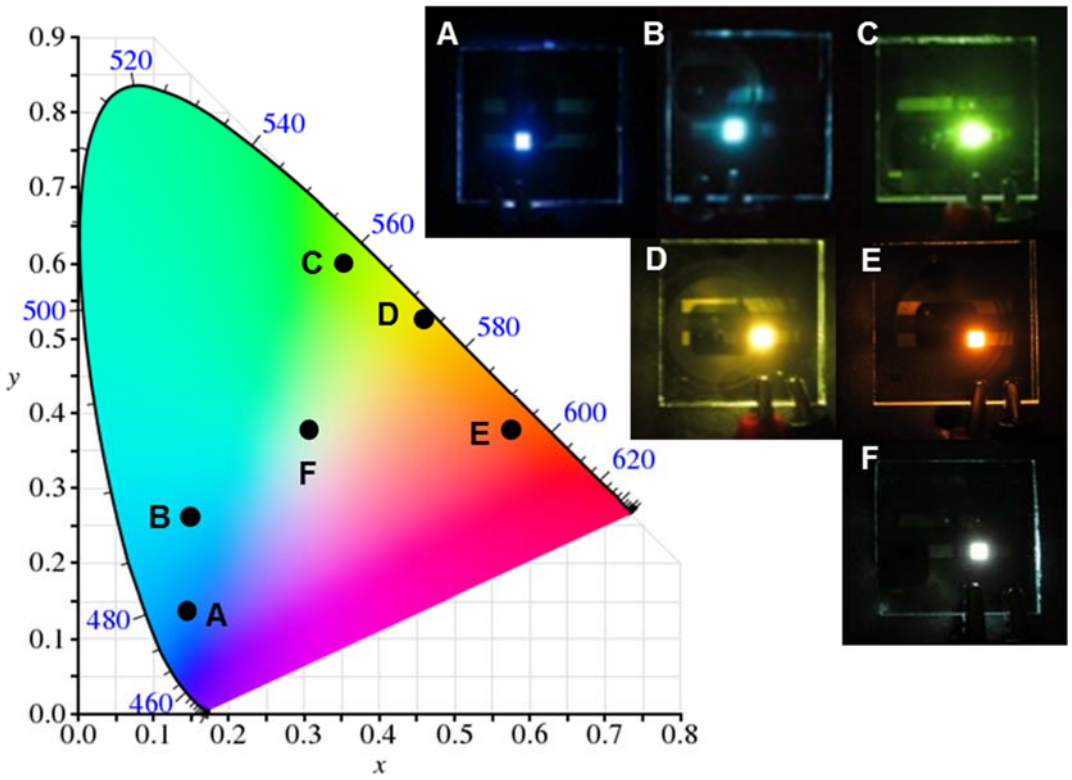

Figure 3-12. EL emission color coordinates in the CIE 1931 chromaticity diagram and photographs of devices **A**−**F**.

3.3 Conclusion

In conclusion, efficient exciton harvesting through spin up-conversion from non-radiative T_1 to radiative S_1 states has been realized using butterfly-shaped benzophenone derivatives. Our results demonstrate that the judicious molecular design of benzophenone based on D-A-D frameworks is suitable for the production of organic luminophores exhibiting highly efficient TADF emission covering the full color spectrum. OLEDs employing the benzophenone derivatives as emitters achieved maximum η_{ext} of up to 14.3%, which far exceed the theoretical limit for conventional fluorescence OLEDs. These purely organic luminophores do not require expensive precious metals, in contrast to phosphorescent emitters, and will therefore benefit large-area applications. Continued exploration of similar materials offers a viable route for producing efficient and stable full-color TADF luminophores for future display and lighting applications.

3.4 Experimental Section

3.4.1 General Methods

NMR spectra were recorded on an Avance III 500 spectrometer (Bruker). Chemical shifts of ^{1}H and ^{13}C NMR signals were quoted to tetramethylsilane ($\delta = 0.00$) and $CDCl_3$ ($\delta = 77.0$) as internal standards, respectively. Matrix-assisted laser desorption ionization time-of-flight (MALDI-TOF) mass spectra were collected on an Autoflex III spectrometer (Bruker Daltonics) using dithranol as the matrix. Elemental analyses were carried out with an MT-5 CHN corder (Yanaco). UV/vis absorption and PL spectra were measured with a UV-2550 spectrometer (Shimadzu) and a Fluoromax-4 spectrophotometer (Horiba Scientific), respectively. The Φ_{PL} were measured using an integration sphere system coupled with a photonic multichannel analyzer (Hamamatsu Photonics C9920-02, PMA-11). The luminescence intensities and lifetimes of solutions and thin films were measured using a Quantaurus-Tau (Hamamatsu Photonics) with an LED lamp (λ = 340 nm, frequency = 50 Hz) under N_2, and a Streak camera (Hamamatsu Photonics C4334) with an N_2 gas laser (λ = 337 nm, pulse width = 500 ps, repetition rate = 20 Hz) under vacuum ($< 4 \times 10^{-1}$ Pa). The HOMO energy levels (or ionization energies) for thin films were determined using an AC-3 ultraviolet photoelectron spectrometer (Riken-Keiki). The LUMO energy levels were estimated by subtracting the optical E_g from the measured HOMO energies; E_g values were determined from the onset position of the absorption spectra of thin films. All quantum chemical calculations were performed using the Gaussian 03 program package.[19] Geometry optimization was carried out using the B3LYP functional with the 6-31G(d,p) basis set. Low-lying excited singlet and triplet states were computed using the optimized structures with time-dependent density functional theory (TD-DFT) at the same level.

3.4.2 OLED device Fabrication and Measurement

ITO (110 nm thick)-coated glass substrates with a sheet resistance of $< 20\ \Omega\ \square^{-1}$ were cleansed with detergent, deionized water, acetone, and isopropanol. They were then subjected to UV-ozone treatment, before being loaded into a vacuum evaporation system. The organic layers were thermally evaporated on the substrates under vacuum ($< 3 \times 10^{-4}$ Pa) with an evaporation

rate of < 0.3 nm s^{-1}. A cathode aluminum layer was then deposited through a shadow mask. The layer thickness and deposition rate were monitored in situ during deposition by an oscillating quartz thickness monitor. The current density–voltage–luminance characteristics of the devices were measured using a semiconductor parameter analyzer (Agilent E5273A) and an optical powermeter (Newport 1930-C). EL spectra were recorded using a multi-channel analyzer (Ocean Optics SD2000).

3.4.3 Determination of Radiative Decay, ISC, and RISC Rate Constants

The transient processes of the TADF benzophenone luminophors **1**–**5** are shown schematically in Fig. 3-1. In the presence of ISC and RISC between the S_1 and T_1 states, the rate constants of the prompt and delayed PL components (k_p and k_d, respectively) can be expressed as follows:[13)]

$$k_{\mathrm{p}} = \frac{1}{\tau_p} = k_{\mathrm{r}}^{\mathrm{S}} + k_{\mathrm{nr}}^{\mathrm{S}} + k_{\mathrm{ISC}} \qquad (3\text{-}2)$$

$$k_{\mathrm{d}} = \frac{1}{\tau_{\mathrm{d}}} = k_{\mathrm{nr}}^{\mathrm{T}} + \left(1 - \frac{k_{\mathrm{ISC}}}{k_{\mathrm{r}}^{\mathrm{S}} + k_{\mathrm{nr}}^{\mathrm{S}} + k_{\mathrm{ISC}}}\right) k_{\mathrm{RISC}} \qquad (3\text{-}3)$$

The rates k_r^S and k_{ISC} are assumed to be much faster than the non-radiative decay rate constant for T_1 states (k_{nr}^T) and k_{RISC}, which is supported by the much longer decay time of the delayed emission component compared to the prompt component in the transient PL data.

The values of Φ_F and Φ_{TADF} and the quantum efficiency of ISC (Φ_{ISC}) are given by the following equations.

$$\Phi_{\mathrm{F}} = \frac{k_{\mathrm{r}}^{\mathrm{S}}}{k_{\mathrm{r}}^{\mathrm{S}} + k_{\mathrm{nr}}^{\mathrm{S}} + k_{\mathrm{ISC}}} \qquad (3\text{-}4)$$

$$\Phi_{\mathrm{TADF}} = \sum_{k=1}^{\infty} (\Phi_{\mathrm{ISC}}\, \Phi_{\mathrm{RISC}})^k\, \Phi_{\mathrm{F}} \qquad (3\text{-}5)$$

$$\Phi_{\mathrm{ISC}} = \frac{k_{\mathrm{ISC}}}{k_{\mathrm{r}}^{\mathrm{S}} + k_{\mathrm{nr}}^{\mathrm{S}} + k_{\mathrm{ISC}}} \qquad (3\text{-}6)$$

From Equ. 3-2 to 6, Equ. 3-1 can be obtained. Since the transient PL prompt component exhibits almost negligible temperature dependence at 5–300 K, we can assume that $k_{nr}^{S} \approx 0$ at ambient temperature. Based on Equ. 3-1 to 6, k_r^S, k_{ISC}, and k_{RISC} of **1–5** in the doped films can be estimated.

3.4.4 Materials and Syntheses of Benzophenone Derivatives

All regents and solvents were purchased from Sigma-Aldrich, Tokyo Chemical Industry (TCI), or Wako Pure Chemical Industries and were used as received unless otherwise noted. The synthetic routes to obtain **Cz2BP (1)**, **CC2BP** (**2**), **Px2BP** (**3**), ***m*-Px2BBP** (**4**), and ***p*-Px2BBP** (**5**) are outlined in Scheme 3-1. All reactions were performed under N_2 atmospheres in dry solvents. The final products were fully characterized by ^1H and ^{13}C NMR spectroscopy, MALDI-TOF mass spectrometry, and elemental analysis, as described later.

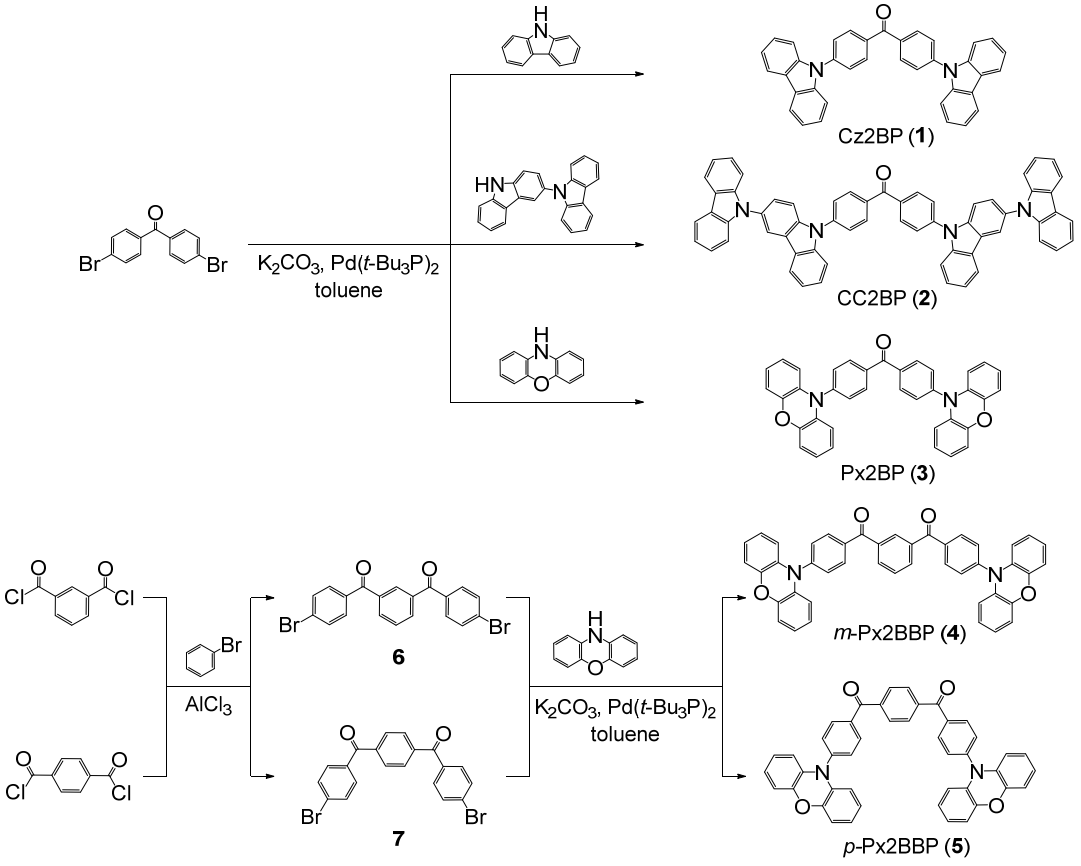

Scheme 3-1. Synthesis of the benzophenone derivatives **1**–**5**.

4,4'-bis(9H-carbazol-9-yl)methanone **(Cz2BP (1)).** A mixture of 4,4'-dibromobenzophenone (1.02 g, 3.0 mmol), 9*H*-carbazol (1.10 g, 6.6 mmol), potassium carbonate (1.04 g, 7.5 mmol), and bis(tri-*tert*-butylphosphine)palladium(0) (Pd(*t*-$Bu_3P)_2$; 0.15 g, 0.3 mmol) in dry toluene (50 mL) was stirred for 24 h at 120 °C. After cooling to room-temperature, the reaction mixture was poured into water and extracted with toluene. The combined organic layers were washed with water and dried over anhydrous $MgSO_4$. The resulting solution was filtered through a Celite pad and then through an alumina pad to remove insoluble materials. The filtrate was concentrated by evaporation. The crude product was purified by column chromatography on silica gel (eluent: chloroform) and dried under vacuum to afford Cz2BP as a yellow powder (yield = 1.38 g, 90%). This compound was further purified by temperature-gradient sublimation under vacuum. ^{1}H NMR (500 MHz, $CDCl_3$): δ 8.19-8.17 (m, 8H), 7.81 (d, J = 8.5 Hz, 4H), 7.57 (d, J = 8.5 Hz, 4H), 7.46 (td, J = 7.5 Hz, 1.0 Hz, 4H), 7.34 (td, J = 7.5 Hz, 1.0 Hz, 4H). ^{13}C{^{1}H} NMR (125 MHz, $CDCl_3$): δ 194.45, 141.92, 140.29, 135.85, 131.86, 126.46, 126.25, 123.91, 120.67, 120.51, 109.80. MS (MALDI-TOF): m/z 512.04 $[M]^+$; calcd 512.19. Anal. calcd (%) for $C_{37}H_{24}N_2O$: C, 86.69; H, 4.72; N, 5.46; found: C, 86.61; H, 4.66; N, 5.43.

4,4'-bis{3-(9H-carbazol-9-yl)-9H-carbazol-9-yl}methanone **(CC2BP (2)).** Compound **2** was synthesized similarly to **1**, using 4,4'-dibromobenzophenone (1.02 g, 3.0 mmol), 9-(9*H*-Carbazol-3-yl)-9*H*-carbazole[11] (2.19 g, 6.6 mmol), and Pd(*t*-$Bu_3P)_2$ (0.15 g, 0.3 mmol). The product was obtained as a pale yellow powder (yield = 2.21 g, 89%). This compound was further purified by recycling preparative gel permeation chromatography before use. ^{1}H NMR (500 MHz, $CDCl_3$): δ 8.35 (d, J = 2.0 Hz, 2H), 8.28 (d, J = 8.5 Hz, 4H), 8.22 (d, J = 8.0 Hz, 4H), 8.17 (d, J = 7.5 Hz, 2H), 7.93 (d, J = 8.5 Hz, 4H), 7.78 (d, J = 8.5 Hz, 2H), 7.66-7.63 (m, 4H), 7.56 (t, J = 8.0 Hz, 2H), 7.47-7.43 (m, 8H), 7.41 (t, J = 8.0 Hz, 2H), 7.35-7.32 (m, 4H). ^{13}C{^{1}H} NMR (125 MHz, $CDCl_3$): δ 194.32, 141.81, 141.66, 139.39, 136.17, 132.04, 130.67, 127.02, 126.61, 125.92, 125.81, 125.01, 123.48, 123.21, 121.15, 120.83, 120.35, 119.74, 119.69, 110.92, 110.15, 109.75. MS (MALDI-TOF): m/z 842.32 $[M]^+$; calcd 842.30. Anal. calcd (%) for $C_{61}H_{38}N_4O$: C, 86.91; H, 4.54; N, 6.65; found: C, 86.72; H, 4.40; N, 6.53.

4,4'-bis(10H-phenoxazin-10-yl)methanone **(Px2BP (3)).** Compound **3** was synthesized similarly to **1**, using 4,4'-dibromobenzophenone (1.02 g, 3.0 mmol), 10*H*-phenoxazine (1.20 g, 6.6 mmol), and Pd(*t*-$Bu_3P)_2$ (0.15 g, 0.3 mmol). The product was obtained as a yellow powder (yield = 1.42 g, 88%). This compound was further purified by temperature-gradient

sublimation under vacuum. ^{1}H NMR (500 MHz, $CDCl_3$): δ 8.10 (d, J = 8.5 Hz, 4H), 7.54 (d, J = 8.5 Hz, 4H), 6.75-6.69 (m, 8H), 6.65 (td, J = 8.0 Hz, 2.0 Hz, 4H), 6.02 (dd, J = 8.0 Hz, 1.5 Hz, 4H). ^{13}C{^{1}H} NMR (125 MHz, $CDCl_3$): δ 194.56, 144.09, 143.47, 136.95, 133.70, 132.75, 130.95, 123.32, 121.96, 115.80, 113.41. MS (MALDI-TOF): m/z 544.12 $[M]^+$; calcd 544.18. Anal. calcd (%) for $C_{37}H_{24}N_2O_3$: C, 81.60; H, 4.44; N, 5.14; found: C, 81.69; H, 4.41; N, 5.11.

1,3-bis(4-bromobenzoyl)benzene **(6).** To a stirred solution of isophthaloyl dichloride (2.60 g, 2.0 mmol) in bromobenzene (10 mL) was slowly added aluminum chloride (2.03 g, 1.0 mmol). The mixture was stirred for 9 h at room-temperature and then heated for 2 h at 90 °C. After cooling to room-temperature, the reaction mixture was poured into ice-cold methanol to form a precipitate. The resulting precipitate was collected by filtration, recrystallized from chloroform/methanol, and dried under vacuum to give **6** as a white solid (yield = 3.97 g, 89%). This compound was used in the next reaction without further purification. ^{1}H NMR (500 MHz, $CDCl_3$): δ 8.13 (s, 1H), 8.00 (dd, J = 7.5 Hz, 1.5 Hz, 2H), 7.70-7.64 (m, 9H). MS (MALDI-TOF): m/z 443.76 $[M+H]^+$; calcd 442.93.

1,3-bis{4-(10H-phenoxazine-10-yl)benzoyl}benzene **(*m*-Px2BBP (4)).** Compound **4** was synthesized similarly to **1**, using **6** (1.33 g, 3.0 mmol), 10*H*-phenoxazine (1.20 g, 6.6 mmol), and Pd(*t*-$Bu_3P)_2$ (0.15 g, 0.3 mmol). The product was obtained as a yellow powder (yield = 1.40 g, 96%). This compound was further purified by temperature-gradient sublimation under vacuum. ^{1}H NMR (500 MHz, $CDCl_3$): δ 8.37 (s, 1H), 8.12-8.08 (m, 6H), 7.72 (t, J = 7.5 Hz, 1H), 7.53 (d, J = 8.5 Hz, 4H), 6.74-6.68 (m, 8H), 6.64-6.61 (m, 4H), 6.01 (dd, J = 7.5 Hz, 1.5 Hz, 4H). ^{13}C{^{1}H} NMR (125 MHz, $CDCl_3$): δ 194.62, 144.09, 143.73, 137.72, 136.63, 133.72, 133.63, 132.84, 130.98, 130.92, 128.76, 123.33, 121.99, 115.80, 113.44. MS (MALDI-TOF): m/z 649.45 $[M+H]^+$; calcd 649.21. Anal. calcd (%) for $C_{44}H_{28}N_2O_4$: C, 81.47; H, 4.35; N, 4.32; found: C, 81.47; H, 4.27; N, 4.29.

1,4-bis(4-bromobenzoyl)benzene **(7).** This compound was prepared using a procedure similar to that for synthesizing **6**, except that terephthaloyl chloride (2.60 g, 2.0 mmol) was used instead of isophthaloyl dichloride. The product was obtained as a white powder (yield = 3.33 g, 75%). This compound was used in the next reaction without further purification. ^{1}H NMR (500 MHz, $CDCl_3$): δ 7.87 (s, 4H), 7.71 (d, J = 8.5 Hz, 4H), 7.67 (d, J = 8.5 Hz, 4H). MS (MALDI-TOF): m/z 443.75 $[M+H]^+$; calcd 442.93.

1,4-bis{4-(10H-phenoxazine-10-yl)benzoyl}benzene **(*p*-Px2BBP (5)).** Compound **5** was synthesized similarly to **1**, using **7** (1.33 g, 3.0 mmol), 10*H*-phenoxazine (1.20 g, 6.6 mmol), and Pd(*t*-$Bu_3P)_2$ (0.15 g, 0.3 mmol). The product was obtained as an orange powder (yield = 1.20 g, 84%). This compound was further purified by temperature-gradient sublimation under vacuum. ^{1}H NMR (500 MHz, $CDCl_3$): δ 8.09 (d, J = 7.0 Hz, 4H), 8.01 (s, 4H), 7.54 (d, J = 8.5 Hz, 4H), 6.75-6.69 (m, 8H), 6.64 (td, J = 7.5 Hz, 1.5 Hz, 4H), 6.02 (dd, J = 7.5 Hz, 1.0 Hz, 4H). ^{13}C{^{1}H} NMR (125 MHz, $CDCl_3$): δ 194.79, 144.12, 140.53, 136.61, 133.64, 132.86, 130.98, 129.88, 123.31, 122.02, 115.82, 113.42. MS (MALDI-TOF): m/z 649.54 $[M+H]^+$; calcd 649.21. Anal. calcd (%) for $C_{44}H_{28}N_2O_4$: C, 81.47; H, 4.35; N, 4.32; found: C, 81.45; H, 4.20; N, 4.28.

3.5 References

[1] B. W. D'Andrade and S. R. Forrest, *Adv. Mater.*, **2004**, 16, 1585.

[2] M. C. Gather, A. Köhnen, and K. Meerholz, *Adv. Mater.*, **2011**, 23, 233.

[3] K. T. Kamtekar, A. P. Monkman, and M. R. Bryce, *Adv. Mater.*, **2010**, 40, 572.

[4] H. Sasabe and J. Kido, *Chem. Mater.*, **2011***, 23*, 621.

[5] M. W. Wolf, K. D. Legg, R. E. Brown, L. A. Singer, and J. H. Parks, *J. Am. Chem. Soc.*, **1975**, 97, 4490.

[6] Y.-P. Sun, D. F. Sears, and Jr., J. Saltiel, *J. Am. Chem. Soc.*, **1989**, 111, 706.

[7] S. Aloïse, C. Ruckebusch, L. Blanchet, J. Réhaut, G. Buntinx, and J.-P. Huvenne, *J. Phys. Chem. A*, **2008**, 112, 224.

[8] S. Hoshino and H. Suzuki, *Appl. Phys. Lett*., **1996**, 69, 224.

[9] K. Honda, *Photochemical Processes in Organized Molecular Systems*, **1991**, Elsevier.

[10] A. Endo, K. Sato, K. Yoshimura, T Kai, A. Kawada, H. Miyazaki, and C. Adachi, *Appl. Phys. Lett*., **2011**, 98, 083302.

[11] C. Han, Y. Zhao, H. Xu, J. Chen, Z. Deng, D. Ma, Q. Li, and P. Yan, *Chem.-Eur. J*., **2011**, 17, 5800.

[12] Y. Liu, S. Chen, J. W. Y. Lam, P. Lu, R. T. K. Kwok, F. Mahtab, H. S. Kwok, and B. Z. Tang, *Chem. Mater.*, **2011**, 23, 2536.

[13] K. Goushi, K. Yoshida, K. Sato, C. Adachi, *Nat. Photon.*, **2012**, 6, 253.

[14] Y. Zhang and S. R. Forrest, *Phys. Rev. Lett.*, **2012**, 108, 267404.

[15] C. Adachi, M. A. Baldo, and S. R. Forrest, *J. Appl. Phys.*, **2000**, 87, 8049.

[16] M. C. Gather, A. Kohnen, and K. Meerholz, *Adv. Mater*., **2011**, 23, 233.

[17] S. Reineke, M. Thomschke, B. Lussem, and K. Leo, *Rev. Mod. Phys*., **2013**, 85, 1245.

[18] P. A. Vecchi, A. B. Padmaperuma, H. Qiao, L. S. Sapochak and P. E. Burrows, *Org. Lett*., **2006**, 8, 4211.

[19] M. J. Frisch, G. W. Trucks, H. B. Schlegel, G. E. Scuseria, M. A. Robb, J. R. Cheeseman, J. A. Montgomery, Jr., T. Vreven, K. N. Kudin, J. C. Burant, J. M. Millam, S. S. Iyengar, J. Tomasi, V. Barone, B. Mennucci, M. Cossi, G. Scalmani, N. Rega, G. A. Petersson, H. Nakatsuji, M. Hada, M. Ehara, K. Toyota, R. Fukuda, J. Hasegawa, M. Ishida, T. Nakajima, Y. Honda, O. Kitao, H. Nakai, M. Klene, X. Li, J. E. Knox, H. P. Hratchian, J. B. Cross, C. Adamo, J. Jaramillo, R. Gomperts, R. E. Stratmann, O. Yazyev, A. J. Austin, R. Cammi, C. Pomelli, J. W. Ochterski, P. Y. Ayala, K. Morokuma, G. A. Voth, P. Salvador, J. J. Dannenberg, V. G. Zakrzewski, S. Dapprich, A. D. Daniels, M. C. Strain, O. Farkas, D. K. Malick, A. D. Rabuck, K. Raghavachari, J. B. Foresman, J. V. Ortiz, Q. Cui, A. G. Baboul, S. Clifford, J. Cioslowski, B. B. Stefanov, G. Liu, A. Liashenko, P. Piskorz, I. Komaromi, R. L. Martin, D. J. Fox, T. Keith, M. A. Al-Laham, C. Y. Peng, A. Nanayakkara, M. Challacombe, P. M. W. Gill, B. Johnson, W. Chen, M. W. Wong, C. Gonzalez, and J. A. Pople, Gaussian 03, Gaussian, Inc., Pittsburgh PA, **2003**.

Chapter 4

X-Shaped Benzoylbenzophenone Derivatives with Crossed Donors and Acceptors for Highly Efficient Thermally Activated Delayed Fluorescence

Chapter 4

X-Shaped Benzoylbenzophenone Derivatives with Crossed Donors and Acceptors for Highly Efficient Thermally Activated Delayed Fluorescence

Abstract

TADF materials based on x-shaped benzoylbenzophenone derivatives with crossed donors and acceptors, **AcPmBPX** and **PxPmBPX**, were designed and synthesized. OLEDs using these materials as emitters exhibited high external EL quantum efficiencies of up to 11%.

4.1 Introduction

In Chapter 3, highly efficient full-color TADF emitters based on benzophenone derivatives were reported. Among them, the yellow-emitting benzoylbenzophenone ***p*-Px2BBP** (Fig. 4-1a) was found to exhibit low Φ_{PL} (36%) and η_{ext} (< 7%) in films and OLEDs compared to the other benzophenone derivatives.[1)] In this chapter, the molecular design strategy is further developed and refined to create highly emissive luminophors based on benzoylbenzophenone derivatives.

In emissive organic molecules, radiative and non-radiative decay are in competition with each other, and non-radiative decay should be suppressed to achieve high luminescence efficiency. Non-radiative decay largely originates from the transfer of excess energy into the vibration, rotation, and translation of surrounding molecules resulting in heat generation. For instance, the free movement of molecules in solution leads to efficient non-radiative decay while strong radiative decay is observed in the thin-film state because of the restriction of intramolecular movement by the aggregation of molecules. This mechanism is called AIE (see more detail in section 1.3.2).[2–4)] Thus, the restriction of intramolecular movement is a key to reducing non-radiative decay in emissive molecules.

In the case of the linear-shaped ***p*-Px2BBP**, free movement of phenyl rings can accelerate non-radiative processes and decrease luminescence efficiency. In this chapter, an advanced molecular design is introduced with crossed donors and acceptors in an x-shaped molecular structure based on benzoylbenzophenone derivatives. The new molecules 1,4-bis(9,9-dimethylacridan-10-yl-*p*-phenyl)-2,5-bis(*p*-tolyl-methanoyl)benzene (**AcPmBPX, 1**) and 1,4-bis(9,9-phenoxazin-10-yl-*p*-phenyl)-2,5-bis(*p*-tolyl-methanoyl)benzene (**PxPmBPX, 2**), shown in Fig. 4-1b, were designed with the expectation of restrained intramolecular movement caused by strong steric hindrance between the bulky donors of phenoxazine and dimethylacridane and the acceptor of benzoylbenzophenone. Furthermore, a twisted molecular structure could yield a small ΔE_{ST} for effective up-conversion through TADF.[5)]

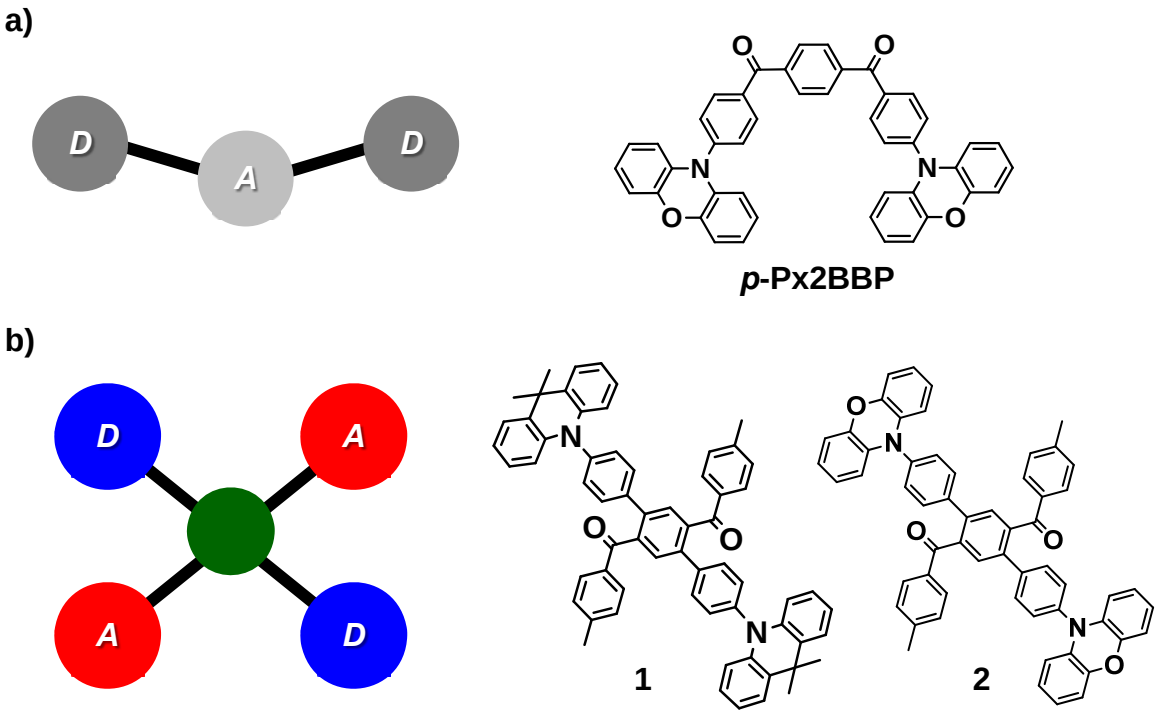

Figure 4-1. Molecular structures of the linear-shaped a) and x-shaped b) benzoylbenzophenone derivatives of ***p*-Px2BBP** and **1** and **2**.

4.2 Results and Discussion

4.2.1 Characterization of Geometric and Electronic Structures by TD-DFT Calculations

The geometric and electronic structures of **1** and **2** were ascertained by time-dependent density functional theory (TD-DFT) calculations performed at the B3LYP/6-31G (d,p) level. As shown in Fig. 4-2, the HOMOs of **1** and **2** are mainly distributed over the electron-donating dimethylacridane and phenoxazine moieties, respectively, because of a large distortion between the electron-donating moieties and neighboring phenylene rings. The LUMOs of **1** and **2** are located on the central electron-accepting benzoylbenzophenone core. Such clear spatial separation of the frontier orbitals resulted in a very small calculated ΔE_{ST} of 0.01 eV for **1** and **2**, which can facilitate fast RISC from T_1 to S_1 states even at room-temperature.

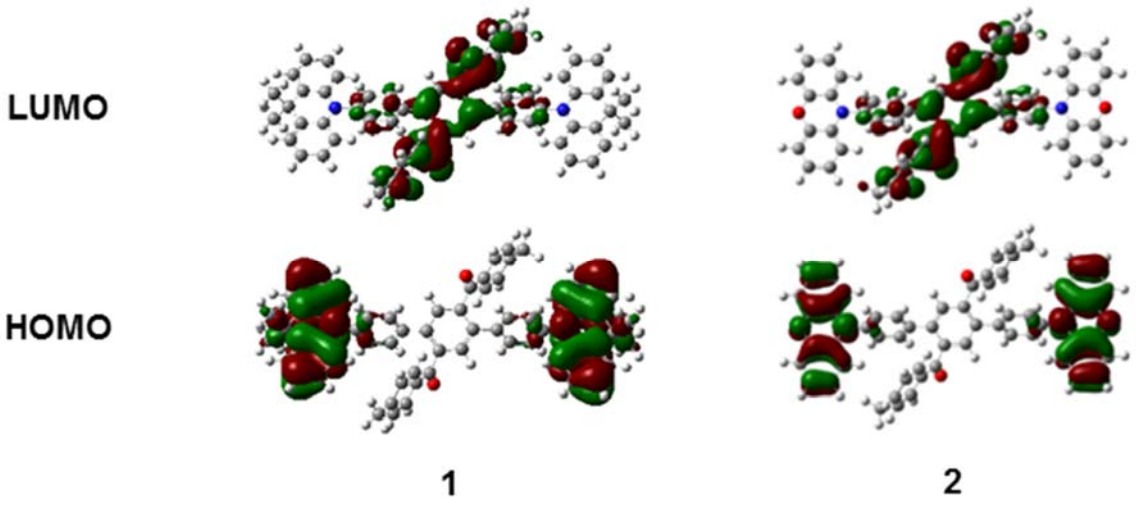

Figure 4-2. Frontier-molecular-orbital distributions of **1** and **2**.

4.2.2 PL Properties of Benzoylbenzophenone Derivatives

The UV/Vis absorption and PL spectra of **1** and **2** in toluene are depicted in Fig. 4-3. Compounds **1** and **2** exhibit structureless sky-blue and green emission with λ_{PL} at 496 and 510 nm, respectively. In oxygen-free toluene solutions, Φ_{PL} of ~20% were obtained for **1** and **2** whilst Φ_{PL} decreased to less than 10% in the presence of triplet oxygen ($^3O_2$) in aerated

solutions. In contrast, films of **1** and **2** doped into mCBP as host exhibited high Φ_{PL} of 46% and 57%, respectively, which suggests that non-radiative exciton quenching processes are suppressed by the restriction of intramolecular rotation in the solid state (Table 4-1).[6)]

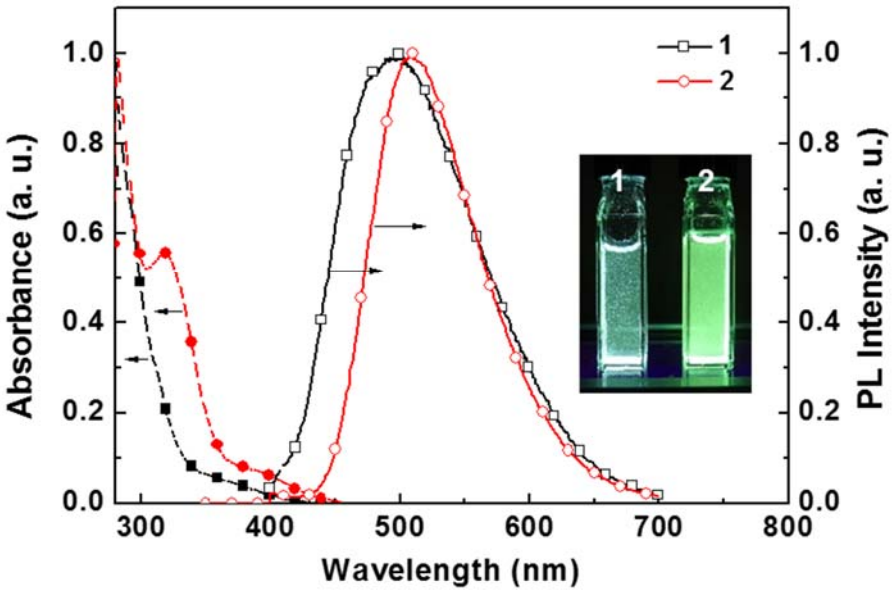

Figure 4-3. Room-temperature absorption (closed symbols) and PL spectra (open symbols) of **1** (black line) and **2** (red line) in toluene (inset: luminescence image of **1** and **2** in toluene).

Table 4-1. Photophysical properties of **1** and **2**

Compound	λ_{abs} (nm) sol[a)]	λ_{PL} (nm) sol[a)] / film[b)]	Φ_{PL} (%) sol[a)] / film[b)]	HOMO (eV)[c)]	LUMO (eV)[d)]	E_S / E_T (eV)[e)]	ΔE_{ST} (eV)[f)]	calc. ΔE_{ST} (eV)[g)]
1	281	496 / 492	20 / 46	−5.80	−2.90	2.79 / 2.74	0.05	0.01
2	282, 318	510 / 530	10 / 57	−5.60	−2.80	2.70 / 2.72	0.02	0.01

a) Measured in oxygen-free toluene solution at room-temperature. b) Measured in 6-wt%-doped films in a host matrix of mCBP. c) Determined by photoelectron yield spectroscopy in thin films. d) Deduced from the HOMO and optical E_g. e) Singlet (E_S) and triplet (E_T) energies estimated from onset wavelengths of the doped film emission spectra at 300 and 5 K, respectively, f) $\Delta E_{ST} = E_S - E_T$. g) Calculated by TD-DFT at the B3LYP/6-31G(d,p) level.

We further analyzed the temperature dependence of the transient PL characteristics of **1** and **2** doped into films of mCBP using a streak camera. As shown in Fig. 4-4, codeposited films of mCBP doped with 6 wt% of **1** and **2** exhibit fluorescence with nanosecond-scale prompt (τ_p = 20 and 30 ns) and microsecond-scale delayed (τ_d = 925 and 314 μs) components at 300 K, respectively. Since the prompt and delayed emission spectra coincide with each other (Fig. 4-5), the delayed PL component can be ascribed to delayed fluorescence. Moreover, Φ_{PL} increased with increasing temperature in the range of 150–300 K because of an acceleration of the RISC process at higher temperatures (Fig. 4-5). These results indicate that the delayed component originates from TADF. Using the PL efficiency and lifetime data measured at 300 K, emitters **1** and **2** in the doped films are estimated to have k_r^S of 1.3×10^7 and 7.0×10^6 s^{-1}, k_{ISC} of 3.7×10^7 and 2.6×10^7 s^{-1}, and k_{RISC} of 1.1×10^3 and 7.0×10^3 s^{-1}, respectively (Table 4-2).[7)]

Table 4-2. Rate constants and quantum efficiencies for decay processes in **1** and **2**[a)]

Compound	τ_p (ns)	τ_d (μs)	k_r^S (s^{-1})	k_{ISC} (s^{-1})	k_{RISC} (s^{-1})	Φ_F (%)	Φ_{TADF} (%)
1	20	925	1.3×10^7	3.7×10^7	1.1×10^3	26	20
2	30	314	7.0×10^6	2.6×10^7	7.0×10^3	21	36

a) Measured in 6 wt%-doped films in a host matrix of mCBP.

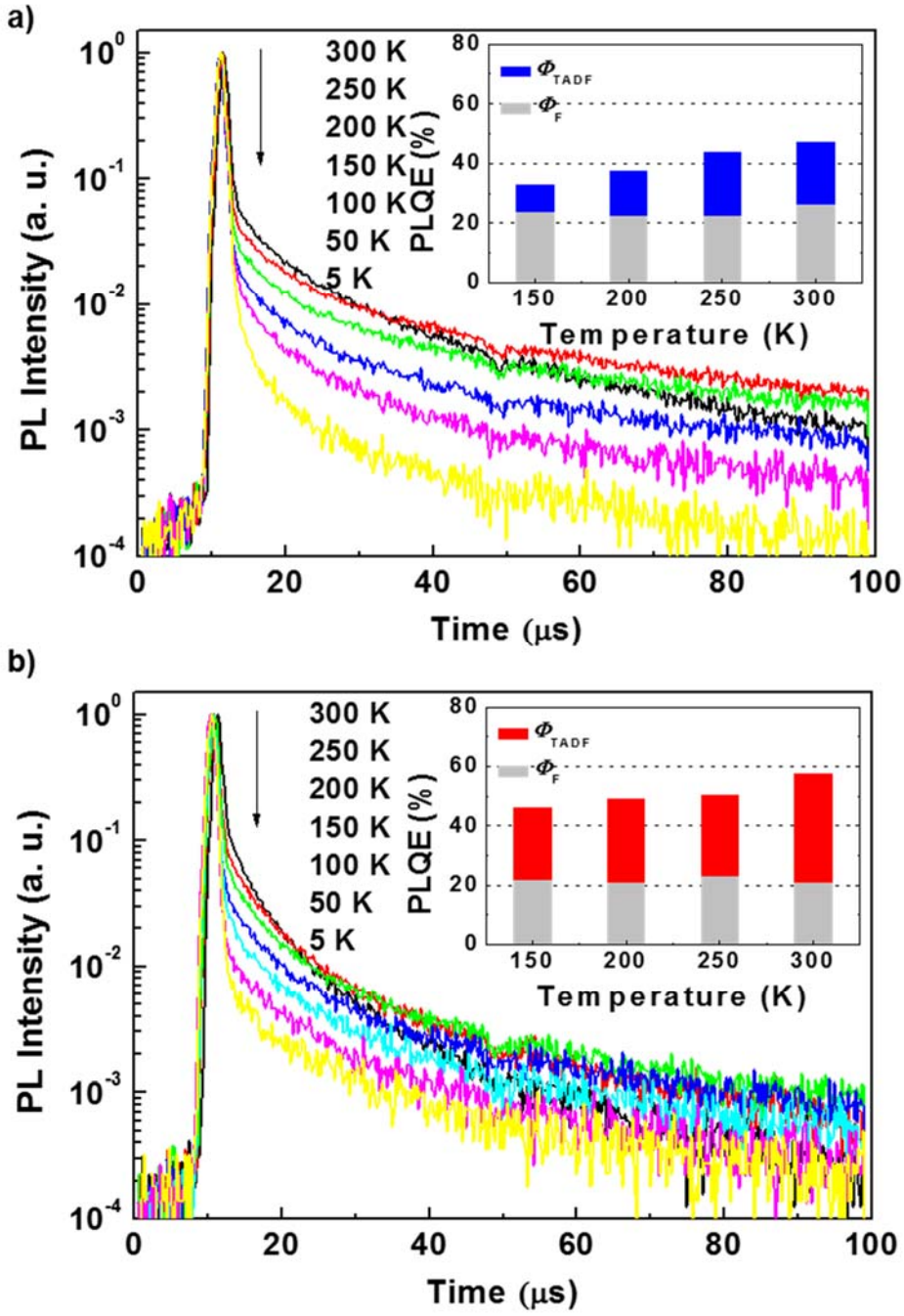

Figure 4-4. Temperature dependence of transient PL decay of 6 wt%-emitter: mCBP films from 300 to 5 K for the emitters **1** a) and **2** b) (insets: the contribution of fluorescence and TADF to the total Φ_{PL}).

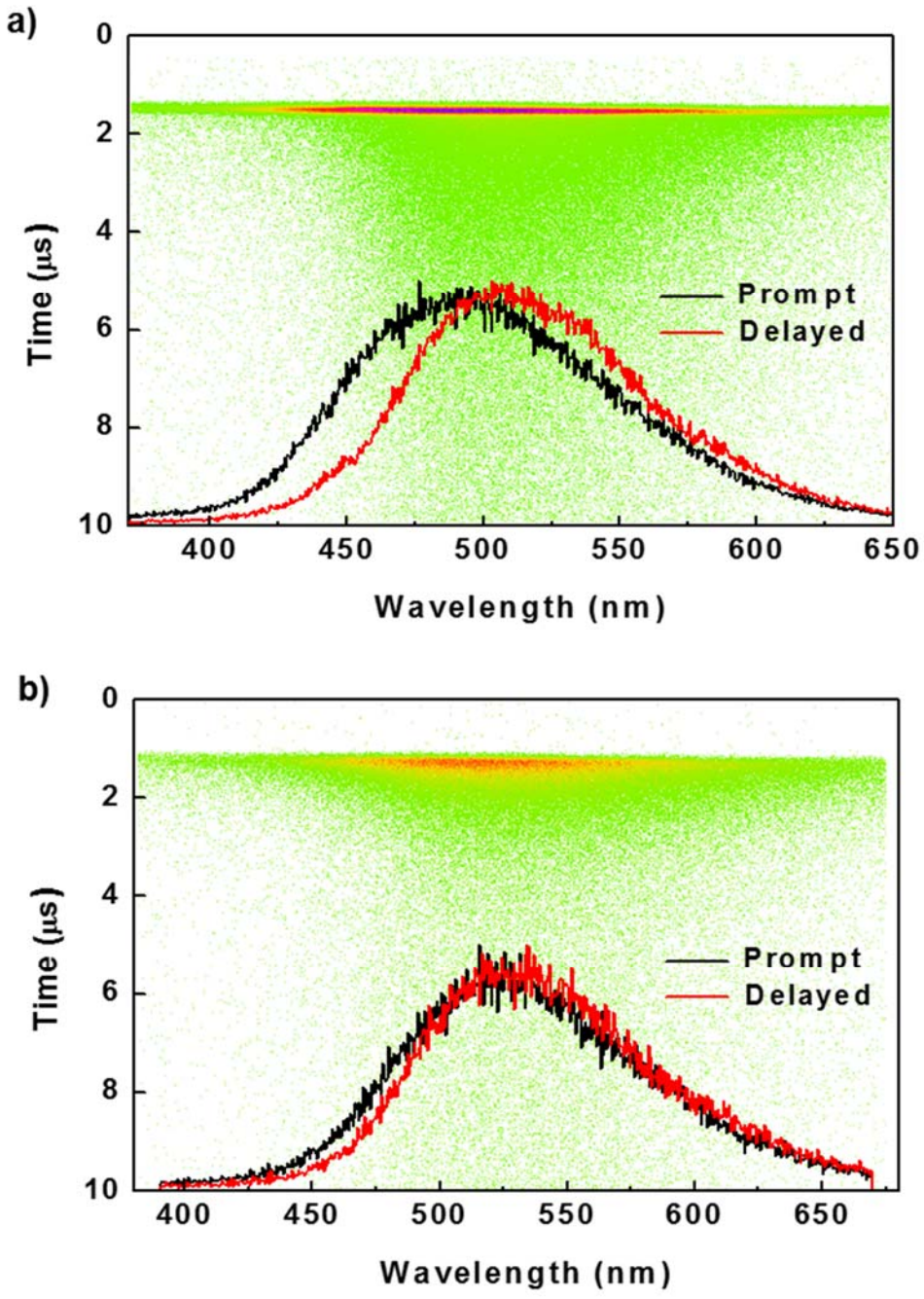

Figure 4-5. Streak image and PL spectra of 6 wt%-emitter: mCBP films showing the prompt (fluorescence, black) and delayed (TADF, red) components for the emitters **1** a) and **2** b).

4.2.3 Decay Processes in Linear- and X-Shaped Benzoylbenzophenone Derivatives

To compare the decay processes of linear- and x-shaped benzoylbenzophenone derivatives, the rate constants of radiative and non-radiative decay constants were calculated for ***p*-Px2BBP** and **2** using the Φ_{PL} and lifetimes of 6 wt%-emitter: mCBP codeposited films at 300 K (Fig. 4-6, Table 4-3). The emitters ***p*-Px2BBP** and **2** exhibited nearly the same k_p while their k_d were slightly different. For the non-radiated decay, k_{nr}^T can be calculated by[7)]

$$k_{nr}^{T} = k_d - (\Phi_F k_{RISC}) \qquad (4\text{-}1)$$

Based on this equation, k_{nr}^T of ***p*-Px2BBP** and **2** are calculated to 2.9×10^5 and 1.7×10^3 s^{-1}, respectively. The much smaller k_{nr}^T for **2** than for the linear-shaped ***p*-Px2BBP** can be attributed to the crossed bulky donor and acceptor substituents of **2** better restricting intramolecular vibrations and rotations, which strongly suppresses non-radiative exciton quenching processes in T_1 states. Even though k_{RISC} of ***p*-Px2BBP** (1.8×10^5 s^{-1}) is faster than **2** (7.0×10^3 s^{-1}), the Φ_{RISC} of **2** (46%) is much higher than that of ***p*-Px2BBP** (14%) because of the slower k_{nr}^T relative to k_{RISC} for **2** reduces the loss of T_1 states before they are up-converted to S_1 states through TADF. These results confirm that the x-shaped molecular design is suitable for highly efficient triplet excitons harvesting by reducing the non-radiative decay of T_1.

Table 4-3. Rate constants and quantum efficiencies for decay processes in ***p*-Px2BBP** and **2**[a)]

Compound	k_r^S (s^{-1})	k_d (s^{-1})	k_{nr}^T (s^{-1})	Φ_{ISC} (%)	Φ_{RISC} (%)	ΔE_{ST} (eV)
***p*-Px2BBP**	1.3×10^7	3.4×10^5	2.9×10^5	74	14	0.06
2	7.0×10^6	3.2×10^3	1.7×10^3	79	46	0.02

a) Measured in 6 wt %-doped films with a host matrix of mCBP.

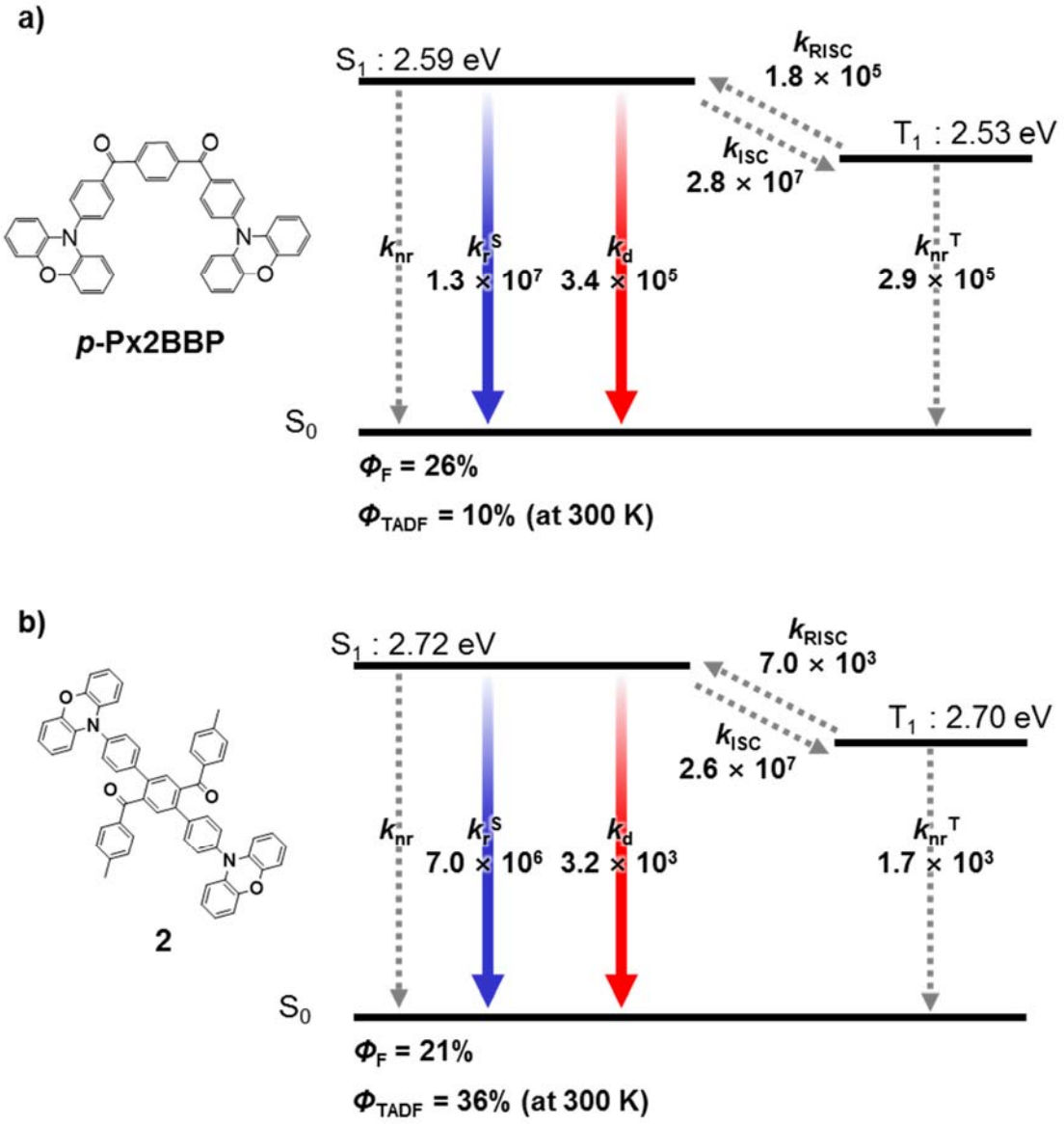

Figure 4-6. Schematic representation of PL decay of ***p*-Px2BBP** a) and **2** b).

4.2.4 Fabrication and EL Properties of OLEDs

Because of their high Φ_{PL} in doped films, emitters **1** and **2** were expected to be useful for fabricating highly efficient TADF-OLEDs. To test their performance as emitters in OLEDs, multilayer OLEDs were fabricated with the following device configuration (Fig. 4-7): ITO/ α-NPD (35 nm)/ mCP (10 nm)/ 6 wt%-**1** or **2**: mCBP (20 nm)/ PPF (10 nm)/ TPBi (30 nm)/ LiF (0.8 nm)/ Al (80 nm). Here, α-NPD and TPBi serve as a HTL and ETL, respectively, and LiF is used as an electron-injecting material. In addition, to confine T_1 excitons to the EML and to suppress quenching by the neighboring layers, mCP and PPF, which have high T_1 energies of 2.9 and 3.1 eV,[8] respectively, were inserted between the HLT/EML and EML/ETL interfaces, respectively.

Figure 4-8 presents the current-density−voltage−luminance ($J-V-L$) and η_{ext} characteristics of OLED devices **A** and **B** based on TADF emitters **1** and **2**, respectively. For devices **A** and **B**, the λ_{EL} at J = 10 mA cm^{-2} were 504 and 541 nm, respectively, which are similar to their corresponding λ_{PL}. The OLEDs based on **1** and **2** achieved high maximum η_{ext} of 10.0% and 11.3%, respectively. Device **B** also exhibited a high η_c of 35.3 cd A^{-1} and a high L_{max} of 61040 cd m^{-2} (Table 4-4).

In the case of device **A**, η_{ext} decreased at high current densities of over 100 mA cm^{-2} (η_{ext} < 3%), indicating a rapid increase of roll-off attributed to the longer τ in doped films for emitter **1** (τ_d = 925 μs) compared to **2** (τ_d = 314 μs).[9] Even though strong roll-off was observed at high current densities in device **A**, its maximum η_{ext} was 10.0%, which is still more than double the 5% theoretical limit of η_{ext} for OLEDs based on conventional fluorescent emitter.

Table 4-4. EL performance of TADF-OLEDs based on **1** and **2** as emitter

Device	Emitter	Host	λ_{EL} (nm)	V_{on} (V)	L_{max} (cd m^{-2})	η_c (cd A^{-1})	η_{ext} (%)
A	**1**	mCBP	504	5.2	43749	23.4	10.0
B	**2**	mCBP	541	3.2	61040	35.3	11.3

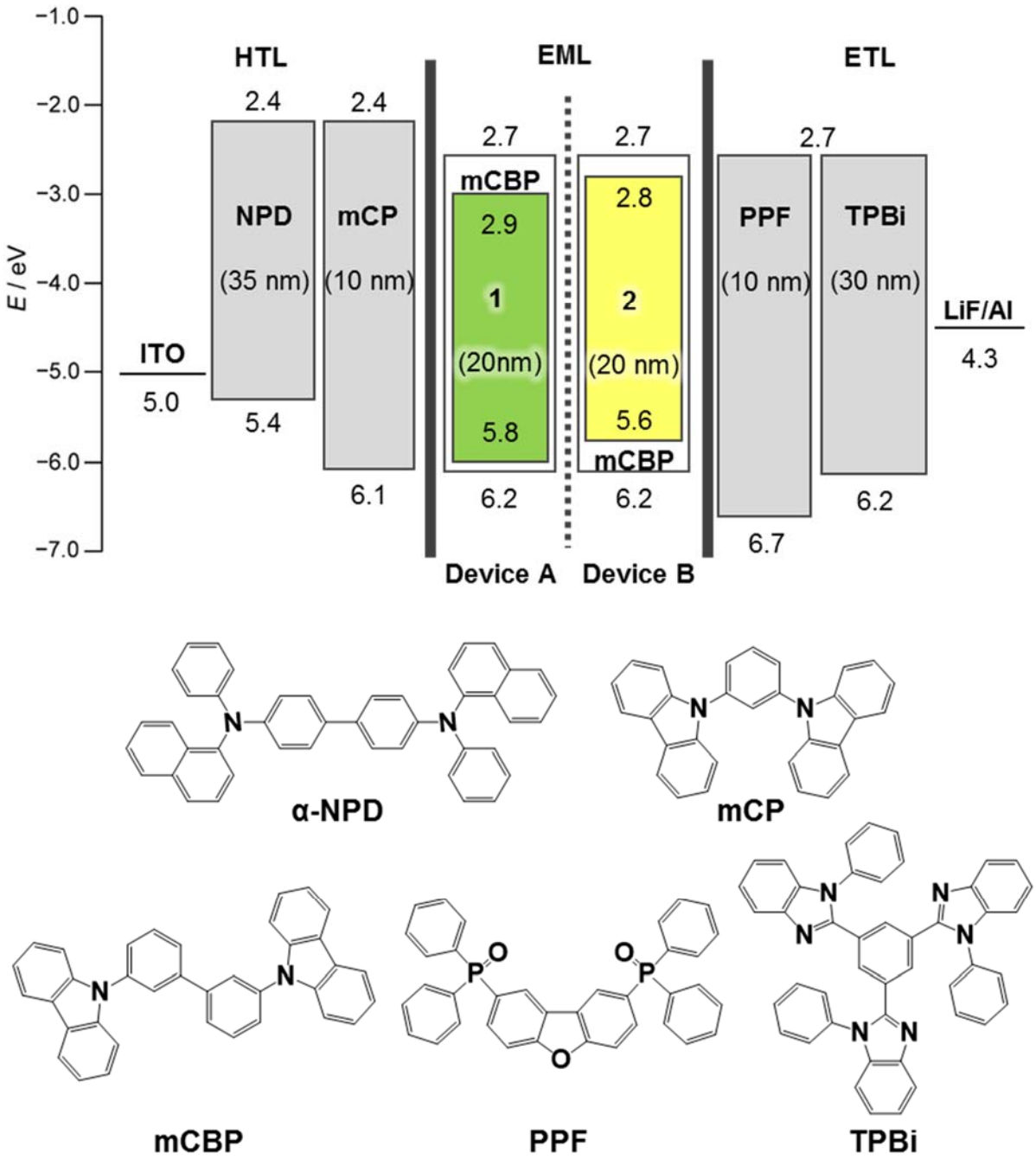

Figure 4-7. Energy level diagram showing the HOMO/LUMO levels and the structures of OLED devices **A** and **B** containing the TADF emitters **1** and **2** and the chemical structures of the materials used for the devices.

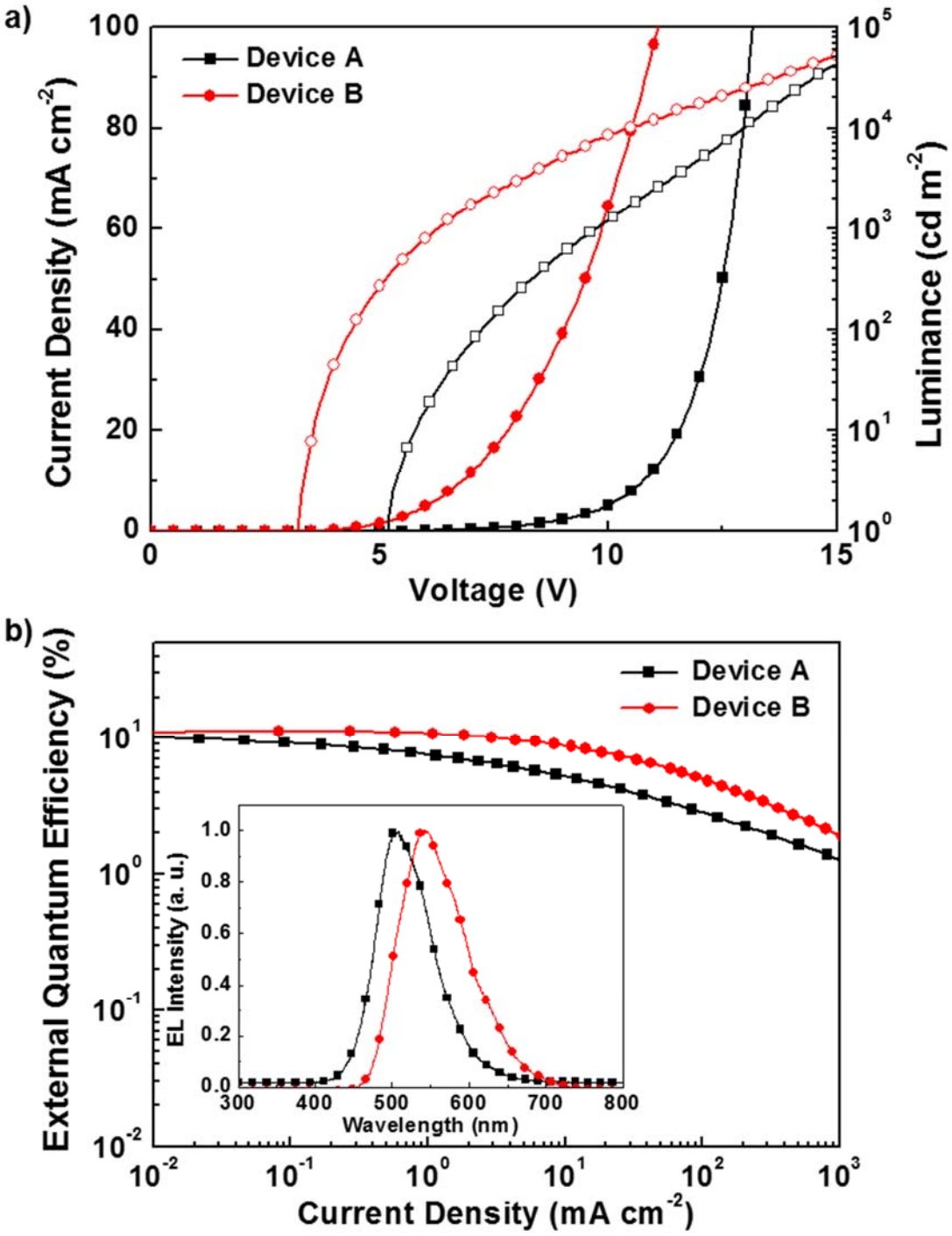

Figure 4-8. a) Current-density−voltage−luminance (J−V−L) curves and b) η_{ext}−J plots of devices **A** and **B** containing the TADF emitters **1** and **2** (inset: normalized EL spectra measured at 10 mA cm^{-2}).

4.3 Conclusion

In summary, the x-shaped molecules **1** and **2** with crossed donors and acceptors were designed and synthesized. The large steric hindrance of the bulky benzoylbenzophenone core units leads to strong distortion between acceptor and donor units, thereby realizing relatively small experimentally-determined ΔE_{ST} of 0.06 and 0.02 eV, which promote efficient TADF emission. The OLEDs based on **1** and **2** as emitters exhibited high η_{ext} of up to 11% for green and yellow emission. We believe that this molecular design strategy offers a way to develop light-emitting materials with small ΔE_{ST} for high-performance TADF-OLEDs.

4.4 Experimental Section

4.1.1 General Methods

NMR spectra were recorded on an Avance III 500 spectrometer (Bruker). Chemical shifts of ^{1}H NMR signals were quoted to tetramethylsilane (δ = 0.00) as an internal standards. Matrix-assisted laser desorption ionization time-of-flight (MALDI-TOF) mass spectra were collected on a Autoflex III spectrometer (Bruker Daltonics) using dithranol as the matrix. Elemental analyses were carried out with a Yanaco MT-5 CHN corder. The UV/vis absorption and PL spectra of organic films were measured with a UV-2550 (Shimadzu) and a FluoroMax-4 spectrofluorometer (Horiba Scientific), respectively. The Φ_{PL} was measured using an absolute PL quantum yield measurement system (Hamamatsu Photonics C9920-02, PMA-11). Luminescence intensity and lifetime of organic films were measured with a Streak camera (Hamamatsu Photonics C4334). The organic films were excited by N_2 gas laser (λ = 337 nm, pulse width = 500 ps, repetition rate 20 Hz) under a vacuum of $< 4 \times 10^{-1}$ Pa. Samples were cooled down at 5 K with a cryostat (Iwatani Industrial Gases). The density-functional theory (DFT) computations were performed on the Gaussian 03 program package,[1] using the B3LYP functional with the 6-31G(d,p) basis set.[10)]

4.1.2 OLED device fabrication and measurements

To measure EL of the Benzoylbenzophenone derivatives based OLEDs, a clean glass substrate precoated with a 110-nm-thick ITO layer with a sheet resistance of < 20 Ω $\square^{-1}$ was used. The substrate was degreased with distilled water, a neutral detergent, acetone, isopropyl alcohol, and cleaned in UV-ozone chamber (Nippon Laser and Electrics lab. NLUV253) before it loaded into an evaporation system. The organic layers were thermally evaporated on the substrates under a vacuum of < 3 × 10^{-4} Pa with an evaporation rate of < 0.3 nm s^{-1}. In all devices, a cathode aluminum (Al) layer was deposited through a 1 mm-diameter opening in a shadow mask. The current density and voltage (*J*−*V*) characteristics of OLEDs were measured using a semiconductor parameter analyzer (Agilent E5273A). The EL spectra were recorded by multi channel analyzer (Ocean Optics SD2000) at current densities of 1, 10, and 100 mA cm^{-2}. The brightness of OLEDs was measured using an optical powermeter (Newport 1930C).

4.4.3 Materials and Syntheses of Benzoylbenzophenone Derivatives

All reagents and solvents were purchased from Sigma-Aldrich, Tokyo Chemical Industry (TCI), or Wako Pure Chemical Industries and used as received unless otherwise noted. The synthetic routes to obtain **1** and **2** are outlined in Scheme 4-1. All reactions were performed under an N_2 atmosphere in dry solvents. The final products were fully characterized by ^1H NMR spectroscopy, MALDI-TOF mass spectrometry, and elemental analysis, as indicated.

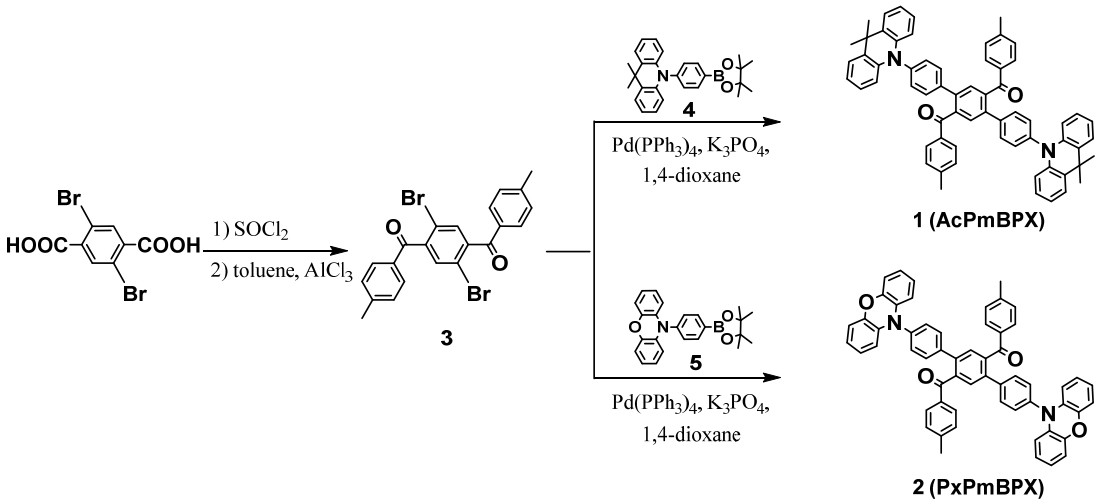

Scheme 4-1. Synthetic routes for **1** and **2**.

1,4-Dibromo-2,5-bis(p-tolyl-methanoyl)benzene **(3).** A mixture of 2,5-diboromoterephtalic acid (6.48 g, 0.02 mol) and thionyl chloride (4.1 mL) was refluxed for 3 h. The excess thionyl chloride was removed under vacuum to give 2,5-dibromoterephtalic acid chloride as a yellow crystalline solid. To a solution of 2,5-dibromoterephtalic acid chloride in toluene (40 mL), aluminum trichloride (5.60 g, 0.04 mol) was added slowly at 0 ºC. The mixture was allowed to react for 1 h at that temperature. Then, the mixture was heated at 90 ºC for 1 h, cooled down to 40 ºC, and reacted overnight. Upon cooling to room-temperature, the reaction mixture was poured into water to precipitate a white solid which was isolated by filtration. The crude product was recrystallized from chloroform and methanol to give a white solid (yield = 7.11 g, 75.3%). ^{1}H NMR (500 MHz, $CDCl_3$): δ 7.75 (d, J = 8.0Hz, 4H), 7.58 (s, 2H), 7.32 (d, J = 8.0 Hz, 4H), 7.32 (d, J = 7.5 Hz, 4H), 2.46 (s, 6H). MS (MALDI): *m/z* 472.32 $[M+H]^+$; calcd 472.17.

1,4-Bis(9,9-dimethylacridan-10-yl-p-phenyl)-2,5-bis(p-tolyl-methanoyl)benzene **(AcPmBPX (1)).** Compounds **3** (0.94 g, 2.0 mmol) and **4** (1.81 g, 4.4 mmol) were dissolved in 1,4-dioxane (40 mL) under N_2 atmosphere. To the solution were added aqueous potassium phosphate (2 M, 10 mL) and tertrakis(triphenylphosphine)palladium(0) (0.14 g, 0.12 mmol). After the complete addition, the mixture was refluxed for 48 h. The reaction mixture was then poured into water. The product was extracted with dichloromethane. The combined organic layers were washed with water and dried over anhydrous $MgSO_4$. After filtration and evaporation, the crude material was purified by column chromatography on silica gel (eluent: dichloromethane/hexane, 1:1 v/v) and dried under vacuum to give a white powder (yield = 1.27 g, 72.1%). This compound was further purified by temperature-gradient sublimation under vacuum. ^{1}H NMR (500 MHz, $CDCl_3$): δ 7.87 (s, 2H), 7.63 (t, J = 7.0 Hz, 8H), 7.43 (d, J = 7.0 Hz, 4H), 7.19-7.16 (m, 8H), 6.91-6.88 (m, 8H), 5.86 (d, J = 7.5 Hz, 4H), 2.41 (s, 6H), 1.65 (s, 12H). MS (MALDI): *m/z* 882.12 $[M]^+$; calcd 882.12. Anal. calcd (%) for $C_{64}H_{52}N_2O_2$: C, 87.24; H, 5.95; N, 3.18; found: C, 87.19; H, 5.87; N, 3.24.

1,4-Bis(9,9-phenoxazin-10-yl-p-phenyl)-2,5-bis(p-tolyl-methanoyl)benzene **(PxPmBPX (2)).** This compound was synthesized using a procedure similar to that employed for the synthesis of **1** except that **5** was used instead of **4** (yield = 1.34 g, 80.7%). This compound was further purified by temperature-gradient sublimation under vacuum. ^{1}H NMR (500 MHz, $CDCl_3$): δ 7.81 (s, 2H), 7.61-7.56 (m, 8H), 7.18 (d, J = 8.0 Hz, 4H), 7.14 (d, J = 8.0 Hz, 4H), 6.67-6.61

(m, 8H), 6.53 (td, J = 8.0 Hz, 2.0 Hz, 4H), 5.53 (dd, J = 8.0 Hz, 1.0 Hz, 4H), 2.37 (s, 6H). MS (MALDI): m/z 828.94 $[M]^+$; calcd 828.95. Anal. calcd (%) for $C_{58}H_{40}N_2O_4$: C, 84.04; H, 4.86; N, 3.38; found: C, 83.98; H, 4.96; N, 3.45.

4.5 References

[1] S. Y. Lee, T. Yasuda, Y. S. Yang, Q. Zhang, and C. Adachi, *Angew. Chem. Int. Ed*., **2014**, 126, 6520.

[2] Y. Hong, J. W. Y. Lam, and B. Z. Tang, *Chem. Commun*., **2009**, 4332.

[3] B.-R. Gao, H.-Y. Wang, Y.-W. Hao, L.-M. Fu, H.-H. Fang, Y. Jiang, L. Wang, Q.-D. Chen, H. Xia, L.-Y. Pan, Y.-G. Ma, and H.-B. Sun, *J. Phys. Chem. B*, **2010**, 114, 128.

[4] Z. Zhao, S. Chen, C. Y. K. Chan, J. W. Y. Lam, C. K. W. Jim P. Lu, Z. Chang, H. S. Kwok, H. Qiu, and B. Z. Tang, *Chem. Asian J*., **2012**, 7, 484.

[5] H. Tanaka, K. Shizu, H. Nakanotani, and C. Adachi, *J. Phys. Chem. C*, **118**, 15985.

[6] W. Z. Yuan, Y. Gong, S. Chen, X. Y. Shen, J. W. Y. Lam, P. Lu, Y. Lu, Z. Wang, R. Hu, N. Xie, H. S. Kwok, Y. Zhang, J. Z. Sun, and B. Z. Tang, *Chem. Mater*., **2012**, 24, 1518.

[7] K. Goushi, K. Yoshida, K. Sato, C. Adachi, *Nat. Photon.*, **2012**, 6, 253.

[8] P. A. Vecchi, A. B. Padmaperuma, H. Qiao, L. S. Sapochak and P. E. Burrows, *Org. Lett*., **2006**, 8, 4211.

[9] C. Murawski, K. Leo and M. C. Gather, *Adv. Mater*., 2013, **25**, 6801.

[10] M. J. Frisch, G. W. Trucks, H. B. Schlegel, G. E. Scuseria, M. A. Robb, J. R. Cheeseman, J. A. Montgomery, Jr., T. Vreven, K. N. Kudin, J. C. Burant, J. M. Millam, S. S. Iyengar, J. Tomasi, V. Barone, B. Mennucci, M. Cossi, G. Scalmani, N. Rega, G. A. Petersson, H. Nakatsuji, M. Hada, M. Ehara, K. Toyota, R. Fukuda, J. Hasegawa, M. Ishida, T. Nakajima, Y. Honda, O. Kitao, H. Nakai, M. Klene, X. Li, J. E. Knox, H. P. Hratchian, J. B. Cross, C. Adamo, J. Jaramillo, R. Gomperts, R. E. Stratmann, O. Yazyev, A. J. Austin, R. Cammi, C. Pomelli, J. W. Ochterski, P. Y. Ayala, K. Morokuma, G. A. Voth, P. Salvador, J. J. Dannenberg, V. G. Zakrzewski, S. Dapprich, A. D. Daniels, M. C. Strain, O. Farkas, D. K. Malick, A. D. Rabuck, K. Raghavachari, J. B. Foresman, J. V. Ortiz, Q. Cui, A. G. Baboul, S. Clifford, J. Cioslowski, B. B. Stefanov, G. Liu, A. Liashenko, P. Piskorz, I. Komaromi, R. L. Martin, D. J. Fox, T. Keith, M. A. Al-Laham, C. Y. Peng, A.

Nanayakkara, M. Challacombe, P. M. W. Gill, B. Johnson, W. Chen, M. W. Wong, C. Gonzalez, and J. A. Pople, Gaussian 03, Gaussian, Inc., Pittsburgh PA, **2003**.

Chapter 5

Thermally Activated Delayed Fluorescence Polymers for Efficient Solution-Processed Organic-Light Emitting Diodes

Chapter 5

Thermally Activated Delayed Fluorescence Polymers for Efficient Solution-Processed Organic-Light Emitting Diodes

Abstract

The first TADF polymer materials of **pCCBP** and **pAcBP** were designed for solution-processable TADF-OLEDs. The benzophenone-based donor-acceptor frameworks of polymers contributed to realize small ΔE_{ST} which enabled efficient exciton-harvesting through TADF. Well optimized OLEDs employing the TADF polymers as emitters fabricated by spin coating and achieved high η_{ext} up to 9.3% in green and yellow emissions.

5.1 Introduction

Generally, OLEDs are fabricated by thermally evaporating small molecules to form multi-layered device structures that realize effective hole and electron injection, transporting, and recombination. However, solution processes for fabricating OLEDs are of great interest because of the potential for simplified processing and low-cost, large-area production.[1)] The performance of solution-processed OLEDs is strongly affected by the solubility of the component molecules. Small-molecule materials having high efficiency and stability have been used as emitters in solution-processed OLEDs,[2)] but they generally suffer from poor solubility and strong crystallization.[3)] Polymers can more easily form uniform thin films having low surface roughness because of their high solubility.[4)] Although various polymers have been extensively studied as emitting materials since the first report of polymer OLEDs based on PPV,[5)] achieving high quantum efficiency in TADF based OLEDs is generally difficult due to the low triplet energy of polymer emitter and host materials.[6,7)]

Recently, TADF has been exploited to achieve high-performance OLEDs based on small-molecule emitters.[10] Through TADF, both singlet and triplet excitons emit light by thermal up-conversion of triplet to singlet and fluorescence from the singlet states, allowing nearly 100% of excitons to contribute to emission.[8] By designing molecules with a small ΔE_{ST}, high efficiency RISC of triplets to the singlet state, and efficient TADF emission have been achieved in purely organic luminophores.[9–13] Thus, applying similar design strategies to create polymers exhibiting TADF offers a possible path to solution processed OLEDs with high performance.

In this study, we design, synthesize, and characterize polymers that emit TADF for highly-efficient, solution-processed OLEDs (Fig. 5-1). The polymer design is based on benzophenone, which we recently used in butterfly-shaped luminescent molecules for full-color TADF-OLEDs with the maximum η_{ext} of up to 14.3%,[14] and features a backbone consisting of electron donor and acceptor units in D-A-D configurations. To control the emission color and realize a small ΔE_{ST} in a polymer, electron−donating substituents of carbazole and dimethylacridane are combined with the electron−withdrawing benzophenone core unit for polymers with green-blue and yellow emission.

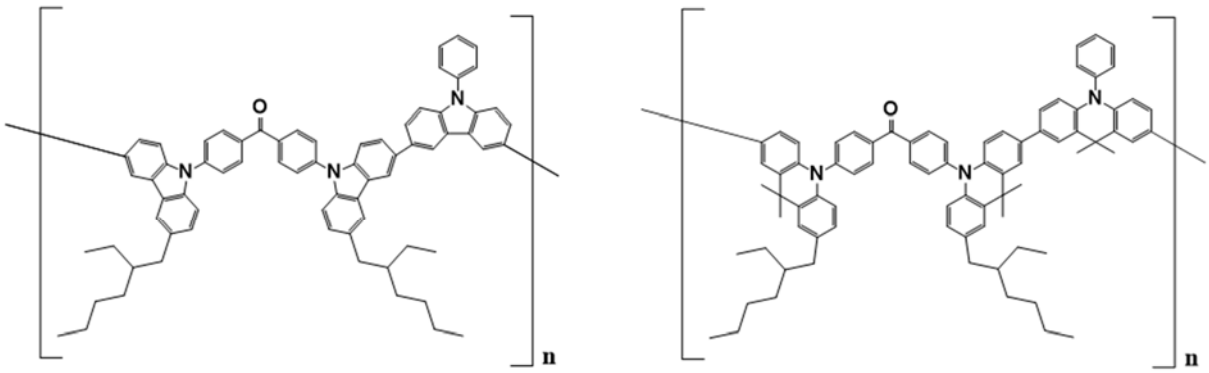

Figure 5-1. Molecular structures of **1** and **2**.

5.2 Results and Discussion

5.2.1 Geometric and Electronic Structures Characterization of TADF Polymers by TD-DFT Calculations

The electronic and geometrical structures of **1** and **2** were investigated using time-dependent density functional theory (TD-DFT) calculations performed at the B3LYP/6-31G (d,p) level. Previous studies have shown that ΔE_{ST} should decrease when the overlap of the HOMO and LUMO wavefunctions of a molecule is reduced,[15] and small-molecule benzophenone derivatives in our recent report exhibited relatively small ΔE_{ST} because of the large dihedral angles between electron-donating and accepting units, leading to clear separation of HOMO and LUMO distribution. As shown in Fig. 5-2, for polymers **1** and **2**, the HOMO is primarily localized on the electron-donating carbazole and dimethylacridane units, whereas the LUMO is mainly localized on central electron-accepting benzophenone units, which result in a small ΔE_{ST}. The ΔE_{ST} of **1** and **2** were calculated to be 0.16 and 0.003 eV, respectively, which is favorable for RISC from T_1 to S_1 states. Thus, this polymer design is expected to demonstrate efficient RISC.

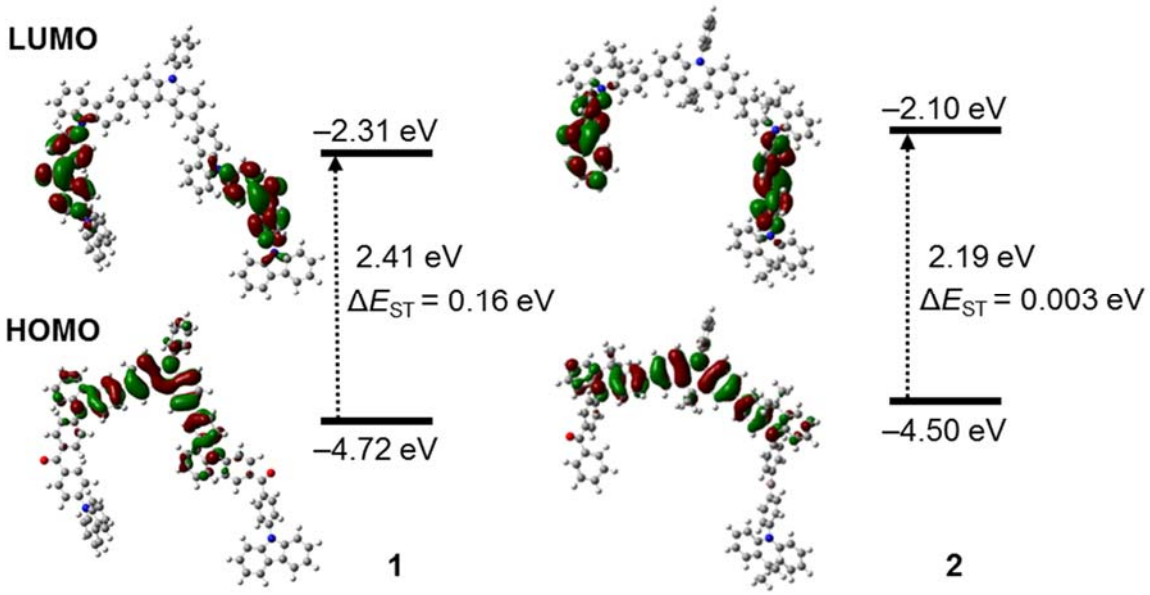

Figure 5-2. Frontier-molecular-orbital distributions, energy levels, and ΔE_{ST} of **1** and **2** characterized by TD-DFT calculations.

5.2.2 PL Properties of TADF Polymers

Steady-state UV/Vis absorption and PL spectra of **1** and **2** in toluene solutions are depicted in Fig. 5-3, and the photophysical properties are summarized in Table 5-1. The lowest-energy absorption peaks of **1** and **2** appear at about 361 and 357 nm, respectively. The polymers exhibit bright PL in solution with emission colors of sky-blue and yellow. The λ_{PL} is red-shifted by 81 nm from **1** (λ_{PL} = 474 nm), with carbazole donor units, to **2** (λ_{PL} = 555 nm), with dimethylacridane units. The considerable red-shift of λ_{PL} depending on the electron-donating substituent suggests that the strong electron-donating dimethylacridane stabilizes the HOMO, resulting in a decreased E_g compared with that of polymer **1**. Thus, fine tuning of the luminescence properties can be achieved by simple chemical modification of the donor unit. The HOMO energy levels of **1** and **2** in thin films were determined to be −5.64 and −5.41 eV, respectively, by photoelectron yield spectroscopy, and the LUMO energy levels were estimated by adding the E_g, determined from the onset of the absorption spectra of the thin films, to the measured HOMO energies (Table 5-1).

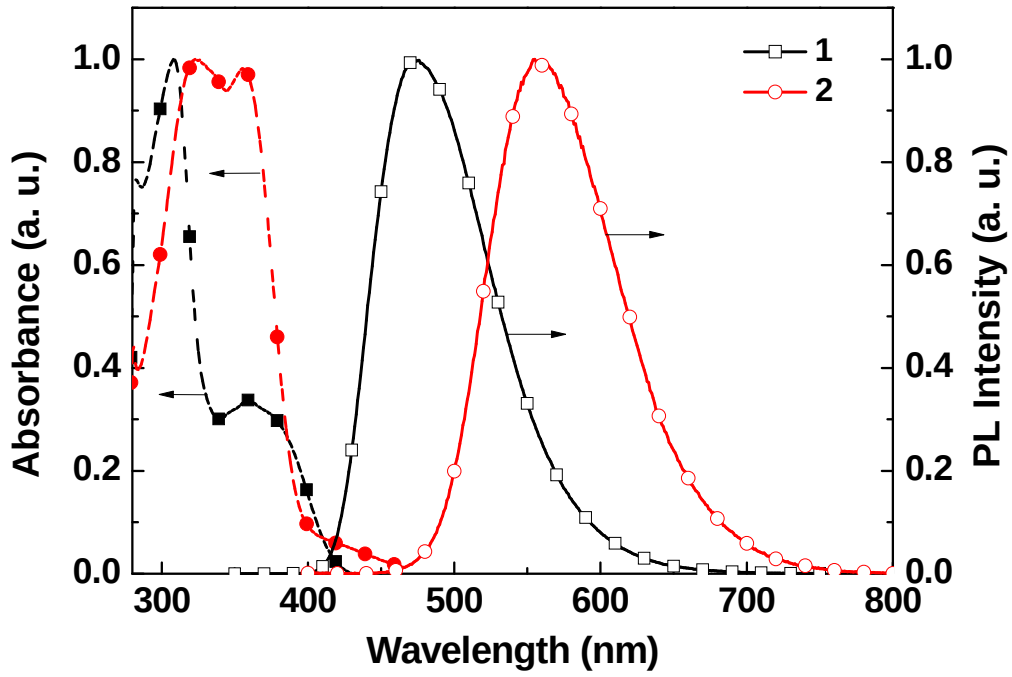

Figure 5-3. Normalized absorption (closed dot) and PL (open dot) spectra of **1** and **2** in toluene solutions at room-temperature.

Table 5-1. Photophysical properties of polymers **1** and **2**

Polymer	λ_{abs} (nm) sol[a)]	λ_{PL} (nm) sol[a)]	Φ_{PL} (%) sol[a)]	HOMO (eV)[b)]	LUMO (eV)[c)]	calc. ΔE_{ST} (eV)[d)]
1	307, 360	474	27.9	–5.64	–2.76	0.15
2	332, 355	555	25.6	–5.41	–2.78	0.003

a) Measured in oxygen-free toluene solution at room-temperature. b) Determined by photoelectron yield spectroscopy in thin films. c) Deduced from the HOMO and optical E_g. d) Calculated by TD-DFT at B3LYP/6-31G(d,p).

5.2.3 Solvatochromic Properties of TADF Polymers

To confirm the origin of the PL emissions of **1** and **2**, solvatochromic properties of the polymers were investigated using various solvent with increasing polarities and plot Lippert-Mataga model (Fig. 5-4).[16)] Most of the conjugated polymer have extended π-conjugation which leads to a decrease of T_1 states and cause low triplet exciton harvesting efficiency. Therefore, for effective TADF emission, reducing the π-conjugation length and isolating the HOMO and LUMO of polymers are effective to realize a small ΔE_{ST} and efficient triplet harvesting. If the molecules has isolated HOMO and LUMO, and the CT-based emission will show a linear increase of Stoke's shifts against Δf observed in Lippert-Mataga model.

The Stoke's shifts is given by following Lippert-Mataga equation (See section 1.3.1):

$$\overline{\nu}_a - \overline{\nu}_f = \frac{2}{hc}\left(\mu_e - \mu_g\right)^2 a^{-3}\Delta f + const. \quad (5\text{-}4)$$

As we can confirm in Equ. 5-4, Stoke's shift depends on the absolute magnitude of the charge transfer dipole moment ($\mu_e - \mu_g$) and polarity of the solvent. In the case of CT based emissive molecules having D-A configuration, PL spectra tend to vary sensitive with surrounding polar environments because of its large different dipole moment between ground and excited states.[17,18)] This large transition dipole moment leads to strong relaxation of excited states and

Stoke's shift in polar solvent. Therefore, Stoke's shift is increased linearly against Δf in Lippert-Mataga model.

The lowest-energy λ_{abs} and λ_{PL} and Stoke's shift ($v_a - v_f$) of **1** and **2** in different solvents are shown in Table 5-2 and the result plotted in Lippert-Mataga model (Fig. 5-4). For polymer **1** and **2**, very large and a linear increase of Stoke's shift versus Δf were observed. It should be originated from strong CT based emission of the D-A combined molecular structure of polymer **1** and **2**.

Table 5-2. Lowest-energy absorption and PL spectra and Stoke's shift ($v_a - v_f$) of **1** and **2** in different solvents

Solvent	Δf[a)]	λ_{abs} (nm)		λ_{PL} (nm)		$v_a - v_f$ (cm^{-1})	
		1	**2**	**1**	**2**	**1**	**2**
cyclohexane	0.001	-	346	-	533	-	10140.00803
toluene	0.013	360	355	474	555	6680.73136	10150.99607
chloroform	0.149	369	359	551	598	8951.45068	11132.74518
THF[b)]	0.210	359	355	523	600	8734.69431	11502.34742
DCM[c)]	0.219	358	-	537	-	9310.98696	-
DMF[d)]	0.275	357	360	557	608	10057.88312	11330.40936

a) Orientation polarizability. b) Tetrahydrofuran. c) Dichloromethane. d) *N*,*N*-Dimethylformamide.

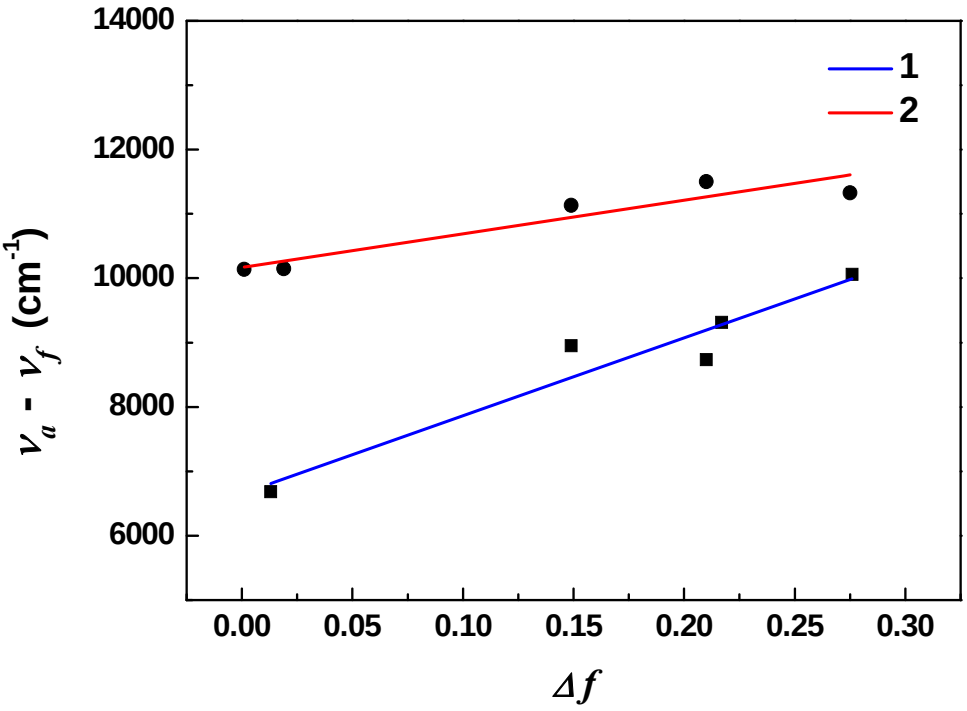

Figure 5-4. Lippert-Mataga model of **1** (square dot) and **2** (circle dot) in differnt solvents.

5.2.4 TADF Properties of Polymers in Mixed Host Thin Films

The presence of TADF emission from these polymers was confirmed by analyzing the temperature dependence of the transient PL characteristics of thin films using a streak camera. To prevent concentration quenching and achieve high Φ_{PL}, emitter molecules are often blended with host molecules. The host molecules should have T_1 levels higher than those of the emitters, which were determined from the onset position of the PL spectra of the neat films at 5 K to be 2.69 and 2.50 eV for **1** and **2**, respectively, to prevent back energy transfer of triplets to the host. Furthermore, to improve charge balance and injection, broaden the recombination zone, and decrease roll-off,[19,20] a mixture of hole- and electron-transporting host molecules can be used. Thus, electron- and hole-transporting hosts of tris(4-carbazoyl-9-ylphenyl)amine (TCTA) and TAPC with high T_1 energies of 2.78 and 2.87 eV, respectively, were employed to fabricate mixed host thin films for the photophysical studies.[21]

The transient PL characteristics displayed in Fig. 5-5 and 5-6 for a **1** and **2** (10 wt%): TCTA (65 wt%): TAPC (25 wt%) blend film deposited by spin-coating from chlorobenzene indicate two-component emission decay, consisting of a nanosecond-scale prompt component (lifetime τ_p = 13 and 24 ns) and a microsecond-scale delayed component (τ_d = 74 and 10 μs) at 300 K (Fig. 5-5). Furthermore, the delayed emission intensity was found to decrease with decreasing temperature from 300 to 5 K, which is expected for TADF since up-conversion from T_1 to S_1 states by thermal energy will be accelerated at higher temperatures. Since the delayed emission has the same spectral profile as the prompt fluorescence and is temperature dependent, the long-lived emission can be assigned to TADF. The Φ_{PL} and PL decay rate constants of the mixed host film with 10 wt% **1** and **2** are shown in Table 5-3. The Φ_{PL} of mixed host films are slightly decreased from 300 K to 100K, because of decreasing Φ_{TADF} in low temperature.

Table 5-3. Rate constants and quantum efficiencies of polymers **1** and **2**[a)]

Polymer	k_r^S (s^{-1})	k_{ISC} (s^{-1})	k_{RISC} (s^{-1})	Φ_F/τ_p (%/nm)	Φ_{TADF}/τ_d (%/μs)	Φ_{ISC} (%)	Φ_{RISC} (%)	ΔE_{ST} (eV)
1	5.6×10^6	7.1×10^7	3.1×10^4	7.29/13	15.5/74	93	17	0.18
2	8.0×10^6	3.4×10^7	1.3×10^5	19.1/24	26.9/10	81	33	0.11

a) Measured with 10 wt% blend film in a host matrix (TCTA (65 wt%): TAPC (25 wt%).

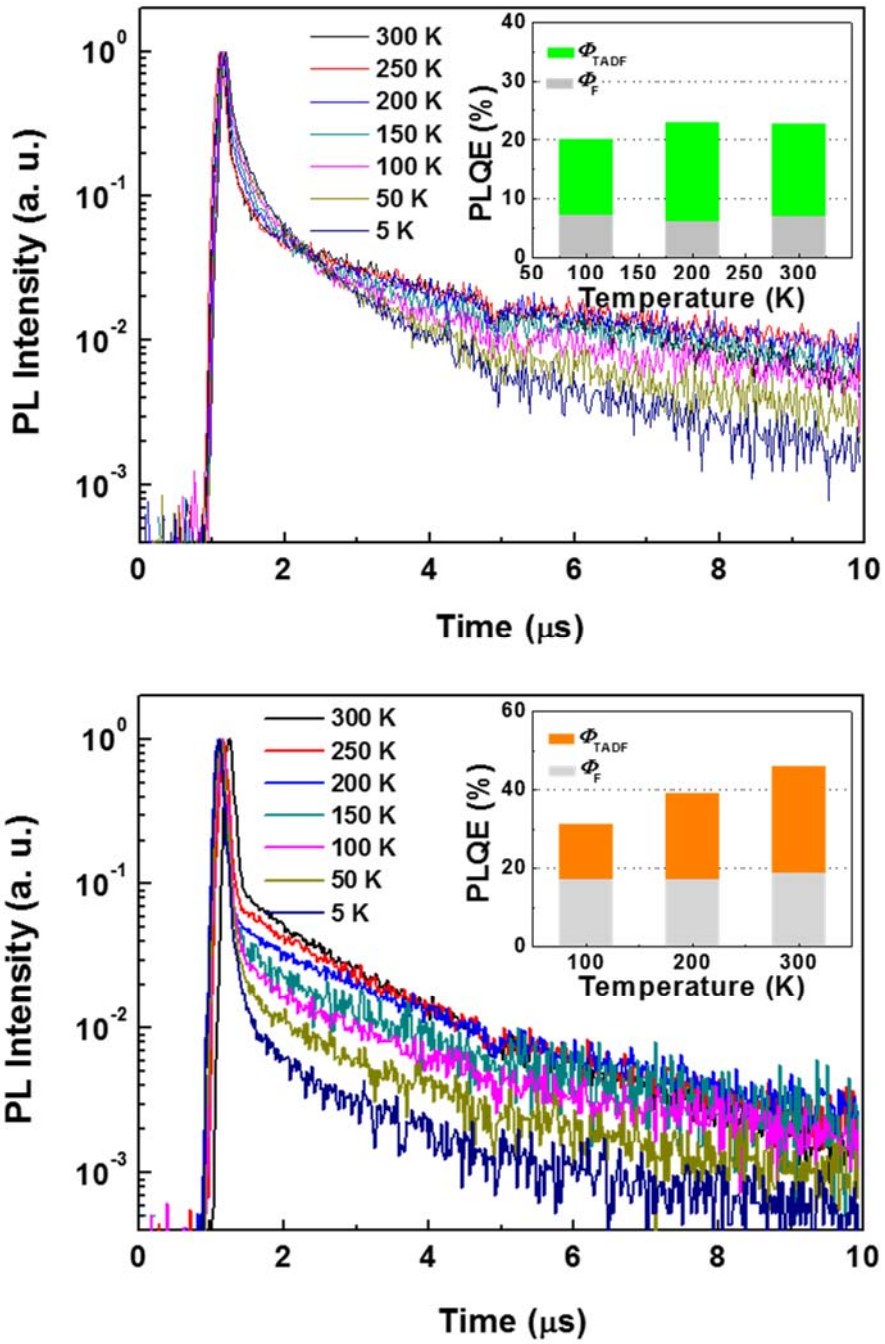

Figure 5-5. Temperature dependence of transient PL decay of 10 wt% **1** a) and **2** b): TAPC: TCTA blend films from 300 to 5 K (inset: the contribution of fluorescence and TADF to the total Φ_{PL}).

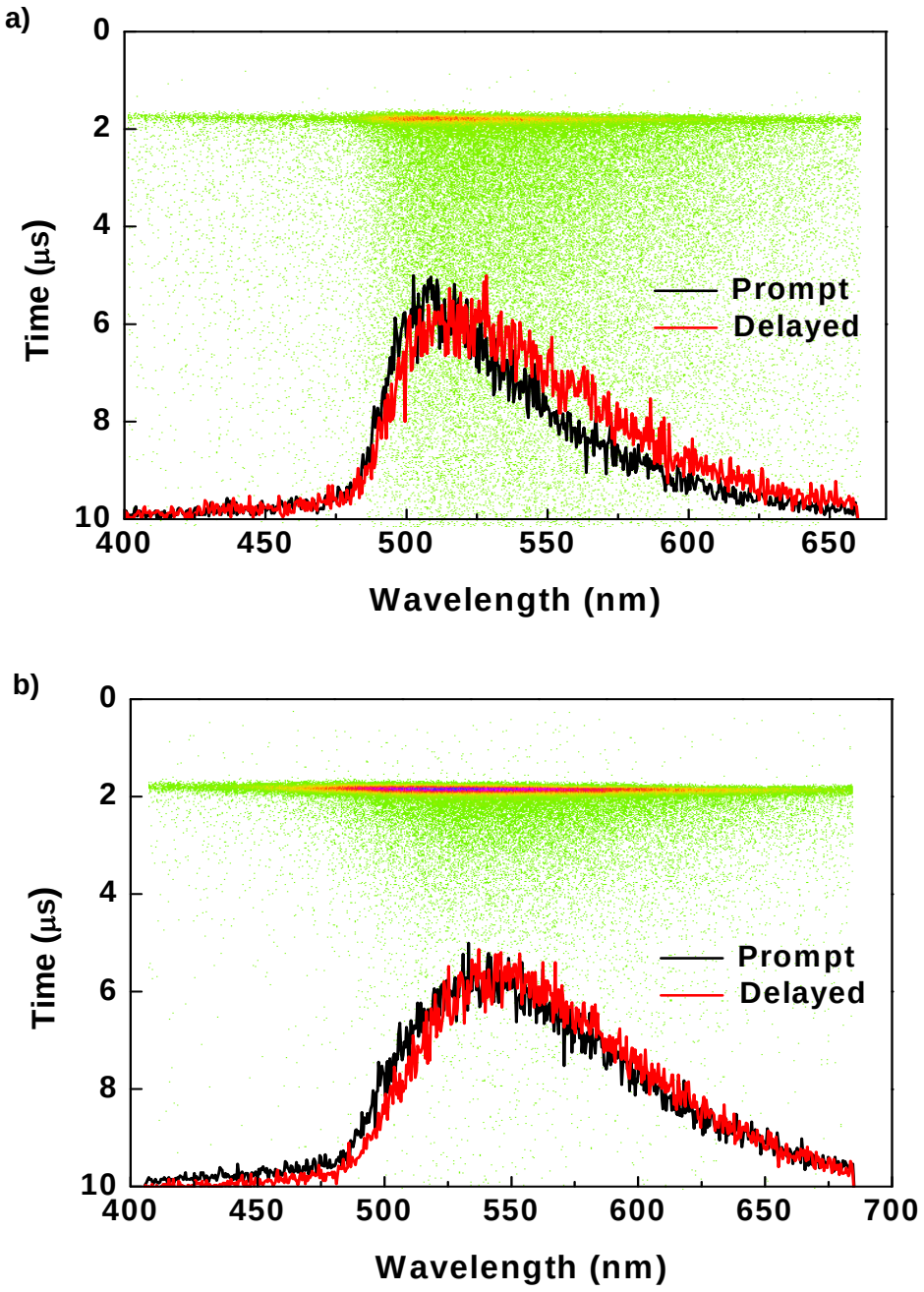

Figure 5-6. Streak image and corresponding time-dependent emission spectra (prompt: black, delayed: red) of a 10 wt% **1** a) and **2** b): TAPC: TCTA blend films recorded at 300 K. Each dot in the streak image represents a PL photon count.

5.2.5 Fabrication and EL Properties of TADF Polymer OLEDs

The EL characteristics of **1** and **2** as emitters were evaluated in multi-layer OLEDs fabricated by spin-coating and vacuum evaporation with device configurations (Fig. 5-7) of ITO/ PEDOT:PSS (40 nm)/ 10 wt % polymer: TCTA: TAPC (40 nm)/ 1,3,5-tri(*m*-pyrid-3-yl-phenyl)benzene (TmPyPB, 50 nm)/ LiF (0.8 nm)/ Al (80 nm) with **1** as an emitter in device **A** and **2** in device **B**. In these devices, PEDOT:PSS and TmPyPB serve as a HTL and an ETL, respectively, and TmPyPB also acts as an exciton blocking layer to prevent quenching of excitons at the metal electrode interface because of its high triplet state energy of 2.78 eV.[22)]

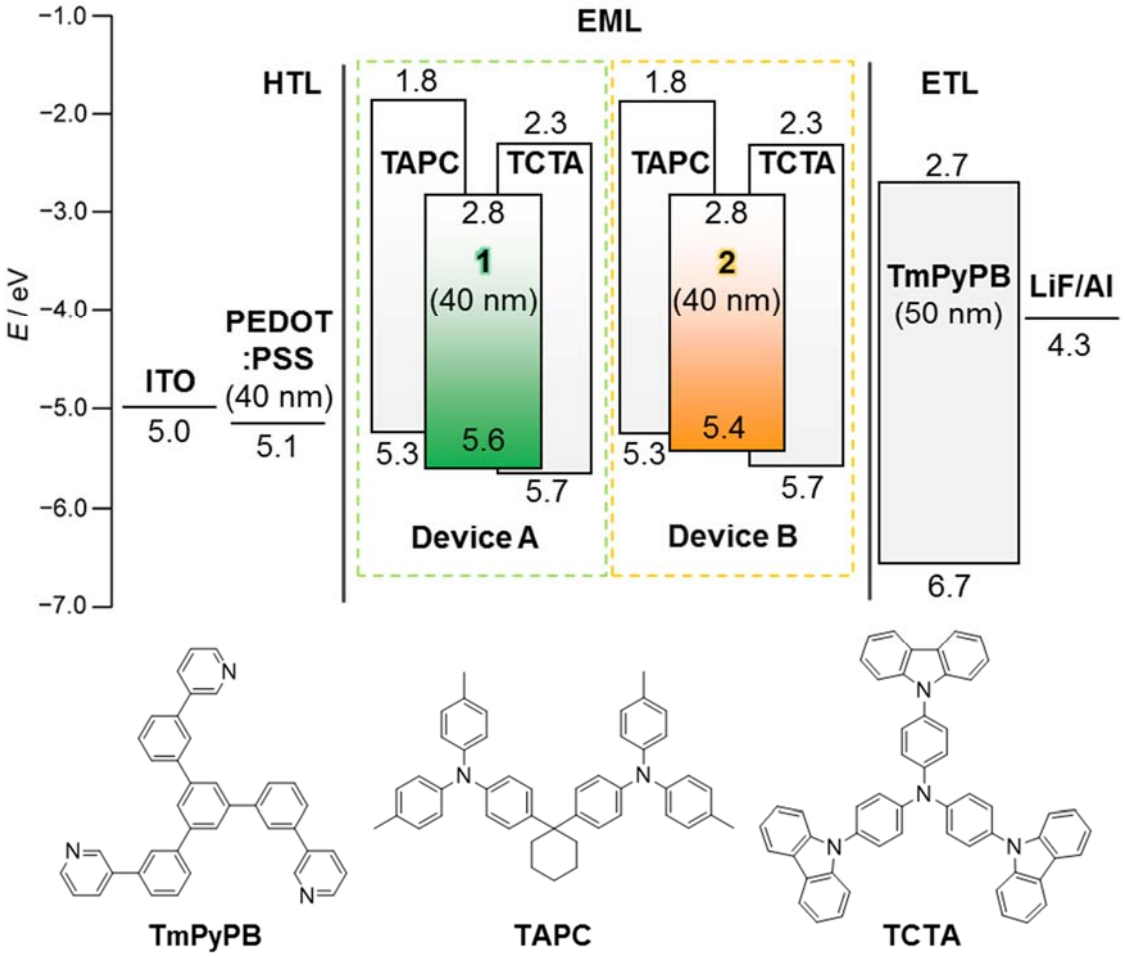

Figure 5-7. Energy level diagram showing the HOMO/LUMO levels and the molecular structures of the materials used in devices **A** and **B**.

Figure 5-8 presents current-density−voltage−luminance (*J*−*V*−*L*) characteristics, EL spectra, and η_{ext}–*J* plots of the fabricated devices. Devices based on **1** and **2** exhibited green-blue and yellow EL, respectively, similar to the corresponding PL of their doped films, indicating that EL was generated solely from the emitters themselves through the same radiative decay process.

The EL characteristics of device **A** and **B** are summarized in Table 5-4. The green-blue-emitting device **A** containing **1** achieved a high maximum η_{ext} of 8.1 % with CIE coordinates of (0.28, 0.43), η_c of 24.9 cd A^{-1}, and η_p of 8.98 lm W^{-1} at a low luminance. With increasing luminance, the η_{ext} decreased, which is mainly attributed to excess T_1 excitons in the EML causing exciton quenching by T−T and/or S−T annihilation.

The yellow-emitting device **B** incorporating **2** exhibited the maximum η_{ext} of 9.3 % with CIE coordinates of (0.38, 0.57), η_c of 31.8 cd A^{-1}, and η_p of 20.3 lm W^{-1}. At a high luminance of 1000 cd m^{-2}, the η_{ext} of device **B** was still as high as 8.0%, indicating a reduced efficiency roll-off, presumably because of the short delayed lifetime (10 μs) for **2**.

Table 5-4. TADF-OLED performance of the devices **A** and **B**

Device	Emitter	λ_{EL} (nm)	V_{on} (V)	L_{max} (cd m^{-2})	η_c (cd A^{-1})	η_p (lm W^{-1})	η_{ext} (%)	CIE (*x*, *y*)
A	**1**	500	6.0	5131	24.9	8.98	8.13	0.28, 0.43
B	**2**	548	4.3	30816	31.8	20.3	9.29	0.38, 0.57

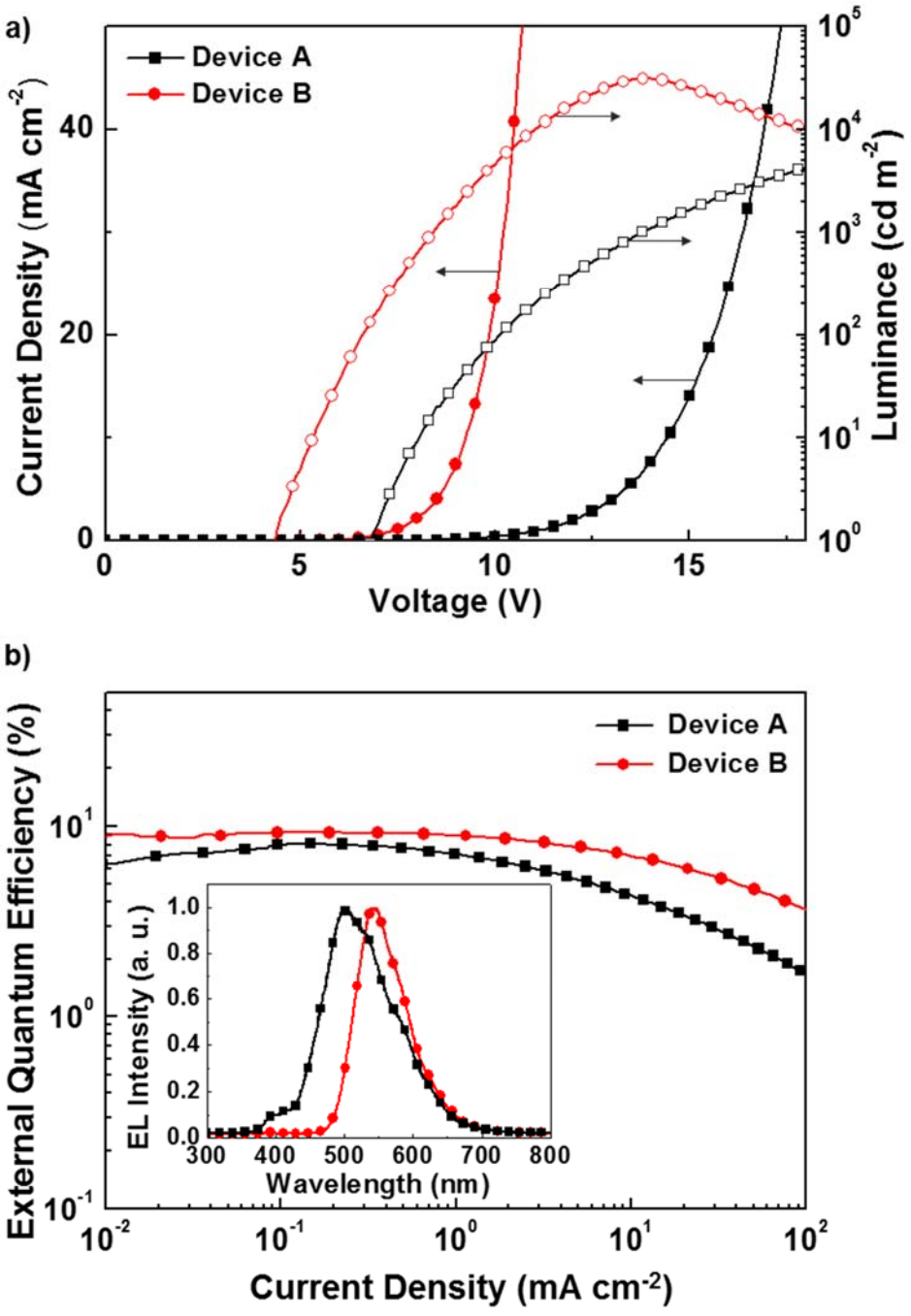

Figure 5-8. a) Current-density−Voltage−Luminance ($J-V-L$) curves of the OLEDs. **A** and **B** containing the TADF polymer emitters **1** and **2**. b) External EL quantum efficiency (η_{ext}) versus luminance plots (inset: normalized EL spectra measured at 10 mA cm^{-2}).

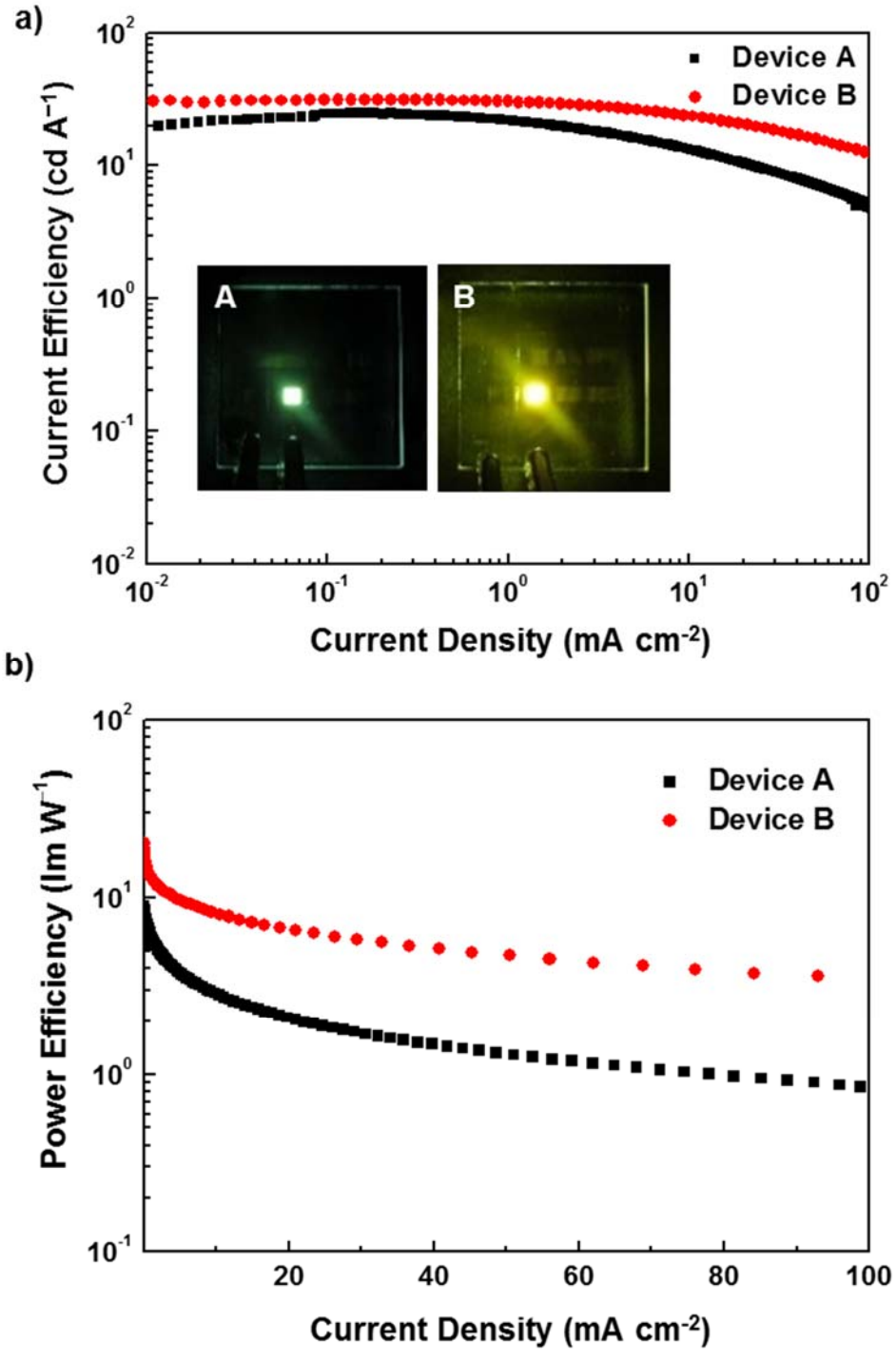

Figure 5-9. a) Current efficiency (inset: photographs of devices **A** and **B**) and b) power efficiency of the OLEDs **A** and **B** containing the TADF polymer emitters **1** and **2**.

5.3 Conclusion

In this study, the first TADF polymers **pCCBP** and **pAcBP** were designed and synthesized using benzophenone-based donor-acceptor frameworks. The TADF polymers exhibited relatively small ΔE_{ST} of ~0.1 eV, which enabled efficient exciton-harvesting through spin up-conversion from non-radiative T_1 states to radiative S_1 states. OLEDs employing the TADF polymers as emitters were fabricated by solution processes and exhibited green-blue and yellow emission with maximum η_{ext} of up to 9.3%, which far exceeds the theoretical limit for conventional fluorescent OLEDs. We believe that these results offer a molecular design strategy for continued exploration of efficient TADF polymer emitters and development of solution-processed TADF-OLEDs.

5.4 Experimental Section

5.4.1 General Methods

NMR spectra were recorded on an Avance III 500 spectrometer (Bruker). Chemical shifts of ^{1}H NMR signals were quoted to tetramethylsilane (δ = 0.00) as an internal standards. Matrix-assisted laser desorption ionization time-of-flight (MALDI-TOF) mass spectra were collected on a Autoflex III spectrometer (Bruker Daltonics) using dithranol as the matrix. Elemental analyses were carried out with a Yanaco MT-5 CHN corder. UV/vis absorption and PL spectra were measured with a UV-2550 spectrometer (Shimadzu) and a Fluoromax-4 spectrophotometer (Horiba Scientific), respectively. The Φ_{PL} were measured using an integrating sphere coupled with a photonic multichannel analyzer (Hamamatsu Photonics C9920-02, PMA-11). The luminescence intensities and lifetimes of thin films were measured under vacuum ($< 4 \times 10^{-1}$ Pa) using a streak camera (Hamamatsu Photonics C4334) with an N_2 gas laser (λ = 337 nm, pulse width = 500 ps, repetition rate = 20 Hz) as excitation source. Samples were cooled down at 5 K with a cryostat (Iwatani Industrial Gases). The HOMO energy levels (or ionization energies) for thin films were determined using an AC-3 ultraviolet photoelectron spectrometer (Riken-Keiki). All quantum chemical calculations were performed using the Gaussian 03 program package.[23] Geometry optimization was performed using the

B3LYP functional with the 6-31G (d,p) basis set. Low-lying excited singlet and triplet states were computed using the optimized structures with TD-DFT at the same level.

5.4.2 OLED device fabrication and Measurements

Glass substrates coated with a 110-nm-thicker layer of ITO with a sheet resistance of < 20 Ω $\square^{-1}$ were cleansed with detergent, deionized water, acetone, and isopropanol and were then subjected to UV-ozone treatment. A thin layer (~ 40 nm) of PEDOT: PSS (Clevios P VP Al 4083) was spin-coated onto the cleaned ITO substrates at 3000 rpm for 60 s and then baked at 130 °C for 30 min in air. The EML was deposited by spin-coating (1000 rpm for 30 s) from a chlorobenzene solution containing 19−20 mg mL^{-1} of the host and guest molecules after passing through a 0.45 μm poly(tetrafluoroethylene) filter. The thickness of the active layers was 35−40 nm, measured with a Dektak profilometer. The TmPyPB was thermally evaporated on top of the active layer under high vacuum (< 3×10^{-4} Pa) at an evaporation rate of < 1.0 nm s^{-1}. Finally, LiF (0.8 nm) and Al (80 nm) layers were thermally evaporated on top of the active layer under high vacuum through a shadow mask defining the active device area of 0.04 cm^2 (Fig. 5-10). The layer thicknesses and deposition rates were monitored in situ during deposition by oscillating quartz thickness monitors. The *J*−*V*−*L* characteristics of the devices were measured using a semiconductor parameter analyzer (Agilent E5273A) and an optical powermeter (Newport 1930-C). EL spectra were recorded using a multi-channel analyzer (Ocean Optics SD2000).

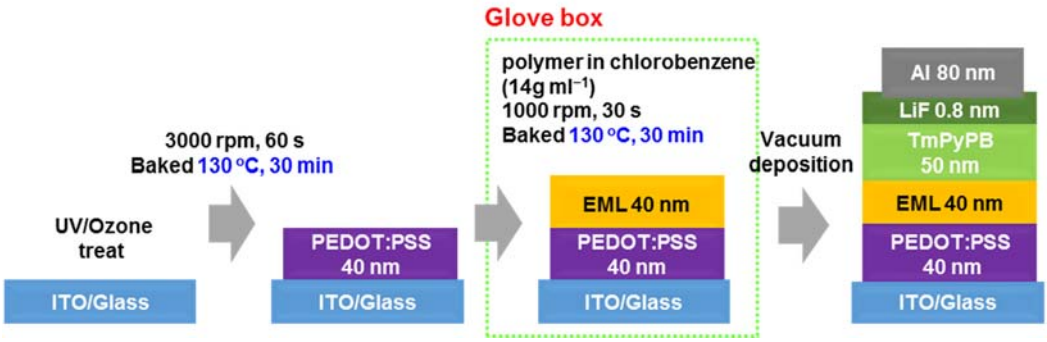

Figure 5-10. Device fabrication process of polymer **1** and **2** containing OLEDs **A** and **B.**

5.4.3 Materials and Syntheses of TADF polymers

All regents and solvents were purchased from Sigma-Aldrich, Tokyo Chemical Industry (TCI) or Wako Pure Chemical Industries and were used as received unless otherwise noted. All reactions were performed under N_2 atmospheres in dry solvents. The final products were fully characterized by ^{1}H and ^{13}C NMR spectroscopy, MALDI-TOF mass spectrometry and GPC, as described below (Scheme 5-1, Table 5-5).

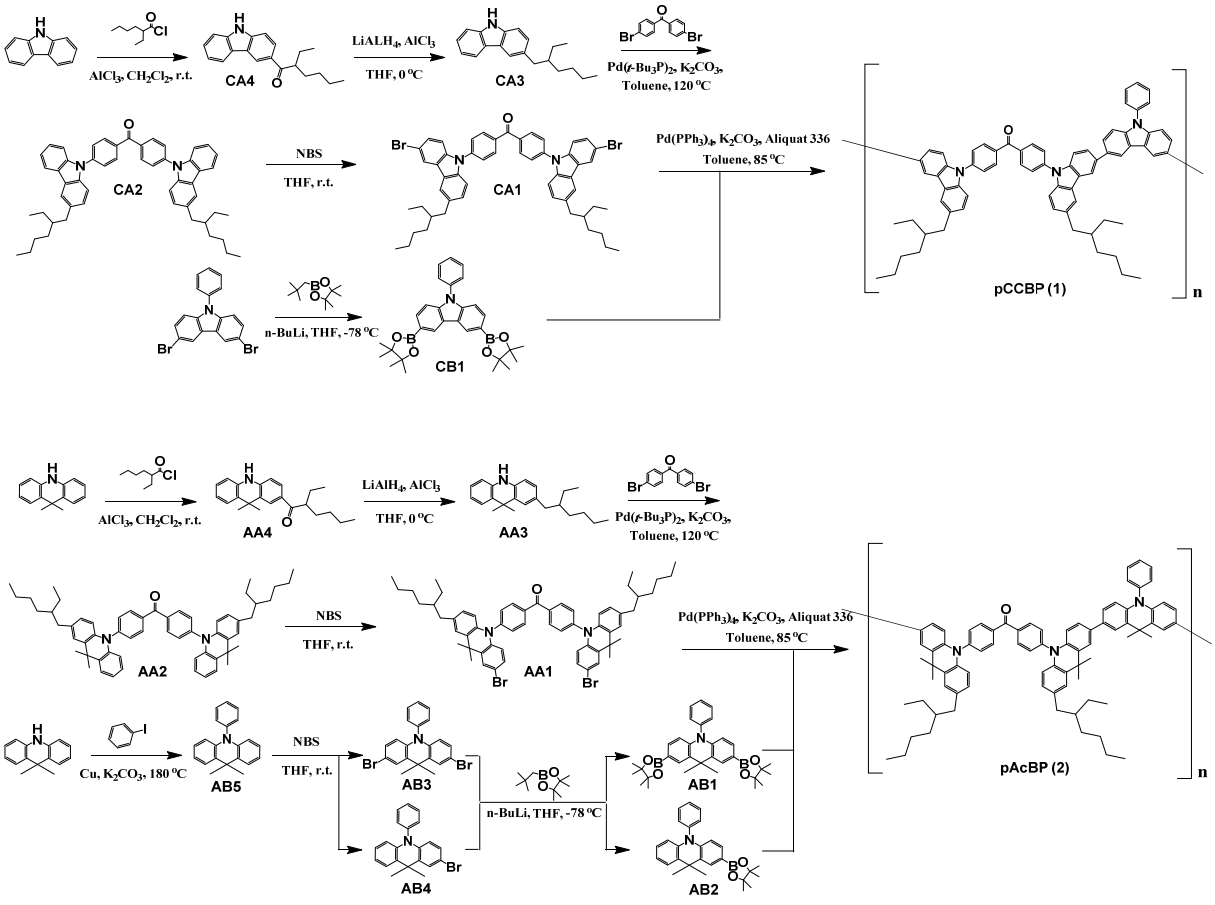

Scheme 5-1. Synthetic route for **1** and **2**.

Table 5-5. Molecular weight and PDI of polymers **1** and **2**[a)]

Polymer	M_w	PDI
1	8800	1.45
2	9200	1.24

a) Solvent: chloroform, reference: PS

3-Ethylhexanoyl-9H-carbazole (**CA4**).[24)] To a suspension of aluminum trichloride (7.99 g, 0.06 mol) in dry CH_2Cl_2 (200 mL) were added ethyl hexanoyl chloride (11.4 mL) and carbazole (10.2 g, 0.06 mol) at 0 ºC. The mixture was stirred for 18h at room-temperature, and then poured onto cool water. The formed precipitate was collected by filtration, and washed with water and methanol. The product was recrystallized from methanol/acetone and dried under vacuum to give **CA4** as white solid (yield = 15.4 g, 87.5%). ^{1}H NMR (500 MHz, $CDCl_3$): δ 8.76 (s, 1H), 8.36 (s, 1H), 8.16 (d, J = 8.0Hz, 1H), 8.12 (dd, J = 8.5Hz, 1.5Hz, 1H), 7.48−7.46 (m, 3H), 7.33−7.31 (m, 1H), 3.54 (m, 1H), 1.91−1.81 (m, 2H), 1.68-1.54 (m, 2H), 1.35−1.25 (m, 4H), 0.94−0.91 (m, 3H), 0.87−0.84 (m, 3H). MS (MALDI): m/z 293.98 $[M]^+$; calcd 293.40.

3-Ethylhexyl-9H-carbazole (**CA3**).[24)] To a suspension of lithium aluminium hydride (3.01 g, 0.08 mol) and aluminum trichloride (5.33 g, 0.04 mol) in dry THF (200 mL) was added dropwise in **CA4** (11.7 g, 0.04 mol) at 0 ºC. The mixture was reacted for 5h at room-temperature, and then quenched by slow addition of ethyl acetate (50 mL) and aqueous hydrochloric acid (ca. 5%, 5 mL). The resulting mixture was filtered through Celite pad to remove in soluble precipitates. The resulting mixture was concentrated by evaporation. The crude product was purified by silica gel chromatography (elunent: $CHCl_3$), recrystallized from methanol, and dried under vacuum to afford **CA3** as a white solid (yield = 9.8 g, 89.3%). ^{1}H NMR (500 MHz, $CDCl_3$): δ 8.06 (dd, J = 8.0Hz, 1.0Hz, 1H), 7.95 (s, 1H), 7.83 (s, 1H), 7.42−7.37 (m, 2H), 7.34 (d, J = 8.5Hz, 1H), 7.23−7.20 (m, 2H), 2.74−2.66 (m, 2H), 1.69−1.63 (m, 1H), 1.38−1.25 (m, 8H), 0.92−0.87 (m, 6H). MS (MALDI): m/z 279.94 $[M]^+$; calcd 279.42.

4,4'-bis(3-Ethylhexyl-9H-carbazole-9-yl)methanone (**CA2**).[14)] A mixture of 4,4'-dibromobenzophenone (1.71 g, 5.00 mmol), **CA3** (3.07 g, 11.0 mmol), potassium carbonate (2.76 g, 20.0 mmol), and bis(tri-tert-butylphosphine)palladium(0) (0.31 g, 0.60 mmol) in dry

toluene (50 mL) was stirred for 24 h at 100 ºC. After cooling to room-temperature, the reaction mixture was poured into water and extracted with toluene. The combined organic layers were washed with water, and dried over anhydrous $MgSO_4$. The resulting solution was filtered through a Celite pad and followed by an aluminium oxide pad to remove insoluble materials. After the filtration, crude product was purified by column chromatography on silica gel (eluent: chloroform) and dried under vacuum to give a pale yellow powder (yield = 3.09 g, 83.9%). ^{1}H NMR (500 MHz, DMSO): δ 8.31 (s, 2H), 8.27 (d, J = 8.0Hz, 2H), 8.17 (d, J = 9.0Hz, 3H), 8.61 (s, 2H), 7.91 (d, J = 8.5Hz, 3H), 7.59 (d, J = 8.5Hz, 2H), 7.52 (d, J = 8.5Hz, 2H), 7.47 (t, J = 8.5Hz, 2H), 7.34−7.29 (m, 4H), 2.71 (d, J = 7.0Hz, 4H), 1.69−1.66 (m, 2H), 1.35−1.26 (m, 16H), 0.91−0.84 (m, 12H). MS (MALDI): m/z 737.99 $[M]^+$; calcd 737.02.

4,4'-bis(3-bromo-6-Ethylhexyl-9H-carbazole-9-yl)methanone (**CA1**). To a stirred solution of 3 (1.11 g, 1.50 mmol) in THF (50 mL) was added *N*-bromosuccinimide (0.53 g, 3.00 mmol) slowly at 0 ºC. The mixture was stirred for 20 h at room-temperature. The reaction mixture was poured into water, and then extracted with ethyl acetate. The combined organic layers were washed with water, and dried over anhydrous $MgSO_4$. After the filtration and evaporation, the crude product was recrystallized from $CHCl_3$ and methanol. The product was dried under vacuum to afford compound **CA1** as a pale yellow solid (yield = 1.22 g, 91.2%). ^{1}H NMR (500 MHz, $CDCl_3$): δ 8.25 (s, 2H), 8.16 (d, J = 8.5Hz, 4H), 7.86 (s, 2H), 7.76 (d, J = 8.5Hz, 4H), 7.51 (dd, J = 8.5Hz, 2.0Hz, 2H), 7.45 (d, J = 8.5Hz, 2H), 7.41 (d, J = 9.0Hz, 2H), 7.27 (dd, J = 8.5Hz, 1.5Hz, 2H), 2.77−2.69 (m, 4H), 1.68−1.65 (m, 2H), 1.38−1.31 (m, 16H), 0.93−0.88 (m, 12H). MS (MALDI): m/z 894.97 $[M]^+$; calcd 894.84.

9-Phenyl-3,6-bis(4,4,5,5-tetramethyl-1,3,2-dioxaborolan-2-yl)-9H-carbazole (**CB1**). To a stirred solution of 3,6-dibromo-9-phenylcarbazole (4.01 g, 0.01 mol) in dry THF (100 mL) was added dropwise *n*-butyllithium (1.6 M in hexane, 12.5 mL) at −78 ºC, and mixture was allowed to react for 1 h at that temperature. 2-Isopropoxy-4,4,5,5-tetramethyl-1,3,2-dioxaborolane (6.1 mL) was then added, and the mixture was stirred overnight at room-temperature. The reaction mixture was poured in to water and extracted with ethyl acetate. The combined organic layer were washed with water, and dried over $MgSO_4$. After the filtration and evaporation, the product was purified by silica gel column chromatography (eluent: hexane/ethyl acetate = 3:1, v/v), and dried under vacuum to afford **CB1** as a white solid (yield = 4.39 g, 88.7%). ^{1}H NMR (500 MHz, $CDCl_3$): δ 8.71 (s, 2H), 7.84 (dd, J = 8.0Hz, 1.0Hz, 2H), 7.72 (t, J = 8.0Hz, 2H),

7.54 (dd, J = 8.5Hz, 1.0Hz, 2H), 7.49 (t, J = 7.5Hz, 1H), 7.36 (d, J = 8.0Hz, 2H), 1.39 (s, 24H). MS (MALDI): m/z 495.81 $[M]^+$; calcd 495.23.

pCCBP (1).[25] A mixture of **CA1** (0.89 g, 1.00 mmol), **CB1** (0.50 g, 1.00 mmol), dry toluene (50 mL), aqueous potassium carbonate (2 M, 7 mL), Aliquat® 336 (0.1 mL), tertrakis(triphenylphosphine)palladium(0) (0.07 g, 0.06 mmol) was refluxed for 72 h, 9-Phenyl-9H-carbazol-3-ylboronic acid (0.03 g, 0.10 mmol, commercially available) was added to cap the bromo end groups. After refluxing for another 24 h, the reaction mixture was poured in to water and extracted with CH_2Cl_2. The combined organic layer were washed with water, and dried over $MgSO_4$. After the filtration and evaporation, the product was recrystallized from $CHCl_3$/methanol and dried under vacuum to give **1** green solid (1.1 g). This compound was further purified by gel permeation chromatography. ^{1}H NMR (500 MHz, $CDCl_3$): δ 8.57 (br, 2H), 8.48 (br, 2H), 8.17 (br, 4H), 8.02 (br, 2H), 7.81 (br, 8H), 7.66 (br, 6H), 7.50 (br, 7H), 2.74 (br, 4H), 1.68 (br, 2H), 1.31-1.28 (m, 16H), 0.91-0.87 (m, 12H). ^{13}C{^{1}H} NMR (125 MHz, $CDCl_3$): δ 194.94, 146.03, 141.20, 139.71, 139.53, 138.27, 136.42, 134.56, 134.29, 133.66, 132.61, 132.10, 131.45, 131.20, 130.92, 130.67, 130.39, 130.13, 128.69, 128.42, 128.33, 127.09, 126.56, 126.13, 124.76, 124.64, 123.85, 123.78, 114.99, 114.45, 41.13, 39.50, 36.30, 36.16, 32.27, 31.84, 31.44, 31.12, 31.05, 30.91, 28.84, 25.43, 23.09, 14.16, 10.84, 10.81. Anal. calcd (%) for Br-$(C_{71}H_{65}N_3O)_5$-$(C_{53}H_{54}N_2O)$-Br: C, 84.84; H, 6.61; N, 4.12; found: C, 85.13; H, 6.72; N, 3.99.

3-Ethylhexanoyl-9,10-dihydro-9,9-dimethylacridine (**AA4**). **AA4** was synthesized similarly to **CA4**, using 9,10-dihydro-9,9-dimethyl acridine (10.5 g, 0.05 mol), aluminum trichloride (6.67 g, 0.05 mol), and ethyl hexanoyl chloride (9.5 mL). The product was obtained as a pale yellow powder (yield = 10.9 g, 65.1%). ^{1}H NMR (500 MHz, $CDCl_3$): δ 8.09 (s, 1H), 7.76 (dd, J = 8.5Hz, 2.0Hz, 1H), 7.40 (d, J = 7.5Hz, 1H), 7.13 (t, J = 7.5Hz, 1H), 6.98 (t, J = 8.0Hz, 1H), 6.73−6.69 (m, 2H), 6.46 (s, 1H), 3.33−3.28 (m, 1H), 1.81-1.74 (m, 2H), 1.63 (s, 6H), 1.58−1.46 (m, 2H), 1.32-1.21 (m, 4H), 0.89−0.84 (m, 6H). MS (MALDI): m/z 336.15 $[M]^+$; calcd 335.48.

3-Ethylhexyl-9,10-dihydro-9,9-dimethylacridine (**AA3**). **AA3** was synthesized similarly to **CA3**, using **AA4** (10.1 g, 0.03 mol), lithium aluminium hydride (2.26 g, 0.06 mol), and aluminum trichloride (4.00 g, 0.03 mol). The product was obtained as pale yellow solid (yield = 7.27 g, 75.4%). ^{1}H NMR (500 MHz, $CDCl_3$): δ 7.45 (d, J = 6.5Hz, 1H), 7.38 (s, 1H),

7.13−7.04 (m, 2H), 6.80 (d, *J* = 7.0Hz, 1H), 6.69 (d, *J* = 7.5Hz, 1H), 6.60 (d, *J* = 7.5Hz, 1H), 6.10 (s, 1H), 3.16−3.11 (m, 2H), 1.64 (s, 6H), 1.52−1.51 (m, 1H), 1.31−1.26 (m, 8H), 0.89−0.84 (m, 6H). MS (MALDI): m/z 322.05 $[M]^+$; calcd 321.50.

4,4'-bis(3-Ethylhexyl-9,10-dihydro-9,9-dimethylacridine-10-yl)methanone (**AA2**). **AA2** was synthesized similarly to **CA2**, using 4,4'-dibromobenzophenone (1.71 g, 5.00 mmol), **AA3** (3.54 g, 11.0 mmol), potassium carbonate (2.76 g, 20.0 mmol), and bis(tri-tert-butylphosphine)palladium(0) (0.31 g, 0.60 mmol). The product was obtained as a yellow powder (yield = 3.50 g, 85.2%). ^{1}H NMR (500 MHz, $CDCl_3$): δ 8.14 (dd, *J* = 6.5Hz, 1.5Hz, 4H), 7.53 (d, *J* = 8.0Hz, 4H), 7.48 (dd, *J* = 6.5Hz, 1.5Hz, 2H), 7.23 (s, 2H), 7.02 (td, *J* = 7.0Hz, 1.5Hz, 2H), 6.96 (td, *J* = 7.5Hz, 1.5Hz, 2H), 6.79 (dd, *J* = 7.5Hz, 2.0Hz, 2H), 6.39 (dd, *J* = 8.0Hz, 1.5Hz, 2H), 6.30 (d, *J* = 7.5Hz, 2H), 2.49 (d, *J* = 7.0Hz, 4H), 1.69 (s, 12H), 1.53−1.51 (m, 2H), 1.32−1.26 (m, 16H), 0.89−0.86 (m, 12H). MS (MALDI): m/z 822.07 $[M]^+$; calcd 821.18.

4,4'-bis(3-bromo-6-Ethylhexyl-9,10-dihydro-9,9-dimethylacridine-10-yl)methanone (**AA1**). **AA1** was synthesized similarly to **CA1**, using **AA2** (1.23 g, 1.50 mmol) and *N*-bromosuccinimide (0.53 g, 3.00 mmol). The product was obtained as a yellow powder (yield = 1.31 g, 89.5%). ^{1}H NMR (500 MHz, $CDCl_3$): δ 8.15 (d, *J* = 8.5Hz, 4H), 7.55 (s, 2H), 7.51 (d, *J* = 8.5Hz, 4H), 7.21 (s, 2H), 7.09 (dd, *J* = 9.0Hz, 2H), 6.80 (dd, *J* = 8.5Hz, 2.0Hz, 2H), 6.26 (d, *J* = 8.5Hz, 2H), 6.23 (d, *J* = 9.0Hz, 2H), 2.49 (d, *J* = 7.0Hz, 4H), 1.67 (s, 12H), 1.53−1.51 (m, 2H), 1.30−1.25 (m, 16H), 0.88−0.85 (m, 12H). MS (MALDI): m/z 979.98 $[M+H]^+$; calcd 978.98.

10-phenyl-9,9-dimethyl-9,10-dihydroacridine (**AB5**). A mixture of 9,10-dihydro-9,9-dimethyl acridine (2.09 g, 0.01 mol), iodobenzene (3.6 mL, 0.03 mol), potassium carbonate (1.38 g, 0.01 mol), and copper (0.08 g, 1.20 mmol) was refluxed for 48 h. After cooling to room-temperature, the reaction mixture was poured into water and extracted with dichloromethane. The combined organic layers were washed with water, and dried over anhydrous $MgSO_4$. The resulting solution was filtered through a Celite pad and followed by an aluminium oxide pad to remove insoluble materials. After the filtration, crude product was purified by column chromatography on silica gel (eluent: chloroform/hexane) and dried under vacuum to give a white powder (yield = 2.55 g, 89.4%). ^{1}H NMR (500 MHz, $CDCl_3$): δ 7.62

(td, J = 7.5Hz, 2H), 7.51 (t, J = 7.5Hz, 1H), 7.45 (dd, J = 7.5Hz, 1.5Hz, 2H), 7.33 (dd, J = 8.5Hz, 1.0Hz, 2H), 6.98−6.90 (m, 4H), 6.26 (dd, J = 8.0Hz, 1.0Hz, 2H), 1.69 (s, 6H). MS (MALDI): m/z 285.89 $[M]^+$; calcd 285.39.

3,7-dibromo-10-phenyl-9,9-dimethyl-9,10-dihydroacridine (**AB3**). **AB3** was synthesized similarly to **CA1**, using **AB5** (1.43 g, 5.00 mmol) and *N*-bromosuccinimide (1.78 g, 10.0 mmol). The product was obtained as a white powder (yield = 1.97 g, 88.9%). ^{1}H NMR (500 MHz, $CDCl_3$): δ 7.63 (t, J = 7.5Hz, 2H), 7.53 (t, J = 9.0Hz, 1H), 7.50 (s, 2H), 7.28 (dd, J = 8.5Hz, 1.0Hz, 2H), 7.05 (dd, J = 8.5Hz, 2.0Hz, 2H), 6.12 (d, J = 8.5Hz, 2H), 1.64 (s, 6H). MS (MALDI): m/z 443.02 $[M]^+$; calcd 443.17.

10-Phenyl-3,7-bis(4,4,5,5-tetramethyl-1,3,2-dioxaborolan-2-yl)-9,9-dimethyl-9,10-dihydroacridine (**AB1**). **AB1** was synthesized similarly to **CB1**, using **AB3** (1.77 g, 4.00 mmol), *n*-butyllithium (1.60 M in hexane, 5.5 mL), and 2-isopropoxy-4,4,5,5-tetramethyl-1,3,2-dioxaborolane (2.5 mL). The product was obtained as white powder (yield = 1.89 g, 87.9%). ^{1}H NMR (500 MHz, $CDCl_3$): δ 7.89 (s, 2H), 7.62 (t, J = 7.5Hz, 2H), 7.52 (t, J = 7.5Hz, 1H), 7.40 (dd, J = 8.0Hz, 1.5Hz, 2H), 7.28 (dd, J = 8.5Hz, 1.5Hz, 2H), 6.21 (d, J = 8.0Hz, 2H), 1.75 (s, 6H), 1.32 (s, 24H). MS (MALDI): m/z 537.41 $[M]^+$; calcd 537.30.

3-bromo-10-phenyl-9,9-dimethyl-9,10-dihydroacridine (**AB4**). **AB4** was synthesized similarly to **CA1**, using **AB5** (0.57 g, 2.00 mmol) and *N*-bromosuccinimide (0.36 g, 2.00 mmol). The product was obtained as a white powder (yield = 0.62 g, 84.5%). ^{1}H NMR (500 MHz, $CDCl_3$): δ 7.63 (t, J = 7.5Hz, 2H), 7.53−7.50 (m, 2H), 7.44 (dd, J = 8.5Hz, 1.0Hz, 1H), 7.30 (dd, J = 8.5Hz, 1.0Hz, 2H), 7.03 (dd, J = 9.0Hz, 2.0Hz, 1H), 6.99−6.92 (m, 2H), 6.25 (dd, J = 8.0Hz, 1.5Hz, 1H), 6.13 (d, J = 9.0Hz, 1H), 1.67 (s, 6H). MS (MALDI): m/z 364.99 $[M]^+$; calcd 364.28.

10-Phenyl-3-(4,4,5,5-tetramethyl-1,3,2-dioxaborolan-2-yl)-9,9-dimethyl-9,10-dihydroacridine (**AB2**). **AB2** was synthesized similarly to **CB1**, using **AB4** (0.55 g, 1.5 mmol), *n*-butyllithium (1.60 M in hexane, 0.9 mL), and 2-isopropoxy-4,4,5,5-tetramethyl-1,3,2-dioxaborolane (0.4 mL). The product was obtained as white powder (yield = 0.55 g, 89.4%). ^{1}H NMR (500 MHz, $CDCl_3$): δ 7.88 (s, 1H), 7.62 (t, J = 7.5Hz, 2H), 7.51 (t, J = 7.5Hz, 1H), 7.46 (dd, J = 7.5Hz, 2.0Hz, 2H), 7.41 (dd, J = 8.0Hz, 1.5Hz, 1H), 7.31 (dd, J = 8.0Hz, 1.0Hz,

2H), 6.98−6.90 (m, 2H), 6.23 (dd, J = 8.5Hz, 1.5Hz, 2H), 1.72 (s, 6H), 1.32 (s, 12H). MS (MALDI): m/z 412.25 $[M]^+$; calcd 411.34.

pAcBP (2). **2** was synthesized similarly to **1**, using **AA1** (0.98 g, 1.00 mmol), **AB1** (0.54 g, 1.00 mmol), dry toluene (50 mL), aqueous potassium carbonate (2 M, 7 mL), Aliquat® 336 (0.1 mL), tertrakis(triphenylphosphine)palladium(0) (0.07 g, 0.06 mmol), and AB2 (0.04 g, 0.10 mmol). The product was obtained as yellow powder (1.2 g). This compound was further purified by gel permeation chromatography. ^{1}H NMR (500 MHz, $CDCl_3$): δ 8.58 (br, 2H), 8.48 (br, 2H), 8.17 (br, 4H), 8.02 (br, 2H), 7.81 (br, 8H), 7.65 (br, 6H), 7.50 (br, 7H), 2.74 (br, 4H), 1.68 (br, 2H), 1.32 (br, 16H), 0.87 (m, 12H), ^{13}C{^{1}H} NMR (125 MHz, $CDCl_3$): δ 142.21, 140.57, 139.50, 139.11, 134.90, 134.49, 134.27, 132.16, 131.89, 129.99, 128.79, 128.54, 127.85, 127.33, 127.00, 126.40, 126.09, 125.97, 125.90, 124.61, 124.24, 124.15, 120.75, 118.97, 110.20, 110.07, 109.52, 41.69, 40.22, 32.39, 30.91, 28.93, 25.46, 23.10, 14.18, 10.88, 1.02. Anal. calcd (%) for Br-($C_{80}H_{83}N_3O$)$_6$-($C_{59}H_{66}N_2O$)-Br: C, 85.25; H, 7.49; N, 3.69; found: C, 85.24; H, 7.60; N, 3.51.

5.5. References

[1] H. B. Wu, G. J. Zhou, J. H. Zou, C. L. Ho, W. Y. Wang, W. Yang, J. B. Peng, and Y. Cao, *Adv. Mater*., **2009**, 21, 4181.

[2] L. Duan, L. Hou, T. -W. Lee, J. Qiao, D. Zhang, G. Dong, L. Wang, and Y. Qiu, *J. Mater. Chem*., **2010**, 20, 6392.

[3] K. S. Yook, S. E. Jang, S. O. Jeon, and J. Y. Lee, *Adv. Mater.*, **2010,** 22, 4479.

[4] G. Gustafsson, Y. Cao, G. M Treacy, F. Klavetter, N. Colaneri, and A. J. Heeger, *Nature*, **1992**, 357, 477.

[5] P. K. H. Ho, J. -S. Kim, J. H. Burroughes, H. Becker, S. F. Y. Li, T. M. Brown, F. Cacialli, and R. H. Friend, *Nature*, **2000**, 404, 481.

[6] V. Cleave, G. Yahioglu, P. L. Barny, D. H. Hwang, A. B. Holmes, R. H. Friend, and N. Tessler, *Adv. Mater*., **2001**, 13, 44.

[7] T. -F. Guo, S.-C. Chang, Y. Yang, R.C. Kwong, and M. E. Thompson, *Org. Electron*., **2000**, 1, 15.

[8] Q. Zhang, B. Li, S. Huang, H. Nomura, H. Tanaka, and C. Adachi, *Nat. Photon.*, **2014**, 8, 326.

[9] A. Endo, M. Ogasawara, A. Takahashi, D. Yokoyama, Y. Kato, and C. Adachi, *Adv. Mater*., **2009**, 21, 4802.

[10] S. Y. Lee, T. Yasuda, H. Nomura, and C. Adachi, *Appl. Phys. Lett*., **2012**, 101, 093306.

[11] H. Uoyama, K. Goushi, K. Shizu, H. Nomura, and C. Adachi, *Nature*, **2012**, 492, 234.

[12] Q. Zhang, J. Li, K. Shizu, S Huang, S. Hirata, H. Miyazaki, and C. Adachi, *J. Am. Chem. Soc.*, **2012**, 134, 14706.

[13] T. Nakagawa, S. -Y. Ku, K.-T. Wong, and C. Adachi, *Chem. Comm*., **2012**, 48, 9580.

[14] S. Y. Lee, T. Yasuda, Y. S. Yang, Q. Zhang, and C. Adachi, *Angew. Chem. Int. Ed*., **2014**, 126, 6520.

[15] A. Endo, K. Sato, K. Yoshimura, T. Kai, A. Kawasa, H. Miyazaki, and C. Adachi, *Appl. Phys. Lett*., **2011**, 98, 083302.

[16] B.Valeur, *Molecular Fluorescence : Principle and Applications*, **2001**, Wiley-VHC.

[17] P. R. Christensen, J. K. Nagle, A. Bhatti, and M. O. Wolf, *J. Am. Chem. Soc*., **2013**, 135, 8109.

[18] M. Shaiki, J. Mohanty, P. K. Singh, A. C. Bhaikuttan, R. N. Rajule, V. S. Satam, S. R. Bendre, V. R. Kanetkar, and H. Pal, *J. Phys. Chem. A*, **2010**, 114, 4507.

[19] Y. Zhang and S. R. Forrest, *Phys. Rev. Lett.*, **2012**, 108, 267404.

[20] C. Murawski, K. Leo, and M. C. Gather, *Adv. Mater*., **2013**, 25, 6801.

[21] Q. Fu, J. Chen, C. Shi, and D. Ma, *Appl. Mater. Interface*, **2012**, 4, 6579.

[22] S.-J. Su, T. Chiba, T. Takeda, and J. Kido, *Adv. Mater*., **2008**, 20, 2125.

[23] M. J. Frisch, G. W. Trucks, H. B. Schlegel, G. E. Scuseria, M. A. Robb, J. R. Cheeseman, J. A. Montgomery, Jr., T. Vreven, K. N. Kudin, J. C. Burant, J. M. Millam, S. S. Iyengar, J. Tomasi, V. Barone, B. Mennucci, M. Cossi, G. Scalmani, N. Rega, G. A. Petersson, H. Nakatsuji, M. Hada, M. Ehara, K. Toyota, R. Fukuda, J. Hasegawa, M. Ishida, T. Nakajima, Y. Honda, O. Kitao, H. Nakai, M. Klene, X. Li, J. E. Knox, H. P. Hratchian, J. B. Cross, C. Adamo, J. Jaramillo, R. Gomperts, R. E. Stratmann, O. Yazyev, A. J. Austin, R. Cammi, C. Pomelli, J. W. Ochterski, P. Y. Ayala, K. Morokuma, G. A. Voth, P. Salvador, J. J. Dannenberg, V. G. Zakrzewski, S. Dapprich, A. D. Daniels, M. C. Strain, O. Farkas, D. K. Malick, A. D. Rabuck, K. Raghavachari, J. B. Foresman, J. V. Ortiz, Q. Cui, A. G. Baboul, S. Clifford, J. Cioslowski, B. B. Stefanov, G. Liu, A. Liashenko, P. Piskorz, I. Komaromi, R. L. Martin, D. J. Fox, T. Keith, M. A. Al-Laham,

C. Y. Peng, A. Nanayakkara, M. Challacombe, P. M. W. Gill, B. Johnson, W. Chen, M. W. Wong, C. Gonzalez, and J. A. Pople, Gaussian 03, Gaussian, Inc., Pittsburgh PA, **2003**.

[24] T. Yasuda, T. Shimizu, F. Liu, G. Ungar, and T. Kato, *J. Am. Chem. Soc*., **2011**, 133, 13437.

[25] M. Sun, L. Lan, L. Wang, J. Peng, and Y. Cao, *Macromol. Chem. Phys*., **2008**, 209, 2504.

Chapter 6

Highly Effective Blue Organic Light-Emitting Diodes based on Heteroatom-Bridged Thermally Activated Delayed Fluorescence molecules

Chapter 6

Highly Effective Blue Organic Light-Emitting Diodes based on Heteroatom-Bridged Thermally Activated Delayed Fluorescence molecules

Abstract

Heteroatom-bridged TADF molecules having a small ΔE_{ST} and short τ are designed for effective TADF emission. OLEDs using heteroatom-bridged TADF molecules as emitters generate deep blue and sky-blue emission, and achieving extremely high η_{ext} of 20.3% with efficient roll-off in high current density.

6.1 Introduction

For extensive commercial application of OLEDs on display and solid-state lighting source, realization of highly effective and stable deep-blue OLEDs is the most important key. However, deep-blue OLEDs suffer from color impurity, low efficiency, and short device lifetime. For instance, Cu and Ir complex based phosphorescence OLEDs are most widely studied for blue emission.[1] However, pure deep blue emission with high η_{ext} is still difficult to solve because a decrease of the emission quantum yield in wide E_g molecules and strong roll-off in high current density originated from long τ.

In the previous chapter 3, we reported highly effective deep-blue emissive TADF-OLEDs based on benzophenone derivative of **Cz2BP** (CIE coordinates of x: 0.16, y: 0.14).[2] However, the large ΔE_{ST} of **Cz2BP** led to long τ and strong roll-off at high current density. Also Φ_{PL} of **Cz2BP** was not enough high (55%) and should be improved for higher η_{ext}.

Our group previously reported highly effective fluorescence OLEDs with a series of heteroatom-annulated dithieno[3,2,-b:2,'3,3'-d]metalloles.[3] Extended π-conjugation

molecular structure contributes to highly effective fluorescence emission and an effective σ*-π* hyperconjugation between the σ* orbital of the heteroatom and π* orbital of the core units control the LUMO energy levels depending on the different kinds of bridged heteroatoms.[4,5] Further, horizontally orientated planar heteroatom-annulated dithieno[3,2,-b:2,'3,3'-d]metalloles improved η_{out} and exceeded the theoretical limitation η_{ext} of conventional fluorescent OLEDs.[6]

In this study, we designed heteroatom-bridged TADF molecules based on D-A configuration using dimethylacridane donor and heteroatom-bridged acceptor (Fig. 6-1). To control the E_g and tune emissive color, germanium (**AXGe**, **1**), silicon (**AXSi**, **2**), phosphours (**AXPO**, **3**), and sulfur (**AXSO**, **4**) atoms are incorporated as the bridged center. Here, planar donor and acceptor units are directly connected to offer the highly distorted molecular structure, realizing a small ΔE_{ST} for effective TADF emission.[7] We expect proper D-A combination of designed molecules afford a wide E_g for deep-blue emission and a small ΔE_{ST}, providing improvement of efficient roll-off by reducing τ.

Figure 6-1. Molecular structures of heteroatom-bridged molecules **1**−**4**.

6.2 Results and Discussion

6.2.1 Characterization of Geometric and Electronic Structures of Heteroatom-Bridged Molecules using TD-DFT Calculations

To confirmed the geometric and electronic structures of **1**−**4**, quantum chemical calculation was performed using TD-DFT/B3LYP/6-31(d,p) method. As described in Fig. 6-2, all of the molecules exhibited clear separation of their HOMO and LUMO. The LUMO of **1**−**4** are mainly located on electron-accepting moieties while the HOMO on electron-donating

dimethylacridane moieties. The directly connected planar acceptor and donor units have strong steric hindrance which contributes to large distortion and clear separation between HOMO and LUMO. This complete separation of the frontier orbitals lead to small ΔE_{ST} of 0.02−0.16 eV. Furthermore, depending on bridged heteroatom elements, E_g between HOMO and LUMO are changed. Interestingly, the HOMO energy levels of **1**−**4** were slightly changed while large variation of LUMO energy levels was observed. It should be noted that the different electronic characteristics of the bridged heteroatoms stabilize the LUMO energy levels. Most electron-sufficient germanium-bridged acceptor of **1** among **1**−**4** exhibited the highest LUMO energy level whilst the low-lying LUMO energy level was observed in most electron-deficient sulfur-bridged **4**.

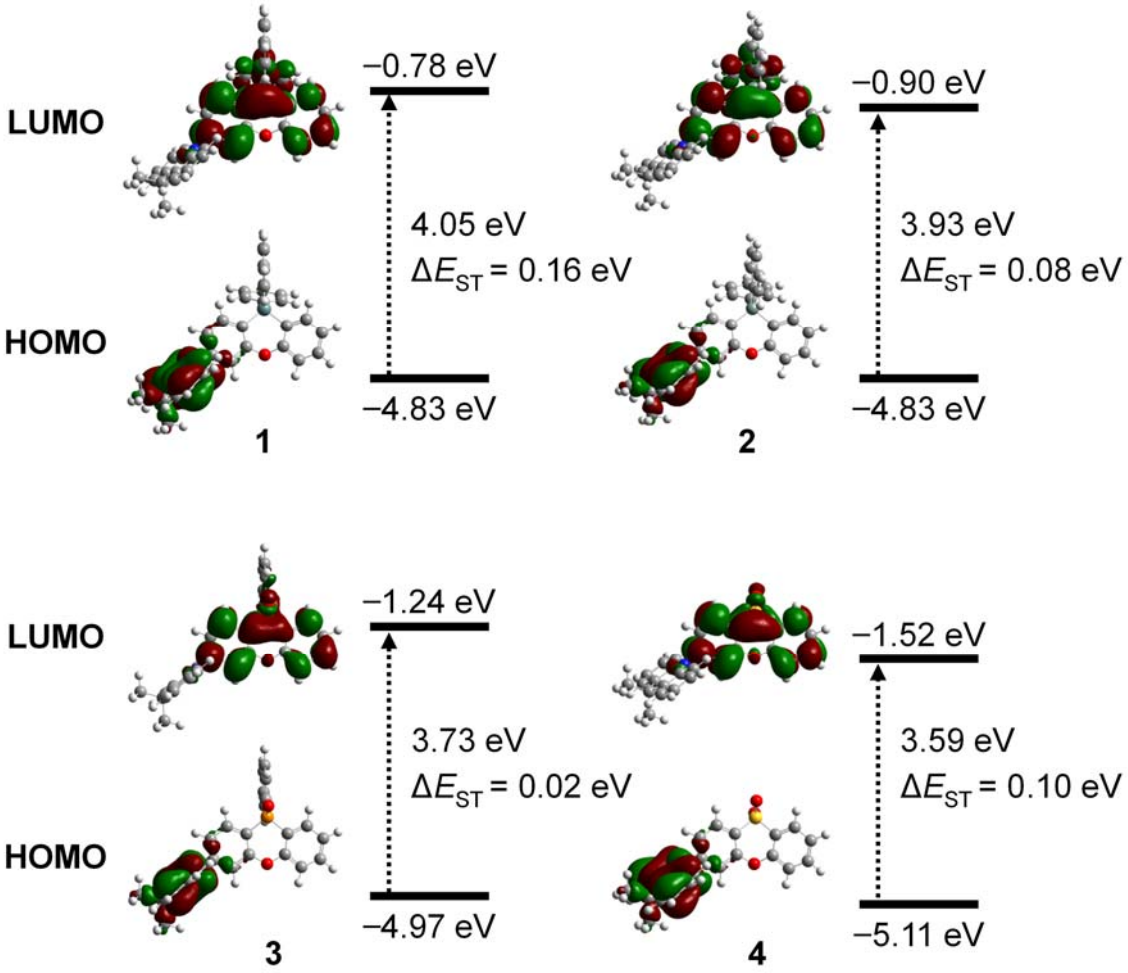

Figure 6-2. Frontier-molecular-orbital distributions, energy levels, and energy gap (ΔE_{ST}) of **1**−**4** characterized by TD-DFT calculations.

6.2.2 Photophysical Properties of Heteroatom-Bridged Molecules

Photophysical properties of **1**−**4** are evaluated in solution. Fig. 6-3 depicts the photograph and absorption and PL spectra of **1**−**4** measured in oxygen free toluene solution. The lowest-energy absorption of **3** and **4** observed at about 350 nm can be originated to the CT absorption. By changing the bridged-heteroatom elements of **1**−**4**, the emission spectra varies from near UV to sky-blue (Fig. 6-3b). Φ_{PL} of 10~50% were obtained for **1**−**4** in oxygen free toluene. In the case of **1** and **2**, Φ_{PL} is independent with the presence of triplet oxygen ($^3O_2$) in aerated solutions (7.8 and 9.3%) whilst Φ_{PL} of **1** and **2** significantly decreased (20 and 21%, Table 6-1).

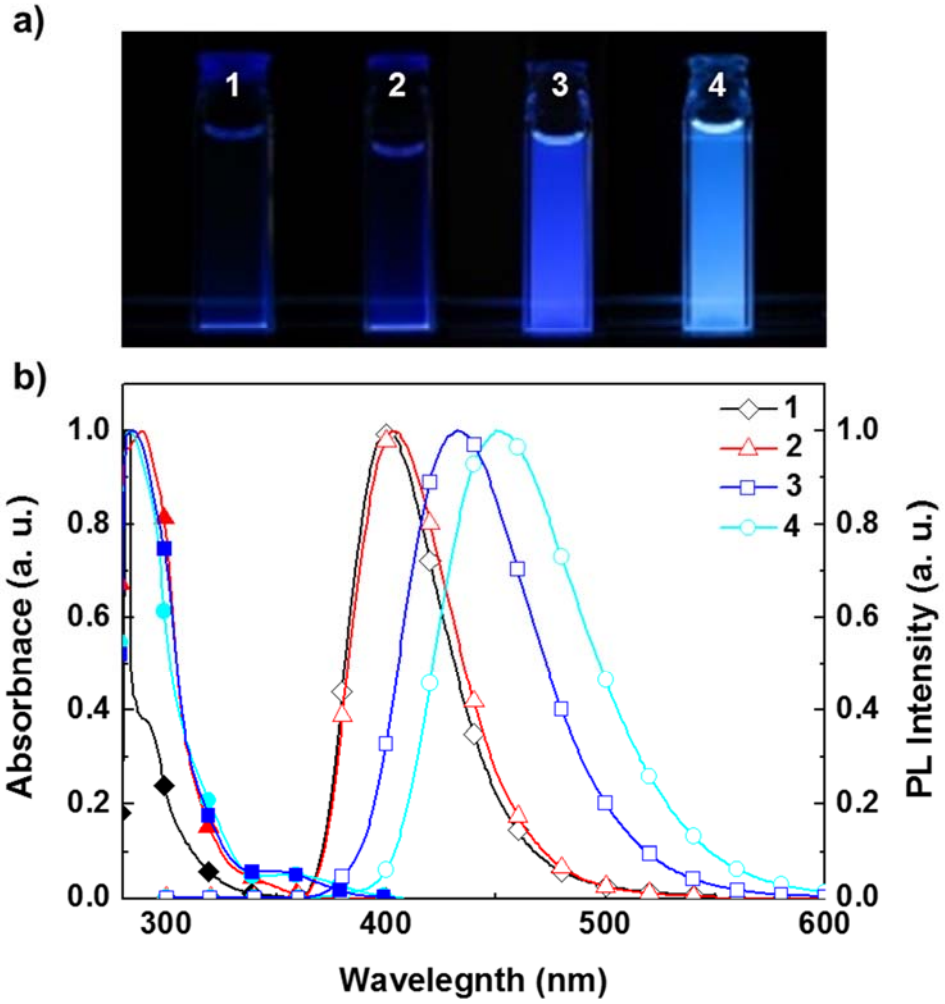

Figure 6-3. a) Images of **1**−**4** in toluene under UV irradiation (365 nm). b) Normalized absorbance (close dot) and PL (open dot) spectra of **1**−**4** in toluene at room-temperature.

Table 6-1. Photophysical properties of benzophenone-based TADF luminophores **1**–**4**

Compound	λ_{abs} (nm) sol[a)]	λ_{PL} (nm) sol[a)]	Φ_{PL} (%)[b)] sol[a)]	HOMO (eV)[c)]	LUMO (eV)[d)]	ΔE_{ST} (eV)[e)]	calc. ΔE_{ST} (eV)[f)]
1	290	385	9.8	−5.82	−1.89	0.03	0.16
2	289	395	13	−5.72	−1.98	0.02	0.08
3	284, 356	432	37	−5.83	−2.64	0.04	0.02
4	282, 349	450	47	−5.74	−2.61	0.06	0.10

a) Measured in oxygen-free toluene solution at room-temperature. b) Absolute Φ_{PL} evaluated using an integrating sphere. c) Determined by photoelectron yield spectroscopy in thin films. d) Deduced from the HOMO and optical E_g. e) $\Delta E_{ST} = E_S - E_T$, Singlet ($E_S$) and triplet ($E_T$) energies estimated from onset wavelengths of the neat film emission spectra at 300 and 5 K in the neat films, respectively, f) Calculated by TD-DFT at B3LYP/6-31G (d,p).

Furthermore, LUMO and HOMO energy levels and experimental ΔE_{ST} determined using the neat films of **1**−**4** (Table 6-1). E_g of **1**−**4** were determined by the onset of the absorption spectra of thin films and the LUMO energy levels were calculated by adding the E_g to measured HOMO energies using photoelectron yield spectroscopy. ΔE_{ST} was decided from the energy difference between S_1 and T_1 which estimated from onset wavelengths of the neat film emission spectra at 300 and 5 K, respectively, in the neat films. All of molecules exhibited a small ΔE_{ST} ~ 0.1 eV. To verify the TADF properties in **1**−**4**, temperature dependence of transient PL intensity and lifetime of neat films were analyzed in the temperature range of 300−5 K using a streak camera. As shown in Fig. 6-4, **3** and **4** exhibit very strong delayed fluorescence and an increase of the delayed PL intensity at high temperature while no delayed fluorescence was observed in **1** and **2**.

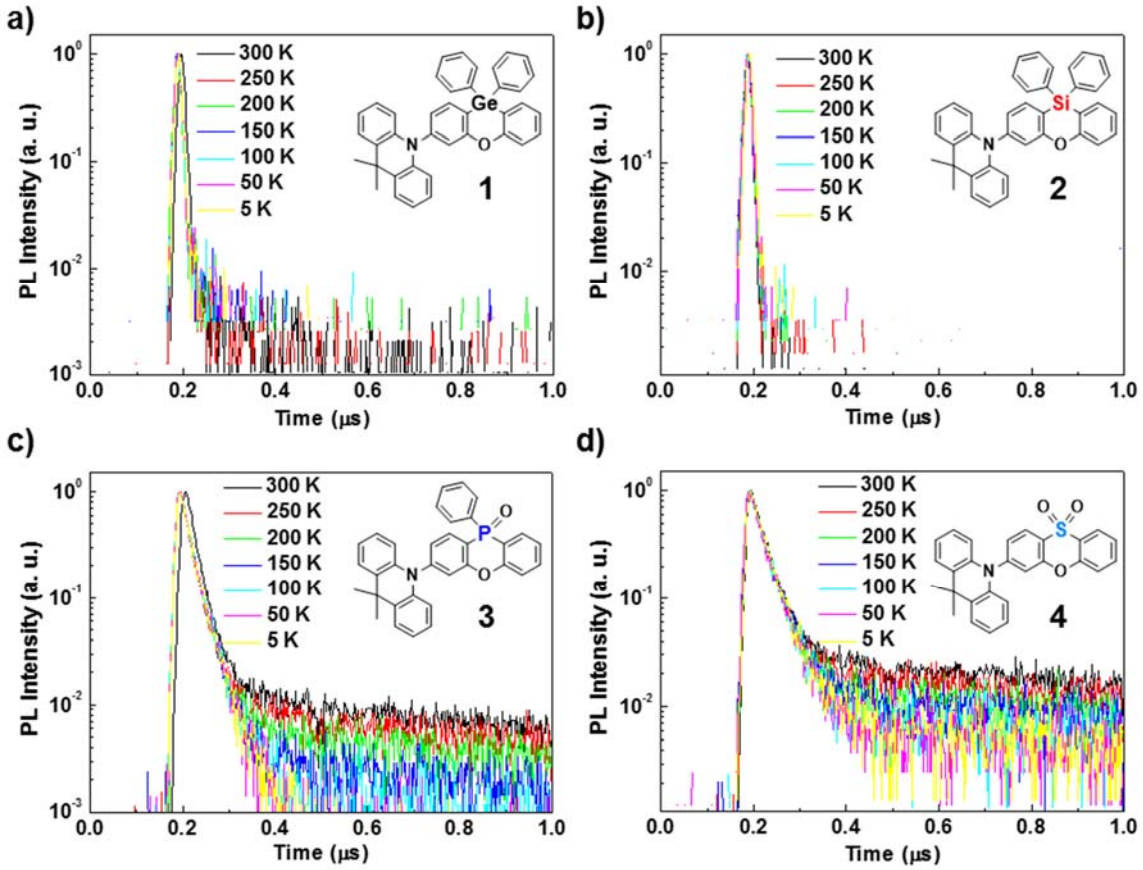

Figure 6-4. Temperature dependence of transient PL decay of **1**−**4** in their neat films.

6.2.3 TADF Properties of Heteroatom based TADF Molecules

From this results, we confirmed the TADF emission of **3** and **4** and apply them to host-guest system for obtaining high efficiency. Because of its high T_1 energy level of **3** (3.08 eV) and **4** (2.97 eV), DPEPO (T_1 = 3.1 eV) was used as a host materials to prevent triplet quenching in host triplet states. PL spectra, luminescence life time and quantum efficiencies in 6 wt%-**3** and **4**: DPEPO co-deposited films are shown in Table 6-2 and Fig. 6-5. The **3** and **4** exhibited deep-blue (434 nm) and sky-blue (457 nm) emissions with very high Φ_{PL} of 62 and 98% and fluorescence with nanosecond-scale prompt component (62 and 65 ns) and microsecond-scale delayed (19 and 12 μs) component at 300 K. An increase of Φ_{PL} increasing with increasing measurement temperature and the same PL spectra of the prompt and delayed components at 300 K confirmed the emissions of **3** and **4** originated from the TADF process (Fig. 6-6).

Table 6-2. PL spectra, luminescence lifetime, and quantum efficiencies of **3** and **4**

Compound	τ_p (ns)	τ_d (μs)	λ_{PL} (nm)	Φ_{PL} (%)	Φ_F (%)	Φ_{TADF} (%)
3	31[a]/62	7.6[a]/19.3[b]	444[a]/434[b]	34[a]/62[b]	26	20
4	84[a]/65	10.2[a]/12.4 [b]	465[a]/458[b]	62[a]/98[b]	30	68

a) Measured in **3** and **4** neat films. b) Measured in 6 wt%-**3** and **4**: DPEPO co-deposited films.

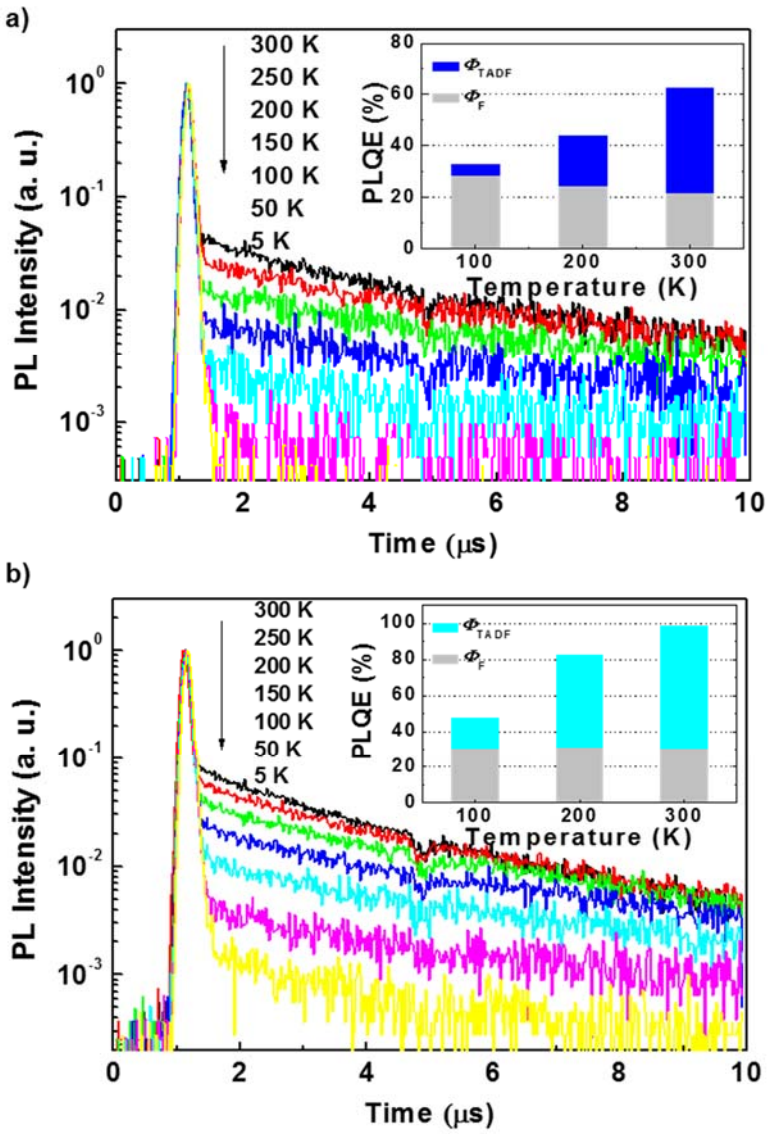

Figure 6-5. Temperature dependence of transient PL decay of 6 wt%-**3** a) and **4** b): DPEPO co-deposited films (inset: fractional contribution of fluorescence and TADF to total Φ_{PL}).

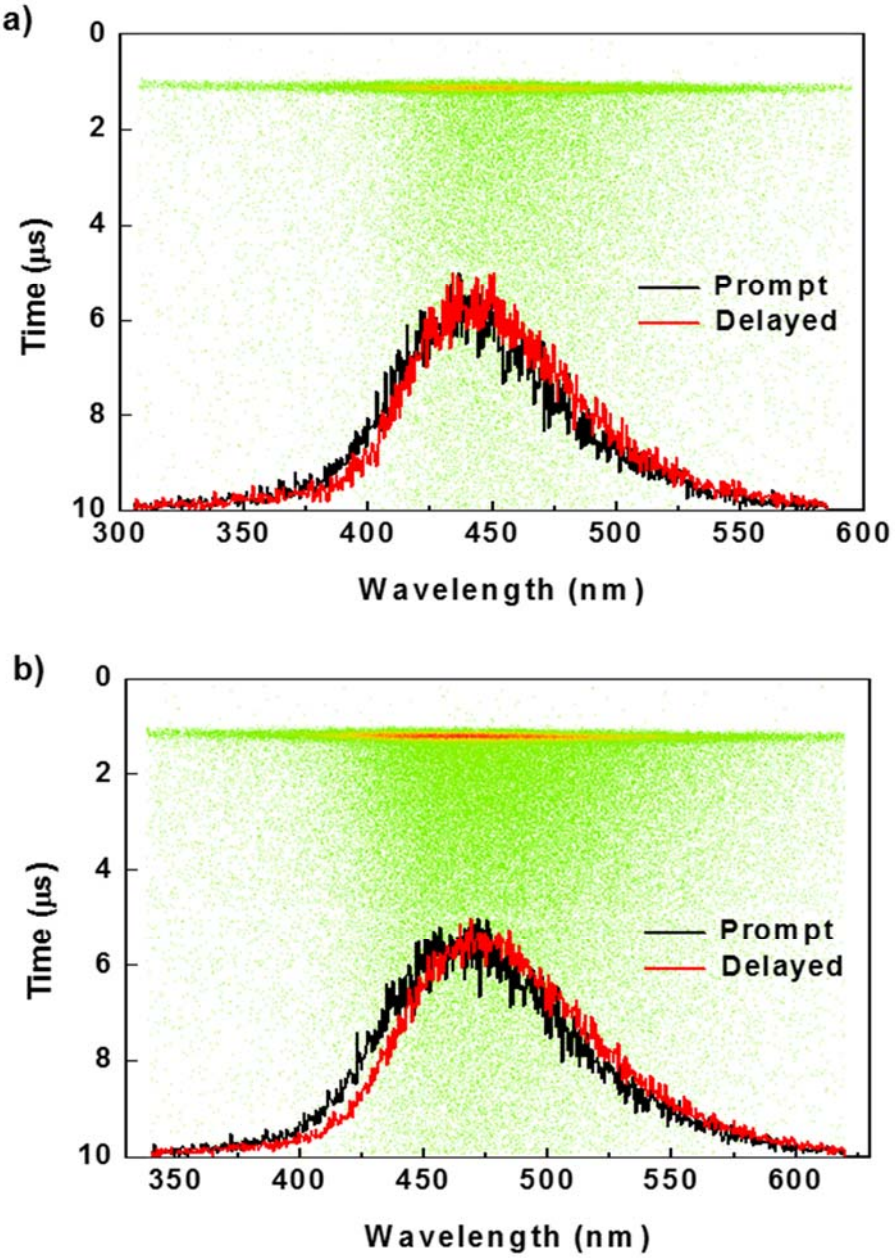

Figure 6-6. Streak image and corresponding time-dependent emission spectra of 6 wt%-**3** a) and **4** b): DPEPO co-deposited films recorded at 300 K. Prompt fluorescence (black) and TADF (red) components are shown. Each dot in the streak image represents a PL photon count.

To investigated details of the PL decay process in co-deposited films of **3** and **4**, decay rate constants and efficiency of each processes were calculated and the results are listed in Table 6-3 and Fig. 6-7.[8] k_r^S, k_{ISC}, and Φ_{ISC} of **3** and **4** (3.5×10^6 and 4.7×10^6 s^{-1}, 1.7×10^7 and 1.1×10^7 s^{-1}, and of 78 and 70%) were almost same with that of the previously reported TADF molecules of **Cz2BP** and **CC2BP** in this thesis (k_r^S and k_{ISC}: 10^5~10^6 s^{-1}). In contrast, k_{nr}^T of **3** and **4** (2.5×10^4 and 1.7×10^3 s^{-1}) were much smaller than that of previously reported TADF molecules (~10^5 s^{-1}). This can be ascribed to that the restriction of intramolecular movement by strong steric hindrance between directly connected donor and acceptor preventing the non-radiative decay processes and decrease (See section 4.2.3). Also, substantially larger k_{RISC} and higher Φ_{RISC} were observed in **3** and **4** (1.2×10^5 and 2.6×10^5 s^{-1} and of 83 and 99%) compared to that of reported TADF molecules (~10^5 s^{-1} and 50~80%) because almost vertically connected donor and acceptor (88 and 90º) contributes to a small energy gap and strong spin orbital coupling (SOC) between S_1 and T_1.[9] The first-order mixing coefficient between S_1 and T_1 (λ) and ΔE_{ST} have reciprocal proportion given by the following equation:[10]

$$\lambda \propto \frac{H_{SO}}{\Delta E_{ST}} \qquad (6\text{-}1)$$

where H_{SO} is spin–orbit interaction. Therefore, the small ΔE_{ST} increases λ and conversion efficiency between S_1 and T_1. These results indicate that our molecular design based on heteroatom-bridged molecules successfully harvest excitons for effective TADF emission.

Table 6-3. Rate constants and quantum efficiencies for decay processes in **3** and **4**[a]

Compound	k_r^S (s^{-1})	k_{ISC} (s^{-1})	k_{RISC} (s^{-1})	k_{nr}^T (s^{-1})	Φ_{ISC} (%)	Φ_{RISC} (%)	Φ_F (%)	Φ_{TADF} (%)
3	3.5×10^6	1.7×10^7	1.2×10^5	2.5×10^4	83	83	26	20
4	4.7×10^6	1.1×10^7	2.6×10^5	1.7×10^3	70	99	30	68

a) Measured in 6 wt%-**3** and **4**: DPEPO co-deposited films.

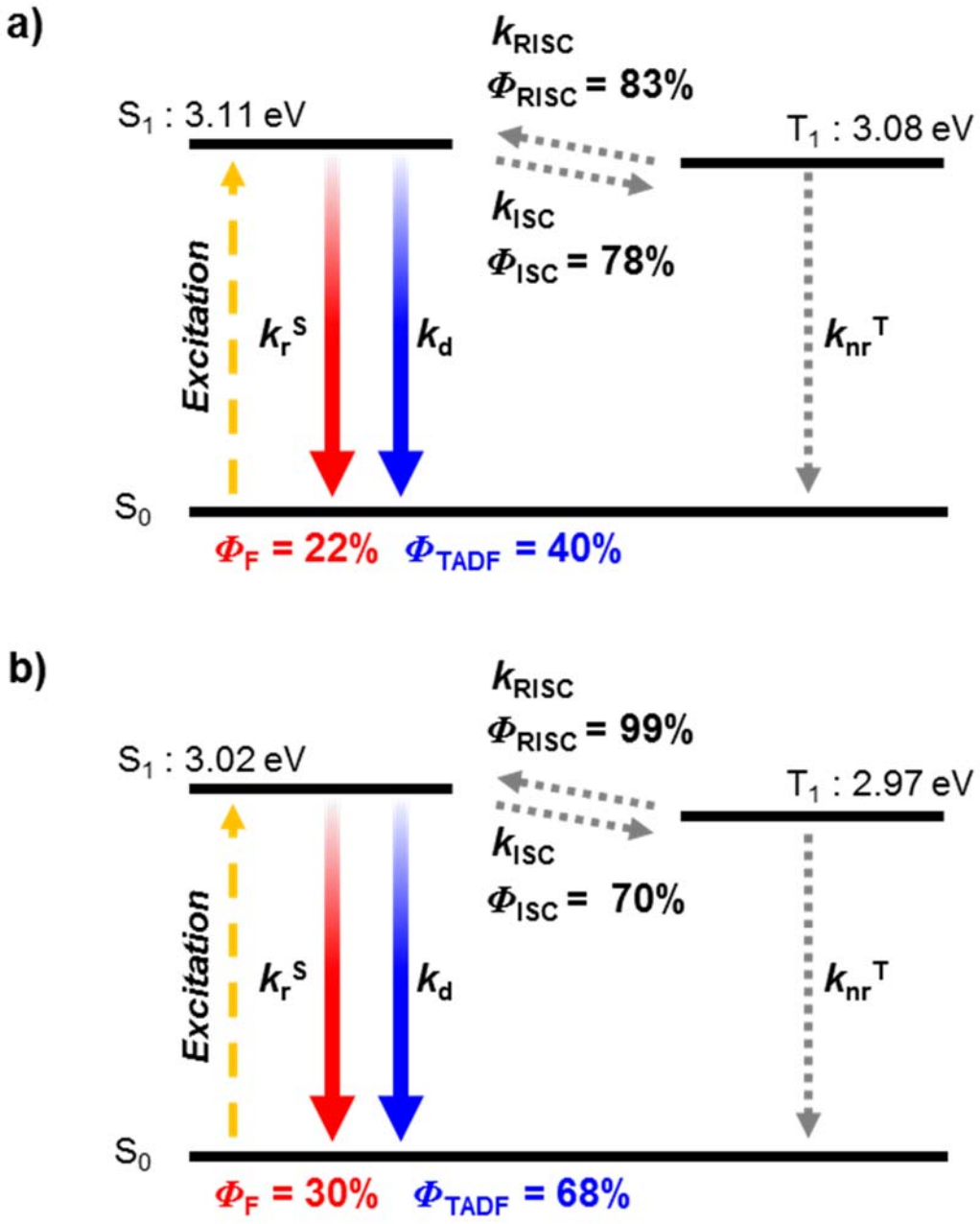

Figure 6-7. Schematic representation of PL decay of 6 wt%-**3** a) and **4** b): DPEPO co-deposited films at room-temperature.

6.2.4 Fabrication and EL Properties of OLEDs

Because of the pure blue emission with high Φ_{PL} of **3** and **4** in the doped films, TADF-OLEDs based on **3** and **4** as an emitter can be possible candidate for expected to realize high efficiency and color purity. The multilayer OLEDs were fabricated with the following device configuration (Fig. 6-7): ITO/ TAPC (35 nm)/ mCBP (5 nm)/ 6 wt%-**3** or **4**: DPEPO (20 nm)/ DPEPO (10 nm)/ bis-1,2-(3,5-di-3-pyridyl-phenyl)benzene (B3PyPB[11], 40 nm)/ LiF (0.8 nm)/ Al (80 nm).

Figure 3-8 presents J–V–L characteristics, η_{ext}–J, and EL spectra of device **A** and **B** based on emitter **3** and **4**. The key characteristics are summarized in Table 6-3. The device **A** achieved high maximum η_{ext} of 11.9% and L_{max} of 1200 cd m^{-2} with deep-blue emission (λ_{EL} = 445 nm). η_c of 15.2 cd A^{-1} and η_p of 7.86 lm W^{-1} were observed (Fig 6-9). CIE coordinate of device **A** was 0.15 and 0.14, corresponding pure blue region (Fig. 6-10).

The device **B** exhibited extremely high η_{ext} of 20.5% which attained the limitation of the theoretical maximum η_{ext} of TADF-OLEDs. This high η_{ext} can be achieved by nearly 100% of Φ_{PL} and η_{ST} of **4**. Also high L_{max}, η_c, and η_p of 1200 cd m^{-2}, 15.2 cd A^{-1}, and 7.86 lm W^{-1} were observed in device **B** (Fig. 6-9). Furthermore, efficient roll-off and high $J_{50\%}$ of 12.6 mA cm^{-2} were observed. It is probable that the short τ of **4** contributes to suppress TTA/STA at high current density. CIE coordinate of device **B** was 0.16 and 0.27 (Fig. 6-10).

Table 6-3. TADF-OLED performance of devices **A** and **B**

	Emitter	λ_{EL} (nm)	V_{on} (V)	L_{max} (cd m^{-2})	η_c (cd A^{-1})	η_p (lm W^{-1})	η_{ext} (%)	CIE (x, y)
Device **A**	**3**	445	6.0	1200	15.2	7.86	11.9	0.15, 0.14
Device **B**	**4**	486	5.1	7771	37.9	20.1	20.5	0.16, 0.27

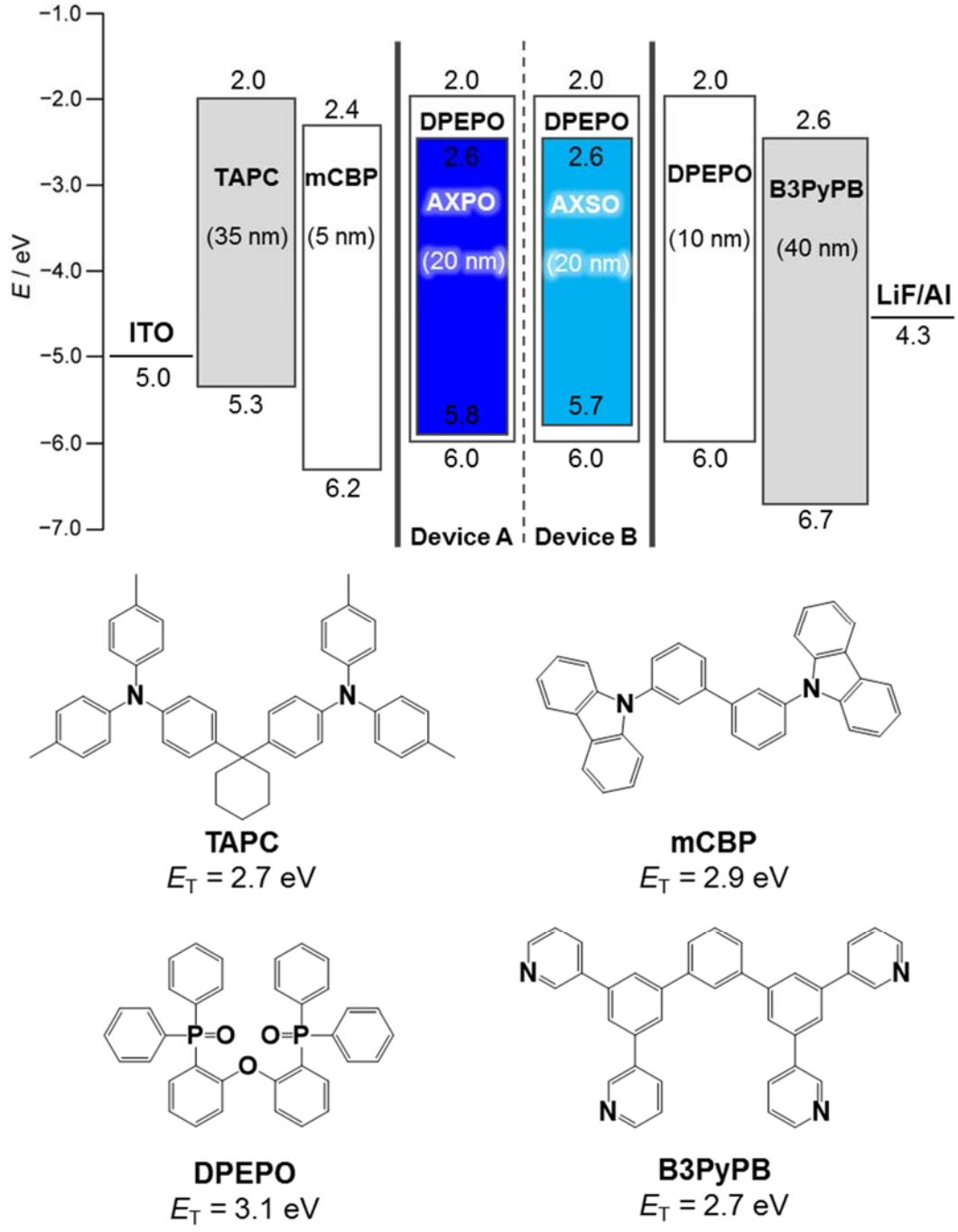

Figure 6-7. Energy level diagram showing the HOMO/LUMO levels of the materials used in devices **A** and **B** and the chemical structures of the materials.

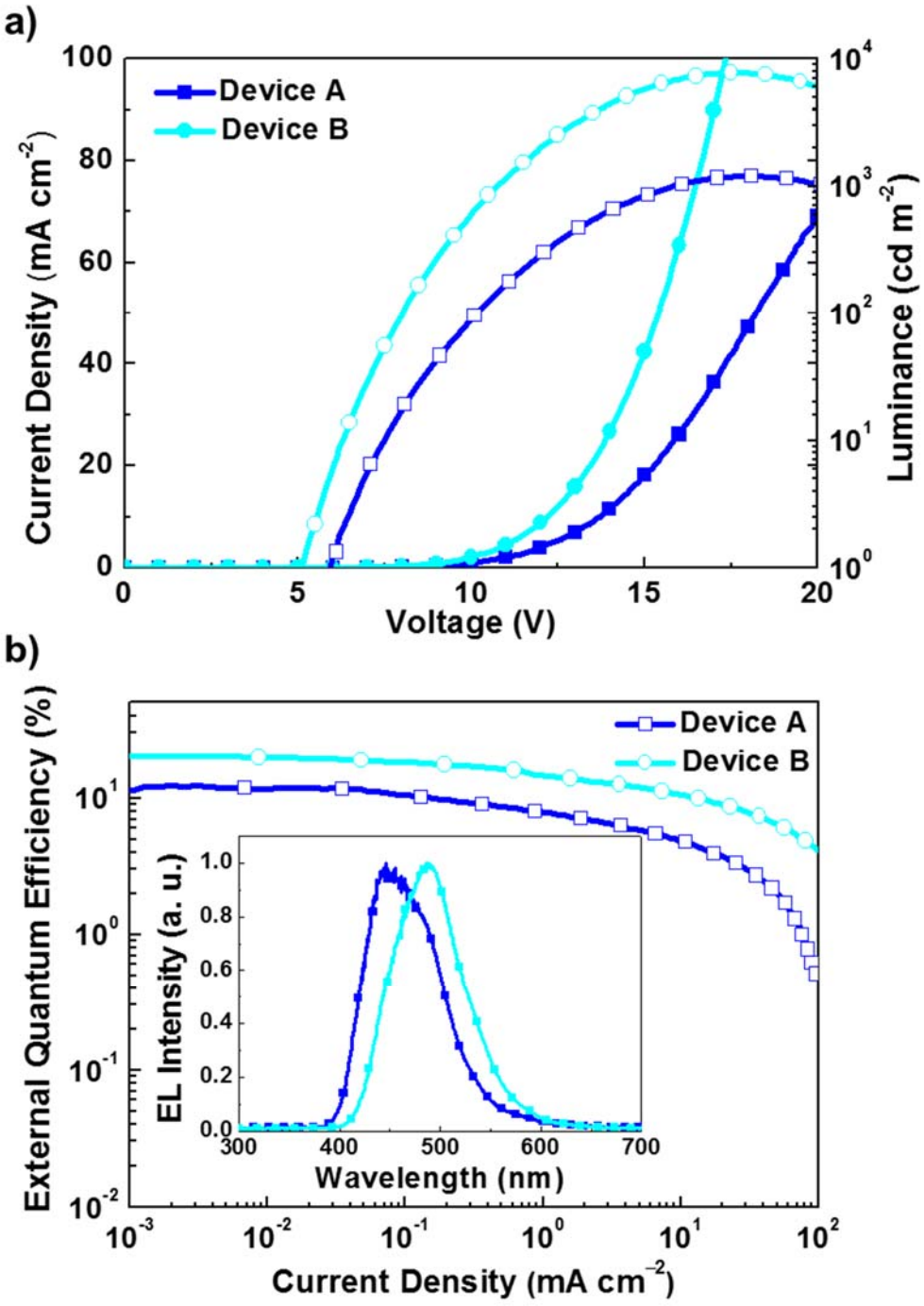

Figure 6-8. a) Current density–voltage–luminance (*J*–*V*–*L*) curves and b) η_{ext}–*J* plots (inset: normalized EL spectra measured at 10 mA cm^{-2}) of the OLEDs **A** and **B** containing the TADF emitters **3** and **4**.

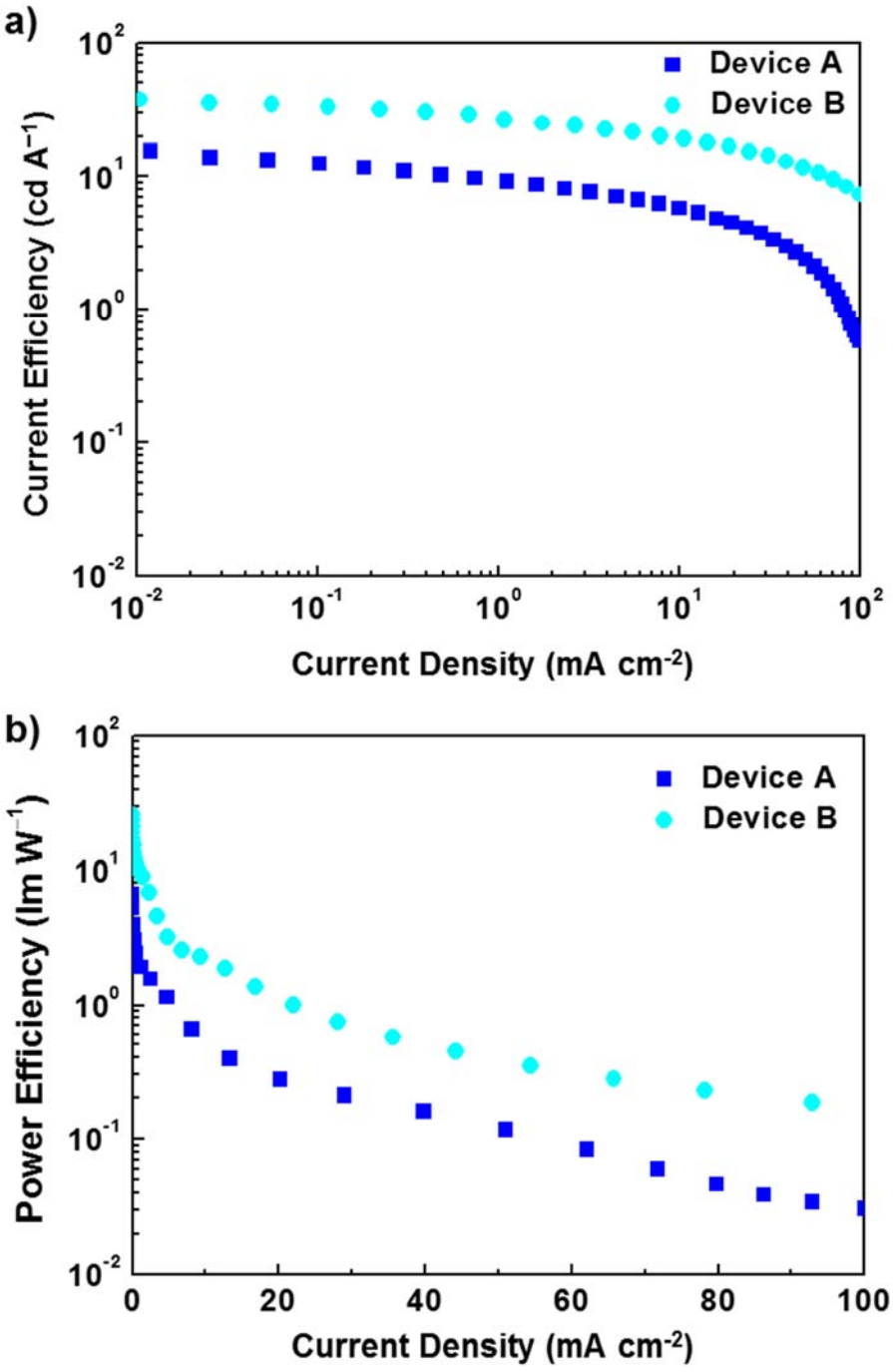

Figure 6-9. a) Current efficiency and b) power efficiency versus *J* plots for devices **A** and **B**.

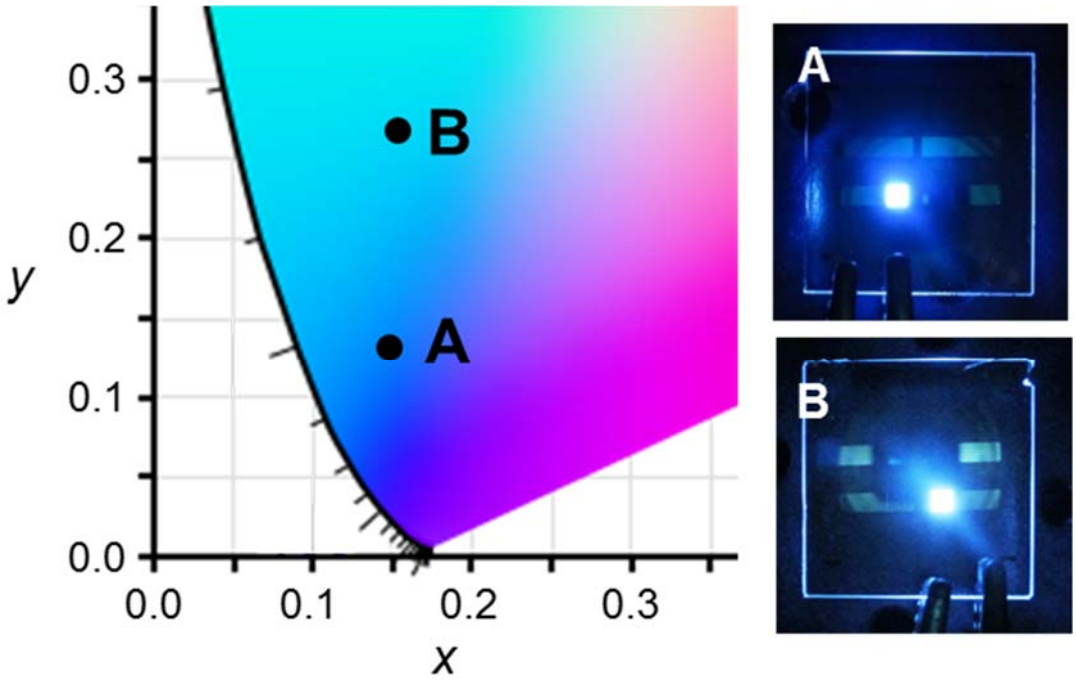

Figure 6-10. EL emission color coordinates in the CIE 1931 chromaticity diagram and photographs of devices **A** and **B**.

6.3 Conclusion

In summary, we developed effective blue OLEDs using newly designed heteroatom-bridged TADF molecules. The phosphours and sulfur bridged molecules of **AXPO** and **AXSO** exhibited relatively small ΔE_{ST} of ~0.06 eV and effective TADF emission with short τ of ~20 μs. The OLEDs employing **AXPO** and **AXSO** as emitters achieved pure deep-blue emission (CIE coordinates of x: 0.15, y: 0.14), 20.5% of η_{ext}, corresponding to the limitation of the theoretical maximum η_{ext} of TADF based OLEDs.

6.4 Experimental Section

6.4.1 General Methods

NMR spectra were recorded on an Avance III 500 spectrometer (Bruker). Chemical shifts of ^{1}H and ^{13}C NMR signals were quoted to tetramethylsilane (δ = 0.00) and $CDCl_3$ (δ = 77.0) as internal standards, respectively. Matrix-assisted laser desorption ionization time-of-flight (MALDI-TOF) mass spectra were collected on an Autoflex III spectrometer (Bruker Daltonics) using dithranol as the matrix. Elemental analyses were carried out with an MT-5 CHN corder (Yanaco). UV/vis absorption and PL spectra were measured with a UV-2550 spectrometer (Shimadzu) and a Fluoromax-4 spectrophotometer (Horiba Scientific), respectively. The Φ_{PL} were measured using an integration sphere system coupled with a photonic multichannel analyzer (Hamamatsu Photonics C9920-02, PMA-11). The luminescence intensities and lifetimes of solutions and thin films were measured using a Quantaurus-Tau (Hamamatsu Photonics) with an LED lamp (λ = 340 nm, frequency = 50 Hz) under N_2, and a Streak camera (Hamamatsu Photonics C4334) with an N_2 gas laser (λ = 337 nm, pulse width = 500 ps, repetition rate = 20 Hz) under vacuum ($< 4 \times 10^{-1}$ Pa). The HOMO energy levels (or ionization energies) for thin films were determined using an AC-3 ultraviolet photoelectron spectrometer (Riken-Keiki). The LUMO energy levels were estimated by subtracting the optical energy gap (E_g) from the measured HOMO energies; E_g values were determined from the onset position of the absorption spectra of thin films. All quantum chemical calculations were performed using the Gaussian 03 program package.[12] Geometry optimization was carried out using the B3LYP functional with the 6-31G(d,p) basis set. Low-lying excited singlet and triplet states were computed using the optimized structures with time-dependent density functional theory (TD-DFT) at the same level.

6.4.2 OLED device fabrication and Measurements

To measure EL of the OLEDs using heteroatom-bridged molecules derivatives as emitter, a clean glass substrate precoated with a 110-nm-thick ITO layer with a sheet resistance of < 20 $\Omega\ \square^{-1}$ was used. The substrate was degreased with distilled water, a neutral detergent, acetone, isopropyl alcohol, and cleaned in UV-ozone chamber (Nippon Laser and Electrics lab.

NLUV253) before it loaded into an evaporation system. The organic layers were thermally evaporated on the substrates under a vacuum of < 3×10^{-4} Pa with an evaporation rate of < 0.3 nm s^{-1}. In all devices, a cathode aluminum (Al) layer was deposited through a 1 mm-diameter opening in a shadow mask. The current density and voltage (J–V) characteristics of OLEDs were measured using a semiconductor parameter analyzer (Agilent E5273A). The EL spectra were recorded by multi channel analyzer (Ocean Optics SD2000) at current densities of 1, 10, and 100 mA cm^{-2}. The brightness of OLEDs was measured using an optical powermeter (Newport 1930C).

6.4.3 Materials and Syntheses of Heteroatom-Bridged Molecules

All reagents and solvents were purchased from Sigma-Aldrich, Tokyo Chemical Industry (TCI), or Wako Pure Chemical Industries and used as received unless otherwise noted. The synthetic routes to obtain **1**–**4** are outlined in Scheme 6-1. All reactions were performed under an N_2 atmosphere in dry solvents. The final products were fully characterized by ^1H and ^{13}C NMR spectroscopy, MALDI-TOF mass spectrometry, and elemental analysis, as indicated.

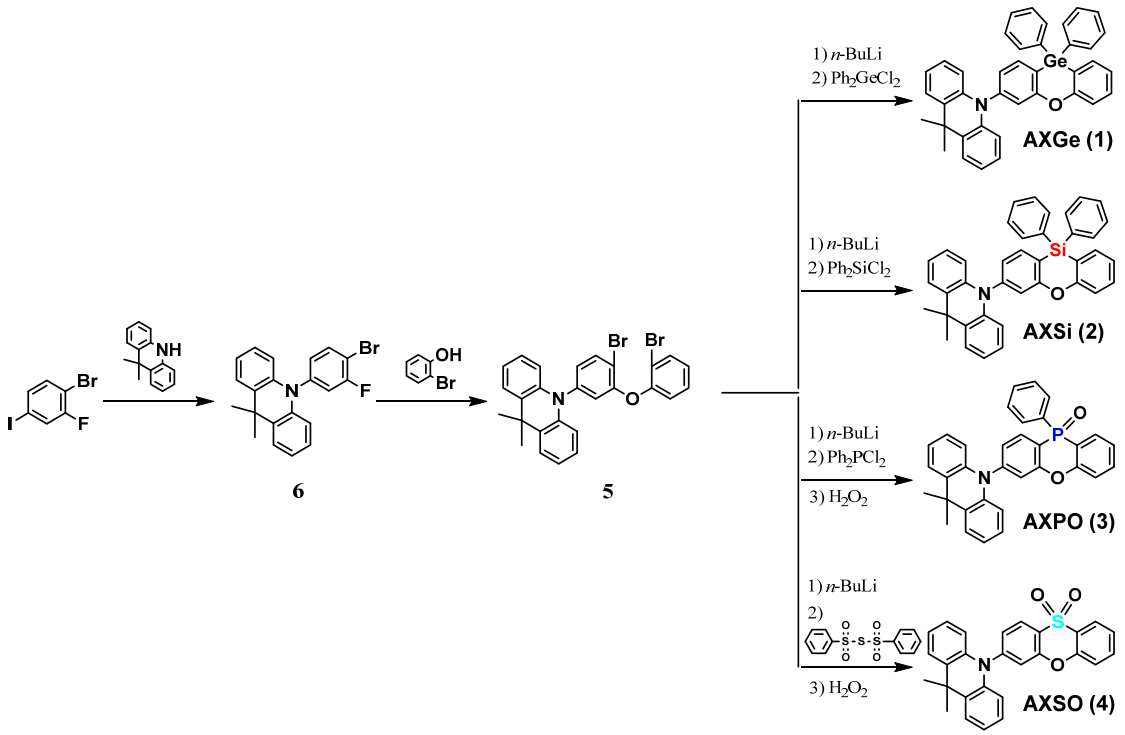

Scheme 6-1. Synthetic routes for **1**–**4**.

10-(4-bromo-3-fluorophenyl)-9,9-dimethyl-9,10-dihydroacridine **(6).** A mixture of 1-bromo-2-fluoro-4-iodobenzene (24.1 g, 80 mmol), 9,9-dimethyl-9,10-dihydroacridine (16.7 g, 80 mol), sodium *tert*-butoxide (11.5 g, 120 mmol), copper(I) iodide (0.3 g , 1.6 mmol), and *trans*-1,2-diaminocyclohexane (0.96 ml, 8.0 mmol) in dry 1,4-dioxane (80 mL) was refluxed for 24 h. The reaction mixture was poured in to water and extracted with toluene. The combined organic layer were washed with water, and dried over $MgSO_4$. After the filtration and evaporation, the product was purified by silica gel column chromatography (eluent: hexane/toluene = 1.5:1, v/v), and recrystallized from hexane and dried under vacuum to afford **6** as a white solid (yield = 22.0 g, 72.0%). ^{1}H NMR (500 MHz, $CDCl_3$): δ 7.81 (t, J = 8.5Hz, 1H), 7.46 (dd, J = 7.5Hz, 1.5Hz, 2H), 7.16 (dd, J = 7.5Hz, 1.0Hz, 1H), 7.06 (dd, J = 8.5Hz, 1.5Hz, 1H), 7.02−6.94 (m, 4H), 6.27 (dd, J = 8.0Hz, 1.5Hz, 2H), 1.67 (s, 6H). MS (MALDI): m/z 382.28 $[M]^+$; calcd 382.48.

10-(4-bromo-3-fluorophenyl)-9,9-dimethyl-9,10-dihydroacridine **(5).** A mixture of compound **6** (7.6 g, 20 mmol), 2-bromophenol (8.4 ml, 80 mmol), potassium carbonate (11.1 g, 80 mmol) in triglyme (10 mL) was stirred for 72 h at 190 °C. After cooling to room temperature, the reaction mixture was poured into water and extracted with toluene. The combined organic layers were washed with water, and dried over anhydrous $MgSO_4$. The resulting solution was filtered through a Celite pad. The filtrate was concentrated by evaporation and the product was purified by silica gel column chromatography (eluent: hexane/CH_2Cl_2 = 1.5:1, v/v), and recrystallized from methanol/CH_2Cl_2 and dried under vacuum to afford **5** as a white solid (yield = 8.69 g, 81.2%). ^{1}H NMR (500 MHz, $CDCl_3$): δ 7.89 (d, J = 8.5Hz, 1H), 7.59 (dd, J = 8.0Hz, 1.5Hz, 1H), 7.42 (dd, J = 7.5Hz, 1.5Hz, 2H), 7.28 (td, J = 8.0Hz, 1.5Hz, 1H), 7.04−6.97 (m, 5H), 6.92 (td, J = 7.5Hz, 1.0Hz, 2H), 6.70 (s, 1H), 6.27 (dd, J = 8.0Hz, 1.0Hz, 2H), 1.63 (s, 6H). MS (MALDI): m/z 535.28 $[M]^+$; calcd 535.51.

AXGe (1). To a stirred solution of compound **5** (1.64 g, 3.0 mmol) in dry THF (50 mL) was added dropwise *n*-butyllithium (3.8 mL, 6.0 mmol) at −78 °C and mixture was allowed to react for 1 h at that temperature. Diphenylgermanium dichloride (0.8 ml, 3.3 mmol) was then added, and the mixture was stirred overnight at room temperature. The reaction mixture was poured into water and extracted with CH_2Cl_2. The combined organic layers were washed with water, and dried over anhydrous $MgSO_4$. The resulting solution was filtered through a Celite pad. The filtrate was concentrated by evaporation and the product was purified by silica gel column

chromatography (eluent: hexane/CH_2Cl_2 = 3:1, v/v), and recrystallized from hexane/EtOAc and dried under vacuum to afford **1** as a white solid (yield = 0.98 g, 54.1%). ^{1}H NMR (500 MHz, $CDCl_3$): δ 7.77 (d, J = 7.5Hz, 1H), 7.61 (dd, J = 7.0Hz, 1.5Hz, 4H), 7.55 (dd, J = 7.5Hz, 1.5Hz, 1H), 7.46−7.41 (m, 9H), 7.28 (s, 1H), 7.25 (td, J = 8.0Hz, 1.0Hz, 1H), 7.16 (td, J = 7.0Hz, 1.0Hz, 1H), 7.11 (dd, J = 7.5Hz, 2.0Hz, 1H), 6.99 (td, J = 7.0Hz, 1.0Hz, 2H), 6.92 (td, J = 7.0Hz, 1.0Hz, 2H), 6.38 (dd, J = 8.0Hz, 1.0Hz, 2H), 1.69 (s, 6H). ^{13}C{^{1}H} NMR (125 MHz, $CDCl_3$): δ 161.35, 159.38, 143.81, 140.64, 137.07, 135.03, 134.93, 131.26, 130.09, 129.68, 128.59, 126.39, 125.75, 125.16, 123.47, 121.35, 120.67, 118.88, 118.74, 118.13, 114.24, 35.98, 31.21. MS (MALDI): m/z 602.31 $[M]^+$; calcd 602.45 Anal. calcd (%) for $C_{39}H_{31}N$: C, 77.77; H, 5.19; N, 2.33; found: C, 77.68; H, 5.32; N, 2.35.

AXSi (2). Compound **2** was synthesized similarly to **1**, using compound **5** (1.64 g, 3.0 mmol), *n*-butyllithium (3.8 mL, 6.0 mmol), and dichlorodiphenylsilane (0.63 ml, 3.3 mmol). The product was obtained as white solid (yield = 0.96 g, 57.2%). ^{1}H NMR (500 MHz, $CDCl_3$): δ 7.82 (d, J = 7.5Hz, 1H), 7.75 (dd, J = 7.5Hz, 1.0Hz, 4H), 7.61 (dd, J = 7.0Hz, 1.5Hz, 1H), 7.49−7.40 (m, 9H), 7.28 (s, 1H), 7.25 (t, J = 8.5Hz, 1H), 7.17 (td, J = 7.0Hz, 1.0Hz, 1H), 7.11 (dd, J = 8.0Hz, 1.5Hz, 1H), 6.99 (td, J = 8.0Hz, 1.5Hz, 2H), 6.38 (dd, J = 7.0Hz, 1.0Hz, 2H), 6.94 (td, J = 7.5Hz, 1.5Hz, 2H), 1.69 (s, 6H). ^{13}C{^{1}H} NMR (125 MHz, $CDCl_3$): δ 162.16, 160.20, 144.37, 140.59, 137.59, 135.96, 135.45, 133.69, 131.85, 130.16, 130.14, 128.18, 126.39, 125.39, 125.15, 123.14, 120.89, 120.72, 118.31, 116.29, 115.70, 114.27, 36.00, 31.15. MS (MALDI): m/z 557.77 $[M]^+$; calcd 557.82. Anal. calcd (%) for $C_{39}H_{31}N$: C, 83.98; H, 5.60; N, 2.51; found: C, 83.51; H, 5.59; N, 2.45.

AXPO (3). To a stirred solution of compound **5** (1.64 g, 3.0 mmol) in dry THF (50 mL) was added dropwise *n*-butyllithium (3.8 mL, 6.0 mmol) at −78 ºC and mixture was allowed to react for 1 h at that temperature. Dichlorophenylphosphine (0.4 ml, 3.3 mmol) was then added, and the mixture was stirred overnight at room temperature. To this solution was added dropwise 0.1 ml of hydrogen peroxide (ca. 30%) and stirred over 6 h at room temperature. The reaction mixture was poured into water and extracted with CH_2Cl_2. The combined organic layers were washed with water, and dried over anhydrous $MgSO_4$. The resulting solution was filtered through a Celite pad. The filtrate was concentrated by evaporation and the product was purified by silica gel column chromatography (eluent: hexane/CH_2Cl_2 = 3:1, v/v), and recrystallized from hexane/EtOAc and dried under vacuum to afford **3** as a white solid (yield = 0.64 g, 42.5%).

^{1}H NMR (500 MHz, DMSO): δ 7.94−7.89 (m, 1H), 7.76 (td, J = 7.0Hz, 1.5Hz, 1H), 7.72−7.49 (m, 10H), 7.39 (t, J = 7.5Hz, 1H), 7.33 (d, J = 8.0Hz, 1H), 7.04 (td, J = 7.5Hz, 1.5Hz, 2H), 6.98 (td, J = 7.5Hz, 1.5Hz, 2H), 6.40 (dd, J = 8.0Hz, 1.0Hz, 2H), 1.62 (s, 6H). ^{13}C{^{1}H} NMR (125 MHz, $CDCl_3$): δ 157.59, 157.57, 155.72, 155.70, 146.86, 140.22, 134.09, 134.04, 133.79, 133.75, 132.06, 132.03, 131.84, 131.76, 131.45, 131.41, 131.28, 128.75, 128.65, 126.45, 126.06, 124.49, 124.41, 121.47, 119.89, 119.84, 118.42, 118.37, 118.37, 115.77, 115.33, 114.90, 114.51, 36.16, 30.89. MS (MALDI): m/z 499.55 [M+H]$^{+}$; calcd 501.20. Anal. calcd (%) for $C_{33}H_{26}N$: C, 79.34; H, 5.25; N, 2.80; found: C, 79.12; H, 5.22; N, 2.76.

AXSO (4). Compound **4** was synthesized similarly to **3**, using compound **5** (1.64 g, 3.0 mmol), *n*-butyllithium (3.8 mL, 6.0 mmol), and bis(phenylsulfonyl)sulfide (0.99 g , 3.2 mmol), and 0.1 ml of hydrogen peroxide (ca. 30%). The product was obtained as white solid (yield = 0.54 g, 40.7%). ^{1}H NMR (500 MHz, $CDCl_3$): δ 8.24 (dd, J = 7.5Hz, 1.5Hz, 1H), 8.11 (dd, J = 8.0Hz, 1.5Hz, 1H), 7.67 (td, J = 7.5Hz, 1.5Hz, 1H), 7.50−7.38 (m, 6H), 7.09−7.02 (m, 4H), 6.49 (dd, J = 8.0Hz, 1.5Hz, 2H), 1.67 (s, 6H). ^{13}C{^{1}H} NMR (125 MHz, $CDCl_3$): δ 153.51, 151.53, 147.63, 140.05, 134.28, 132.77, 126.54, 125.88, 125.40, 125.28, 125.15, 123.48, 123.16, 122.24, 118.96, 118.51, 115.98, 36.41, 30.55. MS (MALDI): m/z 439.53 [M+H]$^{+}$; calcd 439.99 Anal. calcd (%) for $C_{27}H_{21}N$: C, 73.78; H, 4.82; N, 3.19; found: C, 73.44; H, 4.85; N, 3.16.

6.5 References

[1] H. Yersin, *Highly Efficient OLEDs with Phosphorescent Materials*, **2008**, Wiley-VCH.

[2] S. Y. Lee, T. Yasuda, Y. S. Yang, Q. Zhang, and C. Adachi, *Angew. Chem. Int. Ed*., **2014**, 126, 6520.

[3] R. Kondo, T. Yasuda, Y. S. Yang, J. Y. Kim, and C. Adachi, *J. Mater. Chem*., **2012**, 22, 16810.

[4] K. Tamao, M. Uchida, T. Izumizawa, K. Furukawa and S. Yamaguchi, *J. Am. Chem. Soc*., **1996**, 118, 11974;

[5] T. Lee, I. Jung, K. H. Song, H. Lee, J. Choi, K. Lee, B. J. Lee, J. Y. Pak, C. Lee, S. O. Kang and J. Ko, *Organometallics*, **2004**, 23, 5280.

[6] D. Yokoyama and C. Adachi, *J. Appl. Phys*., **2010**, 107, 123512.

[7] H. Uoyama, K. Goushi, K. Shizu, H. Nomura, C. Adachi, *Nature*, **2012**, 492, 234.

[8] K. Goushi, K. Yoshida, K. Sato, and C. Adachi, *Nat. Photon*., **2012**, 6, 253.

[9] D. Beljonne, Z. Shuai, G. Pourtois, and J. L. Bredas, *J. Phys. Chem. A*, **2001**, 105, 3899.

[10] N. J. Turro, *Modern Molecular Photochemistry*, **1991**, University science book.

[11] H. Sasabe and J. Kido, *Chem. Mater*., **2011**, 23, 621.

[12] M. J. Frisch, G. W. Trucks, H. B. Schlegel, G. E. Scuseria, M. A. Robb, J. R. Cheeseman, J. A. Montgomery, Jr., T. Vreven, K. N. Kudin, J. C. Burant, J. M. Millam, S. S. Iyengar, J. Tomasi, V. Barone, B. Mennucci, M. Cossi, G. Scalmani, N. Rega, G. A. Petersson, H. Nakatsuji, M. Hada, M. Ehara, K. Toyota, R. Fukuda, J. Hasegawa, M. Ishida, T. Nakajima, Y. Honda, O. Kitao, H. Nakai, M. Klene, X. Li, J. E. Knox, H. P. Hratchian, J. B. Cross, C. Adamo, J. Jaramillo, R. Gomperts, R. E. Stratmann, O. Yazyev, A. J. Austin, R. Cammi, C. Pomelli, J. W. Ochterski, P. Y. Ayala, K. Morokuma, G. A. Voth, P. Salvador, J. J. Dannenberg, V. G. Zakrzewski, S. Dapprich, A. D. Daniels, M. C. Strain, O. Farkas, D. K. Malick, A. D. Rabuck, K. Raghavachari, J. B. Foresman, J. V. Ortiz, Q. Cui, A. G. Baboul, S. Clifford, J. Cioslowski, B. B. Stefanov, G. Liu, A. Liashenko, P. Piskorz, I. Komaromi, R. L. Martin, D. J. Fox, T. Keith, M. A. Al-Laham, C. Y. Peng, A. Nanayakkara, M. Challacombe, P. M. W. Gill, B. Johnson, W. Chen, M. W. Wong, C. Gonzalez, and J. A. Pople, Gaussian 03, Gaussian, Inc., Pittsburgh PA, **2003**.

Chapter 7
Conclusions and Perspective

Chapter 7
Conclusions and Perspective

In this study, we developed highly efficient TADF materials and these materials were applied to OLEDs. Well-desigend TADF molecules exbihited a small ΔE_{ST} between S_1 and T_1 and OLEDs using TADF molecules as an emitter exhibited high η_{ext} which exceeded conventional fluorescence OLEDs. Various photophysical characterisitics of TADF molecules were investigated under photo- and electrical-excitaions.

Chapter 2: A new design concept to control ΔE_{ST} by tunning the donor and acceptor units in carbazole-triazine combined TADF material **CC2TA** has been developed. Host dependent TADF properties are investigated for maximizing TADF emission. The optimized TADF device based on **CC2TA** achieved relatively high η_{ext} of 11.2%. The newly designed molecular structure provide a guideline for strong delayed fluorescence.

Chapter 3: Benzophenone based butterfly-shaped materials are designed for efficient full-color delayed fluorescence emission. The benzophenone based on D-A-D frameworks is suitable for the production of organic luminophores exhibiting highly efficient TADF emission covering the full color spectrum. OLEDs employing the benzophenone derivatives as emitters generated EL spectra ranging from blue to orange-red and achieved maximum η_{ext} of up to 14.3%. Moreover, high color purity WOLEDs is fabricated to combination of yellow and sky-blue emissive benzophenone derivatives.

Chapter 4: Donor-acceptor crossed x-shaped TADF materials were designed using benzoyl benzophenone derivatives. The bulky phenyl rings of benzoyl benzophenone unit led to strong steric hindrance between donor and acceptor units which contribute to realize a small ΔE_{ST} for efficient TADF emission. Decay processes in linear- and x-shaped benzoylbenzophenone were investigated and the non-radiative decay processes of linear- and x-shaped-molecules are investigated and determined the relation between molecular structure and Φ_{PL}. OLEDs based

on x-shaped benzophenone derivatives as emitters exhibited high η_{ext} of up to 11% for green and yellow emissions.

Chapter 5: First TADF polymer materials were designed for solution-processable TADF-OLEDs. The benzophenone-based donor-acceptor frameworks of polymers having isolated HOMO and LUMO contributed to realize a small ΔE_{ST} which enabled efficient exciton-harvesting through TADF. Solvatochromic properties of polymers in polar solvent was examined and the strong CT emission were confirmed. Well optimized OLEDs employing the TADF polymers as emitters were fabricated by solution process and achieved high efficiency in green and yellow emissions.

Chapter 6: Heteroatom-bridged TADF molecules having a small ΔE_{ST} and short τ were designed for effective TADF emission. The isolated π-conjugation of the molecular structure provide a very high T_1 energy level and the vertically connected donor-acceptor structure contributed to a small ΔE_{ST} and short τ. Phosphor and sulfur bridged molecules of **AXPO** and **AXSO** exhibited deep-blue and sky-blue emission with high Φ_{PL} and strong TADF characteristics. OLEDs employing **AXPO** and **AXSO** as emitters achieved pure deep-blue emission (CIE coordinates of x: 0.15, y: 0.14) and η_{ext} = 20.5%.

A wide variety of TADF materials are newly explored and designed through this thesis. The author confirmed a wide variety of emission colors and sufficiently high η_{ext} ~ 20%. However, for commercial applications, further molecular design should be considered from the aspect of stability of radical cation and anion of TADF molecules.

Accomplishments

Accomplishments

Publication

Original Papers

[1] "High-efficiency Organic Light-emitting Diodes utilizing Thermally-activated Delayed Fluorescence from Triazine-based donor-acceptor Hybrid Molecules" (chapter 2)
Sae Youn Lee, Takuma Yasuda, Hiroko Nomura, and Chihaya Adachi, *Appl. Phys. Lett.*, **2012**, 101, 093306.

[2] "Luminous Butterflies: Efficient Exciton Harvesting by Benzophenone Derivatives for Full-Color Delayed Fluorescence OLEDs" (chapter 3)
Sae Youn Lee, Takuma Yasuda, Yu Seok Yang, Qisheng Zhang, and Chihaya Adachi, *Angew. Chem. Int. Ed.*, **2014**, 126, 6520.

[3] "X-Shaped Benzoylbenzophenone Derivatives with Crossed Donors and Acceptors for Highly Efficient Thermally Activated Delayed Fluorescence" (chapter 4)
Sae Youn Lee, Takuma Yasuda, In Seob Park, and Chihaya Adachi, *Dalton. Trans.*, *in press*.

[4] "Thermally Activated Delayed Fluorescence Polymers for Efficient Solution-Processed Organic Light-Emitting Diodes" (chapter 5)
Sae Youn Lee, Takuma Yasuda, Takuro Nishimoto, and Chihaya Adachi, in preparation.

[5] "Highly Effective Blue Organic Light-Emitting Diodes based on Heteroatom-Bridged Thermally Activated Delayed Fluorescence molecules" (chapter 6)
Sae Youn Lee, Takuma Yasuda, Masaki Numata, and Chihaya Adachi, in preparation.

Reference Papers

[1] “A Six-carbazole-decorated Cyclophosphazene as a Host with High Triplet Energy to Realize Efficient Delayed-fluorescence OLEDs”
Takuro Nishimoto, Takuma Yasuda, Sae Youn Lee, Ryosuke Kondo, and Chihaya Adachi, *Mater. Horizons*, **2014**, 1, 264.

[2] “Efficiency enhancement of Organic Light-emitting Diodes incorporating a Highly Oriented Thermally-activated Delayed Fluorescence Emitter”
Christian Mayr, Sae Youn Lee, Tobias D. Schmidt, Takeshi Komino, Takuma Yasuda, Chihaya Adachi, and Wolfgang Brütting, *Adv. Funct. Mater*., **2014**, 24, 5232.

[3] “Highly Efficient Blue Electroluminescence based on Thermally Activated Delayed Fluorescence”
Shuzo Hirata, Yumi Sakai, Kensuke Masui, Hiroyuki Tanaka, Sae Youn Lee, Hiroko Nomura, Nozomi Nakamura, Mao Yasumatsu, Hajime Nakanotani, Qishing Zhang, Katsuyuki Shizu, Hiroshi Miyazaki, and Chihaya Adachi, *Nat. Mater*., *in press*.

Reviews

[1]「高効率熱活性遅延蛍光材料の開発と有機ELへの展開」
安田 琢麿, 李 世淵, 安達 千波矢, 科学と工業, 第88巻, 第10号, pp. 363−367, **2014**.

Symposium

International Symposium

[1] "Molecular Design of Triazine Derivatives Having a High Up-conversion Efficiency from Triplet into Singlet Excited States and their Application for OLEDs"
Sae Youn Lee, Hiroko Nomura, Takuma Yasuda, and Chihaya Adachi, *SPIE Photonics Europe 2012*, **Oral presentation**, 8435-9, Brussels, Belgium, April 2012.

[2] "Molecular Design of Triazine Derivatives Having a High Up-conversion Efficiency from Triplet into Singlet Excited States and their Application for OLEDs"
Sae Youn Lee, Hiroko Nomura, Takuma Yasuda, and Chihaya Adachi, *The 9th International Conference on Electroluminescence & Organic Optoelectronics (ICEL 2012)*, **Oral presentation**, O-28, Fukuoka, Japan, September, 2012.

[3] "Organic Light-emitting Diodes Employing Efficient Reverse intersystem Crossing Aimed for Ultimate EL efficiency"
Sae Youn Lee, *The International Conference on Electronic Materials and Nanotechnology for Green Environment 2012 (ENGE 2012)*, **Oral presentation**, TB-0987, Jeju, Korea, September 2012.

[4] "Triazine-based Donor-acceptor Hybrid Molecules for High-efficiency Thermally-activated Delayed Fluorescence OLEDs"
Sae Youn Lee, Hiroko Nomura, Takuma Yasuda, and Chihaya Adachi, *2013 MRS Spring Meeting & Exhibit*, **Poster presentation**, JJ13.29, San Francisco, USA, April 2013.

[5] "Design of Highly Luminescent and Stable Benzophenone-based Molecules for OLEDs Displaying Efficient Thermally-activated Delayed Fluorescence"
Sae Youn Lee, Takuma Yasuda, Yu Seok Yang, Qisheng Zhang, and Chihaya Adachi, *SPIE Photonics Europe 2014*, **Oral presentation**, 9137-17, Brussels, Belgium, April 2014.

[6] “Molecular Design of Butterfly-Shaped Benzophenone Derivatives and Their Application to OLEDs Displaying Efficient Thermally Activated Delayed Fluorescence”
Sae Youn Lee, Takuma Yasuda, Yu Seok Yang, Qisheng Zhang, and Chihaya Adachi, *2014 MRS Spring Meeting & Exhibit*, **Poster presentation**, C6.48, San Francisco, USA, April 2014.

[7] “Molecular Design of Butterfly-Shaped Benzophenone Derivatives and Their Application to OLEDs Based on Thermally-activated Delayed Fluorescence”
Sae Youn Lee, Takuma Yasuda, Yu Seok Yang, Qisheng Zhang, and Chihaya Adachi, *The 5th International Conference on White LEDs and Solid State Lighting (WLED-5)*, **Poster presentation**, P2-1, Jeju, Korea, June 2014.

Awards

[1] “Organic Light-emitting Diodes Employing Efficient Reverse intersystem Crossing Aimed for Ultimate EL efficiency”
Sae Youn Lee, Hiroko Nomura, Takuma Yasuda, and Chihaya Adachi
ICEL 2012, Oral presentation, O-28, Fukuoka, Japan, September 2012, **The Best Oral Presentation Awards for Young Scientist**.

[2] “Enhancement of SiRNA delivery for effective gene therapy using conductive polymer carrier”
Sae Youn Lee
平成24年度リサーチプロポーザル，九州大学，2013年12月，**優秀賞**.

[3] “Triazine-based Donor-acceptor Hybrid Molecules for High-efficiency Thermally-activated Delayed Fluorescence OLEDs”
Sae Youn Lee, Hiroko Nomura, Takuma Yasuda, and Chihaya Adachi
2013 MRS Spring Meeting & Exhibit, Poster presentation, C6.48, San Francisco, USA, April 2013, **MRS Poster Awards**.

Patent

[1] “有機発光素子ならびにそれに用いる遅延蛍光材料および化合物”, **PCT disclosure**
Sae Youn Lee, Hiroko Nomura, Tetsuya Nakagawa, Takuma Yasuda, and Chihaya Adachi, Publication No. WO/2013/081088 (2013/6/6).

[2] “電荷輸送材料、ホスト材料、薄膜及び有機発光素子”, **PCT application**
Sae Youn Lee, Takuro Nishimoto, Takuma Yasuda, and Chihaya Adachi, Application No. PCT/JP2014/055427(2014/3/4).

[3] “電荷輸送材料、ホスト材料、薄膜及び有機発光素子”, **Taiwan application**
Sae Youn Lee, Takuro Nishimoto, Takuma Yasuda, and Chihaya Adachi, Application No. 103107523 (2014/3/5).

[4] “発光材料、有機発光素子および化合物”, **PCT application**
Sae Youn Lee, Takuma Yasuda, and Chihaya Adachi, Application No. PCT/JP2014/060051 (2014/4/7).

[5] “発光材料、有機発光素子および化合物”, **Japan application**
Sae Youn Lee, Takuma Yasuda, M. Numata, In Seob Park, and Chihaya Adachi, Application No. 特願 2013-246519 (2013/11/28).

[6] “有機発光素子、ホスト材料、発光材料および化合物”, **Japan application**
Sae Youn Lee, Takuro Nishimoto, Takuma Yasuda, and Chihaya Adachi, Application No. 特願 2014-047342 (2014/3/11).

Acknowledgement

Acknowledgement

Firstly, the author would like to express his gratitude to Professor Chihaya Adachi at Kyushu University for his helpful advice and sincere assistance during the research. His definite guidance of research and firm belief in author's work were called up author's courage and became power of the study.

The author would like to acknowledge the continuing counseling and encouragement of Professor Takuma Yasuda in synthesis and summarizing this work. His valuable advices of studies are became the foundation for success of the synthesis.

The author also would like to thank Ms. Hiroko Nomura and Dr. Yu Seok Yang for their great help in synthesis and Dr. William Jr. Potscavage for correction of the content of this thesis.

Worm thanks are dedicated to Research Associate Professor Qisheng Zhang for supplying very precious sample and to Mr. Keigo Sato and Dr. Jun Youn Kim for the activity measurements, Ms. Jiyoung Lee for help for molecular orbital calculation.

The author also thanks to my group members, Dr. Shigeyuki Matsunami, Mr. Hiroshi Miyazaki, Ms. Yumi Sakai, Assistant Professor. Shuzo Hirata, Assistant Professor. Kenichi Goushi, Assistant Professor. Masatsu Taneda, Assistant Professor Takeshi Komino, Professor Hajime Nakanotani, Assistant Professor. Ryota Kabe, Dr. Tetsuya Nakagawa, Dr. Gabor Mehes, Dr. Kazunori Togashi, Dr. Masaya Hirade, Mr. Nomura Shintaro, Mr. Keiro Nasu, Mr. Mao Sumino, Mr. Hayato Kakizoe, Ms. Hyun Jung Seo, Mr. Kou Yoshida, Ms. Miki Kamoto, Mr. Yuji Aramaki, Mr. Toshiharu Arai, Mr. Ryosuke Kondo, Mr. Yuta Sagara, Mr. Ryosuke Nakamichi, Mr. Issei Otani, Mr. Takahiro Komori, Mr. Keiske Asahi, Mr. Yuta Fukutomi, Mr. Takuro Nishimoto, Mr. Hiroyuki Mieno, Mr. Takahiro Higuchi, Yuta Hirayama, Mr. Yu Hidaka, Mr. Seichi Furukawa, Mr. Chao-Jen Tsou, Mr. Tatsuya Oyama, Mr. Hiroki Tachibana, Mr. Dae Hyun Kim, Mr. In Seob Park, Ms. Myung Eun Jang, Ms. Nozomi Nakamura, Ms. Akiko Hamada, Ms. Mao Yasumasu, Ms. Yuko Morimoto, Ms. Michiko Kita, Ms. Sachiko Higashikawa, Ms. Sayoko Otomo, Ms. Rei Sasagawa, Ms. Mayumi Kudo, Ms. Yoshiko Oohara, and Ms. Hiromo Aizaki.

The author is greatly indebted to Professor Sung-Kyu Hong who gave him to great opportunity of study in Kyushu University.

This work was supported by a Grant-in-Aid from the Funding Program for World-Leading Innovation R&D on Science and Technology (FIRST) and by grants from JSPS Young

Scientists (A) (No. 25708032) and Challenging Exploratory Research (No. 26620168).

Finally, author deeply appreciates grandparents Bum Ju Lee, Byung Il Yu, his parents Yong Cheol Lee, Eun Soon Choi, his younger sister Bu Yeon Lee and Eun Kyung Lee of genuine encouragement and constant supporting throughout his matser and doctoral course in Japan.

February, 2015

Sae Youn Lee